Control Strategies for Series Hybrid Electric Vehicles

Wassif Shabbir

A thesis submitted for the degree of
Doctor of Philosophy
August 2015

Control and Power Group
Electrical and Electronic Engineering
Imperial College London

I declare that this thesis is the result of my own work, and that any ideas or quotations from the work of other people are appropriately referenced.

Abstract

This thesis deals with the energy management problem of series hybrid electric vehicles (HEVs), where the objective is to maximize fuel economy for general driving. The work employs a high-fidelity model that has been refined to deliver appropriate level of dynamics (for the purposes of this research) at an acceptable computational burden. The model is then used to design, test and study established conventional control strategies, which then act as benchmarks and inspiration for proposed novel control strategies.

A family of efficiency maximizing map strategies (EMMS) are developed based on a thorough and holistic analysis of the powertrain efficiencies. The real-time variants are found to deliver impressive fuel economy, and the global variant is found to outperform the conventional global benchmark. Two heuristic strategies are developed (exclusive operation strategy (XOS) and optimal primary source strategy (OPSS)) that are found to deliver significantly better fuel economy results, compared to conventional alternatives, and further desirable traits. This is found to be particularly related to the better use of modern start stop systems (SSSs) that has not been considered sufficiently in the past.

A global heuristic strategy (GHS) is presented that successfully outperforms the conventional global benchmark without any particularly complex analysis. This exposes some of the limitations of optimization-based techniques that have been developed for simple vehicle models. Lastly, the sensitivity of the performance of the control strategies has been studied for variations in tuning accuracy, SSS efficiency, vehicle initial conditions, and general driving conditions. This allows a deeper insight into each control strategy, exposing strengths and limitations that have not been apparent from past work.

Acknowledgments

First and foremost, I would like to thank my supervisor Dr. Simos Evangelou, who has offered timely support and guidance whenever needed. He encouraged me to explore a wide range of research interests, which kept expanding from our stimulating conversations, contributing greatly to my productivity as well as how much I enjoyed my research. Aside from the happy times at Imperial, I will cherish the memories of our amazing time in South Carolina, Hawaii and South Africa together.

It has also been a privilege to work with Prof. Meisel, whose immense practical knowledge of vehicles has been invaluable to me. Working and publishing together with him has undoubtedly made me a better researcher, and made me appreciate my research in a broader context.

A special thanks to Carlos, who has been taking his PhD journey alongside me. When I got stuck or had a problem, he would be the first person I would discuss it with. Apart from the research, I have also really enjoyed our frequent breaks, together with Hadi and Zohaib, discussing anything between heaven and earth. Every day has been a joy.

These years would have been less incredible, if it was not for all the friends I met in London. A lot of great memories with Andy, Atsushi, Cheng and Saad throughout the Imperial days, always providing perspective. I am also grateful for all the amazing people I got to work with through ICCS and ICG: these times have been an integral part of my life at Imperial.

Finally, I am deeply grateful for my family and their unconditional love and encouragement. Particular thanks to Saddaf who offered valuable feedback in the completion of this thesis. My visits back home were always refreshing, in particular when seeing my niece and nephews Isabella, Fawad and Noah.

Contents

List of Figures

List of Tables

List of Publications

Journal Articles

- M. Roche, W. Shabbir, and S. A. Evangelou, "Voltage control for enhanced power electronic efficiency in series hybrid electric vehicles," IEEE Transactions on Vehicular Technology, in review.
- W. Shabbir and S. A. Evangelou, "Exclusive operation strategy for the supervisory control of series hybrid electric vehicles," IEEE Transactions on Control Systems Technology, in press.
- W. Shabbir and S. A. Evangelou, "Real-time control strategy to maximize hybrid electric vehicle powertrain efficiency," Applied Energy, vol. 135, pp. 512–522, 2014.

Conference Articles

- S. A. Evangelou and W. Shabbir, "Dynamic modeling platform for series hybrid electric vehicles," in Advances in Automotive Control (AAC), IFAC, in review.
- J. Meisel, W. Shabbir, and S. A. Evangelou, "Control of PHEV and HEV parallel powertrains using a sequential linearization algorithm," in SAE World Congress, SAE Technical Paper, 2015.
- W. Shabbir and S. A. Evangelou, "Efficiency analysis of a continuously variable transmission with linear control for a series hybrid electric vehicle," in IFAC World Congress, vol. 19, pp. 6264–6269, 2014.
- J. Meisel, W. Shabbir, and S. A. Evangelou, "Evaluation of the through-the-road architecture for plug-in hybrid electric vehicle powertrains," in International Electric Vehicle Conference (IEVC), pp. 1–5, IEEE, 2013.
- J. Meisel, W. Shabbir, and S. A. Evangelou, "A practical control methodology for parallel plug-in hybrid electric vehicle powertrains," in Vehicle Power and Propulsion Conference (VPPC), pp. 1–6, IEEE, 2013.
- W. Shabbir and S. A. Evangelou, "Efficiency maximizing and charge sustaining supervisory control for series hybrid electric vehicles," in Conference on Decision and Control (CDC), pp. 6327–6332, IEEE, 2012.
- W. Shabbir, C. Arana, and S. A. Evangelou, "Series hybrid electric vehicle supervisory control based on off-line efficiency optimization," in International Electric Vehicle Conference (IEVC), pp. 1–5, IEEE, 2012.

Abbreviations

AL	Algebraic Loop
BSFC	Break Specific Fuel Consumption
CS	Charge Sustaining
CSI	Charge Sustaining Intensity
CVT	Continuously Variable Transmission
DP	Dynamic Programming
ECMS	Equivalent Consumption Minimization Strategy
EFC	Equivalent Fuel Consumption
FLC	Fuzzy Logic Controller
EMMS	Efficiency Maximizing Map Strategy
GECMS	Global Equivalent Consumption Minimization Strategy
GEMMS	Global Efficiency Maximizing Map Strategy
GHS	Global Heuristic Strategy
HEV	Hybrid Electric Vehicle
ICE	Internal Combustion Engine
MPC	Model Predictive Control
NN	Neural Networks
OPSS	Optimal Primary Source Strategy
PFCS	Power Follower Control Strategy
PHEV	Plug-in Hybrid Electric Vehicle
PL	Propulsion Load
PMP	Pontryagin's Minimum Principle

PMSG	Permanent Magnet Synchronous Generator
PMSM	Permanent Magnet Synchronous Motor
PS	Primary Source of energy
SCS	Supervisory Control System
SOC	State Of Charge
SS	Secondary Source of energy
SSS	Start Stop System
TCS	Thermostat Control Strategy
WLTP	Worldwide harmonized Light vehicles Test Procedure
XOS	Exclusive Operation Strategy

Chapter 1

Introduction

1.1 Rationale

The world is facing tremendous challenges ahead: CO2 levels are alarmingly high and are steadily rising; consumption of the finite supply of oil is increasing; and world energy consumption is unreservedly on the rise. These issues are critically relevant in addressing the threat of climate change, which is by many seen as the greatest challenge for this generation. A concerted push by NGOs, scientists and activists has seen these challenges receive an increasing amount of attention from regulators, industry and consumers. In particular, the personal transport industry has been recognized as a major area of improvement. Since the 1970s the greenhouse gas (GHG) emissions from transport have doubled, and the rapid adoption of personal vehicles in India and China has made the necessity of sustainable transport more urgent.

An essential step towards addressing these stated problems has to be a reduction of energy consumed by cars. Shifting from fossil fuels to electric energy is quite useful, as the macro-level generation of energy is going to be more efficient than a small engine in each car (even with consideration for the transmission of energy). However, the average consumer is not willing to sacrifice the convenience of easy and quick refueling for a limited gain in fuel economy. A balance can be found in the design of hybrid electric vehicles (HEVs), which enjoys both the convenience

and range (due to fuel density) from engines, and the cleaner and cheaper energy of electric motors.

This pursuit of HEVs has seen commercial success for the past decade, with Toyota and Honda leading the way at the turn of the millennium. However, there is an ongoing effort to push for even better fuel economy from these vehicles and make them more competitive. This can be done by refining the component design, choice of materials and aerodynamics. However, an essential and cost effective measure is to improve upon the supervisory control system (SCS) of the HEV, such that the powertrain is operated more efficiently. The key decision for the SCS is to determine how the load power should be split between the multiple energy sources of the powertrain. There is scope to significantly improve the fuel economy of a vehicle at some developmental cost but a negligible variable cost for each manufactured car.

The academic research in this field has been active for the past two decades and has seen several significant developments. Tools and frameworks have been developed that help the design, implementation or validation of SCSs. A majority of the techniques being used recently are established concepts from other applications, such as dynamic programming (DP), model predictive control (MPC), game theory (GT), genetic algorithms (GA) and neural networks (NN). However, the research on control of HEVs has seen the development of the equivalent consumption minimization strategy (ECMS) and the concept of equivalent fuel consumption (EFC) which are novel and powerful. This area of research is thus not simply applying old techniques to new problems, but fundamentally developing new tools to address these new problems.

However, a vast majority of the research so far has been done with quite simple static models. The few publications that have experimental data often show a larger error between simulation and experimental data, than between the various studied control strategies. As the research community has pursued the more advanced control theory concepts, it has often been at the expense of the model complexity and accuracy. The validity of a control strategy will ever only be as good as the model it is tested on. Also, with regard to heuristic or rule-based strategies (which are still dominant in commercial HEVs) the research has been quite stagnant. The main heuristic strategies are from the mid-1990s.

Despite this being an active research topic, there has been several calls for further research in this field. The IEEE Control Systems Society published a document on the most important areas of research for control theory and control engineering, and the SCS for HEVs was among the recommended focus areas [1]. Several recent review papers on the control of HEVs have highlighted the stagnant nature of recent work, and the need for control strategies to be designed and tested on more realistic models [2, 3].

1.2 Scope and Objectives

This work builds on past work by Dr. Evangelou that has involved developing a high-fidelity HEV model [4–6]. This model can be employed to test and analyze the conventional control strategies from the literature, as well as to develop novel control strategies. The richness of the model is expected to not only allow for more reliable results, but to also expose different dynamics which lead to new control requirements. Also, as the model is of a series architecture, it allows the study and design of SCSs for series HEVs that have received less attention in the academic literature than the parallel or power-split architecture.

The research conducted as part of this PhD, has involved a very wide range of problems being studied. A significant portion of the research activity was on control of through-the-road (TTR) parallel plug-in hybrid electric vehicles (PHEVs). This research was done together with Prof. Meisel from Georgia Institute of Technology, and has led to three publications [7–9]. However, being a PHEV, with a TTR architecture, this research meant a very different control problem. The vehicle used for that research was a hybridized Ford Explorer and the model was very different as well. As such, it was considered best to limit the scope of this thesis to only my work on series HEVs.

For the work on series HEVs, an additional fifteen projects were pursued together with final year undergraduate and postgraduate students. This included: four projects on controlling the voltage of the DC bus (some results being published in [10]); four projects on modeling and controlling emissions; four projects on modeling and controlling the battery health; two projects on optimal control; and one project on model predictive control (MPC). The work on each of these research

paths have evolved quite far over the past four years, mainly by the students themselves but with significant guidance from me. These work packages could have been a chapter each, but they still have many remaining loose ends. This work will need to be refined and consolidated at a later stage.

A few additional research paths were also explored, almost as a necessity to facilitate the main objectives of this project. In particular, significant efforts were put into refining the vehicle model that is at the core of this project. Some of these contributions are mentioned in Chapter 2 where appropriate, but have not been expanded upon in detail. This modeling work is being published in [6]. Quite related to this, an efficiency study was done on the continuously variable transmission (CVT) used in the vehicle model, which was published separately in [11]. This has not been included in this thesis either.

Thus, this thesis will be exclusively focused on the supervisory control of series HEVs with the objective to improve the fuel economy. The efficiency maximizing map strategy 0 (EMMS0) has been previously published [12–14], but all the results in this thesis are new and based on an updated model (from the past few months). Also, the control strategy has been evolved further, which will be presented as EMMS1 and EMMS2 in Chapter 4. Similarly, the exclusive operation strategy (XOS) in Chapter 5 is being published in [15] but the results in this thesis have been updated. The approach has been to reimplement and resimulate all past work to ensure that all results are obtained for the same vehicle model, thus allowing valid comparison.

The main objectives of this thesis can be stated as follows:

1. To employ a high-fidelity HEV model that is suitable to test control strategies
2. To study and learn from existing work on control strategies
3. To design control strategies for HEVs based on analysis of the powertrain
4. To design heuristic control strategies that are suitable for modern HEVs
5. To expose the benefits of a high-fidelity model when testing control strategies
6. To understand the sensitivity of control strategies

These objectives can in order loosely be associated with each of the chapters from Chapter 2 to Chapter 7.

1.3 Outline

This thesis will begin by describing the vehicle model, which will be used throughout the rest of the thesis. Thereafter the conventional strategies from the literature will be described and a few will be implemented into Simulink. This will be followed by the design of a family of novel control strategies that aim to maximize the powertrain efficiency. The insights gained from these strategies, as well as the conventional strategies, will be used to design two novel heuristic strategies, which are found to perform well. The remarkable performance of the heuristic strategies will lead to a discussion about the nature of global optimal solution for HEVs and their reliability. Finally, a sensitivity study will be done to test the various designed strategies. Each chapter is described briefly below.

Chapter 2 The modeling of the powertrain components are described together with their interconnection. Emphasis is given on core operational behavior related to the efficiency and performance of the components, as well as the significant changes and updates from the original model. Simulation methods and how they are applied within latter chapters of the thesis are also introduced and clarified.

Chapter 3 The conventional strategies are introduced by a brief literature review, covering separately the heuristic strategies, the real-time optimization-based strategies and the global optimization-based strategies. This is followed by the description, tuning and implementation of three conventional control strategies: thermostat control strategy (TCS), power follower control strategy (PFCS) and global equivalent consumption minimization strategy (GECMS).

Chapter 4 A family of control strategies are developed, with the objective of maximizing powertrain efficiency. The powertrain efficiency is analyzed, which includes the use of replenishing efficiencies to consider the battery usage more holistically. Based on the definition of the replenishing efficiencies, three different real-time control strategies are developed: EMMS0, EMMS1 and EMMS2. These outperform the conventional rule-based strategies and approach the GECMS performance. A global version of the developed strategies, GEMMS, is found to be more effective than the GECMS.

Chapter 5 Insights from past control strategies are discussed and formalized into design principles, which are then used to design two distinct heuristic strategies: the exclusive operation strategy (XOS) and optimal primary source strategy (OPSS). Both of these are found to deliver good performance, with the latter approaching the fuel economy realized by GECMS.

Chapter 6 The impressive performance of OPSS is developed further with the global heuristic strategy (GHS), which allows two tunable parameters with advance knowledge of the driving cycle. This heuristic strategy is found to outperform the GECMS and GEMMS by a significant margin. The causes for this unexpected result are explored and its impact on the wider body of work is discussed.

Chapter 7 The sensitivity of the real-time strategies presented in this work is studied. This includes the sensitivity of the strategies to: correct tuning; effectiveness of the start stop system (SSS); initial conditions of the battery; and changes in driving cycle. It is found that the proposed novel strategies are more suitable for modern HEVs with good SSSs.

Chapter 8 Conclusions are made for the whole thesis and contributions are summarized. This is followed by an outline of future directions for this research.

Chapter 2

Vehicle Model

The vehicle model used in this work is based on work by Dr. Evangelou and Dr. Shukla [4–6]. When referring to earlier versions of the model, this work will often refer to Model0 and Model1. Model0 refers to the model inherited at the start of this research (September 2012), and is documented in [4]. Model1 refers to an improved model, which has been used for most of the past publications during this research, and is documented in [6]. However significant changes have been made since Model1 for the work presented in this thesis that will be discussed in this chapter.

The vehicle model represents a general-purpose passenger car with a series hybrid powertrain as shown in Fig. 2.1. This dynamic model is capable of realistic transient response in the frequency range appropriate for standard driving. The powertrain of the vehicle comprises three branches: the Propulsion Load (PL), which is an inverter driven Permanent Magnet Synchronous Motor (PMSM), mechanically connected to the wheels of the car via a continuously variable transmission (CVT); the Primary Source of energy (PS) which consists of a turbocharged 2.0L diesel internal combustion engine (ICE), mechanically coupled to a Permanent Magnet Synchronous Generator (PMSG) which is electrically connected to a three-phase rectifier; and the Secondary Source of energy (SS) which contains a lithium-ion battery connected to a bi-directional dual active bridge DC-DC converter. Regenerative braking is possible by the PMSM behaving as a PMSG while capturing the kinetic energy from the wheels and converting it to electrical energy, which then gets stored in the SS.

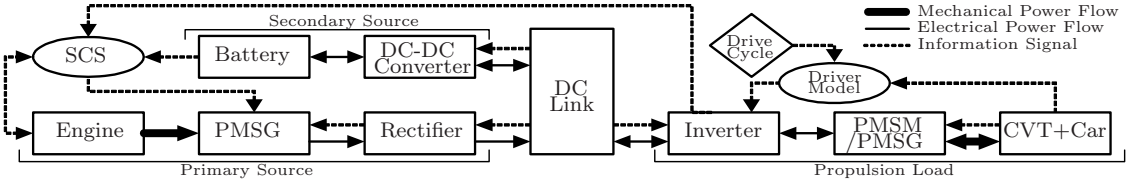

FIGURE 2.1: Overall structure of the series HEV model. Thin and thick arrows correspond to electrical and mechanical energy flow respectively, while the direction of the arrows shows the direction of the flow.

The PL is powered by the PS and SS, all connected to a common DC bus through which energy transfer takes place, giving

$$P_{PS} + P_{SS} = P_{PL}, \tag{2.1}$$

where P_{PS} and P_{SS} are the output powers of the PS and SS respectively, and P_{PL} is the load power requested by the PL. Given the power ratings of the components, the PS and SS are constrained to operate within their rated limits, which are defined to be $P_{PS} \in [0, 58]$ kW and $P_{SS} \in [-21, 42]$ kW.

The vehicle also includes a supervisory control system (SCS) that manages the power split of the powertrain by following a control strategy (of which the design is the main focus of this work). In parallel with the SCS, the powertrain makes use of a start-stop system (SSS) that enables the ICE to be switched off to reduce idling losses. These kinds of systems are becoming standard in commercial vehicles and significantly improve the fuel economy.

This chapter will provide some background on hybrid vehicles before describing the component models of the PL (car dynamics, PMSM, inverter and CVT), PS (ICE, PMSG and rectifier) and SS (battery and DC-DC converter), and then describing their interconnection and overall control (including the use of a SSS). Lastly, the applied methods of simulations will be discussed.

2.1 Background

2.1.1 Brief History

There have been several historical attempts to bring HEVs to the market, with limited success. The first HEV, the Lohner-Porsche of 1900 , was a series HEV designed by Ferdinand Porsche. It was impressive, but too expensive for popular consumption. A revival in the 1970s seemed imminent, following the Arab oil embargo of 1973 which resulted in a hike in fuel prices. The pioneering work of Victor Wouk, who has been called the "godfather of the hybrid", saw several promising hybrid prototypes developed but would eventually be controversially stopped by the US Environmental Protection Agency. The American car industry would thereafter not pursue any further hybrid technology, and with the exception of a few European projects (by Audi and Volvo) the technology would enter a long hiatus.

The true HEV revival occurred in the late 1990s when the Japanese car manufacturers produced affordable, efficient and practical HEVs. The Toyota Prius was the first mass-market hybrid to be launched in 1997 (originally in only Japan), and Honda Insight was first to the American market in 1999. There has since then been an effort by most major manufacturers to include HEVs in their vehicle fleet, but Toyota remains the leader as they now sell more than 1 million new hybrid cars each year (in a world where global total accumulated sales for all hybrids reached 10 million just this year).

2.1.2 Electrification

As cars are becoming more electrified, there is a large range of possible arrangements, and degrees of electrification. The closest to a conventional car would be a mild hybrid which only has a small motor to enable quick restarts of the car, allowing the engine to be switched off rather than waste fuel idling. They may also be capable of recovering energy through regenerative braking, further improving fuel economy. Hybrids with a larger hybridization factor (relative size of the motor to the engine), are referred to as full hybrids (or strong hybrids) and make much more use of the electric motor even during normal driving. These can typically operate in pure electric mode during low-speed urban driving.

The next level of electrification is a hybrid which has a larger battery and can be charged from the electric grid. These plug-in hybrid electric vehicles (PHEVs) are often operated in pure electric mode most of the time, but use the engine as a back-up option in case the battery is approaching depletion. However, it is also possible to use the engine and the motor in a blended mode at all times. This latter approach tends to be optimal only for longer journeys. The fact that electric energy is available from the grid is a fundamental difference from ordinary HEVs, where even the electric energy of the battery has to come from either direct charging by the engine or through regenerative braking.

Lastly the pure electric vehicle (EV), also often called battery electric vehicle (BEV), is a fully electrified vehicle. The engine has been removed from the PHEV and the battery capacity is typically increased, to allow for a decent range. Although, the EV is considered the most environmental friendly (zero emissions, and no fossil fuel consumption), it is still not considered cost effective. Also, if the battery runs out of charge, a significant amount of recharge time is required.

According to experts, and judging by adoption trends, the electric vehicles are still not ready for the mass-market. Significant innovation in battery technology will be required for the battery capacity to increase, and for recharge times to be more palatable. Also, the charging infrastructure is developing fast but is still not widespread. PHEVs on the other hand have been gaining traction and are expected to overtake the conventional HEVs, which are by many seen as a stepping stone towards further electrification.

It is worth mentioning that hybrid powertrains are not limited to electric motors and engines. A significant amount of research is happening in the area of fuel cell electric vehicles (FCEVs), which uses compressed hydrogen to produce energy by reacting with oxygen, resulting in only heat and water as by-products. Also, fuel cells have been shown to be more efficient than combustion engines. However, there are major challenges for mass-market adoption, including the requirement of completely new infrastructure to allow refueling of hydrogen. A handful of commercial FCEVs are currently available, but are practically limited to a few select regions with developed hydrogen infrastructure.

2.1.3 Architectures

Series

A HEV with a series powertrain is sometimes referred to as a range-extended electric vehicle. This reflects the fact that it can be operated purely as a BEV, with the battery powering the motor to drive the wheels. Although such operation (with no emissions) is great during urban driving, the battery offers a limited range for highway driving. This is addressed by the series architecture with an internal combustion engine (ICE) connected to a generator that can either charge the battery or power the motor driving the vehicle. Due to the high energy density of fuel, this addition greatly benefits the range of the vehicle. The fact that the ICE is not mechanically connected to the wheels decouples the engine speed from the wheel speed, allowing the ICE to operate at its optimal point persistently. Furthermore, it allows the ICE to be located flexibly and simplifies packaging, as it is unconstrained by any mechanical connections. Also, as the motor singlehandedly provides the torque for the propulsion of the vehicle, both transmission and control can be kept quite simple.

However, these benefits come at the expense of an additional electrical machine. The generator not only adds to weight, bulk and cost but also introduces another stage of energy conversion. The mechanical energy of the ICE is converted to electrical energy by the generator before being reconverted to mechanical energy by the motor to drive the wheels. These conversions are particularly significant during sustained highway driving. Lastly, as the series powertrain is solely powered by the motor, it needs to be sized for peak power requirements. Additionally, both the ICE and generator need to be sized for maximum sustained road load to allow full battery redundancy. Consequently the series powertrain is quite bulky, and mainly suitable for heavy and large vehicles. However, as components are becoming more compact, the architecture is becoming more attractive.

Parallel

As the name suggests, a parallel powertrain allows the HEV to be propelled by the ICE and motor in parallel, simultaneously. This not only eliminates the need of a generator, but also reduces size of ICE and motor due to the synergistic operation.

This power share also improves performance, as both ICE and motor can provide propulsion during heavy acceleration. The direct connection between the ICE and the wheels (through transmission) avoids the conversion losses associated with the series architecture, and it thus offers superior efficiency for sustained highway driving.

However, the mechanical connection between the ICE and the wheels couples their speed through finite number of gear ratios, limiting the ICE efficiency. This is particularly significant during urban driving when both requested power and wheel speed vary across a wide range. The parallel architecture faces more complicated control and transmission compared to the series architecture as it requires torque blending. There are many approaches to connecting the ICE, motor and transmission system so the parallel architecture is often sub-categorized into pre-transmission, post-transmission and through-the-road configurations.

Pre-transmission In the pre-transmission configuration, both the motor and ICE are located before the transmission system. This allows the ICE to drive the motor like a generator (as with regenerative braking) to charge the battery, even during stand-still. More importantly, as the motor is driven at a higher speed than the wheels, it can operate at a lower torque which results in a smaller sized motor. However, it also means that the ICE and the motor have to operate at the same speeds as they both share the same transmission system. This configuration is primarily used in mild hybrid passenger cars.

Post-transmission In the post-transmission configuration, the motor is coupled to ICE branch after the transmission system. Therefore the power is delivered to and from the motor without suffering transmission losses, and the transmission system is kept relatively simple. However, with the motor coupled to the wheels, it must be specified to operate across all vehicle speeds. Consequently, it is also required to operate at higher torques, resulting in a larger sized motor. It is therefore typically used in full hybrids of passenger cars and light-duty trucks.

Through-the-road As the previous two configurations have the ICE and motor driving the same axle in the vehicle, they have to use speed or torque couplers to connect the power flow of the ICE and motor. Through-the-road is an alternative

configuration where the motor and ICE are acting on separate axles, avoiding any kind of direct coupling. Instead, the road acts as a speed coupling device, fixing both sets of wheels to the same rotational speed, enabling power flow from the ICE to the motor/generator. This configuration has a low mechanical complexity, with a simple transmission, no coupling device and is essentially identical to a conventional powertrain for one of the axles. It is therefore very suitable for hybridization of conventional vehicles. Also, it benefits from improved traction due to the four-wheel drive. However, consequently, it requires more complex control as the two axles are driven simultaneously by two indirectly coupled machines.

Split power

The increasingly popular split power architecture delivers the benefits of both the series and parallel architectures. It decouples the ICE speed from vehicle speed, but still allows some of the ICE power to transfer mechanically to the wheels. Such operation enables the split power powertrain to perform efficiently in urban as well as highway driving conditions.

These benefits come at the expense of complexity. Not only does it require an additional electrical machine (like the series architecture) but it also needs a power split device, typically a planetary gear set, which couples the ICE, the motor, the generator and the transmission shaft. This adds weight, bulk, cost and complexity (mechanical as well as control). There are many configurations of this architecture, which have evolved from the single-mode of Toyota Prius to the latest three-mode configuration of GM Volt. The increasing complexity is pushing the boundary of realized efficiency across wide ranges of operation, but again it is at the expense of bulk and cost as multiple planetary gears and other components are required.

2.2 Propulsion Load

As mentioned, the PL comprises the car dynamics, PMSM, inverter and CVT. Each of these will be briefly described and discussed in this subsection, with emphasis on the differences from previous versions of the model.

2.2.1 Car dynamics

This work is mainly focused on the control of the powertrain, but this necessitates a sufficiently accurate model of not only the powertrain but also the car response. The modeled car describes the longitudinal vehicle dynamics and employs a mechanical multibody system model based on [16]. The constituent masses are introduced in a tree structure with the freedoms and forces between them specified. Thus the main body of the vehicle is allowed forward and vertical translation, and pitch rotation. The front and rear hub carriers are attached to it with vertical translation freedoms, with their motion restricted by spring and damper suspension forces. The model also has spinning wheels attached to the hub carriers. The rear wheel is connected via a crown wheel and pinion, and a CVT to the motor shaft. The model employed here includes also aerodynamic lift and drag forces which are proportional to the square of the speed. The tires are treated as vertically compliant, with associated spring and damper forces, and the tire longitudinal force is generated from normal load and longitudinal slip using standard 'magic formulas' [17]. Tyre rolling resistance proportional to tire normal load is also included. The vehicle is decelerated by regenerative braking only, via the rear wheels and transmission, and the useful energy is captured. The parameter values used in the model are representative of a contemporary European family saloon and are taken from [16] where the total mass is 1475.6 kg, the pitch inertia is 2152.1 kgm^2, and the drag coefficient is 0.35. Further vehicle parameters are presented in [6]

Model0 and Model1 implemented these vehicle dynamics in LISP with the multibody modeling code VehicleSim®, formerly called Autosim [18]. The VehicleSim model was then imported into the Simulink environment as an S-Function. However, this implementation was restrictive in several aspects. Any change to the vehicle dynamics (including the CVT, which used to be implemented in VehicleSim as well)

required changes to the VehicleSim code, followed by stages of compiling and integration with the remaining Simulink vehicle model. Having the model split up between Simulink and VehicleSim also increased computational load, resulting in slower simulations. Furthermore, the use of an imported S-function prohibited the use of simulation accelerators within Simulink that can potentially reduce simulation time into a fraction of the original. Therefore, all of the car dynamics were reimplemented in Simulink directly, using the SimMechanics library.

2.2.2 Permanent Magnet Synchronous Motor

The model uses a surface mounted PMSM, which offers a high torque-to-inertia ratio and power density. It is a 3-phase system with a star-connection to the inverter that links it with the DC bus of the powertrain. However, rather than dealing with the three phases individually, the model converts these into a standard 2-phase *d*-*q* rotating reference system, using the non-power-invariant Park Transform [19], greatly simplifying its control. The resulting nonlinear coupled differential equations for the electrical dynamics of the PMSM [19] are thus as follows:

$$\frac{di_{dm}}{dt} = (v_{dm} - R_m i_{dm} + \omega_{sm} L_{qm} i_{qm})/L_{dm}, \tag{2.2}$$

$$\frac{di_{qm}}{dt} = (v_{qm} - R_m i_{qm} - \omega_{sm}(L_{dm} i_{dm} + \lambda_{fm}))/L_{qm}, \tag{2.3}$$

where i_{dm} and i_{qm} are the *d*- (direct) and *q*- (quadrature) axis components of stator current, v_{dm} and v_{qm} are the *d*- and *q*-axis components of stator voltage, and L_{dm} and L_{qm} are the *d*- and *q*-axis stator inductances. The electromagnetic torque produced by the motor is given by [19]

$$T_{em} = \frac{3}{2} p_m \left(\lambda_{fm} i_{qm} + (L_{dm} - L_{qm}) i_{dm} i_{qm}\right) \tag{2.4}$$

which in the case of $L_{dm} = L_{qm}$ (surface-mounted PMSM) is simplified to

$$T_{em} = \frac{3}{2} p_m \lambda_{fm} i_{qm}. \tag{2.5}$$

This torque is reduced by a friction torque, T_{fm}, to produce a load toque, T_{lm}, according to

$$T_{lm} = T_{em} - T_{fm}. \tag{2.6}$$

TABLE 2.1: Parameter values for friction torques T_{fm} (and T_{fg})

Constant	Value
a_1	10
a_2	4
a_3	0.3
p_0	1.779
p_1	-1.116×10^{-2}
p_2	1.307×10^{-4}
p_3	-1.321×10^{-6}
p_4	6.699×10^{-9}
p_5	-1.300×10^{-11}
p_6	8.685×10^{-15}

TABLE 2.2: Parameters for PMSM (and PMSG)

Parameter	Symbol	Value
Nominal rated power	P_n	75 kW
Maximum speed	ω_n	5000 rpm
Stator resistance	R	0.04 Ω
D-axis stator inductance	L_d	0.20 mH
Q-axis stator inductance	L_q	0.20 mH
Rotor magnetic flux	λ_f	0.125 Wb
Moment of inertia	J	0.05 kgm^2
Number of pole pairs	p	6

The proposed friction torque is identified to be a function of rotor speed as follows

$$T_{fm} = \frac{2}{\pi} \tan^{-1}(a_{1m}\omega_{rm}) \cdot \left(a_{2m} \exp(-a_{3m}\omega_{rm}) + \sum_{i=0}^{6} p_{im}\omega_{rm}^{i} \right) \tag{2.7}$$

with parameter values given in Table 2.1. T_{lm} is applied on the rotor shaft that is connected to the car transmission, thereby driving the car forward. Therefore, T_{lm} is an output of the motor model and an input to the transmission model of the car, while the rotor speed, ω_{rm}, is calculated in the transmission model of the car and fed back to the motor as an input.

The remaining parameter values for the PMSM are given in Table 2.2. The basis of this selection is the EVO Electric AFM-140 motor [20]. The chosen parameters, together with the tuned friction torque, are found to deliver a qualitatively correct representation of the efficiency based on experimental results from the manufacturer. The PMSM efficiency is presented in Fig. 2.2.

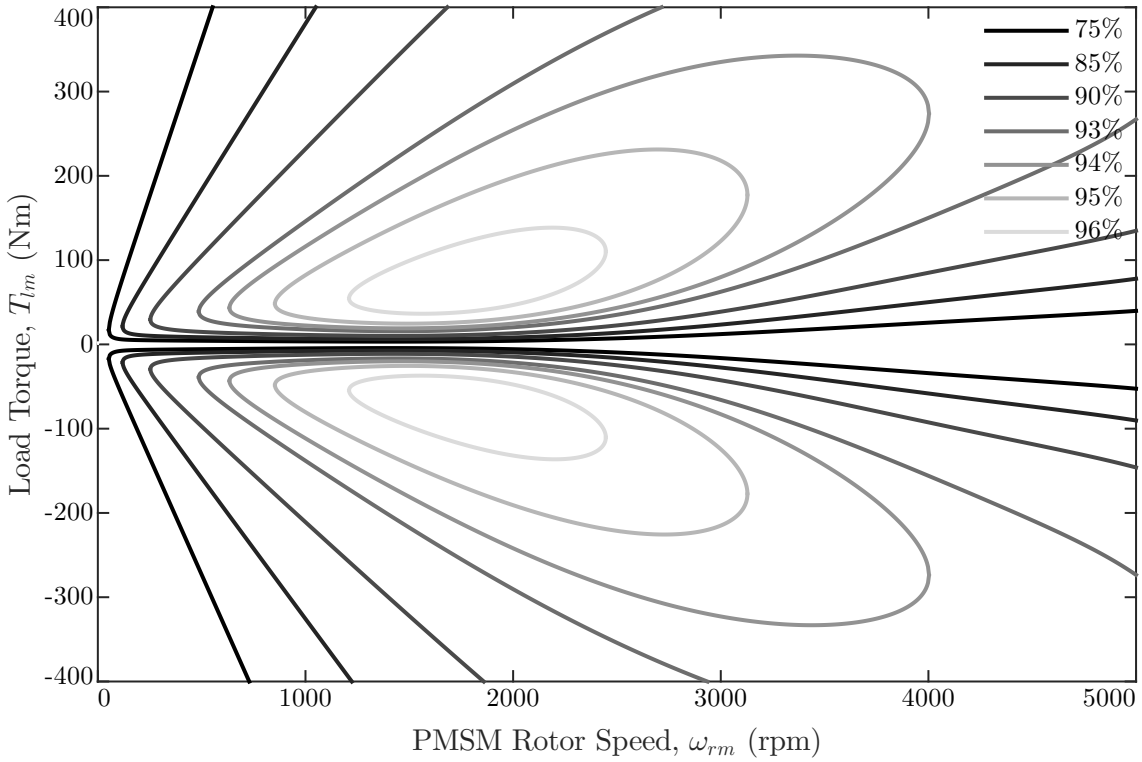

FIGURE 2.2: PMSM steady-state power efficiency map for variations in load torque, T_{lm}, and rotor speed, ω_{rm} for the PMSM model. As only forward vehicle motion is of interest, the rotor speed is always non-negative and the PMSM can operate in two quadrants: a) positive T_{lm} (motoring) and b) negative T_{lm} (regenerating). The contours correspond to constant efficiencies in the range 75%-96%.

2.2.3 Inverter

The PMSM is connected to the DC bus through a bi-directional inverter (operating as a rectifier during regenerative braking). This component is described with an averaged model. The converter switches are first treated like voltage and current sources, making the circuit topology time-invariant, before averaging the signals. The negligible (for the purposes of energy management of the overall powertrain) high frequency switching harmonics are thus removed, balancing precision with computational load. The resulting average model of the PWM inverter in the *d-q* frame is described by the following equations [21, 22]:

$$i'_{PL} = \frac{3}{2}(d_{qm}i_{qm} + d_{dm}i_{dm}), \tag{2.8}$$

$$v_{dm} = d_{dm}v_{dc}, \tag{2.9}$$

$$v_{qm} = d_{qm}v_{dc}, \tag{2.10}$$

in which v_{dc} is the DC-link voltage, i'_{PL} is the modified (before inverter losses are applied) DC current drawn by the inverter from the DC-link, and d_{dm}, d_{qm} are continuous duty cycle functions in the d- and q-axis respectively.

Model0 and Model1 used a constant efficiency term for the inverter ($\eta_{inv} = 95\%$). However, unlike the assumption of using an averaged model, this choice does impact the overall energy flow of the powertrain. Therefore, additional dynamics are included to consider the conduction and switching losses of the inverter based on the work in [23]. The conduction losses of the inverter are given by [24, 25]:

$$P_{cond} = 6\left(i_{pk}v_{f0}\left(\frac{1}{2\pi} - \frac{M}{8}\right) + i_{pk}^2 r_f\left(\frac{1}{8} - \frac{M}{3\pi}\right)\right) + 6\left(r_{ce}i_{pk}^2\left(\frac{1}{8} + \frac{M}{3\pi}\right) + v_{c0}i_{pk}\left(\frac{1}{2\pi} - \frac{M}{8}\right)\right), \quad (2.11)$$

where i_{pk} is the peak AC current from the inverter, v_{f0} is the diode forward voltage corresponding to zero current, r_f is the diode forward resistance, r_{ce} is the IGBT (insulated-gate bipolar transistor) collector emitter resistance and v_{c0} is the IGBT forward voltage corresponding to zero collector current. The switching losses of the inverter are given by [25]:

$$P_{sw} = 6\frac{f_i v_{dc} i_{pk}}{v_{ref} i_{ref} \pi}\left(E_{on,ref} + E_{off,ref} + E_{rr,ref}\right) \quad (2.12)$$

where f_i is the switching frequency (carrier signal frequency) of the inverter; $E_{on,ref}$ and $E_{off,ref}$ are the reference IGBT turn on and turn off energy losses respectively; v_{ref} and i_{ref} are the voltage and current respectively at which reference energy loss is measured; and $E_{rr,ref}$ is the reference diode reverse recovery energy loss. Reference values are obtained from the device datasheet of Infineon for $FS150R12KT4$ [26]. The dynamic efficiency expression of the inverter is implemented as

$$\eta_{inv} = \begin{cases} \frac{i'_{PL}v_{dc}}{i'_{PL}v_{dc}+P_{cond}+P_{sw}} & i'_{PL} \geq 0 \\ \frac{i'_{PL}v_{dc}+P_{cond}+P_{sw}}{i'_{PL}v_{dc}} & i'_{PL} < 0 \end{cases}, \quad (2.13)$$

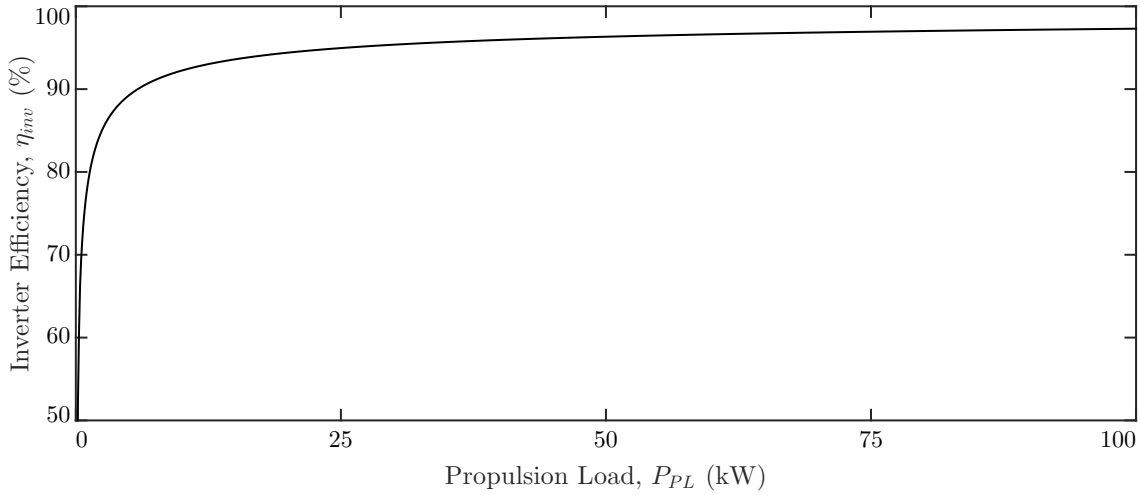

FIGURE 2.3: Inverter efficiency for varying values of propulsion load.

which can also be expressed more simply as

$$\eta_{inv} = \begin{cases} \frac{P_{PL}-P_{cond}-P_{sw}}{P_{PL}} & P_{PL} \geq 0 \\ \\ \frac{P_{PL}}{P_{PL}-P_{cond}-P_{sw}} & P_{PL} < 0 \end{cases}. \tag{2.14}$$

The simulated steady state inverter efficiency is presented in Fig. 2.3, where it can be seen to gradually rise towards about $\eta_{inv} = 97\%$. The efficiency is however quite low at very low power loads. The efficiency dynamics are very symmetrical, so a similar but mirrored profile is applied during regenerative braking when the inverter is engaged in AC to DC conversion. However, note that this steady state efficiency map is only included for illustrative purposes. The actual inverter model deals with transients and is dependent on the state of the vehicle (mainly PMSM rotor speed ω_{rm}).

2.2.4 Continuously Variable Transmission

Lastly, the model uses a toroidal CVT to connect the PMSM to the wheels. The stepless gear ratios offered by the CVT enables the PMSM to rotate at its optimum speed while driving the wheels of the car at any speed. This is done by defining the appropriate final drive ratio N, as $\omega_{rm} = N\omega_{wc}$ (where ω_{wc} is the rotational speed of the wheel). However, this is compromised to some extent due to the fine range of final drive ratios that are realizable ($N \in [1.47, 10.67]$ in this work).

The CVT control strategy pursued is to operate it in a straight line through the PMSM torque-speed map such that

$$T'_{lm} = k_{CVT}\,\omega_{rm}, \tag{2.15}$$

in which k_{CVT} is a constant and T'_{lm} is the PMSM load torque after the CVT losses. This is not only easy to implement but also allows the line of operation to intersect with the most efficient region of the PMSM. This is realized by setting the reference final gear reduction ratio to:

$$N_{ref} = \frac{|T'_{lm}|}{k_{CVT}\,\omega_{wc}}. \tag{2.16}$$

Here N_{ref} is the total (requested) gear reduction from the motor shaft to the rear wheels of the car ($N = N_{ref}$ in steady-state).

The dynamic response of the CVT is characterized by a first order lag with a corresponding time constant, τ, of 200 ms [27]. The CVT losses are simplified to be expressed as a constant efficiency of $\eta_{CVT} = 93\%$, which was found to be the average efficiency for a toroidal CVT [28–31]. The CVT model is shown in Fig. 2.4.

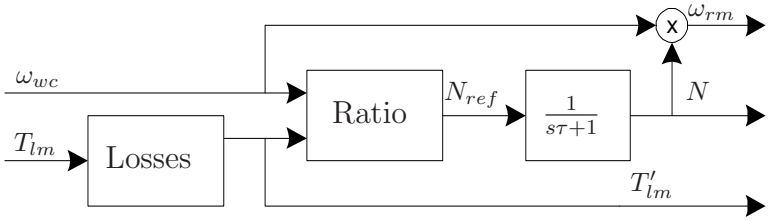

FIGURE 2.4: CVT implementation block diagram, with Ratio defined in Eq. 2.16 while Losses is the application of a constant $\eta_{CVT} = 93\%$.

2.3 Primary Source

The PS consists of three components: an internal combustion engine (ICE), a Permanent Magnet Synchronous Generator (PMSG), and a three-phase rectifier. Each of these will be described here, together with some analysis of the PS as a whole.

2.3.1 Internal Combustion Engine

The ICE is the main energy source of the HEV, and the only source of a conventional vehicle. It converts the chemical energy of the fuel into mechanical energy to power the propulsion of the vehicle. The ICE model in the work represents a turbocharged 2.0L Puma diesel engine. It is based on mean-value torque maps for the engine cylinders, turbocharger turbine and turbocharger compressor, but includes dynamics for the filling and emptying of the inlet and outlet manifolds; the interaction of engine and turbocharger inertia; and fuel-injection valve dynamics. These dynamics consider the pressures, temperatures and mass flows through the various parts of the engine. As such, this model can partly capture transient dynamics that are essential for the application of HEVs, where the operating state changes from one second to another. This is in contrast to other vehicle models that will typically use static look-up tables for either fuel consumption or engine efficiency. The ICE model used thus allows a more accurate representation of a real engine. Furthermore, the steady-state operation of the model have been validated against Ricardo WAVE full computational fluid dynamics (CFD) model simulation results, which were previously validated against experimental results. This model has been fully detailed in [4].

The ICE model used in this work has implemented a few significant changes from Model0. The initial fuel injection constraints were restricting the ICE to operate with a maximum power rating of 42 kW, which is lower than the validated region of operation and the maximum rating of the Puma 2.0L engine. These constraints have therefore been eased, such that the ICE can operate up to $P_{ICEmax} = 64.7$ kW. In fact, the constraint has been made a function of the reference PS power P_{PSref} such that higher reference loads to the ICE allows higher fuel injection. The key purpose of this is to avoid open throttle fuel injection during sudden changes from

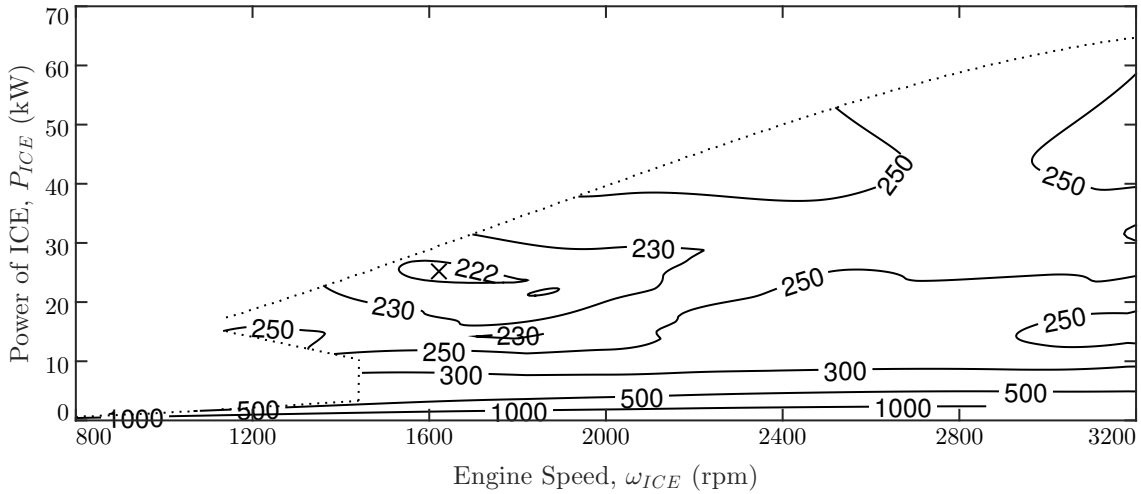

FIGURE 2.5: BSFC of ICE, $BSFC_{ICE}$ (g/kWh), for varying ICE power demand and engine speed. Minimum is marked with a cross.

very low to low power requirements. As part of these changes, the PID control (with anti-windup) for the fuel-injection has been retuned as well.

The brake specific fuel consumption (BSFC) of the ICE is defined as

$$BSFC_{ICE} = \frac{\dot{m}_{fuel}}{P_{ICE}}, \tag{2.17}$$

where $\dot{m}_{fuel}$ is the mass rate of fuel consumption and P_{ICE} is the output power of the ICE that is defined as

$$P_{ICE} = T_{ICE}\omega_{ICE}, \tag{2.18}$$

where ω_{ICE} is the engine speed (in rad/s) and T_{ICE} is the output torque of the ICE. To determine the BSFC at various operating points, the ICE model is simulated for $P_{ICE} \in [0, P_{ICEmax}]$ kW in 0.1 kW steps and $\omega_{ICE} \in [800, 3200]$ rpm in 10 rpm steps. The resulting BSFC map is presented in Fig. 2.5. It can be seen that the minimum BSFC (marked with a cross in the figure) is found in the island around $\omega_{ICE} = 1620$ rpm and $P_{ICE} = 25.2$ kW. The envelope of the efficiency map is determined by feasibility of the ICE. The omitted data points at very low power requirements are either not operationally feasible or the model is not validated in that range. Furthermore, the engine has an internal control constraint for the air fuel ratio that essentially limits the power output at any engine speed (the uppermost diagonal limit), in order to reduce emissions [5].

2.3.2 Permanent Magnet Synchronous Generator

The ICE is connected to a PMSG, which is based on the same equations and parameter values as the PMSM in Section 2.2.2. However, it is only operated with a negative torque. Thus, the energy flow is reversed and the machine converts mechanical energy to electrical energy (similar to the regenerative braking case of the PMSM). The efficiency of this process is given by

$$\eta_g = \frac{\frac{3}{2}(v_{qg}i_{qg} + v_{dg}i_{dg})}{T_{ICE}\omega_{ICE}}, \tag{2.19}$$

where v_{dg}, i_{dg}, v_{qg} and i_{qg} represent *d-q* voltages and currents respectively corresponding to the three-phase output of the PMSG. The efficiency plot of the PMSG is presented in Fig. 2.6. Note that the output power is expressed as a negative value, due to the aforementioned negative torque convention.

In Model0 and Model1 the PMSG was sized at 95 kVA, due to legacy reasons. However, as the PMSG is connected to an ICE barely capable of 65 kW, the PMSG was clearly oversized. Therefore, the old PMSG has been reduced, and now employs the same machine as is used for the PMSM (with parameters given in Table 2.2). This should be beneficial when the project is expanded to include hardware-in-the-loop simulations.

While the PMSM rotor shaft was connected to the wheels through a CVT, the PMSG connects to the ICE through a fixed gear ratio G, such that $\omega_{rg} = G\omega_{ICE}$. In this work $G = 1.2$ is used, as it was found to deliver improved overall efficiency (the efficient ICE operation island around $\omega_{rg} \in [1600, 1800]$ rpm is matched up with the efficient PMSG operation around $\omega_{ICE} \in [1900, 2150]$ rpm). The mechanical dynamics of this connection are given by

$$GT_{ICE} + G^2(T_{eg} - T_{fg}) = (J_{ICE} + G^2 J_g)\frac{d\omega_{rg}}{dt}, \tag{2.20}$$

with T_{ICE} the mechanical torque applied by the ICE on its inertia, T_{eg} the electromagnetic torque applied by the PMSG on its shaft, T_{fg} the friction torque in the generator, and J_{ICE} and J_g the moments of inertia of the ICE and generator respectively.

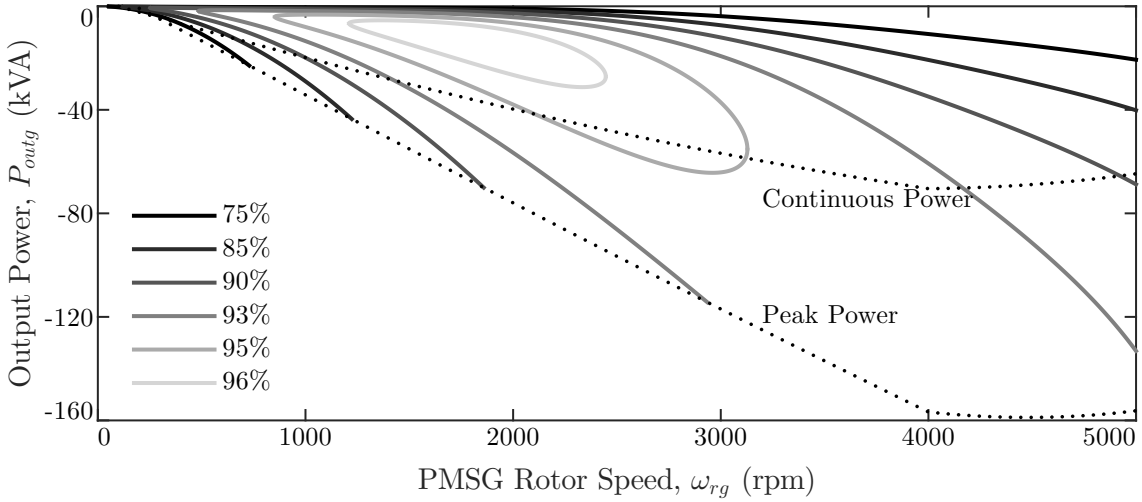

FIGURE 2.6: PMSG steady-state power efficiency contours η_g (%) for varying output power and rotor speed.

2.3.3 Rectifier

Lastly, the energy flows through the rectifier, which is modeled identically (with conduction and switching losses) to the inverter in Section 2.2.3, as opposed to the fixed efficiency model in Model0 and Model1. However, the expression for the rectifier efficiency is not the same as that of the inverter in Eq. 2.13 as the rectifier operates in a single direction and the PMSG makes use of the negative sign convention, but the PS does not. The rectifier efficiency is thus implemented as

$$\eta_{rec} = \frac{i'_{PS} v_{dc} - P_{cond} - P_{sw}}{i'_{PS} v_{dc}}, \tag{2.21}$$

which can also be expressed more simply as

$$\eta_{rec} = \frac{P_{PS}}{P_{PS} + P_{cond} + P_{sw}}, \tag{2.22}$$

which is the ratio between the input power of the DC link to the output power of the PMSG.

The simulated rectifier efficiency is presented in Fig. 2.7. Unlike the inverter efficiency in Fig. 2.3, the rectifier achieves good performance even at very low loads. As the efficiency is indirectly dependent on the rotor speed of the connected machine, the rectifier always enjoys high-speed operation with the engine-generator set (which always operates at $\geq$800 rpm). However, as the PMSM is delivering low

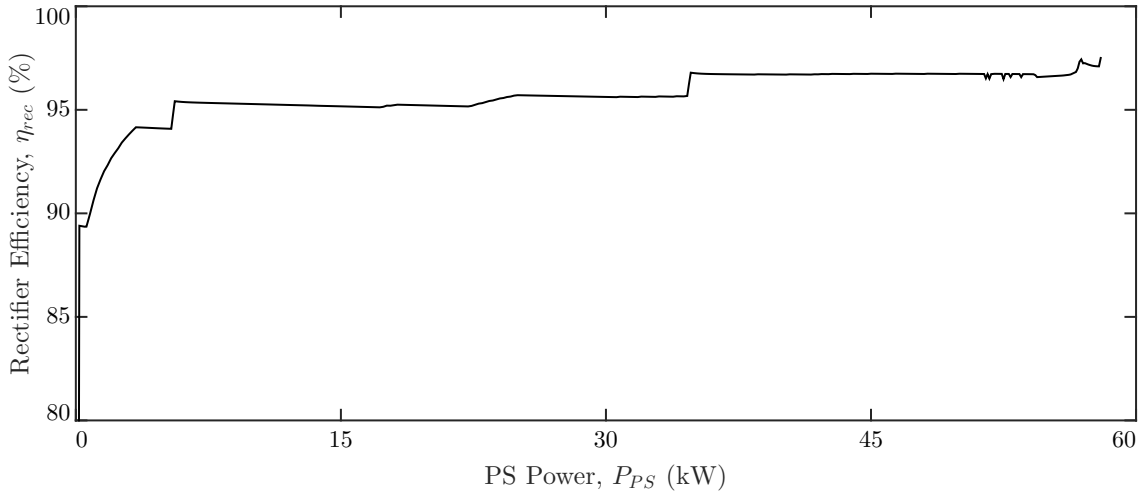

FIGURE 2.7: Rectifier efficiency for varying values of PS power.

loads, or the wheel speed is very low, the inverter experiences quite inefficient operation. Furthermore, the correlation between the rectifier efficiency and the operating engine speed is clearly visible when comparing the profile of the rectifier efficiency in Fig. 2.7 with the profile of the operating engine speed for varying P_{PS} in Fig. 2.9 later in this section.

2.3.4 Overall Operation

As each component of the PS has been modeled, the combined operation can be analyzed to determine the optimal operating points. This analysis and optimization was originally performed as part of the EMMS in Chapter 4 but was later adopted for all strategies. It is therefore briefly presented here.

By considering the ICE, PMSG and rectifier together, the BSFC of the PS can be expressed as

$$BSFC_{PS}(P_{PS}, \omega_{ICE}) = \frac{\dot{m}_{fuel}(P_{PS}, \omega_{ICE})}{P_{PS}}, \tag{2.23}$$

in which P_{PS} is the PS power flowing to the DC-link. Thus, for any given P_{PS} the BSFC of the PS can be determined by measuring the fuel rate $\dot{m}_{fuel}$. This is done for $P_{PS} \in [0, P_{PSmax}]$ with $\omega_{ICE} \in [800, 3200]$ rpm to produce the BSFC map in Fig. 2.8. It demonstrates that the PS is generally more efficient at higher levels of power demand and medium speeds. Note that the minimum BSFC is found at 20.1 kW at 1870 rpm and is marked with a cross in the chart. This point has moved

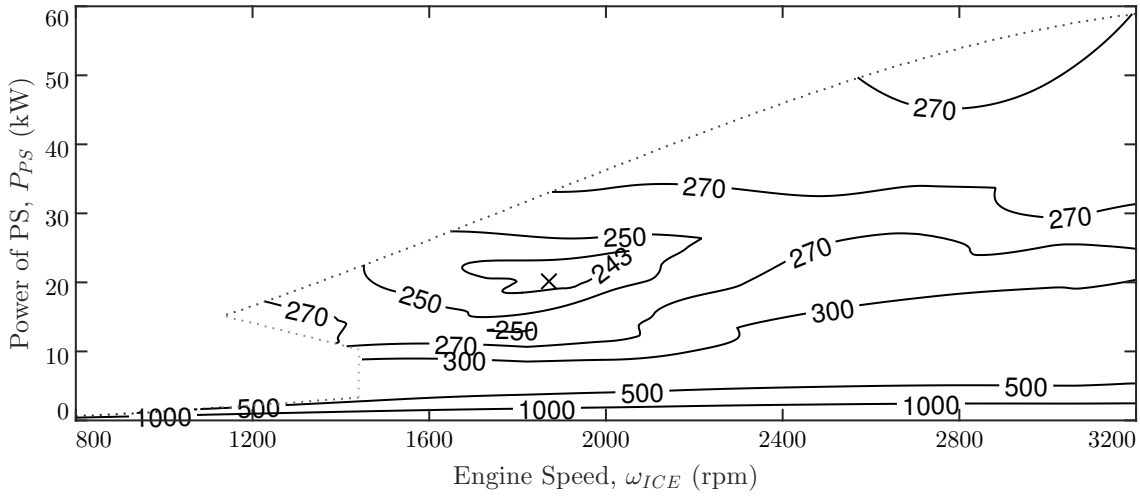

FIGURE 2.8: BSFC of PS, $BSFC_{PS}$ (g/kWh), for varying PS power demand and engine speed. Minimum is marked with a cross.

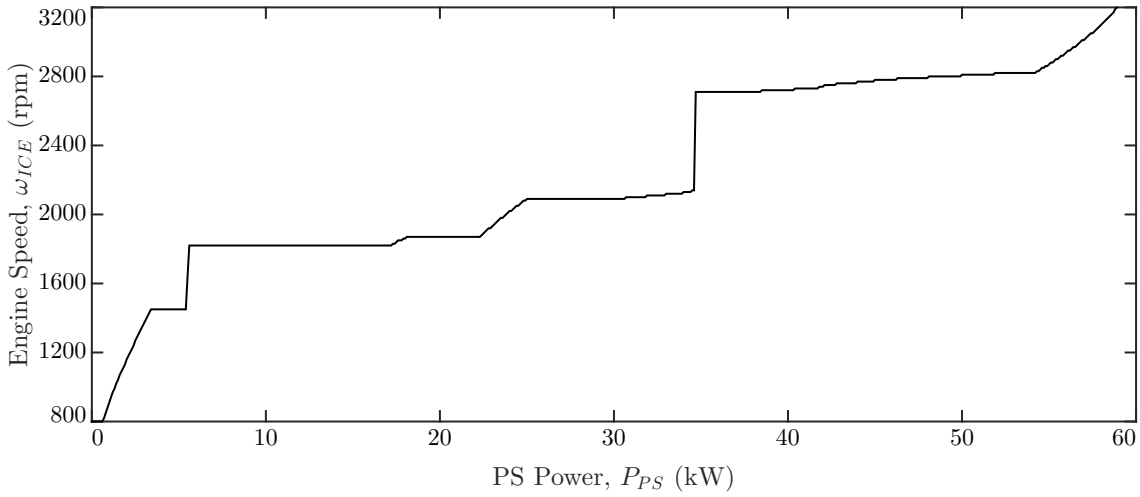

FIGURE 2.9: Look-up profile for preferred engine speed for varying power requirements of the PS.

to a higher speed and lower power as compared to the optimal $BSFC_{ICE}$ due to the efficiency profiles of the PMSG and rectifier.

It can be noted that $BSFC_{PS}$ in Eq. 2.23 is a function of ω_{ICE} as well as P_{PS}. However, with the obtained BSFC map in Fig. 2.8 we can now determine the optimal ω_{ICE} for a given P_{PS} such that $BSFC_{PS}$ is minimized (with some adjustments to ensure smooth transitions). This relationship, as shown in Fig. 2.9 is independent of any choice by the SCS and can therefore be used in the optimization problem later.

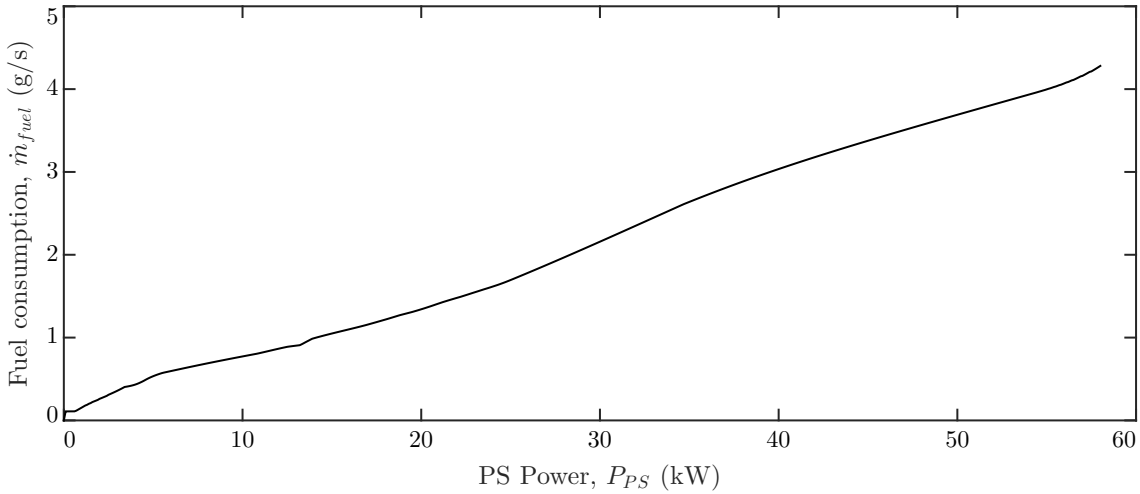

FIGURE 2.10: Steady-state fuel consumption for varying power requirements of the PS.

With $\omega_{ICE}(P_{PS})$ defined, the expression for $BSFC_{PS}$ can simply be expressed as

$$BSFC_{PS}(P_{PS}) = \frac{\dot{m}_{fuel}(P_{PS})}{P_{PS}}, \tag{2.24}$$

Consequently, the control problem of the powertrain is reduced by one degree of freedom and the steady state fuel consumption of the PS can be treated (neglecting transient behavior) as a one-dimensional look-up table for control purposes, as shown in Fig. 2.10. Note that the vehicle model is still using the full dynamics of the engine model, and this fuel consumption profile is only to be used for control designs in later chapters.

2.4 Secondary Source

2.4.1 Battery

The Li-ion battery model in this work is based on the battery model from the SimPowerSystems library in Simulink that has been described in [32, 33]. It uses the physical parameters of the battery in electrochemical equations to describe the battery dynamics. It is able to capture the generic dynamic response of a Li-ion battery. The battery voltage is defined as

$$v_{bat} = E_{bat} - R_{bat} \cdot i_{bat} \tag{2.25}$$

where R_{bat} is the battery internal resistance and i_{bat} is the average current drawn from the battery. The open circuit voltage E_{bat} is given by

$$E_{bat} = \begin{cases} E_0 - \frac{Q_{max} \cdot K_1 Q}{Q_{max} - Q} - \frac{Q_{max} \cdot K_2 i^*_{bat})}{Q_{max} - Q} + A \exp(-B \cdot Q) & i^*_{bat} \geq 0 \\ E_0 - \frac{Q_{max} \cdot K_1 Q}{0.1 Q_{max} + Q} - \frac{Q_{max} \cdot K_2 i^*_{bat})}{Q_{max} - Q} + A \exp(-B \cdot Q) & i^*_{bat} < 0 \end{cases} \tag{2.26}$$

where Q represents the consumed charge and the i^*_{bat} variable is a filtered version of i_{bat} flowing through the polarization resistance, and are defined as

$$Q = (1 - SOC_{init}) \cdot Q_{max} + \int_0^t i_{bat} dt \tag{2.27}$$

$$i^*_{bat} = \frac{1}{\tau_r s + 1} i_{bat}, \tag{2.28}$$

where 's' is the standard Laplace variable. However, rather than considering the absolute level of consumed charge Q, the key state variable of interest for the battery is the state of charge (SOC) given by

$$SOC = 1 - \frac{Q}{Q_{max}}. \tag{2.29}$$

Model0 and Model1 employed a battery with a maximum battery capacity of 20 Ah and nominal voltage of 215 V, with further parameters populated through the experimental look-up tables provided by the Simulink library. This battery was then operated within the range of $P_{SS} \in [-30, 30]$ kW. However, the battery has now been resized and is based on a stack of Kokam SLPB11043140H cells (3.7 V and 4.8 Ah)

Table 2.3: Parameter values of the Li-Ion battery

Parameter	Symbol	Li-Ion Battery
Rated capacity	Q_{max}	14.4 Ah
Nominal Voltage	V_{nom}	296 V
Initial state of charge	SOC_{init}	65%
Battery constant voltage	E_0	320.6795 V
Polarization constant	K_1	0.116 V/(Ah)
Polarization resistance	K_2	0.116 Ω
Internal resistance	R_{bat}	0.2056 Ω
Time constant for filtered current (i^*_{bat})	τ_r	10 s
Exponential zone amplitude	A	25.1477 V
Exponential zone time constant inverse	B	4.2404 $(\text{Ah})^{-1}$

[34], with three parallel connected modules of 80 cells in series, giving a nominal voltage of 296 V and rated capacity of 14.4 Ah. This gives a power capacity of 4.26 kWh, which is practically identical to that of the old model. The power rating of the battery is defined by limiting the battery to C ratings of 5 C during charging and 10 C during discharging, which would correspond to $P_{bat} \in [-21, 42]$ kW. For simplicity, these have been applied as power ratings for the SS. The remaining model parameters are found through the mentioned experimental look-up tables of the Simulink library, and these have been summarized in Table 2.3.

The efficiency of the battery is conventionally based on charge and discharge cycles, but this will not be done in this work. Instead, the aim is to express the charging and discharging efficiencies separately. This will be done in Section 4.2.2.

2.4.2 DC-DC Converter

To connect the battery, which has a variable voltage, to the 700 V DC link requires a bi-directional DC-DC converter. Model0 and Model1 utilized a half-bridge converter based on the work in [35]. However, the model in this work has instead considered a dual active bridge (DAB) converter (as shown in Fig. 2.12 in the next section). This is based on the investigation and modeling in [23], which identified the DAB architecture to be suitable. However, much of the modeling work, which required in-depth modeling of the converter to assess its losses, is very detailed and thus too heavy in terms of computational load for our purposes. Therefore, the dynamics of the DC-DC converter model have been simplified. The main converting dynamic is

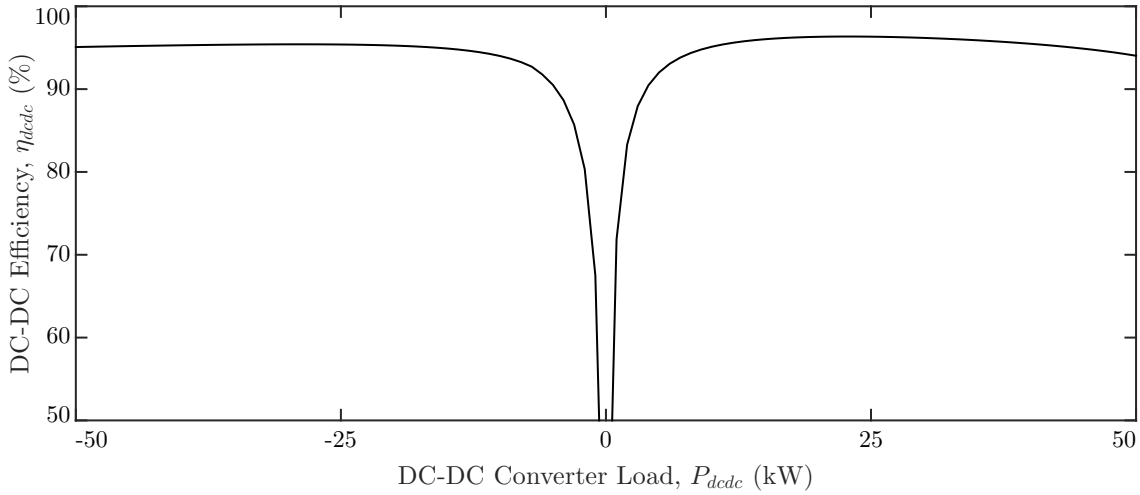

FIGURE 2.11: DC-DC converter efficiency for varying values of load power.

governed by the following equation for the average power flow [36, 37]:

$$P_{dcdc} = \frac{v_{bat} v_{dc} \phi(\pi - \phi)}{2n\pi^2 L_{dcdc} f_{dcdc}}, \tag{2.30}$$

where ϕ is the phase shift between the primary and secondary switch gating signals of the DAB converter, determining the direction of power flow (positive phase shift results in power flow from battery to DC link, and negative in the opposite direction); n is the transformer turns ratio; L_{dcdc} is the primary referred leakage inductance of the intermediate isolation transformer; and f_{dcdc} is the switching frequency of the DC-DC converter.

The model individually models the average current flows through the inductors, capacitors, transistors (IGBTs) for a large set of operating modes. This is the most computationally intensive part of the model. These signals are then used to compute the conduction, switching and core losses of the transistors as well as component losses for diodes and snubber capacitors. However, rather than employing the full model, this work has first implemented the model and thereafter determined the steady-state efficiencies at different loads through simulation. This data has been used to produce a look-up table for the DC-DC converter efficiency as shown in Fig. 2.11. It can be seen that the efficiency is very low at low loads but quickly rises to peak around 96.4% for positive flow (at $P_{dcdc} = 23$ kW) and 95.4% for negative flow (at $P_{dcdc} = -28$ kW). The efficiency is generally quite flat around 95%, but it is clear that the SS should not be operated at very low loads.

2.5 System Integration

This section describes the integration and control of the the PL, PS and SS branches; the overall control by the SCS and SSS; as well as an overview of model time constants and states.

2.5.1 Overall Powertrain

Each of the described branches (PL, PS and SS) of the powertrain are connected together at the DC link, as shown in Fig. 2.12. This diagram illustrates the electrical integration of the powertrain branches.

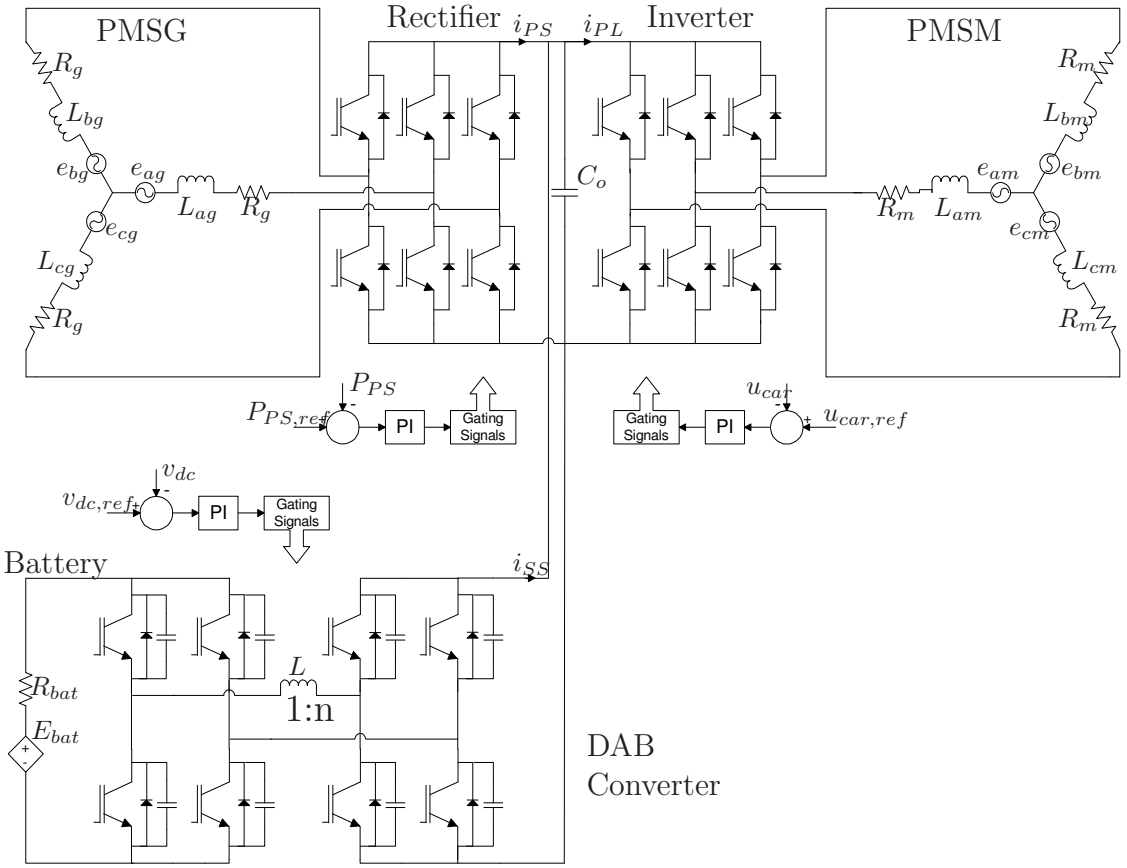

FIGURE 2.12: The electric connection of the powertrain includes the PMSG, rectifier, battery, DAB converter, inverter and PMSM. Symbols R, L and e represent phase resistances, inductances and induced emfs; subscripts a, b and c correspond to the individual phases; and subscripts g, m and ref correspond to 'generator', 'motor' and 'reference'.

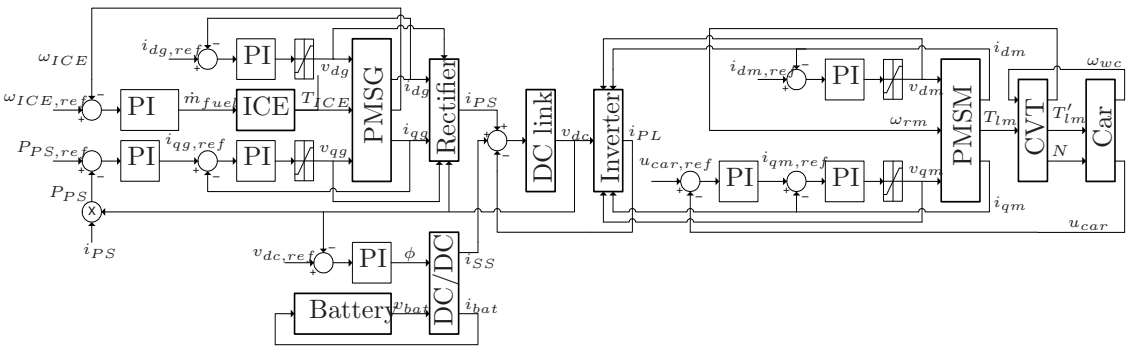

FIGURE 2.13: Block diagram showing the interconnection of the ICE, PMSG, rectifier, battery, DC/DC converter, inverter, PMSM, CVT and car, and the related control loops.

The DC link comprises a capacitor ($C_o = 3$ mF) that is operated at a constant voltage, with $v_{dc,ref} = 700$ V, by controlling the power flowing from the SS into the DC link. The voltage is governed by the standard capacitor differential equation:

$$i_{PS} + i_{SS} - i_{PL} = C_o \frac{dv_{dc}}{dt}, \tag{2.31}$$

where the directions of the currents involved are consistent with the direction of power flow. For example, when $i_{SS} < 0$ the battery is being charged and when $i_{PL} > 0$ the PMSM is being driven.

The powertrain is managed by controlling the converters. The inverter is controlled such that the the forward speed of the car u_{car} is following the reference speed $u_{car,ref}$, defined by a specified driving cycle (discussed further in Section 2.6.1). This results in the necessary energy being pulled from the DC link to power the propulsion of the vehicle. The rectifier is controlled by the SCS which determines the reference PS power $P_{PS,ref}$. Lastly, as mentioned, the DC-DC converter is controlled such that the DC link voltage is operated at its reference voltage, meaning that the inflowing and outflowing current of the DC link, as described in Eq. 2.31, are balanced (resulting in the power balance described in Eq. 2.1). A block diagram of the overall powertrain control can be seen in Fig. 2.13.

In addition to the overarching control loops, it can be seen that the vehicle model employs PI control schemes at eight instances. The values for these have largely been determined through trial and error and have been summarized in Table 2.4. These are slightly different from Model1, as the components have been sized differently.

Table 2.4: Parameter values for PI controllers

Block	K_P	K_I
Engine speed ω_{ICE}	10^{-5}	$2 \cdot 10^{-5}$
Generator power P_{PS}	0	-0.04
Generator direct current i_{dg}	5	100
Generator quadrature current i_{qg}	5	100
DC-link voltage v_{dc}	0.08	0.008
Motor direct current i_{dm}	5	40
Motor quadrature current i_{qm}	5	40
Car speed u_{car}	1000	500

Note that the PMSM and PMSG are described with their three individual phases (a, b and c) in Fig. 2.12, representing the physical nature of the components, while they are described using the d-q frame convention in Fig. 2.13, representing the control signals employed.

2.5.2 Supervisory Control System

The control diagram in Fig. 2.13 clearly shows the interconnected nature of the powertrain. It can be noted that all the control loops are closed apart from the necessity to provide $P_{PS,ref}$, $\omega_{ICE,ref}$, $v_{dc,ref}$ and $u_{car,ref}$. From these, the car speed reference $u_{car,ref}$ is set as the driving cycle profile, which is discussed in the next section. The DC link voltage reference is always defined as $v_{dc,ref} = 700$ V in this work, although it has been controlled in real time in [10]. Furthermore, in Section 2.3.4 the preferred engine speed was determined to be a function of P_{PS} (as shown in Fig. 2.9), meaning that the reference engine speed can be given as $\omega_{ICE,ref} = f(P_{PS,ref})$. Thus, the only control signal that needs to be determined externally is $P_{PS,ref}$. This is the role of the SCS. However, as the control strategies often deal with both the PS and SS in their optimization process, the control variable is often defined to be the power share factor u as:

$$u = \frac{P_{PS}}{P_{PL}}. \tag{2.32}$$

Several SCSs will be presented in this work, but they all operate under certain common constraints. In terms of inputs for the SCS, it will depend on the nature of the choice of control strategy. In this work, only the load power P_{PL} and SOC

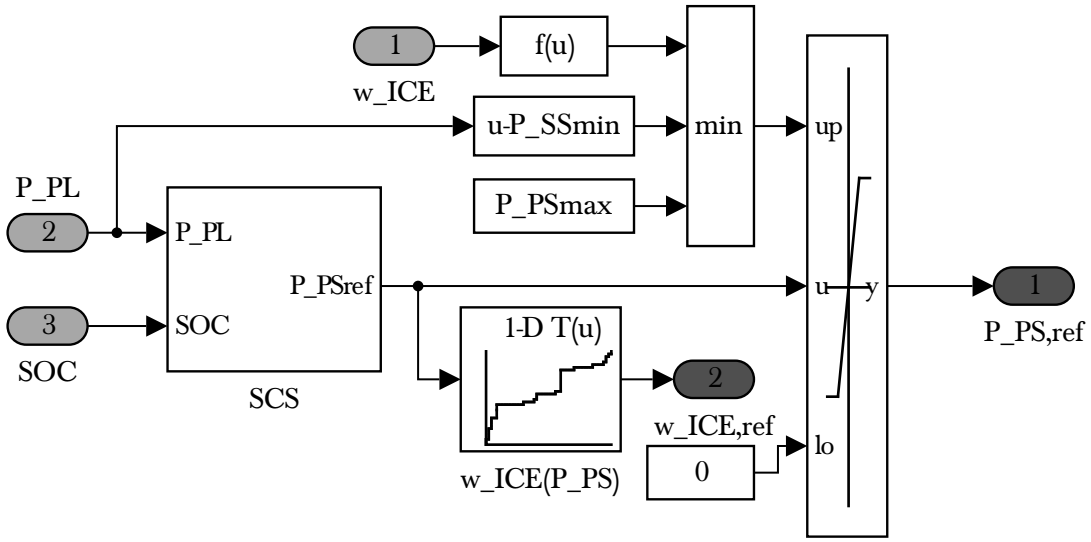

FIGURE 2.14: Simulink implementation of the SCS and its constraints. Note that $f(u)$ implements Eq. 2.36 to limit $P_{PS,ref}$.

will be used, but it is not uncommon for control strategies in the literature to also use the vehicle speed (u_{car}). In the work on regulating the DC link voltage in [10], even v_{dc} is a required input (and output).

The SCS output in each case is the reference PS power $P_{PS,ref}$, but it needs to be checked to meet four different constraints. The first three of these are quite simple: the PS can not be required to deliver negative power; the PS power demand can not exceed its maximum rating; and finally the PS can not be allowed to exceed the load power of the PL by such a margin that the SS can not absorb the surplus power. The fourth constraint concerns the maximum realizable PS power for the current engine speed. Essentially, the PS should not be loaded with more power than it is capable of at the current engine speed. An alternative understanding of this constraint is that the increasing of engine speed is prioritized in order of execution over the increasing of PS power. In summary:

$$P_{PS,ref}(t) \geq 0 \tag{2.33}$$

$$P_{PS,ref}(t) \leq P_{PSmax} \tag{2.34}$$

$$P_{PS,ref}(t) \leq P_{PL}(t) + P_{SSmin} \tag{2.35}$$

$$P_{PS,ref}(t) \leq max(P_{PS}(\omega_{ICE}(t))) \tag{2.36}$$

These constraints, together with the required inputs/outputs, form the surrounding structure for each SCS. This is implemented in Simulink as shown in Fig. 2.14.

2.5.3 Start Stop System

As the SCS instructs the PS to operate at different power levels, it will quite often request the PS to deliver no power at all ($P_{PS,ref} = 0$ kW). Such a request would have the net effect of the PS producing 0 kW overall, but the ICE would need to "idle" at 800 rpm with enough torque to overcome the losses within the ICE and PMSG. This state of operation requires about $\dot{m}_{fuel} = 0.11$ g/s. This waste of fuel is not desirable, but switching off the engine has several drawbacks. Once the ICE has been switched off, some amount of fuel is consumed (and emissions are emitted) to turn on the ICE again. Furthermore, this turn-on is not instantaneous, compromising the vehicle's ability to follow a driving cycle, compromising the drivability of the vehicle. The drivability is further affected by the jerk and vibrations involved in the turn-on of the ICE. Nevertheless, drivers of conventional cars have often used the rule of thumb that it is worth turning off the engine any time the duration of the stop is greater than 10 seconds.

However, a HEV is not as restricted as a conventional car. The availability of electric power to drive the car, allows the powertrain to deliver instantaneous power even if the engine has been switched off. Furthermore, modern SSSs are highly efficient, with the associated fuel consumption becoming negligible. There are industrial reports that show that a modern SSS allows the ICE to break even with the idling losses for short stops of 0.7 seconds [38].

As these types of SSSs are installed by default in most modern HEVs, it is essential to include this capability within the model to allow relevant design of control strategies. However these are rarely seen within models employed in the literature. Either the losses associated with turning on the ICE are neglected altogether or the ICE is kept idling when not in use. This can partly be attributed to the very complex dynamics involved in modeling the turning on of an engine. Including such dynamics are not only beyond the scope of this work, but would also negatively impact the computational speed of the model.

Instead, the model used makes use of a simplified SSS, as shown in Fig. 2.15, which crudely considers the fuel losses of switching the engine on. This subsystem is installed in the cylinder model of the ICE and modifies the base fuel consumption $\dot{m}_{fuel*}$ with a penalty. The SSS takes the reference engine speed $\omega_{ICE,ref}$ as input, and as long as the ICE model is idling, the fuel consumption is zero. However, the

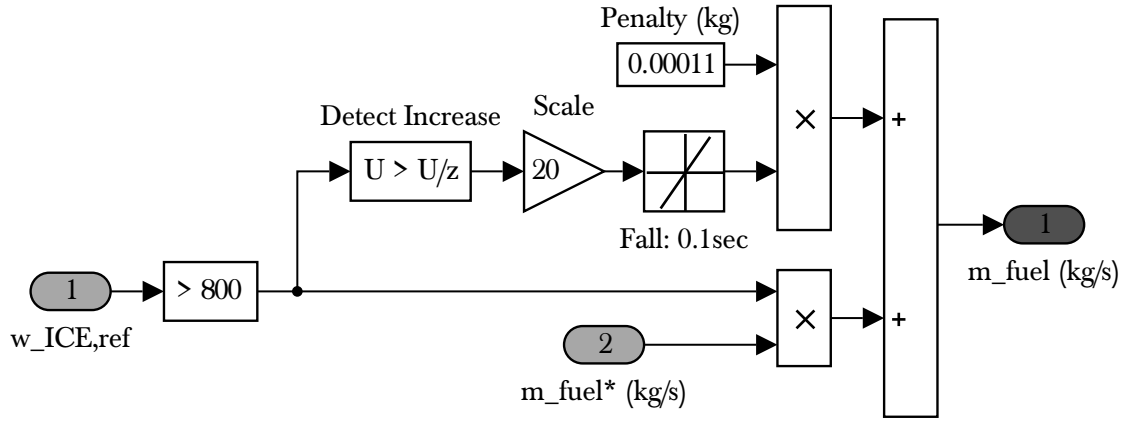

FIGURE 2.15: Simulink implementation of the SSS. Note that the threshold of 801 rpm corresponds to the idling speed of the ICE.

instance the signal exceeds 800 rpm (the idling speed) this signals that the ICE has been turned on. This event results in a spike of magnitude 1 by the "Detect Increase" block, but is scaled by a gain of 20 immediately afterwards. To make use of this spike, the slew rate of the falling signal is restricted to -200 units/second, such that the fall from 20 to 0 takes 0.1 seconds, producing a triangular signal with an area of 1 unit. This signal is multiplied by the defined "Penalty" and finally added to the base fuel consumption to produce the modified fuel consumption $\dot{m}_{fuel}$. In this work the penalty has been defined such that it corresponds to the fuel consumed by idling the ICE for 1 second ($m_{penalty} = 0.11$ g). However, a sensitivity study of this parameter is presented later in Section 7.2.

The main limitation of this simplified SSS is the lack of delay for the availability of the PS and the distinction between the actual engine speed ω_{ICE} and the reference $\omega_{ICE,ref}$ (the reference typically reaches the idling speed faster than the actual speed). Furthermore, the effects on emissions have not been studied within this work and that will affect the break-even time of idling. However, the use of this SSS is nevertheless an improvement upon Model0 and other work in the literature.

2.5.4 Overall Model Characteristics

For the purposes of this work an appropriately high fidelity has been achieved, balanced by the level of complexity and computational load. The model is simulated with a fine sample time (0.1 ms) and requires 35 (model and control) states.

The overall model is non-linear and has come together with consideration of what dynamics are of interest for each component. The PL is mainly affected by the vehicle dynamics with time constants of about 100-500 ms and the CVT, which has a time constant of 200 ms. At least one of the PS and SS need to keep up with these transients. The PS is mainly governed by the ICE, which is quite slow. The combustion in the cylinder is a very fast process and has been replaced by a map that is accessed instantaneously. The fuel injection has a time constant of 5 ms, but due to the slower air flow and mechanical inertia the output power has a time constant of about 200-500 ms. Consequently, the PS often struggles to keep up with the changing load requirements from the PL, and thus the faster SS is often called into action during faster transients.

The battery and the electric dynamics of the PMSM and PMSG have time constants in the order of 1 ms, so they have an easy time keeping up with the required transient loads. These dynamics were considered significant enough to justify being included in the model, but this requires the simulations to be run at sample time steps of just 0.1 ms. The DC-DC converter, rectifier and inverter have even faster switching dynamics (time constants of 0.05 ms). However, with consideration of the balance between the benefits of faster dynamics and the negative impact on simulation time, these very fast dynamics have been averaged in this model.

As the model has been modeled in great detail, it consists of a large number of states. While most models employed in literature to study control strategies have 3-5 states (typically vehicle speed, SOC and gear ratio), the presented model comprises 27 physical states and 8 control states (PI component controllers within the model, as shown in Table 2.4). Furthermore, there are also a number of additional output states (typically seven of these), due to integrators being introduced to process output signals (for example, to measure total fuel consumed by integrating the fuel consumption rate). These are not strictly speaking part of the model, but would nevertheless affect simulation speed. All states discussed above are continuous states that are evaluated at each time step. In contrast, there are an additional 14 delay states introduced to resolve algebraic loops and reduce component interdependencies, with the aim to increase simulation speed. Each delay state is a discrete state that stores the value of some continuous state at the previous simulation time step (delayed by one sampling time step).

Of the 27 model states, 13 describe the powertrain components while the remaining 14 describe the vehicle dynamics (car body, suspensions and wheels). Each of these states are listed in Table 2.5. For the purposes of designing control strategies, the vehicle dynamics are not playing a significant role, in particular with consideration of how many states are dedicated towards it. However, the upcoming section will discuss methods to retain some of these detailed vehicles dynamics while removing the corresponding states from the model. Thus, allowing the model to enjoy high accuracy without compromising simulation speed. However, when studying the designed control strategies, these dynamics and the corresponding states are retained.

Table 2.5: Physical states in the vehicle model

Symbol	Component	Description
ω_{ICE}	ICE	Engine speed
ω_{tc}	ICE	Turbocharger speed
$\dot{m}_{ae}$	ICE	Air exhaust mass flow rate
$\dot{m}_{ai}$	ICE	Air inlet mass flow rate
$\dot{m}_f$	ICE	Fuel mass flow rate
i_{dg}	PMSG	Direct current
i_{qg}	PMSG	Quadrature current
i_{dm}	PMSM	Direct current
i_{qg}	PMSM	Quadrature current
Q	Battery	Charge
i^*_{bat}	Battery	Filtered current
v_{dc}	DC link	Bus voltage
N_{cvt}	CVT	Final drive ratio
p_{xc}	Car body	Longitudinal displacement, x-axis
v_{xc}	Car body	Longitudinal speed, x-axis
p_{yc}	Car body	Vertical displacement, y-axis
v_{yc}	Car body	Vertical speed, y-axis
θ_{rc}	Car body	Pitch angle, r-axis
ω_{rc}	Car body	Pitch angular speed, r-axis
p_{fs}	Suspensions	Deflection, front
v_{fs}	Suspensions	Deflection rate, front
p_{rs}	Suspensions	Deflection, rear
v_{rs}	Suspensions	Deflection rate, rear
θ_{fw}	Wheels	Rotational angle, front
ω_{fw}	Wheels	Angular speed, front
θ_{rw}	Wheels	Rotational angle, rear
ω_{rw}	Wheels	Angular speed, rear

2.6 Simulation Methods

With the vehicle model described, it is important to discuss the simulation methods that will be applied in this work. Even with a good model, the validity of the developed control strategies rely on them being tested on representative driving cycles and that the fuel economy is evaluated in a robust way. There are thus three important aspects that will be explored in this section: the speed profile of the driving cycles; the method of assessing fuel economy; and approaches to improve simulation speed. Each of these will be discussed in turn in this section.

2.6.1 Driving Cycles

To run the simulation model, it is necessary to test it for a specific driving cycle, which essentially defines the speed profile for the vehicle to follow. The choice of driving cycle heavily influences the operation and fuel economy of the driving and it is therefore essential to have an arsenal of driving cycles to apply for the results to be representative.

The standard European driving cycles are the ECE15 (low-speed urban), EUDC (medium speed rural/highway) and NEDC (composite of ECE15 and EUDC). These are quite common in the literature, as they are very simple and the European regulators apply these to test commercial vehicles and assign official fuel economies. These type of driving cycles are called modal cycles, and consist of acceleration and speed profiles of straight lines. These features make them easy to define and, more importantly, easy to implement. However, both academic work and the industry have pointed out the significant flaws in these designs. They are overly smooth and not representative of real-world driving. Also, the load during acceleration stages of these driving cycles are not representative of modern vehicles, which tend to be lighter and more powerful. The Japanese driving cycles are also modal cycles.

In contrast, the American driving cycles by the EPA (Environmental Protection Agency) do not use modal cycles. These cycles, which include the NYCC (low-speed urban), UDDS (medium-speed urban), HWFET (medium-speed highway), FTP (medium-speed urban) and US06 (aggressive high-speed rural/highway), are defined with transient data and are thus much more realistic. However, there is a

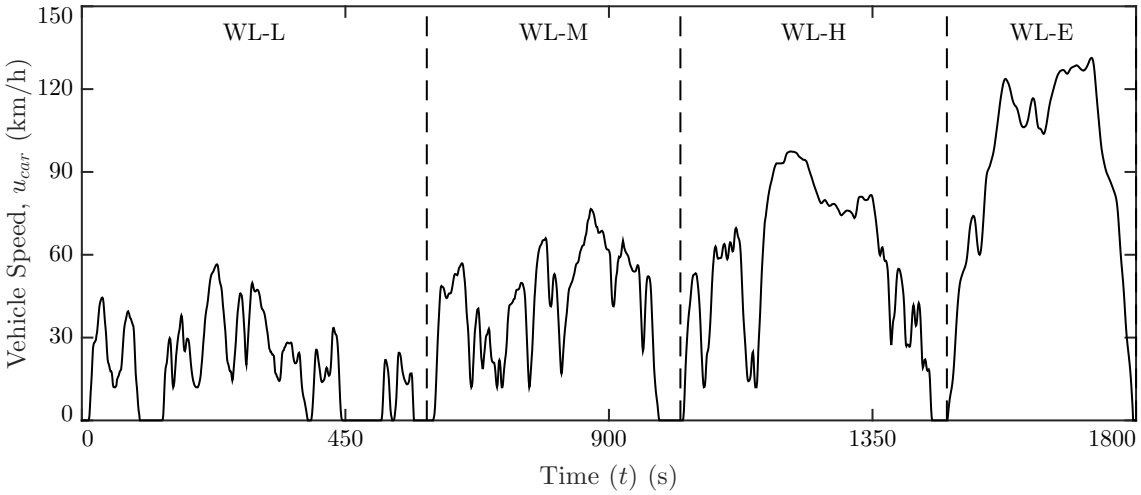

FIGURE 2.16: Speed profile of the WLTP, with the four different stages (WL-L, WL-M, WL-H and WL-E) demarcated.

large number of cycles with no intuitively clear choice of cycles to be tested. Furthermore, the driving cycles are US-centric in their speed and acceleration profiles. Nevertheless, these American cycles were considered the most suitable ones in the past, and all previously published results are based on these (with some usage of the EUDC).

However, there is a new driving cycle in development that is called the WLTP (worldwide harmonized light vehicles test procedure). This project is led by the United Nations, but has had wide international support and participation. It has been noted that the deviation between laboratory-based results (based on cycles like the NEDC) and real-world driving have been increasing over the past decades, and the effect is particularly pronounced for hybrid vehicles [39]. The WLTP profiles are therefore based on internationally collected data of real driving to be as representative as possible.

The cycle is being developed right now and will be adopted by the EU in 2017 to replace current cycles [39]. The WLTP is a single driving cycle with four stages that can be considered as independent driving cycles of their own. These are defined by their speeds: low (WL-L), medium (WL-M), high (WL-H) and extra high (WL-E). These speed profiles are shown in Fig. 2.16. Some particular features of the profiles are given in Table 2.6 (note that the power features are specific for the vehicle design in this work).

TABLE 2.6: Features of the speed profiles for the four driving cycles

	WL-L	WL-M	WL-H	WL-E
Duration (s)	589	433	455	323
Stationary time (s)	156	48	31	7
Distance (m)	3095	4756	7158	8254
Maximum Speed (km/h)	56.5	76.6	97.4	131.3
Average Speed excl. stops (km/h)	25.7	44.5	60.8	94.0
Average Speed incl. stops (km/h)	18.9	39.5	56.6	92.0
Minimum acceleration (m/s^2)	-1.47	-1.49	-1.49	-1.21
Maximum acceleration (m/s^2)	1.47	1.57	1.58	1.03
Maximum load, P_{PLmax} (kW)	25.69	35.97	41.59	50.36
Average load, $\bar{P}_{PL}$ (kW)	1.96	4.52	7.36	17.32

In this work, it is often necessary to simulate multiple iterations of a particular driving cycle to exhibit or reliably measure the features of interest. Therefore, whenever driving cycles are repeated, the notation $\times N$ will be used to indicate N iterations. For example WL-H×4 refers to a driving cycle comprising four repetitions of the WL-H driving cycle. It was found that the most useful number of iterations to run is WL-L×8, WL-M×8, WL-H×4 and WL-E×4, which in total takes just more than three hours to drive. Although this makes the WL-L part of the simulations much longer and more time consuming, it keeps the fuel consumption reasonably balanced across the different driving cycles. Also, it is sufficient to expose most relevant long-term characteristics (in particular SOC evolution) of the control strategies.

A vast majority of the results in this thesis are based on the above number of iterations, so whenever WL-L, WL-M, WL-H and WL-E are mentioned without any explicit information about the number of iterations, then 8, 8, 4 and 4 iterations have been used for each driving cycle respectively.

2.6.2 Fuel Economy Evaluation

The essence of this work relates to the fuel economy achieved by various control strategies for a series HEV. However, the definition of fuel economy is not trivial for a vehicle with multiple energy sources. This subsection will consider various possible methods to assess the fuel economy of the vehicle for a driving cycle, before pursuing a particular method in more depth.

The first approach is to only consider the fuel consumed by the ICE, and ignore the usage of the SS. This can be justified by the fact that all the energy of the SS ultimately originates from the PS anyway (either through direct charging or through regenerative braking). Thus, the fuel is the only true energy source of the vehicle while the battery acts merely as a buffer and temporary storage. However, this perspective neglects the short-term effects of the battery. A low-speed urban driving cycle is often quite short (WL-L is 589 s, NYCC is 599 s and ECE15 is 195 s) and can often be driven purely by the SS. With this method of assessing the fuel economy, the vehicle would be assigned a fuel consumption of zero, and thus an infinite fuel economy. Thus, this method is clearly flawed for shorter driving cycles.

A second approach is to apply the first method (of only measuring the fuel consumed) but complement it with the following SOC constraint: $SOC_{final} = SOC_{initial}$. As this forces the control strategy to be strictly charge sustaining, with zero charge consumed over a full driving cycle, the fuel consumed by the ICE is the only relevant parameter left. This is a very popular approach in the academic literature when investigating and proposing optimization based control strategies. However, this method requires prior knowledge of the driving cycle for the control strategy to ensure that the artificially strict SOC constraint is met. This is not representative of real driving and thus this approach of assessing fuel economy loses validity. Furthermore, many SCSs operate in a charge sustaining but charge oscillatory manner (e.g. TCS (thermostat control strategy) in Section 3.2). Forcing such a control strategy to meet the SOC constraint might not only be unrealizable, but would severely compromise the integrity of the fuel-saving nature of the control strategy. This approach is therefore not suitable, with the possible exception of evaluating global optimization-based strategies for benchmarking purposes.

The third approach also applies the first method but with repeated iterations of the driving cycle being studied. Thus, if the control strategy initially applies SS-only

driving for a low-speed urban driving cycle, it will not be able to do so indefinitely. After a few iterations, the SOC will reach its lower limit and the control strategy will have to operate in a CS manner. Furthermore, as the number of iterations is increased, the contribution of the ICE fuel to the fuel economy increases. For example, if a single driving cycle requires 0.1 kg of fuel, and consumes 5% of the battery charge, the control strategy will need to adjust for the coming two driving cycles such that the constraint of $SOC \geq SOC_L$ is not violated. The vehicle may therefore consume 0.3 kg of fuel and 15% ($SOC_{initial} - SOC_L$) of the battery charge over 3 iterations, with no further ability to consume charge over another driving cycle. However, it remains problematic to determine how 0.3 kg and 15% of battery charge can be evaluated overall (e.g. against 0.4 kg fuel and 10% battery charge). But this can be resolved by increasing the number of iterations. After 100 iterations of the driving cycle, the vehicle will have consumed 10 kg fuel and 15% battery charge. At this point the battery charge becomes negligible and only considering the fuel consumption is sufficient. However, running such a high number of iterations is not desirable from a computational point of view. Not only will running simulations become onerous, it will be outright prohibitive for tuning processes.

The fourth approach is therefore to evaluate the fuel and charge consumption under a single paradigm. It is possible to consider the efficiency of the components, the cost of operation, or any other factor which both fuel and charge can be translated to. However, the most suitable approach that is often used in the literature is to convert the consumed charge into an equivalent fuel consumption (EFC). It allows comparison of the overall fuel economy by considering the actual fuel consumption as well as the shortage/surplus of final SOC. Many analytical methods have been described in the literature to define such an equivalence between SOC and fuel consumption [40–42]. For the purposes of analyzing the results in this work, the line-chart approach described in [42] is adopted as it is a natural extension of the GECMS (which will be described in Section 3.4). The total EFC is defined as

$$m_{efc} = \begin{cases} m_f + S_{d,efc} \cdot \Delta SOC \frac{Q_{max} v_{b,OC}}{Q_{LHV}} & \Delta SOC \geq 0 \\ m_f + S_{c,efc} \cdot \Delta SOC \frac{Q_{max} v_{b,OC}}{Q_{LHV}} & \Delta SOC < 0 \end{cases}, \tag{2.37}$$

where $\Delta SOC = SOC_{initial} - SOC_{final}$, Q_{max} is the battery capacity and $v_{b,OC}$ is the battery open-circuit voltage. The two equivalence factors $S_{d,efc}$ and $S_{c,efc}$ need to be identified for each driving cycle by determining the correlation of the electrical

energy E_e and the fuel energy E_f required to drive the driving cycle in question, where

$$E_f = m_f Q_{LHV} \tag{2.38}$$

$$E_e = \Delta SOC Q_{max} v_{b,OC}. \tag{2.39}$$

To run these simulations it is necessary to operate with some control strategy, and this choice will influence the resulting equivalence factors. The SCS suggested in [42] is to apply a simple proportional control strategy as

$$P_{PSref} = u_{efc} P_{PL} \tag{2.40}$$

where u_{efc} is a constant.

A sweep is therefore performed for $u_{efc} \in [0, 2]$, in steps of 0.05 units, to obtain a wide set of power shares between the PS and SS. The obtained values of E_e and E_f (for WL-L×2, WL-M×2, WL-H×1 and WL-E×1) are plotted against each other in Fig. 2.17. It can be seen that the slopes of the correlation has two distinct sections for each driving cycle, separated by the reference electric energy E_{e0}. This term is the value of E_e for the case when the SS is only used during regenerative braking (corresponding to $u_{efc} = 1$). The slope of the E_e-E_f charts for $E_e \leq E_{e0}$ gives the negative values of $S_{d,efc}$, while the case of $E_e \geq E_{e0}$ gives the negative values of $S_{c,efc}$. These can intuitively be understood as the conversion factors between fuel energy and electrical energy, for the cases of discharging (data marked as plus signs) and charging (data marked as circles) respectively.

However, the lines are not completely linear. For higher u_{efc} values, the results are distorted as the battery approaches $SOC = 100\%$ and for lower values the inefficient use of the PS, and the SSS begin influencing the operation. The latter is particularly true for WL-L where low load combined with low u_{efc} results in the PS being operated very inefficiently (in a way it would never operate during real driving). The applied method for determining the equivalence factors, as suggested in [42], has limitations in which points to consider when calculating the slope. The suggestion of setting the lower and upper limit by the values corresponding to SOC_U and SOC_L respectively is only appropriate if the E_{e0} is quite close to the center of the sloped lines. This can best be understood by considering the case of WL-M×2, where the E_{e0} appears quite close to the lower constraint (checked line corresponding

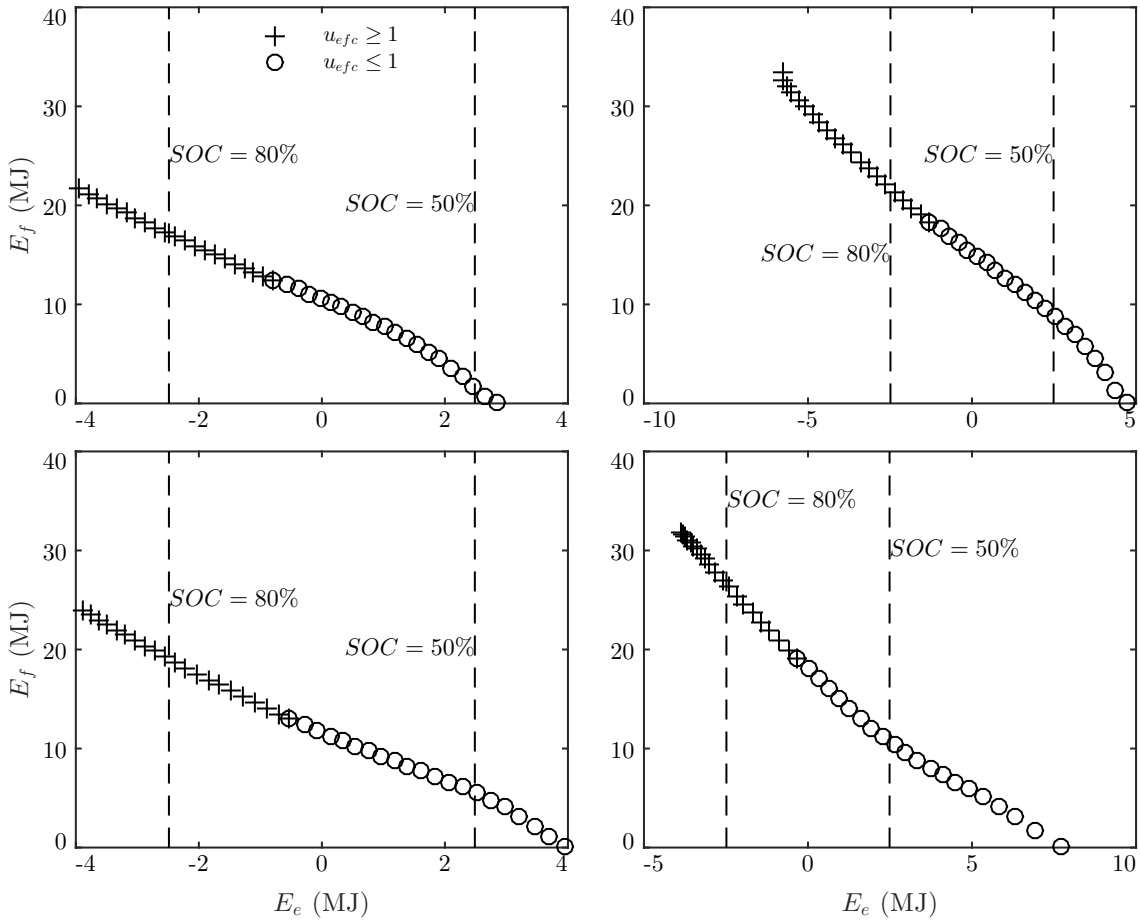

FIGURE 2.17: Correlations between electrical energy E_e and fuel energy E_f with $u_{efc} \in [0, 2]$ for WL-L, WL-M, WL-H and WL-E (left to right, top to bottom).

to $SOC_U = 80\%$ in Fig. 2.17), only allowing five points to be considered when determining the slope and $S_{d,efc}$. A more extreme case can be considered with WL-M×4 for which all the tested points within the span $SOC_L < SOC_{final} < SOC_U$ would have $E_e > E_{e0}$, thereby making it impossible to determine $S_{d,efc}$.

An alternative approach is to limit the testing range in terms of u_{efc} rather than SOC. By only plotting and considering the slopes of $u_{efc} \in [1-\alpha, 1+\alpha]$ the testing points will always be symmetric around E_{e0} (corresponding to $u_{efc} = 1$). This method is applied here with $\alpha = 0.5$ and the resulting E_e-E_f charts are presented in Fig. 2.18.

The lines of best fit are also shown in the charts, and the resulting equivalence factors can be obtained my measuring their slopes. To confirm the validity of this method, these values are applied to assess the fuel economy of a strategy (GECMS, which is described in Section 3.4) which is known to produce optimal result such

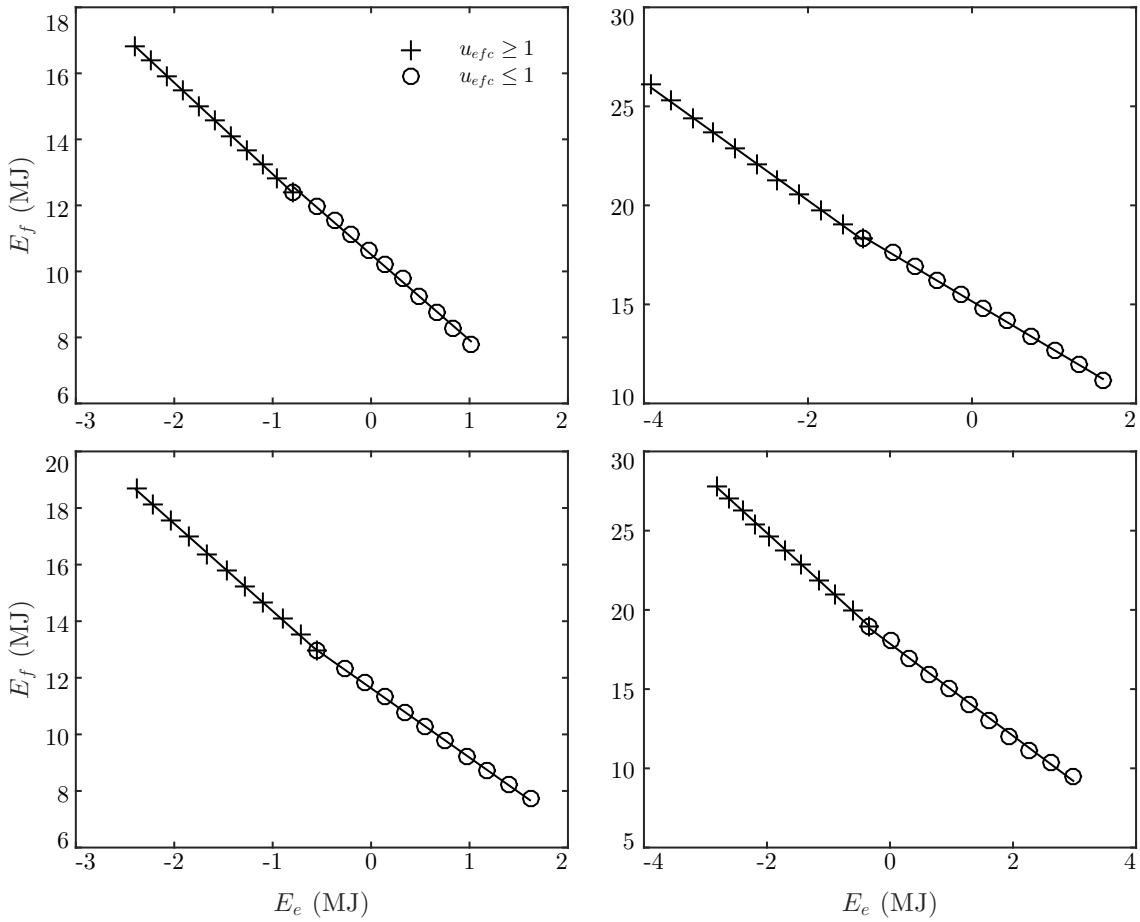

FIGURE 2.18: Correlations between electrical energy E_e and fuel energy E_f with $u_{efc} \in [0.5, 1.5]$ for WL-L (top left), WL-M(top right), WL-H (bottom left) and WL-E (bottom right), together with the line of best fit for both charging and discharging cases.

TABLE 2.7: EFC factors as determined by the correlation between E_f and E_e

Driving cycle	$S_{d,efc}$	$S_{c,efc}$
WL-L	2.80	2.59
WL-M	2.98	2.46
WL-H	3.09	2.45
WL-E	3.54	2.91

that $SOC_{final} \approx SOC_{initial}$. Badly selected equivalence factors will not yield this result. However, it is possible to have false positives, so this criterion is a necessary condition but not sufficient. The equivalence factors obtained by the mentioned line-chart method for $\alpha = 0.5$ satisfied these tests (although the $S_{d,efc}$ value for WL-L×2 had to be modified from 2.77 to 2.80), and the final equivalence factors are presented in Table 2.7.

Recognizing the fallibility of these equivalence factors, the fuel economy results in this work will apply these together with the approach of running multiple iterations of each driving cycle. Even if the equivalence factor for a particular driving cycle is off by 0.1, the worst case scenario ($SOC_{final} = 50\%$ with WL-L) would result in a an error in fuel economy assessment of 1.1%, while for normal driving conditions ($60\% \leq SOC_{final} \leq 70\%$ the error would be less than 0.36%.

It is useful to be able to evaluate the fuel economy of several driving cycles together. In this work, when evaluating the total fuel economy of a particular control strategy, the four mentioned driving cycles will be used (WL-L, WL-M, WL-H, WL-E). However, the defined number of iterations (8, 8, 4 and 4 respectively) is found to bias the summed fuel economy too heavily towards the WL-E driving cycle, which consumes a significant amount of fuel. Therefore the total fuel economy will only consider half the EFC contribution from WL-E, as follows:

$$m_{tot} = m_{efc,WL-L} + m_{efc,WL-M} + m_{efc,WL-H} + m_{efc,WL-E}/2. \tag{2.41}$$

Furthermore, the fuel economy results will typically be normalized against the optimal performing strategy or tuning parameter selection as follows (unless explicitly defined otherwise):

$$M_{efc} = \frac{m_{efc}}{m_{efc,opt}}, \tag{2.42}$$

$$M_{tot} = \frac{m_{tot}}{m_{tot,opt}}. \tag{2.43}$$

Finally, for all the control strategies implemented in this work, the GECMS will be used as a benchmark to express the fuel economy. Thus, the relative performance to the GECMS will often be used, which is defined as:

$$\Delta_{GECMS} = \frac{m_{efc}}{m_{efc,GECMS}} \tag{2.44}$$

where m_{efc} is the EFC of the control strategy being evaluated and $m_{efc,GECMS}$ is the EFC of the GECMS for the same driving conditions.

2.6.3 Simulation Speed Improvements

The developed high-fidelity model captures detailed dynamics of the hybrid powertrain and offers more accurate results compared to other models in the literature. However, this depth and accuracy comes at the expense of computational burden and simulation time. Whilst other models can simulate a second of driving within a few milliseconds, this used to take about 14 seconds for Model0. This is a serious bottle-neck for any work on the model, and thus measures were taken to speed up simulations.

The conventional approach would be to simply reduce the model by removing some of the model dynamics. This is indeed the reason why most control strategy work is done on very simplistic models. However, a core part of the motivation for this work is to study control strategies when applied to high-fidelity models. Thus, it is essential to maintain at least one full-scale version of the model. The approach taken here is therefore to speed up the full model as much as possible with negligible effect on simulation results, and then accompany it with a significantly faster model with limited deviation in simulation results. The reduced model will be particularly useful for various debugging and tuning processes where hundreds of iterations might be required, translating into months of simulation time, which is unacceptable.

The first technique that is applied to speed up simulations is to re-implement the model with simpler and leaner tools in Simulink, to realize the same dynamics with lower computational burden. Rather than implementing an equation with a dozen graphical mathematical blocks, it can be expressed with a single user-defined function. These are not only more efficient in terms of computational burden, but also make the model more user-friendly and concise. Furthermore, nested subsystems adversely affect simulation time and have therefore been minimized as much as reasonable without compromising clarity.

A second technique that has been applied is the reduction of required memory. Although the required memory has small impact on simulation time, it affects the ability to run multiple simulations in parallel. If each simulation (the longest types) requires 4 GB of RAM to complete and there is only 8 GB spare RAM, then only two parallel simulations can be run. However, if the required memory is reduced to 2 GB per simulation, then four parallel simulations can be run. This can practically

be considered as doubling the simulation speed. This is primarily achieved by removing superfluous signals, scopes and outputs, but it is also necessary to reduce the sampling frequency of some of the data collection. Furthermore, attention is given to the data type of signals stored and time-arrays are not collected for each individual signal, but instead as a single array overall.

A third technique is to resolve any algebraic loop (AL) within the model. ALs occur when a signal A is needed to compute a signal B, but at the same time signal A needs signal B to be defined. Simulink can generally solve these iteratively but the process is very inefficient. Therefore, each of the ALs within the model were solved, using the following three approaches: redefining the dynamic to avoid the loop; introducing an "initialization value" for one of the signals; or introducing a unit delay (0.1 ms) between the signals. Each of these changes had negligible effect on the simulation results, but significantly sped up simulations.

A fourth technique is to introduce unit delays in other parts of the model to reduce the interconnectivity of the model blocks. This allows Simulink to compute the model and its components with fewer interdependencies, again resulting in faster simulations. However, these need to be applied carefully and appropriately. Thus, unit delays were included for reference signals (e.g. ω_{ICEref} and P_{PSref}) which would experience a minor lag in a real vehicle as well. The DC link voltage v_{dc} is practically constant at 700 V and connects to most components in the vehicle. It is therefore a prime candidate for a unit delay. However, the SS is somewhat sensitive to the v_{dc} in determining P_{SS}, which if disturbed would affect the simulation results noticeably. As a result, v_{dc} has only been delayed within the PS and PL).

A fifth technique is to apply accelerators within Simulink. This is related to the earlier point about removing ALs. A model without any ALs can make use of acceleration tools within Simulink. When running the model, Simulink will generate a C-MEX S-function to perform the simulation external to the Simulink environment. This significantly speeds up the simulation, while only taking a few seconds of additional compilation and build time. Additional drawbacks, such as limited interactivity during run-time, are not very relevant for our purposes.

All of the mentioned techniques can be applied with negligible loss of precision in results and deliver significant improvements in simulation speed. However, the simulation speed has only been sped up by a factor of about five. To truly begin speeding

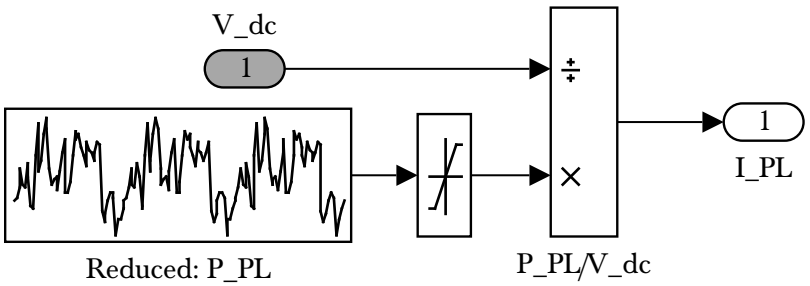

FIGURE 2.19: Simulink implementation of the reduced model, where a pre-recorded P_{PL} signal is used to produce the i_{PL} signal for the model.

up the model, a separate reduced model is considered, where we will compromise on precision to a slightly larger extent.

The vast majority of simulations that are performed within this work are interested in the fuel economy of the vehicle for a particular driving cycle for a particular control strategy. The main signals of interest are therefore the accumulated fuel consumption (m_f) and final value of battery SOC (SOC_{final}), which will provide the EFC (m_{efc}), as described in the previous section. By studying the series powertrain in Fig. 2.1, or the control diagram of the model in Fig. 2.13, it can be understood that the operation of the PL is independent of the control strategy being used. The PL simply determines the PL current i_{PL} that flows into the DC link, after which the SCS determines how the PS and SS should share in meeting this load. The PL only depends on the driving cycle $u_{car,ref}$ (and on the DC bus voltage to a negligible extent).

It thus follows that the PL can be replaced by a pre-defined signal. The full model can be simulated for all driving cycles of interest, and the resulting P_{PL} for each case is recorded. Then a separate reduced model can be produced where the recorded P_{PL} signal is a pre-defined input, as shown in Fig. 2.19. This block replaces the PL and driver model in the overall model, as shown in Fig. 2.20. Note that the Propulsion Load and Driver models have been "commented out" (as indicated by the % sign) and are not simulated. The removal of the inverter, PMSM, driver and CVT models are very helpful, but it is particularly the car dynamics that are worth removing. Even though the car dynamics have been made faster by implementing them with SimMechanics within Simulink (as opposed to with VehicleSim in Model0 and Model1), this remains one of of the most computationally heavy blocks of the model. Consequently, the simulation speed is dramatically improved.

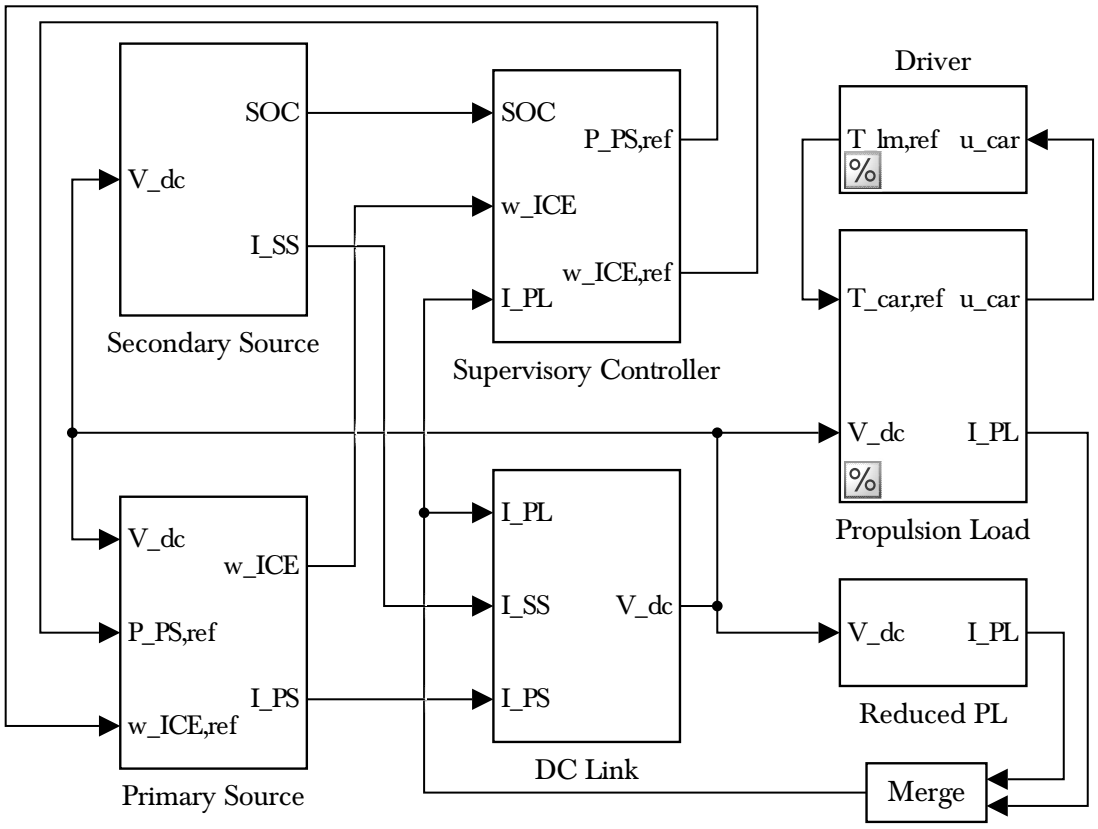

FIGURE 2.20: Overall Simulink model where the Reduced PL is integrated to override the full PL and driver that have been commented out (as indicated by the % symbol).

To quantify the benefits and costs of these procedures, simulations are run for various versions of the model and simulation speed S_{sim} (seconds of simulated driving in 1 real second) and EFC m_{efc} are measured. The results for S_{sim} and E_{efc} (the error in m_{efc} relative to the "Full model") are presented in Table 2.8 and Table 2.9 respectively for WLTP as well as separate simulation of its individual stages (WL-L, WL-M, WL-H and WL-E). Note that the "Full model" does not have all the ALs that were present in Model0 and that the latter can not be compared in terms of EFC due to differences in component sizing.

The speed results are quite consistent across driving cycles, but it can be noted that the speed tends to be higher for longer driving cycles. This is mainly due to the effect of the building and compilation times becoming increasingly negligible as a proportion for longer simulations. Thus, the WLTP results can be considered most representative for simulations required in this work. The EFC results on the other hand are very dependent on the individual driving characteristics of the driving

TABLE 2.8: Comparison of simulation speeds S_{sim} for original, full and reduced models for various driving cycles (all results for Model0 were obtained for NEDC). Simulations with acceleration mode are marked with "Acc".

Model	WLTP	WL-L	WL-M	WL-H	WL-E
Model0	0.0714	0.0714	0.0714	0.0714	0.0714
Full model	0.1217	0.1175	0.1226	0.1232	0.1227
Full model, Acc	0.4401	0.4401	0.4375	0.4227	0.4150
Reduced model	0.3039	0.2928	0.2971	0.2974	0.2965
Reduced model, Acc	3.7336	3.6555	3.4456	3.5747	3.3936

TABLE 2.9: Comparison of error in EFC E_{efc} (%) with regards to the Full model results for various driving cycles. Simulations with acceleration mode are marked with "Acc".

Model	WLTP	WL-L	WL-M	WL-H	WL-E
Full model	0.0000	0.0000	0.0000	0.0000	0.0000
Full model, Acc	-0.0004	-0.0005	0.0001	-0.0003	-0.0005
Reduced model	-0.0352	-0.1227	-0.0658	-0.0488	-0.0111
Reduced model, Acc	-0.0355	-0.1226	-0.0657	-0.0489	-0.0111

cycles and thus vary significantly. However, the WLTP (which comprises the four other driving cycles) can be considered to include a variety of all these driving dynamics and is quite representative of all types of driving. Nevertheless, many upcoming simulations will include repetitions of a particular type of driving, so the worst case scenario is of most interest.

Comparing the models for WLTP, it is clear that the Full model improved the simulations significantly (+70% in speed) over Model0, just by reimplementing the blocks and introducing some minor delays (the first four techniques mentioned above) despite the new model having more complex converter models. As the accelerator mode is used, the full model increased simulation speed by another 262% while having a negligible impact on EFC. This is the model that will be used to generate final results within this work. Lastly, the reduced model with acceleration mode is able to improve the simulation speed by another 748% while compromising the m_{efc} precision by about 0.12% at worst (0.04% for WLTP overall). This reduced model will be used for the tuning processes for all control strategies in this work.

2.7 Summary

This chapter has described the vehicle model that will be used within this work. It is a series HEV, where the PL comprises an inverter, PMSM, CVT and car dynamics; the PS includes a turbo-charged diesel engine, PMSG and rectifier; and the SS consists of a Li-ion battery and a DAB DC-DC converter. The three branches are connected together at the DC link where energy is exchanged. The SCS determines how the load power P_{PL} should be distributed between the PS and SS.

The model has been changed and improved upon in several respects since Model0. Several of the components have adjusted power ratings (e.g. ICE from 34 kW to 58 kW, PMSG from 92kVA to 75 kVA, battery from 30 kW to 42 kW), new loss dynamics have been included (e.g. detailed loss models for inverter, rectifier and DC-DC converter, rather than fixed efficiencies), and the overall control of the powertrain has been redesigned (e.g. introducing a SSS, retuning most PI loops, and optimizing engine speed as a function of P_{PS}).

This chapter has also presented the driving cycles that will be employed within this work: WL-L, WL-M, WL-H and WL-E (the four stages of WLTP). Each of these will typically be repeated multiple times in each simulation to allow more reliable results and to investigate dynamics that only appear over longer time frames. Furthermore, the concept of EFC is introduced as a means to express the fuel economy of the vehicle with consideration for the charge consumed by the SS over a driving cycle. To this end, the equivalence factors $S_{d,efc}$ and $S_{c,efc}$ have been identified for each driving cycle, to be used to evaluate fuel economy results in upcoming chapters.

These changes to the model dynamics have been accompanied with significant improvements in modeling implementation, allowing simulations to run more than six times faster than Model0. In addition a reduced model has been designed that enables simulations at more than 50 times the speed of Model0 with only minor loss in precision. This reduced model has allowed this work to progress much faster, as the time spent on the tuning and debugging processes for each control strategy have been dramatically reduced. This will benefit all future work as well.

Chapter 3

Conventional Strategies

The research area of SCSs for HEVs has been quite active for the past two decades, and a handful of techniques and strategies have established themselves as the default choice for benchmarking, prototyping or inspiration for novel strategies. These conventional strategies are the topic of this chapter.

The chapter will begin by describing past work in the literature, exploring rule-based strategies, real-time optimization-based strategies, and global optimization-based strategies. The aim is to briefly introduce the reader to a wider body of work in this research area, and set this work in both its research and historical context. Particular attention will be given to the thermostat control strategy (TCS), power follower control strategy (PFCS), equivalent consumption minimization strategy (ECMS), its globally tuned version GECMS, and dynamic programming (DP), as these have been most influential in this research area.

Based on this review, the TCS, PFCS and GECMS will be implemented for the purpose of study and benchmarking. Each of the three control strategies is designed, implemented and tuned before its operation and performance is evaluated. These strategies (the GECMS in particular) will serve as both inspiration and benchmarks for novel control strategies in upcoming chapters.

3.1 Background

As mentioned in the last chapter, the earliest HEVs employed series architecture, and practically operated as an electric vehicle with an engine-generator set aboard to recharge the battery. There was thus barely any designed control strategy. As the concept of hybrid vehicles evolved, and the engine-generator set would increasingly power the propulsion motor at the same time as the battery, the role of the control system became more important. However, this proved to be a challenging task, and the interaction between the battery, engine and the control system remained one of the biggest challenges for these early HEVs (in addition to cost) [43].

The early implementation of simple rules to control the powertrain, was arguably more concerned with meeting the operational constraints of the components than any type of optimization of the fuel economy. However, in the early 1990s the academic research on SCSs accelerated significantly [44], developing and consolidating several key control strategies that are popular even today. It is worth noting that this boom in control strategy research happened years before the Toyota Prius was released in Japan in 1997 and was later brought to the US market in 2000.

This section will discuss some of the most conventional control strategies in the literature from the past two decades. Although the thesis overall deals primarily with series HEVs, there has been such a rich exchange of ideas and concepts between HEVs of varying architectures that this section will explore the evolution of control strategies without limiting the scope to just series HEVs (although this will be given some prominence). The section will begin by discussing rule-based controllers, followed by real-time control strategies and finally the global optimization-based strategies.

3.1.1 Rule-based Strategies

Most commercial vehicles apply rule-based control strategies due to their ease of use and reliability. For series HEVs the two most conventional strategies are the TCS and PFCS. The evolution of these two will be discussed, followed by some alternative heuristic strategies.

Thermostat and Power Follower Control Strategy

In 1995, Anderson and Petit discussed several concepts for the design of control strategies for series HEVs in [45], where the essential features of the TCS are defined. This was followed up by work in 1996 by Hochgraf et al., that made a more detailed study of the TCS in [46]. Since then, the TCS has been established as the most conventional control strategy for series HEVs and is used as a benchmark to this day [47–50]. It operates the powertrain in two distinct modes: battery only mode and active engine mode. The default mode of operation is with the battery only, making the propulsion of the vehicle completely electrical. However as the battery depletes its charge and reaches a defined lower limit, the engine-generator set is activated and is thereafter operated at its optimal operating point. This point of operation of the engine-generator set is typically higher than the load of the vehicle during driving, so the surplus energy is directed to the battery, which is thus gradually recharged. As the battery SOC reaches a defined upper limit, the engine-generator set is switched off, and the vehicle operates in pure electric mode once again. This control strategy is implemented later in Section 3.2.

Two years later, in 1997, Cuddy and Wipke implemented a PFCS in a series HEV [51], just a few months before Jalil et al. would do the same in [52]. These were the first implementations for a series HEV, but early work on control strategies operating on the same principles can be found as early as 1987 for parallel HEVs [53]. This control system has several modes of operation, but the two main ones are: battery only mode and power following mode. At very low loads (sometimes also constrained to low speeds) the battery is used to drive the powertrain. However, above a minimum load, the PS is responsible for meeting the full load of the driving. Later developments of the PFCS include a small deviation from pure power following that is proportional to the change in SOC of the battery [54]. This deviation ensures that the battery is charged for lower SOC and discharged at higher SOC values, thus making the strategy charge sustaining (CS). The PFCS has been used for series HEVs but has seen particular success when implemented in HEVs of parallel architecture. Most importantly, the control strategies of most commercial HEVs so far are based on this control strategy [55, 56]. This control strategy is implemented later in Section 3.3.

The principle of operating the PS at a constant load and using the battery as an equalizer, like the TCS, is commonly referred to as load leveling. In contrast, the principle of having the PS power follow the load power, like the PFCS, is called load following. Each of these will be explored further in Section 5.1, discussing the design principles of heuristic strategies. The advantages and disadvantages of the load leveling and load following methods have been further understood over the past two decades and several control strategies have been proposed to exploit the best of each. This is exemplified by the more recent work by Kim et al. [57], which proposed the hybrid thermostat strategy (HTS) which has its basis in the TCS, but applied concepts from the PFCS to achieve improved performance. A similar approach was also taken in [58] by Ko et al. This more comprehensive approach is particularly relevant when considering multi-objective control. For example, Zhang et al. designed a control strategy in [59] which is based on TCS to achieve good fuel economy but, recognizing the resulting harsh usage of the battery, the control is modified to not operate the engine-generator set strictly at its most efficient point at all times. In this particular case a sliding mode controller is applied to achieve this result.

Maximum SOC-of-PPS

Although the TCS and PFCS can be considered the parents of most deterministic rule-based strategies, there are a few exceptions. One noteworthy alternative to the TCS for series HEVs, is the Maximum SOC-of-PPS (MSP) that is presented in [47]. It aims to keep the SOC at a high level persistently by often operating with only the engine-generator set to meet the load. In doing so, it often operates the engine-generator set inefficiently, which is why it is not as popular. However, it offers benefits beyond fuel economy.

MSP recognizes a few limitations of the TCS in terms of reliability. Firstly, the TCS does not guarantee CS operation for any driving cycle (as will be demonstrated later in Section 3.2) [47]. If the average load exceeds the optimal operating point of the engine-generator set, the SOC will keep on decreasing even when the engine is on. Secondly, as the SOC of the battery oscillates between its lower and upper bound, the performance of the powertrain will be compromised at the lower bound [47]. The lower battery voltage at this stage will reduce the battery efficiency and possibly (if no DC-DC converter is present) reduce the voltage level (and thus power

rating) of the electric machines in the powertrain. Both of these limitations can be unacceptable in mission critical situations, such as for a military vehicle (which is one of the common applications of series architecture) [47]. The MSP addresses these issues by maintaining the SOC high, and operating the engine-generator set more flexibly.

Other

The heuristic strategies mentioned so far have all been deterministic. A second category of heuristic strategies include the fuzzy logic controllers (FLCs), which apply fuzzy logic to handle different operating modes, as opposed to discrete thresholds. This makes the control strategy more robust to disturbances and less sensitive to imprecise data input [56]. Like the PFCS, these control systems have historically and typically been developed for parallel HEVs, but have seen implementation in series HEVs as well [60, 61]. Although the FLCs are rule-based, they are not as heuristic as the previously mentioned strategies. As FLCs excel at handling multiple inputs and outputs, it is not uncommon for them to work with additional inputs, such as GPS data in [60].

A third category of heuristic control strategies that is often mentioned is the State machine controllers (SMCs), with the only prolific contribution being by Phillips et al. in 2000 in [62]. It involves a set of dynamic rules to govern the hybrid powertrain in numerous different conditions and ten distinct states. With such clear operating conditions and well defined state transitions, the resulting control strategy is very robust. However, arguably, this category of systems is not a separate category of rules, but rather a different method of implementation. In fact, control strategies such as TCS and PFCS might have historically been implemented with simple logic gates or if-else statements, but they are now often implemented with state machines.

Overall, two decades from inception, the TCS and PFCS remain the go to control strategies for both prototype and benchmarking purposes. Not only are they simple to implement but they have historically performed quite well. The advancement of fuzzy logic based controllers is seen to hold high potential but the impact so far has mainly been within academic circles. Among commercial vehicles, the heuristic strategies are still more prevalent than optimization based strategies due to their simplicity and effectiveness [55, 63].

3.1.2 Real-time Optimization-based Strategies

This subsection explores various real-time optimization-based control strategies that have been applied for the supervisory control of HEVs. As the dominant approach in this field is the ECMS, this will be treated first separately. Thereafter the model predictive control (MPC) approach will be explored and lastly some alternative techniques will be mentioned briefly.

Equivalent Consumption Minimization Strategy

Although the heuristic strategies are able to deliver good performance with a simple approach they are unlikely to deliver fuel economies (or any other control objective) close to the global optimal. Thus, to achieve improved results, researchers have applied concepts from optimal control theory in the context of a hybrid powertrain.

The first step is to determine a cost function. The general problem for a vehicle is to minimize the fuel consumption:

$$J = \int_0^{t_f} \dot{m}_f(t, u(t))\ \mathrm{d}t \tag{3.1}$$

However, such an objective would result in persistent use of the battery (to achieve $J = 0$). It is thus necessary to include a penalty for the discharging of the battery (as well as a reward for charging it):

$$J = \int_0^{t_f} \dot{m}_f(t, u(t)) + w \cdot \dot{SOC}(t)\ \mathrm{d}t \tag{3.2}$$

As pointed out in [44], this approach has often been used with an arbitrary weight w [64–66].

The ECMS takes the approach of defining w by an analytical equivalence between fuel and charge. The concept of such an equivalent fuel consumption (EFC) factor was introduced by Kim et al. in 1999 [67] and it established the foundation for the real-time strategy presented by Paganelli et al. in 2000 [68]. This work evolved over several years in Ohio with several publications [69–72], and gained traction around 2004 when several influential publications developed the ECMS further. Pisu, Rizzoni and the team at Ohio State University would continue and build on the work

of Paganelli, and apply the ECMS to series HEVs as well [73, 74]. This also resulted in the development of an adaptive ECMS (A-ECMS), which added an estimating algorithm onto the ECMS, to adapt the equivalence factor based on the propulsion load during driving [75]. This work also compares the optimally tuned ECMS to a DP solution, and finds the results to be practically identical. However, the work notes that the DP solution were executed on a simpler quasi-static model to allow reasonable computation time. This makes the comparison of results less valid, but nevertheless suggests that the ECMS technique is potent.

At the same time in ETH Zurich, the ECMS is being applied and refined by Sciarretta, Guzzella and their team. In [42], the equivalence factor is redefined to be applied at each time instant as:

$$J(t,u) = \Delta E_f(t,u(t)) + s(t) \cdot \Delta E_e(t,u(t)) \tag{3.3}$$

where ΔE_f and ΔE_e are the used amount of fuel and electrical energy respectively. Unlike previous versions of ECMS, this definition does not rely on average efficiencies for the powertrain components [56]. Also, it considers each operating condition and control input when defining the equivalence factor at each time instant. Intuitively, this can be considered as the association of use of electrical energy to the future change in fuel consumption (as the battery is merely an energy buffer). However, during implementation, the equivalence factor is actually simplified to

$$s(t) = p(t)S_{dis} + (1 - p(t))S_{chg} \tag{3.4}$$

where S_{dis} and S_{chg} are the discharging and charging equivalence factors (that are either tuned or defined by the process described in Section 2.6.2) respectively. The probability function $p(t)$ expresses the probability of the final amount of electrical energy E_e being positive. Thus, it is unable to precisely implement the optimal equivalence factor $s(t)$ that would yield the best possible fuel economy. However, simulation results have shown that the resulting performance is very close to the global optimal results (as obtained through DP solutions), with a gap of 0.1 to 2%. Considering the relative simplicity of this method, it is very powerful.

The next evolution of the ECMS was the association to the Pontryagin's minimum principle (PMP), which offers a set of necessary conditions for the optimal control, allowing a reduction of the search space for candidate solutions. The PMP was

applied in two separate control strategies proposed in 2008: [76] for a parallel HEV and [77] for a series HEV. It was thereafter evaluated in relation to the ECMS for a series HEV in 2009 by Serrao et al. at Ohio [78]. It was shown that the ECMS, under certain circumstances, is equivalent to the global optimal solution offered by the application of PMP. But while the PMP requires prior access to the whole driving cycle, the ECMS allows a real-time and straightforward approach for implementation. One of the assumptions in this work is a constant battery efficiency as it simplifies the problem significantly. The conclusion of this work is that ECMS allows the identification of the global optimal solution. However, this equivalence between ECMS and PMP was re-evaluated in 2011 by Kim et al. in [79]. Although the strong link between the two approaches is re-affirmed, it emphasizes the simplifications required for the ECMS to be equivalent to the PMP. One of the possible suggestions to improve performance would be to consider multiple equivalence factors (e.g. S_1, S_2, S_3, S_4 and S_5) rather than just two (e.g. S_{dis} and S_{chg}) when determining the overall equivalence factor $s(t)$. Nevertheless, by comparing to DP, it found that the solutions are practically identical. However, it is worth noting that some of the PMP results were superior to the DP solutions (which should be impossible). This was attributed to truncation and numerical errors in the simulations, which were run for a static model.

More recent developments for the ECMS have been incremental rather than conceptual. The framework of the ECMS has not changed in concept, but has rather expanded to deal with a larger set of control objectives. The nature of the problem formulation of the ECMS lends itself towards including additional variables and constraints with additional equivalence factors. Several contributions have been made that also consider emissions, battery health [80, 81] and drivability. Other work has expanded the ECMS by considering additional input information, by using a GPS [82] or telematics [83]. This has led to more work taking the MPC approach to the control problem.

In 2013, the collaborative paper [3] (authors include Serrao and Sciarretta) was published to discuss open issues within supervisory control of HEVs, from the perspective of the ECMS and PMP framework. One of the main issues raised was that the simplicity of the models (quasi-static, isothermal) used to design ECMS (and other optimal control strategies) are unrealistic. Typically, the SOC is considered the only state of the powertrain. In particular engine temperatures are identified as

having a significant impact on the resulting fuel economy. Interestingly, it is found that heuristic strategies might perform better than ECMS strategies that are based on engine models that do not consider engine temperature (as heuristic strategies are less dependent on engine models).

Model Predictive Control

The MPC approach has a great track record in industrial applications and has been applied to HEVs as well over the past decade. It is a success story for optimal control theory, as it was adopted in chemical plants and oil refineries already in the 1980s and has expanded to other areas since then. The basic principle is to design a predictive model that allows you to determine the impact of your control input. By solving such an optimization problem over a finite time horizon, it allows the determination of a the optimal control input at the immediate time instant, which is then implemented. The time horizon is chosen such that the problem can be solved in real-time. The approach is particularly useful when it is essential to avoid certain types of operation (typically due to system instability or regulation).

The earliest example of the use of MPC for the supervisory control of HEVs can be found in [84] in 2004, although a few other earlier work had considered the use of predictive data. MPC was also being used for other purposes: [85] used it to prevent depletion of hydrogen in hybrid fuel cell vehicles; [86] applied it to steer autonomous vehicles; and [87] applied it for adaptive cruise control in vehicles. The consequence of bad control in the two latter applications is a collision of vehicles which is clearly essential to avoid. However, it has become increasingly more common to apply MPC solely for the purpose of improving the fuel economy of the HEV.

The publication of the paper [88] by Johannesson et al. in 2007 (based on the paper with the same name in 2005 [89]), might be considered an important moment in the development of MPCs for HEVs. The emphasis of the paper was to evaluate the potential of predictive control for HEVs, assuming that accurate data could be obtained through GPS and telematics. The results were promising and were followed by a significant amount of research the coming years. This has also been boosted further by the trend of navigation systems becoming standard in new commercial vehicles, and developments towards communication between vehicles and infrastructure [90]. Also, as computational power is becoming cheaper and more available on

vehicles, the MPC becomes more attractive. MPC techniques have become particularly popular for power split HEVs [2], but [91] presented a stochastic MPC for a series HEV.

However, the suitability of MPC for HEV application has limitations. Wang and Boyd state in [92] that MPC is only suitable for systems with slow dynamics, which a HEV wouldn't really qualify as. Also, the benefits offered by MPC might be more useful as a safety system rather than an energy management system.

Other

One of the weaknesses of DP (see next subsection) is that it produces a driving cycle specific control policy that is not generally applicable. This has been dealt by the development of stochastic DP, where the driving load is determined by a random Markov process [93, 94]. The same effect has also been achieved by training neural networks (NN) with various driving profiles [50, 95]. In each of these cases a significant amount of offline analysis is required, but the resulting control policy can be implemented in real-time.

3.1.3 Global Optimization-based Controllers

Finally, this subsection will present a few global control strategies. Here, global refers to the available data: a global controller is acausal and has access to the full driving cycle at all times. Such an infinite-horizon problem is not real-time implementable, but serves other purposes (benchmarking, inspiration, etc.). The first technique to be discussed will be DP, which has established itself as the default global optimal approach for HEV control systems. This will be followed by the GECMS, which is the global solution preferred in this work, and will be followed by briefly mentioning alternative strategies.

Dynamic Programming

DP is a numerical optimization technique based on the Bellman's principle of optimality [96], which has been expressed in [97] as: "An optimal control policy has

the property that no matter what the previous decisions (i.e. controls) have been, the remaining decisions must constitute an optimal policy with regard to the state resulting from those previous decisions." This allows the problem to be solved in a backwards fashion, based on a defined final state. This requires the evolution of states to be incremental:

$$x(t+1) = f(x(t), u(t)). \tag{3.5}$$

The essence of the DP method is to discretize the problem (time-domain, states and control inputs), such that the solution space is made finite. Naturally, the precision of the optimality of the DP solution is proportional to how finely these spaces are discretized. As the technique requires access to the whole driving cycle in advance to determine the optimal solution, the process is acausal and not implementable in real time. Furthermore, it is worth noting that the computational time increases linearly with the drive cycle duration, but increases exponentially with the number of model states [44]. Thus, the main restriction of DP is that it can only be applied to relatively simple models.

The first DP implementation was done for a series HEV, due to the fewer number of decision variables in this architecture, by Brahma et al. in 2000 [98]. The model used a single state, a sampling time of 1 second and a power discretization of 5 kW. This simple model yielded useful results in about 10 minutes on a general purpose PC. This inspired the work of Lin et al. in 2001 for a parallel truck [99], which was further improved and developed in 2003 in [100]. A model with three states was used: SOC, vehicle speed and transmission gear. They simplified their normal vehicle mode such that Eq. 3.5 is abided for each state. Despite these simplifications, the optimization process required a sampling time of 1 second, and resulted in errors in vehicle speed of up to 3 km/h. However, the solution was useful enough to provide insights to design a refined rule-based controller that outperformed a conventional heuristic strategy.

Many further implementations of DP have been made since then, but they have always been limited to simplified models. However, techniques have been suggested to reduce the computational burden by, for example, reducing the control space without compromising the optimality of the solution [101]. Nevertheless, it has been very popular as a benchmark [42, 75, 102], inspiration for control design [99], and inspiration for powertrain design [103].

Although DP is one of the most robust optimization techniques available it is still being held back by the "curse of dimensionality". It is definitely not realizable in real-time, and even as a benchmark it is not great as it is only able to operate on very simple models. Considering the high-fidelity model being considered in this work, implementing a DP is beyond feasibility.

Global Equivalent Consumption Minimization Strategy

It was mentioned in the previous subsection that the ECMS has been shown to be equivalent to the PMP (under certain conditions), which in turn is practically equivalent to DP [75, 78, 79, 104]. This has been shown to be the case for both optimally tuned and adaptive equivalence factors for the ECMS. It is therefore possible to consider a GECMS, which has been tuned for each individual driving cycle separately, as a close approximation of the global optimal solution. Considering the foundation on the ECMS, which is the most established framework of analysis within the control strategy literature, it can be considered a reliable benchmark for this work.

The GECMS is relatively easy to implement. The determination of the equivalence factors can be done either through the line-method described in Section 2.6.2 or through a brute force approach. Although the line-method offers a good selection of equivalence factors, they have not been found to be optimal. Instead, a variety of combinations of equivalence factors are tested for each driving cycle, and the EFC is measured to determine the best set of equivalence factor that yield the optimal fuel economy. This solution can be considered to be a close approximation of the global optimal. The production of optimal control inputs for each set of equivalence factors can be somewhat tedious but is easy to automate. The implementation of the GECMS in this work is based on [78] and is described more fully later in Section 3.4.

Another advantage of the GECMS is the medium computational requirements. The testing of each candidate set of equivalence factors can take an hour for repeated iterations of a driving cycle. Nevertheless, identifying the optimal set of equivalence factors to three significant digits (beyond which the impact is quite small) is a process that will typically take a few days for our model, as opposed to times greater than the age of the universe (for DP). Thus the global benchmarking solution can be

obtained for the same vehicle model as the other proposed control strategies, unlike DP which is typically implemented on simplified models.

Other

Several other established control theory methods have also been tested and applied on HEVs. Genetic algorithms (GAs) search for the optimal solution by allowing each candidate solution to evolve towards its minimum. Implementations have been published frequently, from as early as 2001 [105, 106]. It is based on biological evolution and is useful for complex non-linear optimization problems [56]. However, they are not considered suitable for constrained optimization, and are generally not considered suitable to be applied to the control of HEVs [63].

A second approach has been to apply game theory to HEVs [107, 108], where the vehicle operation is evaluated as a non-cooperative game between the driver and the powertrain. Recent results have been quite positive but the literature is still quite limited. Other applied approaches include linear programming (LP) [109] and convex optimization (CO) [110–112].

3.2 Thermostat Control Strategy

The thermostat control strategy (TCS) is a simple, robust SCS that achieves a good fuel economy and is the most conventional control strategy for series HEVs. It oscillates between battery-only operation (with the engine off), and using the engine at its most efficient point of operation (with the battery leveling out the load).

3.2.1 Design

The basic principle is to run the PS at its optimal point and have the SS act as an equalizer, as

$$P_{SS} = P_{PL} - P_{PS,cop} \tag{3.6}$$

where $P_{PS,cop}$ is the selected constant operating point of the PS. Typically this is set to be the most power efficient point of operation of the PS ($P_{PS,cop} = P_{PS,opt}$). This mode of operation is valid until the SOC reaches its upper threshold ($SOC_U = 80\%$), at which point it enters a mode of SS-only operation. This mode quickly depletes the SS and once the SOC hits the lower threshold ($SOC_L = 50\%$) it returns to operate the PS at its optimal point. This logic is implemented by $S(t)$, which is the state determining whether the PS is generally (with the exception of insufficient power) active ($S(t) = 1$) or not ($S(t) = 0$):

$$S(t) = \begin{cases} 0 & SOC(t) \geq SOC_U \\ 1 & SOC(t) \leq SOC_L \\ S(t^-) & SOC_L < SOC(t) < SOC_U \end{cases} . \tag{3.7}$$

Here, $S(t^-)$ is the state S in the previous time sample. The rules and different modes of operation of the TCS are presented graphically in Fig. 3.1. Note that the PS will be requested to supplement power (at $P_{PS} = P_{PS,cop}$) if the load power exceeds the capability of the SS ($P_{PL} > P_{SSmax}$), without changing $S(t)$ to 1. For the purpose of stable operation an additional rule is also introduced: the PS reduces its supply of power if the battery is about to be charged beyond its power capacity (typically occurs during the event of regenerative braking), to avoid damage to the battery.

This two-state SCS is best implemented using a state machine, which can easily be designed using the Stateflow tool in Simulink, as shown in Fig. 3.2.

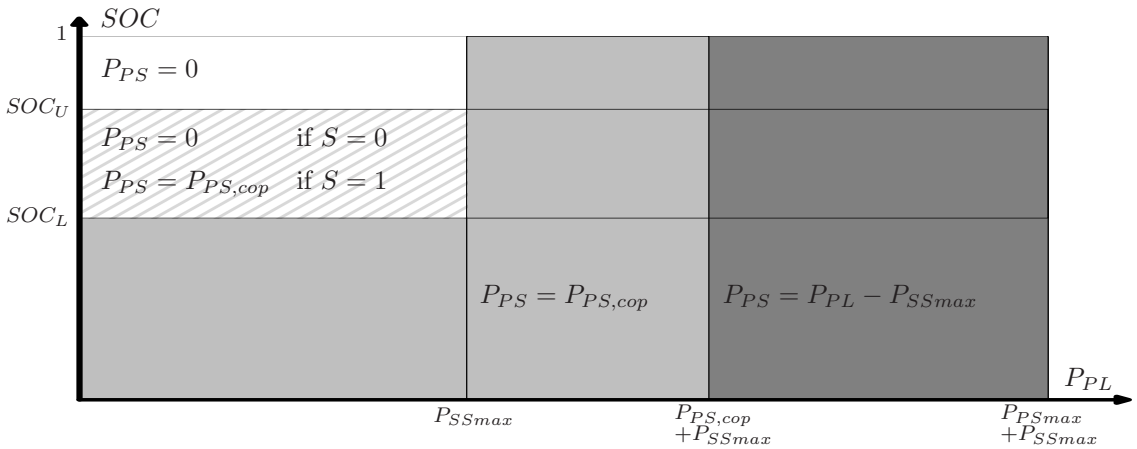

FIGURE 3.1: The TCS operates in two different modes, depending on given SOC and P_{PL}: SS-only or hybrid-mode with PS operating at a constant operating point.

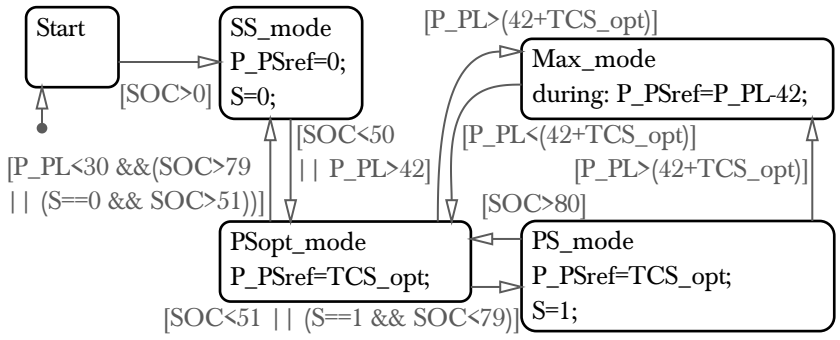

FIGURE 3.2: Stateflow diagram of the TCS, illustrating the control laws governing this SCS. TCS_opt is the optimal value for $P_{PS,cop}$.

3.2.2 Tuning

The TCS has a single control parameter, $P_{PS,cop}$, that needs to be set appropriately. By design, this should be the optimal operating point of the PS (although certain work in literature looks solely on the engine), which corresponds to $P_{PS,opt} = 20.1$ kW in the case of the vehicle model used in this work. However, although this intuitively is an appropriate selection, it is worth validating this choice with an objective tuning process.

Simulations are therefore run for the four driving cycles (WL-L, WL-M, WL-H and WL-E) with a range of $P_{PS,cop}$ values. Tuning results are presented in Fig. 3.3. It can be seen that the ideal value of $P_{PS,cop}$ varies between each driving cycle (19.6 kW, 17.8 kW, 17.0 kW and 23.8 kW for the four driving cycles respectively). It is interesting to observe that the optimal power level is reduced as the average power consumption increases from WL-L to WL-M to WL-H. This can be explained by the

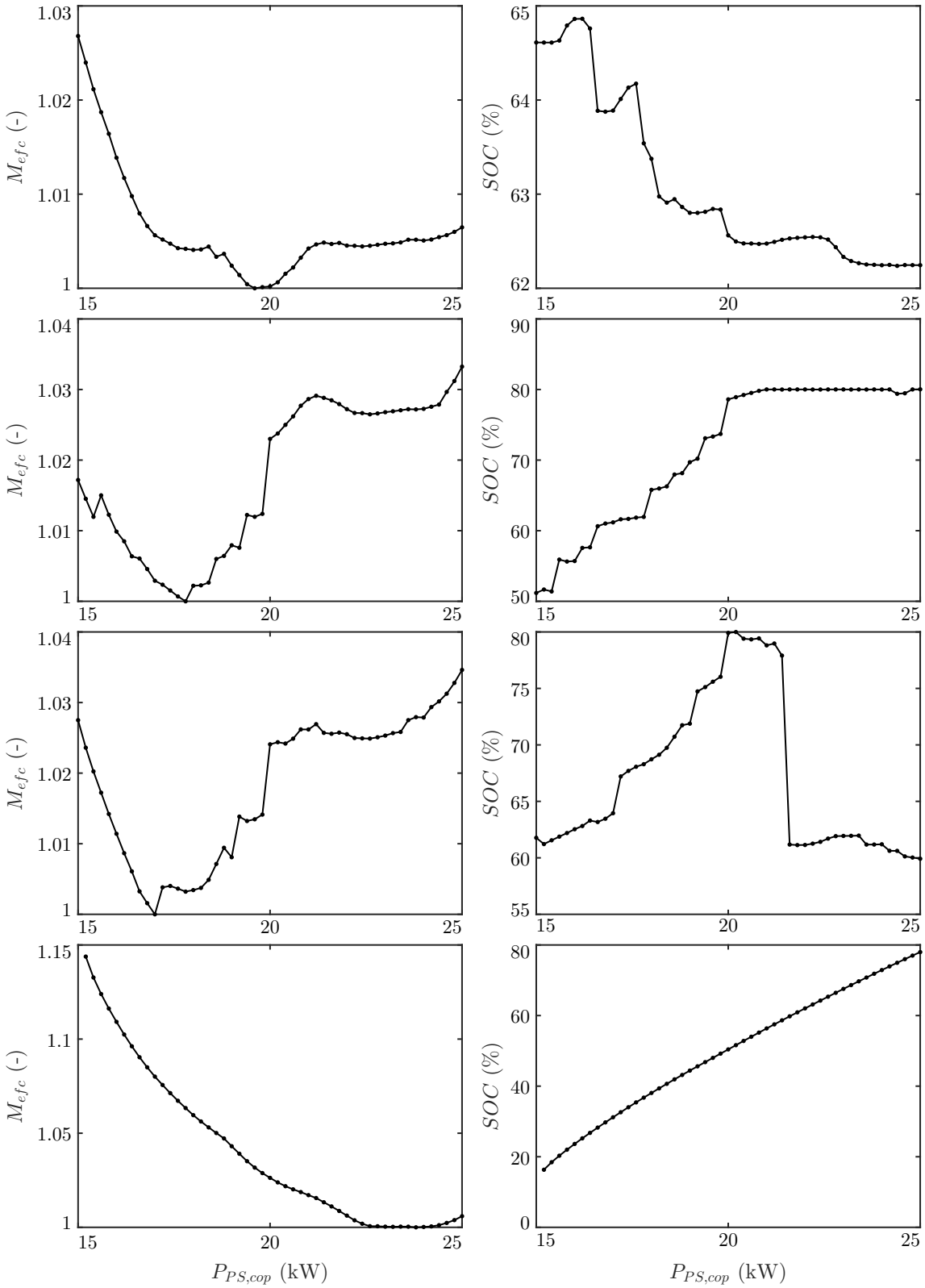

FIGURE 3.3: Normalized EFC (left) and final SOC (right) for varying $P_{PS,cop}$ when driving WL-L, WL-M, WL-H and WL-E (from top to bottom) with TCS.

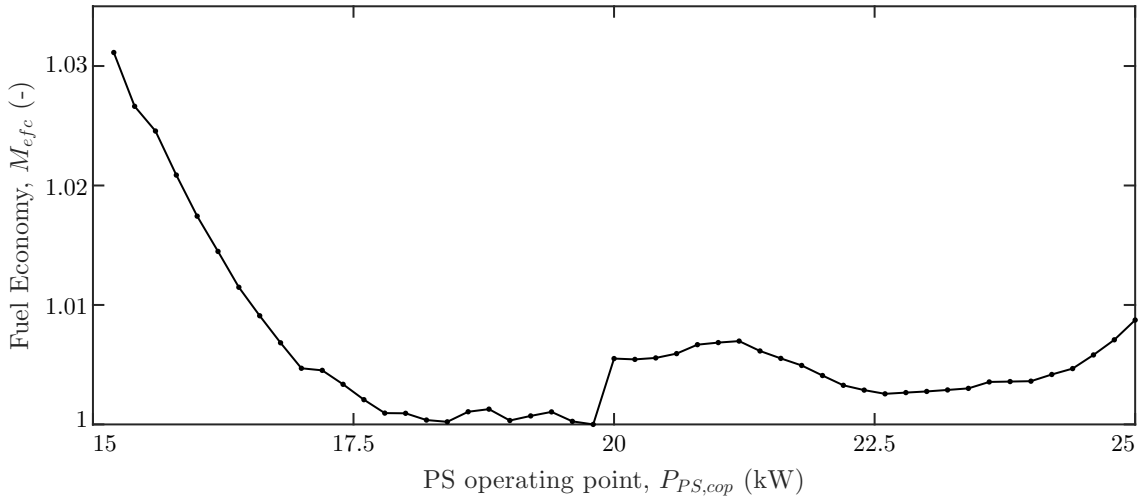

FIGURE 3.4: Normalized total EFC M_{tot} for varying $P_{PS,cop}$ with TCS.

benefits gained from reducing the amount of SS operation at high loads (where it is inefficient). A lower power level $P_{PS,cop}$ results in longer duration of PS operation, meaning that the SS can avoid a large part of its high load operation. However, if the average power load is high enough (like the WL-E) then the SS is typically required to be active and discharging during PS mode as well. Thus, the control strategy can't be CS for lower values of $P_{PS,cop}$ (the SOC can be seen to drop to 20% for $P_{PS,cop} = 15$ kW). Instead, by increasing the power levels of the PS, the burden on the SS is reduced.

To determine a single value for $P_{PS,cop}$ to be used during real-time driving, the four driving cycles are considered together (as described in Section 2.6.2). The normalized total EFC results are presented in Fig. 3.4, where the optimal tuning value is found to be $P_{PS,cop} = 19.8$ kW. It can thus be seen that the preliminary guess of $P_{PSopt} = 20.1$ kW is a very good estimate of the most suitable choice. For the purposes of this work, $P_{PS,cop} = 19.8$ kW will be used to allow the TCS to perform at its best when benchmarking against other control strategies.

It is worth mentioning that the parameter $P_{PS,cop}$ could be defined as an adaptive variable to persistently remain close to the optimal value for each driving cycle that yields the best fuel economy results, but such a variable would add undesirable complexity as well as move away from the heuristic nature intended for the TCS. Nevertheless, it is worth considering further why a single constant $P_{PS,cop}$ is not a universally suitable parameter value (as evidenced by the WL-E simulations).

Selecting $P_{PS,cop}$ to correspond with the peak efficiency operating point of the PS ensures optimal performance of the PS in the powertrain. However, the efficiency of the SS is not accounted for by any means, and is completely dictated by the propulsion load required to meet the driving cycle. If a driving cycle typically requires power loads comparable to the optimal power supply of the PS, then the SS efficiency does not significantly impact the overall fuel economy of the powertrain during PS mode. However, if the propulsion load greatly exceeds the optimal power supply of the PS ($P_{PL} >> P_{PS,cop}$) then the magnitude of power from the SS becomes significant and its efficiency dynamics impact the overall fuel economy. Conversely, if the propulsion load is very low (and $P_{PL} << P_{PSopt}$), then the battery is being charged at a very high C-rating, and thus a lower efficiency, again resulting in reduced overall powertrain efficiency. Also, there are further non-linear effects of P_{PSopt} on the timing of the on-set of PS ($S(t) = 1$) that are very driving cycle specific (you would ideally like to have the PS switch on just before high loads within the driving cycle).

3.2.3 Operation

Based on above findings, $P_{PS,cop} = 19.8$ kW is found to be the most suitable choice and will be used hereafter for all driving cycles. To understand the operation of the TCS, it is useful to study its power profiles. Figures 3.5 and 3.6 show the power profiles for the first and second iteration respectively of the four driving cycles.

For WL-L and WL-M, the vehicle is only powered by the SS in the first iteration of the cycles (as the TCS is in its charge depleting state $S = 0$). As the required load is quite low, it takes a long time for the SOC to drop sufficiently for the TCS to enter charging mode. This happens in the second iteration (Fig. 3.6) for both of these driving cycles. It can be seen that the SS is charged rapidly once the PS is on as typically the load is much lower than the PS power being delivered ($P_{PL} < P_{PS,cop}$). The TCS will actually return to charge depleting mode very soon after finishing the second iteration of the cycle. It's also worth noting that the PS deviates from its steady operation during significant regenerative braking, to respect the battery limits ($P_{SSmin} = -21$ kW).

In contrast, WL-M and WL-E both enter charging mode within the first iteration of the cycles (in fact, in less than a quarter of the time it took WL-L). However,

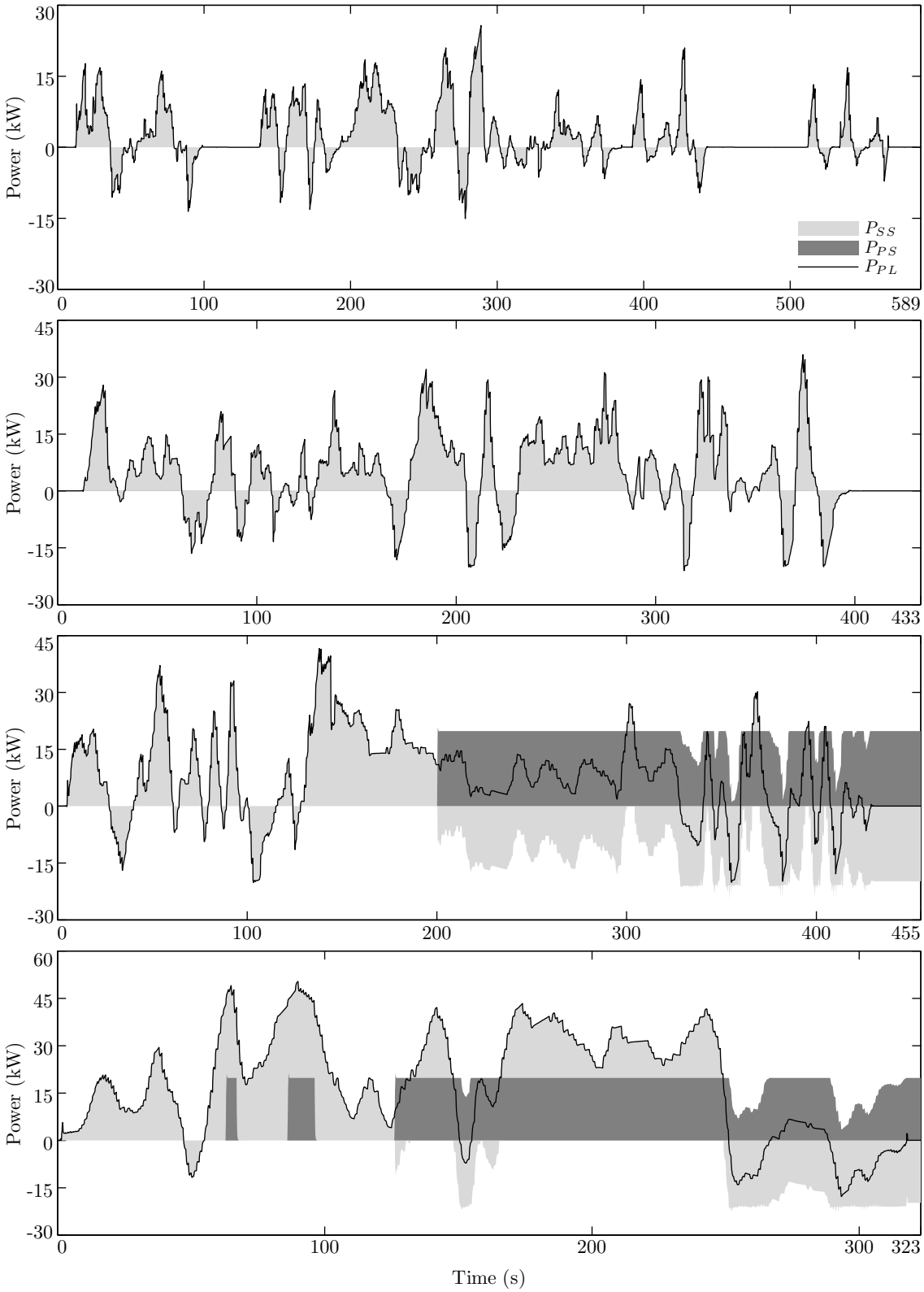

FIGURE 3.5: Power time histories for PS, SS and PL for the first iteration of driving WL-L, WL-M, WL-H and WL-E (top to bottom) with the TCS.

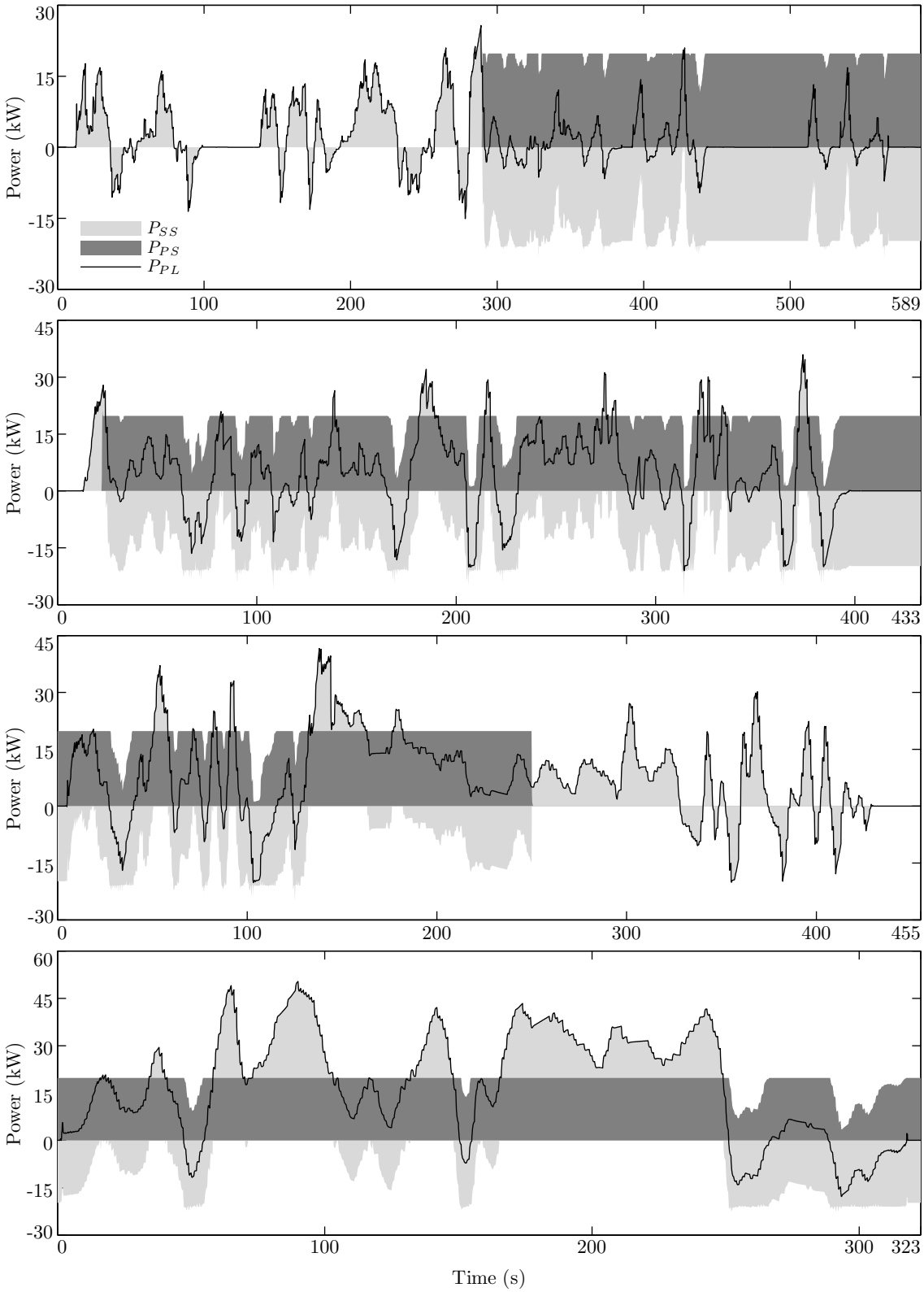

FIGURE 3.6: Power time histories for PS, SS and PL for the second iteration of driving WL-L, WL-M, WL-H and WL-E (top to bottom) with the TCS.

this change of state could not have arrived soon enough, as it can be seen that the SS was being exposed to very heavy loads, which is inefficient and accelerates battery degradation. The PS is in fact required to briefly assist the SS during peak loads for the WL-E, as the load exceeds the SS limits ($P_{PL} > P_{SSmax}$). It can also be seen in both iterations of the WL-E cycle that the SS is often being discharged despite the TCS operating in charging mode ($S = 1$). Thus, for any driving cycle that frequently or persistently uses more power than the steady supply of the PS ($P_{PL} < P_{PS,cop}$), the TCS will not be able to be CS (in the case WL-E for the vehicle design being tested, the TCS is just barely CS).

Overall, it can be seen that the TCS is able to operate the PS quite steadily in a very efficient manner, but at the expense of extreme types of operation by the SS. The latter is often charged at its limit P_{SSmin}, and it is also often required to deliver very heavy loads (at times matching P_{SSmax}). This stems from the PS-centric design of the TCS and does not serve the overall powertrain very well.

The resulting fuel economy for the four driving cycles for the TCS is shown in Table 3.1. It can be seen that the final SOC varies considerably, as could be expected from the oscillating nature of the control. The fuel economy is also compared to the GECMS (presented in Section 3.4) which can be considered an approximate global optimal solution. Thus, the TCS is found to lag the GECMS results by 7.13-17.89%, with a combined difference (as computed for M_{tot}) of 14.35%. This leaves plenty of room for improvement.

Table 3.1: Fuel economy results for TCS

Driving Cycle	SOC_{final} (%)	m_f (kg)	m_{efc} (kg)	Δ_{GECMS} (%)
WL-L	62.84	0.8115	0.8350	+17.89
WL-M	73.71	1.4174	1.3345	+17.18
WL-H	76.03	1.1912	1.0865	+14.34
WL-E	49.21	1.4818	1.6983	+7.13

3.3 Power Follower Control Strategy

The power follower control strategy (PFCS) is the second most conventional control strategy for series HEVs. Its key characteristic is having the engine deliver the required power to drive the car, unless high loads are required, in which case the battery adds support.

3.3.1 Design

The PFCS follows a set of rules. Generally, the PS follows the load of the PL, with some deviation to correct and consider the varying SOC. When the load from the PL (P_{PL}) is low and SOC is high, the SS is selected to deliver the power to the vehicle ($S(t) = 0$). Conversely, when P_{PL} is high or SOC is low, the PS is selected to meet the load ($S(t) = 1$). These states are defined as follows:

$$S(t) = \begin{cases} 0 & SOC(t) \geq SOC_U \text{ and } P_{PL} < P_{min} \\ 1 & SOC(t) \leq SOC_L \text{ or } P_{PL} > P_{SSmax} \\ S(t^-) & SOC(t) \geq SOC_L \text{ and } P_{PL} < P_{SSmax} \end{cases}. \tag{3.8}$$

For $S(t) = 0$, we always have $P_{PS} = 0$. For $S(t) = 1$, the operation of the PS is defined as

$$P_{PS}(t) = \begin{cases} P_{min} & SOC(t) \geq SOC_U \\ P_m(t) & SOC_L < SOC(t) < SOC_U \\ P_{PSmax} & SOC(t) \leq SOC_L \end{cases} \tag{3.9}$$

where P_m is given by

$$P_m(t) = P_{PL} + P_{ch}\left[\frac{SOC_U + SOC_L}{2} - SOC(t)\right]. \tag{3.10}$$

It can be understood that the PS power is essentially following the load P_{PL} when the SOC is at the midpoint between SOC_L and SOC_U, but biases the operation in favor of charging or discharging the SS in the cases of low and high SOC respectively. The bias is scaled by P_{ch} to achieve CS operation. Note that in general $P_{SS} \neq 0$ when $S(t) = 1$. These rules are shown visually in Fig. 3.7 and the implementation of the rules within a state-flow diagram is shown in Fig. 3.8. Note that the PS is constrained to operate within $P_{min} \leq P_{PS} \leq P_{PSmax}$ (where P_{min} is a tunable

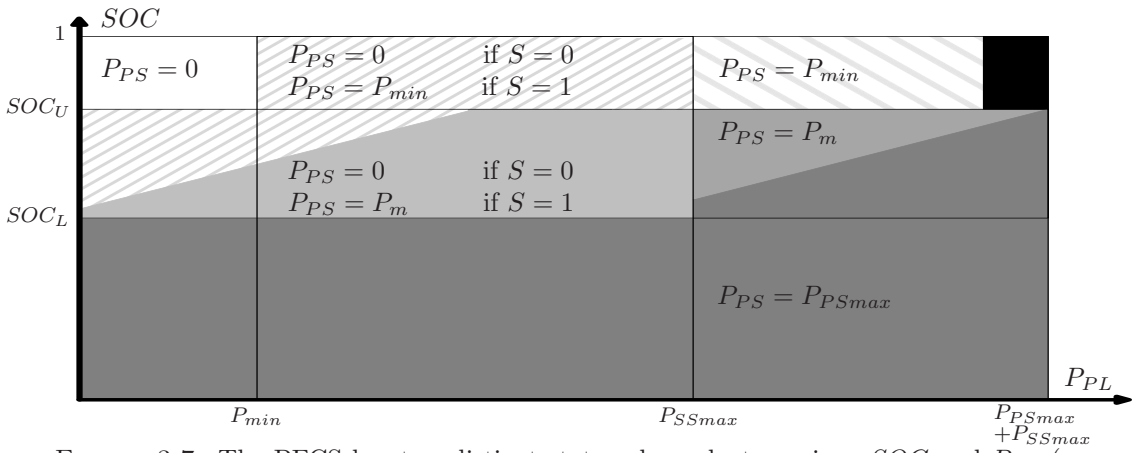

FIGURE 3.7: The PFCS has two distinct states, dependent on given SOC and P_{PL} (as defined in (3.8)), and has an area of hysteresis in between where the PS delivers zero, P_{min} or P_m power. Note that the vehicle can't deliver maximum power for $SOC > SOC_U$.

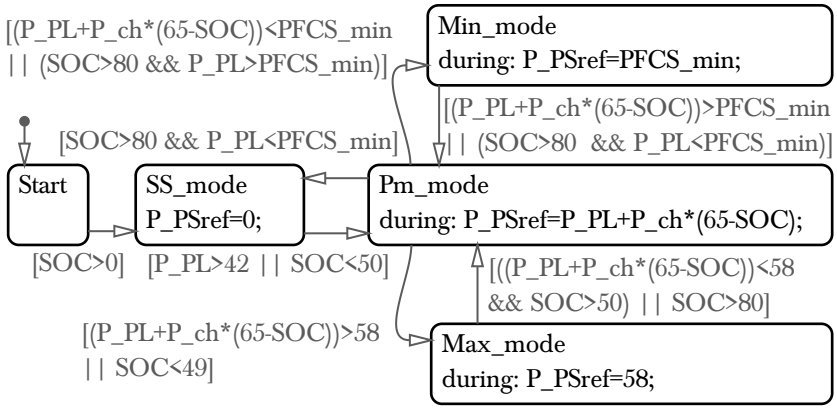

FIGURE 3.8: Stateflow diagram of the PFCS, illustrating the control laws governing this SCS. PFCS_min is the minimum power P_{min}.

parameter whilst $P_{PSmax} = 58$ kW is a physical constraint of the PS) when it is on, thus resulting in the diagonal boundaries (with slope $1/P_{ch}$) in Fig. 3.7.

The PFCS therefore has two tunable parameters: the charging factor P_{ch} and the minimum power P_{min}. The charging factor needs to be positive to contribute towards making the control strategy more CS, but $P_{ch} = 0$ is permissible as well. Furthermore, as the charging factor scales the amount the battery is recharged, it should respect the maximum power the battery can absorb, such that

$$P_{ch}\frac{100(SOC_L - SOC_U)}{2} \leq P_{SSmin}. \tag{3.11}$$

Note that the factor of 100 is to convert the SOC units to percentage, as this is the convention when defining P_{ch}. Thus, for $P_{SSmin} = -21$ kW the charging factor P_{ch}

should be defined such that it's limited to $P_{ch} \in [0, 1.4]$ kW. Similarly, the charging factor is also limited by the maximum power limit of the SS, such that

$$P_{ch} \frac{100(SOC_U - SOC_L)}{2} \leq P_{SSmax}. \tag{3.12}$$

Thus, for $P_{SSmax} = 42$ kW the charging factor P_{ch} should be defined such that it's limited to $P_{ch} \in [0, 2.8]$ kW. To allow the charging factor to achieve all its potential influence, it will be explored in the range $P_{ch} \in [0, 3]$ kW, but limits in the model will ensure that the SS is not overloaded.

In the literature, the minimum power P_{min} is sometimes defined by a physical constraint of the engine-generator set, but the magnitude of this parameter varies widely across different work. The powertrain used in this work can operate at very low power levels, and the PFCS inherently imposes $P_{min} < P_{SSmax}$ (as can be understood by Fig. 3.7). Thus the feasible range for the minimum power is $P_{min} \in [0, 42]$ kW.

3.3.2 Tuning

The implemented PFCS is simulated for various driving cycles with different P_{ch} and P_{min} values and the resulting normalized EFC and final SOC values for these tests are presented in Fig. 3.9. The optimal selection of parameters for each driving cycle is marked with a cross sign.

As can be seen in the charts, the optimal tuning for each driving cycle is unique. However, in each case the optimal P_{min} is found to be close to 20 kW, which is the PS peak efficiency operating point, or just below it. Considering the fact that the PFCS often operates at $P_{PS} = P_{min}$, it is not a surprising outcome, although it is not a typical setup in the literature (where lower values are typically used). Furthermore, in the first three of the driving cycles, $P_{ch} = 0$ is found to be the ideal selection, thus having the PFCS truly operate such that the PS follows the load power ($P_{PS} = P_{PL}$) with no additional CS action. Instead, the control strategy remains CS through switching between it's charge depleting state ($S(t) = 0$) and charge replenishing state ($S(t) = 1$). However, it can be seen that the control strategy is operating close to the upper bound of the SOC for WL-E if $P_{ch} = 0$ is used.

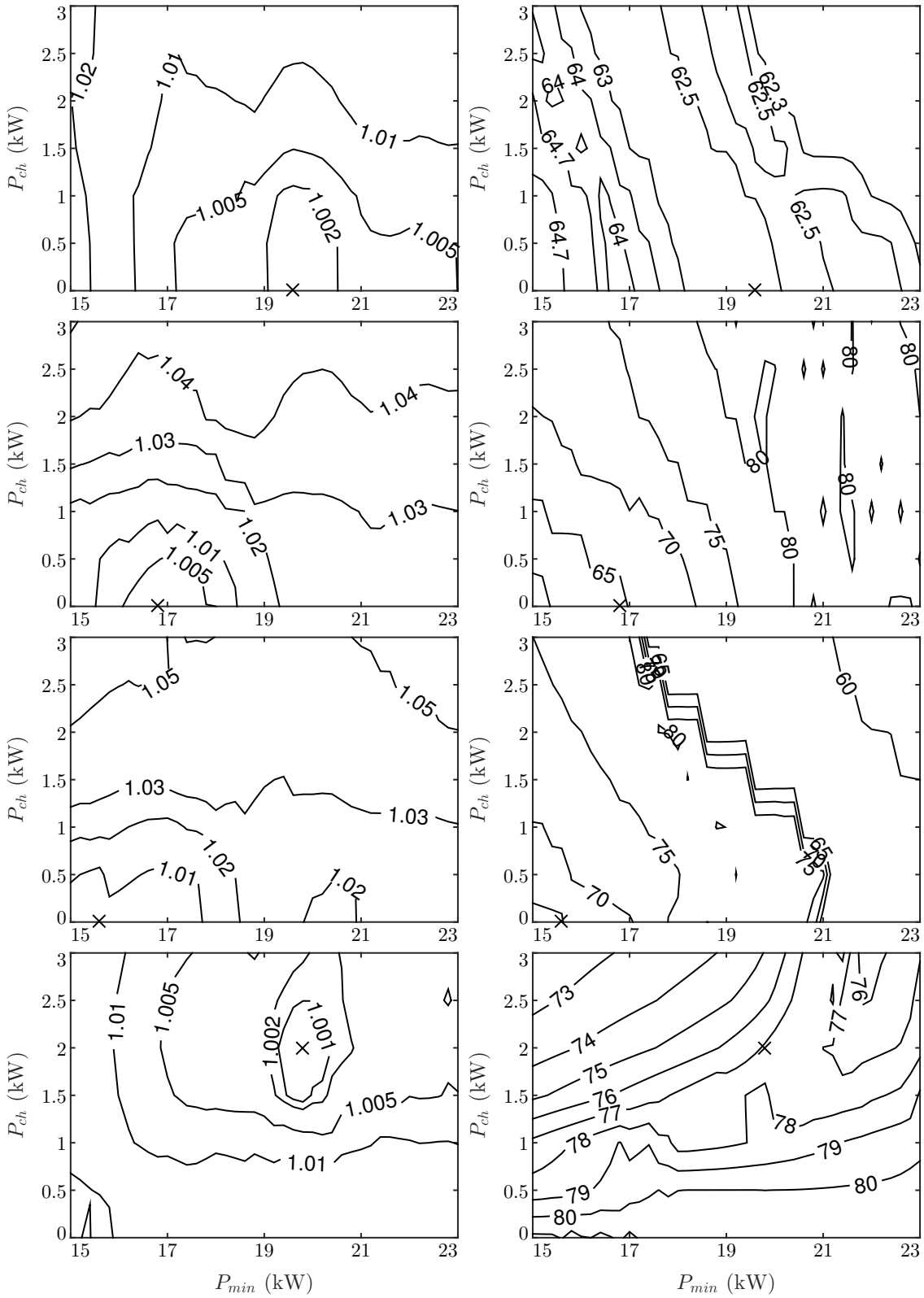

FIGURE 3.9: Normalized EFC M_{efc} (left) ($M_{efc} = 1$ is marked with a cross) and final SOC (right) for varying P_{min} and P_{ch} when driving WL-L, WL-M, WL-H and WL-E (from top to bottom) with PFCS.

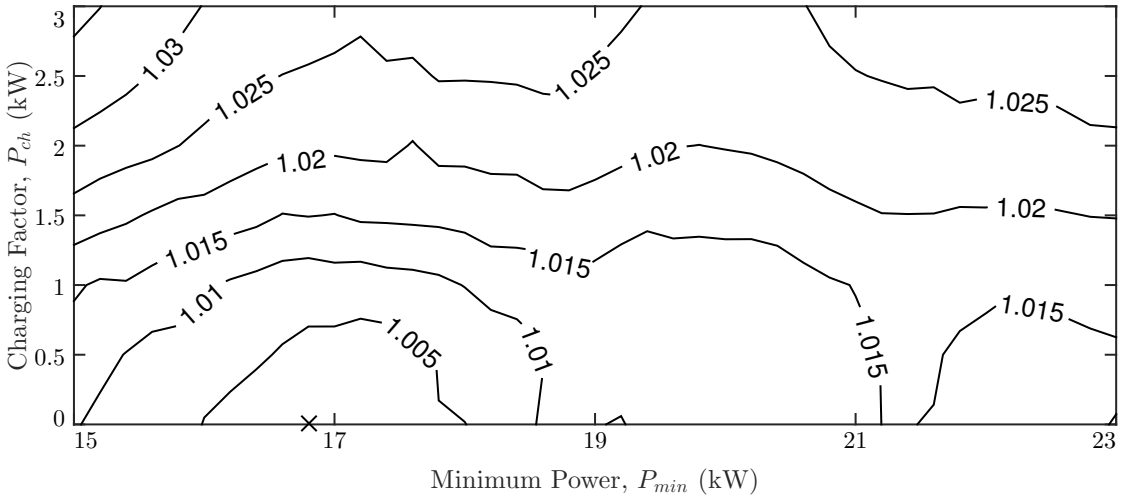

FIGURE 3.10: Normalized total EFC M_{tot} for varying P_{min} and P_{ch} with PFCS.

To obtain the optimal tuning parameters for implementation during real-time driving, a single set is found by evaluating the total fuel economy of the four driving cycles combined. The results are presented in Fig. 3.10, and the total EFC is found to be at its minimum for $P_{ch} = 0$ and $P_{min} = 16.8$ kW. This selection will therefore be used henceforth within this work.

3.3.3 Operation

Using the tuned values for the control parameter it is now possible to look closer at the resulting operation. Figure 3.11 shows the power profiles of the powertrain when driving the first iteration of the four driving cycles, and Fig. 3.12 shows the second iteration.

For WL-L, the PFCS operation is very similar to the operation of TCS from Figs. 3.5 and 3.6. As it opens with pure SS operation it operates identically to the TCS until halfway through the second iteration, when the PS is switched on. The PFCS operates at P_{min} quite persistently as the required load is very low. The power level is however different, as P_{min} is of a lower magnitude than the $P_{PS,cop}$ of the TCS. Consequently, the PFCS can expect to operate in a charge replenishing mode ($S = 1$) for a longer duration than the TCS, while exposing the SS for less intensive charging.

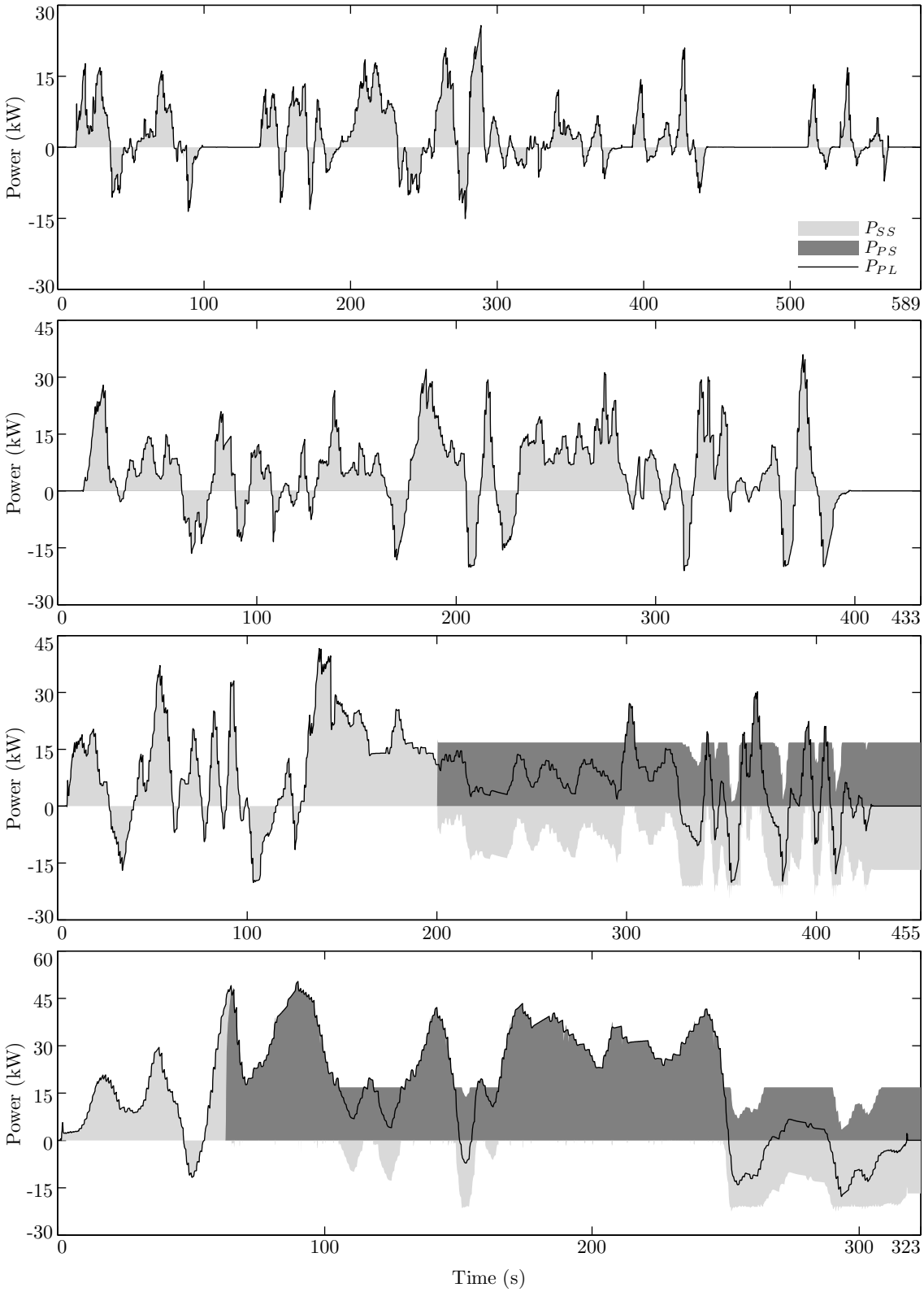

FIGURE 3.11: Power time histories for PS, SS and PL for the first iteration of driving WL-L, WL-M, WL-H and WL-E (top to bottom) with the PFCS.

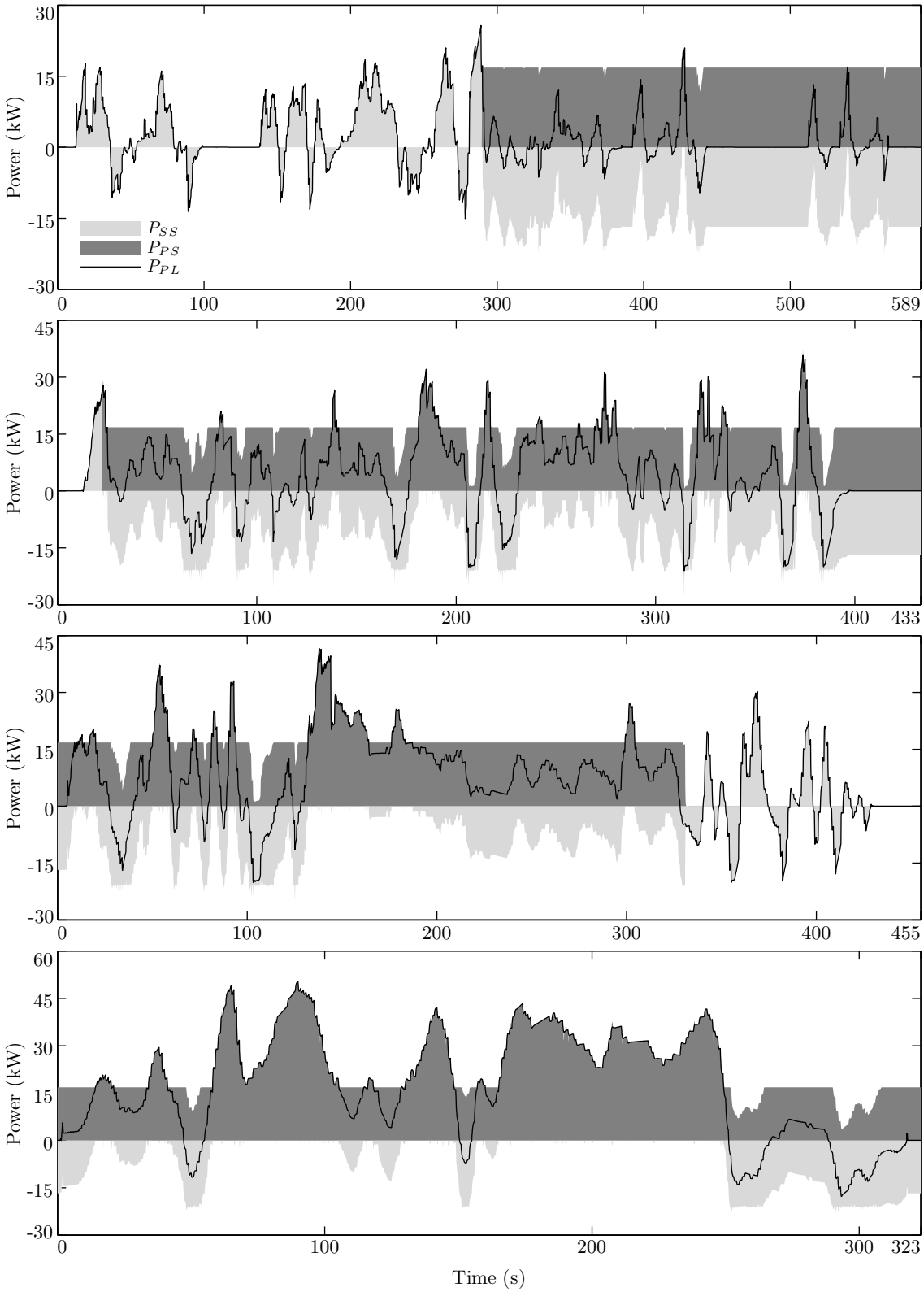

FIGURE 3.12: Power time histories for PS, SS and PL for the second iteration of driving WL-L, WL-M, WL-H and WL-E (top to bottom) with the PFCS.

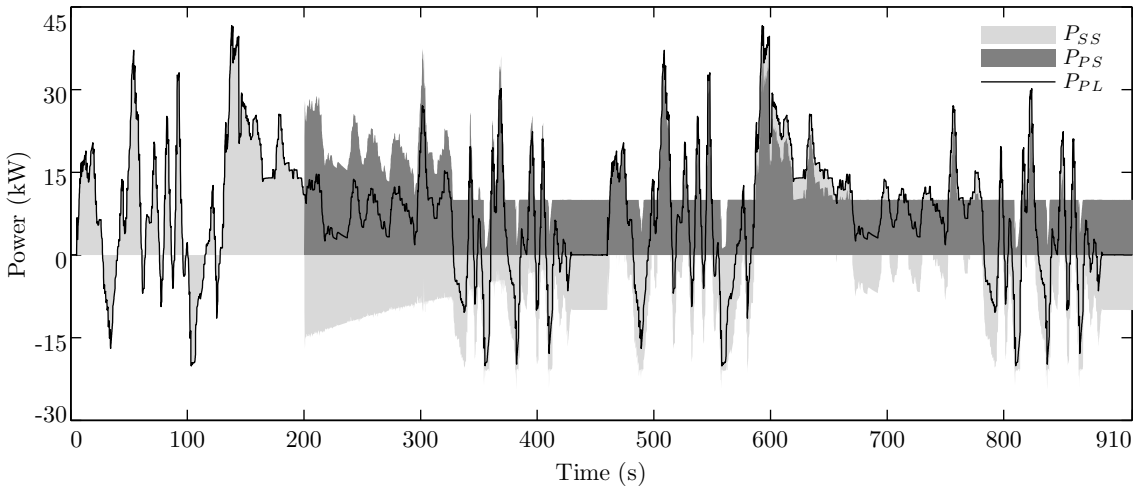

FIGURE 3.13: Power time histories for PS, SS and PL for the first two iterations of driving WL-H with the PFCS with $P_ch = 1$ kW and $P_{min} = 10$ kW.

The operation for WL-M is the same as the TCS for the first iteration, but it begins to display its power following characteristics in the second iteration. As the PS is switched on (as SOC has dropped to its lower limit), the PS will operate typically at P_{min}, but whenever the required load exceeds this threshold, the PS will adjust and meet the load fully.

This operation becomes even clearer for WL-H and WL-E, where a higher amount of time is spent with $P_{PL} > P_{min}$, allowing the PFCS to operate in its power following mode for a significant part of the driving cycle. As the SS is not discharged in this mode of operation, the SOC can be expected to recover quite fast, which is comparable to TCS for WL-H, despite $P_{min} < P_{PS,cop}$. It also worth noting that the PFCS enters charge replenishing mode already around $t = 60$ s, which is earlier than the TCS. This is an effect of the power conditions that are given in Eq. 3.8, which makes the PFCS change state if the load becomes high. This allows the PFCS to enable the PS at an earlier stage than the TCS, which is clearly advantageous for WL-E.

The resulting operation from the optimal tuning parameters is not the typical PFCS operation (although it arguably is more "power following"), which would have a higher P_{ch} and lower P_{min}. To illustrate this, Fig. 3.13 shows the power profile for WL-H×2 with $P_{ch} = 1$ kW and $P_{min} = 10$ kW. The PFCS starts the driving cycle starts with SS-only mode, just like the optimal setting in Fig. 3.11. As the PS is switched on around $t = 200$ s (because SOC reaches SOC_L), the power from the

PS generally follows the shape of the load power but exceeds it with some margin ($P_{PS} > P_{PL}$) resulting in the SS being charged. This offset is due to the contribution from the charging factor P_{ch} as seen in Eq. 3.10.

However, with time (as SOC increases), the margin between P_{PS} and P_{PL} is gradually reduced, resulting in the SS being charged at a slower rate, until the PS is briefly following the load power quite precisely (as $SOC = \frac{SOC_U + SOC_L}{2}$). As the SS is generally charged (and the SOC thus increases), the SS begins supplementing the PS in meeting the load power. This type of operation is clearly more CS (rather than just rapid charging) than the operation shown in Fig. 3.12, and thus keeps the PS on even at the end of the two iterations of WL-L. However, having the SS operate at very low power levels is not efficient due to the high DC-DC converter losses for this type of operation. Consequently, the PFCS setting of $P_{ch} = 0$ and $P_{min} = 16.8$ kW is find to be the best. As the nature of the PFCS is dependent on the particular powertrain in which it is implemented, it is expected to exhibit some variance in behavior. Thus, the appropriate way to proceed is to use the tuned parameters that were found to be optimal for the PFCS in terms of equivalent fuel economy, despite its somewhat unconventional operation (albeit within the power follower framework).

Lastly, the fuel economy of the PFCS is presented in Table 3.2 for the four driving cycles. Similar to the TCS, it can be seen that the final SOC varies considerably, as the high setting of P_{min} has the PFCS partly mimic the operation of the TCS. The fuel economy is also compared to the GECMS (presented in the next section) which can be considered an approximate global optimal solution. The PFCS is found to lag the GECMS results by 6.57-18.60%, with a combined difference of 13.55%. This is a small improvement on the TCS, but further improvements can be expected for better designed strategies.

Table 3.2: Fuel economy results for PFCS

Driving Cycle	SOC_{final} (%)	m_f (kg)	m_{efc} (kg)	Δ_{GECMS} (%)
WL-L	63.88	0.8278	0.8400	+18.60
WL-M	62.02	1.2824	1.3145	+15.43
WL-H	69.49	1.1198	1.0772	+13.35
WL-E	80.86	1.8681	1.6894	+6.57

3.4 Global Equivalent Consumption Minimization Strategy

The GECMS is a globally tuned ECMS. The strategy determines the equivalent fuel consumption (EFC) of the powertrain for various driving conditions to produce an offline control map, instructing how to best share the power between engine and battery. To compute the EFC, the equivalence factors S_d and S_c need to be estimated, but the GECMS operates with the luxury of being allowed to use optimally tuned equivalence factors, in order to achieve close to optimal fuel economy.

3.4.1 Design

The ECMS has been widely described in the literature, both as a proposed SCS as well as for benchmarking [70, 78, 113]. There are many variants, but the presented work implements a GECMS (globally tuned ECMS), based on [78]. It has been shown that the GECMS is able to realize operation almost identical to the global optimal solution as determined through DP [104]. This makes the GECMS a very suitable benchmark, as it provides a close to optimal solution to benchmark any proposed SCS without employing DP, which might be unfeasible to implement for a complex and dynamic vehicle model. As the principles of GECMS, and its foundation on PMP, have been discussed previously in this chapter (and in more depth in the literature), this section will solely focus on the implementation of this SCS.

The objective of a GECMS is to minimize the EFC m_{eq}, which is defined as

$$m_{eq} = \int_o^{t_f} \dot{m}_{eq}(t, u(t))\ \mathrm{d}t, \tag{3.13}$$

where

$$\dot{m}_{eq} = \begin{cases} \dot{m}_f(P_{PS}) - S_d \frac{P_{SS}}{Q_{LHV}} & P_{SS} \geq 0 \\ \dot{m}_f(P_{PS}) - S_c \frac{P_{SS}}{Q_{LHV}} & P_{SS} < 0 \end{cases}, \tag{3.14}$$

where $\dot{m}_f$ is the fuel consumption rate of the ICE in the PS and Q_{LHV} is the lower heating value of the fuel. The two constants S_d and S_c are equivalence factors that translate the energy discharged/charged by the SS into a corresponding amount of

fuel consumed/stored. The values of these constants can be determined by trial-and-error or numerical optimization, to identify the optimal selection of equivalence factors for each driving cycle being tested. Although such tuning can be time-consuming for very complex vehicle models, it's likely to be faster and simpler than implementing alternative global SCSs (such as DP solutions).

The optimization problem can now be reduced to a local minimization problem as follows:

$$P_{GECMS} \begin{cases} \min\limits_{u} \dot{m}_{eq}(t,u) \ \forall t \in [0,t_f] \\ 0 \leq u \leq \frac{P_{PSmax}}{P_{PL}} \\ SOC_L \leq SOC \leq SOC_U \end{cases} \tag{3.15}$$

Thus, for each time instant t of a given driving cycle (for which we obtain the P_{PL} profile), an optimal power share factor u_{opt} can be defined for each set of equivalence factors S_d and S_c. Using a map of fuel consumption $m_f(P_{PS})$, as shown in Fig. 2.10, a sweep can be performed for Eq. 3.14 with $u \in [0, \frac{P_{PSmax}}{P_{PL}}]$ for $P_{PL}(t)$ to produce an optimal control input. This process is repeated for each candidate set of S_d and S_c. For m number of S_d values investigated and n number of S_c values investigated, there are $m \times n$ number of control maps produced for each driving cycle investigated. Consequently, to identify the optimal selection of equivalence factors, within a range of e.g. $S_d \in [2.9, 3.1]$ and $S_c \in [2.6, 2.9]$ with intervals of 0.01 for the four driving cycles would require approximately 2000 hours of driving simulation.

3.4.2 Tuning

To tune the GECMS, the computational time needs to be reduced. A coarser search (with 0.02 intervals) is therefore performed on a quarter of the number of iterations that are typically used in this work for each driving cycle (i.e. WL-L×2, WL-M×2, WL-H×1 and WL-E×1). As the GECMS control variable is independent of SOC, or any other model state, the applied control is identical for each iteration of each driving cycle. Thus, these initial simulations will yield quite accurate equivalence factor values. The fuel economy results for these tests, together with final SOC values, are shown in Fig. 3.14.

It can be seen that the optimality of the driving cycle is highly sensitive to the selected equivalence factors S_d and S_c (e.g. an error of 2% in S_c could cause a 20%

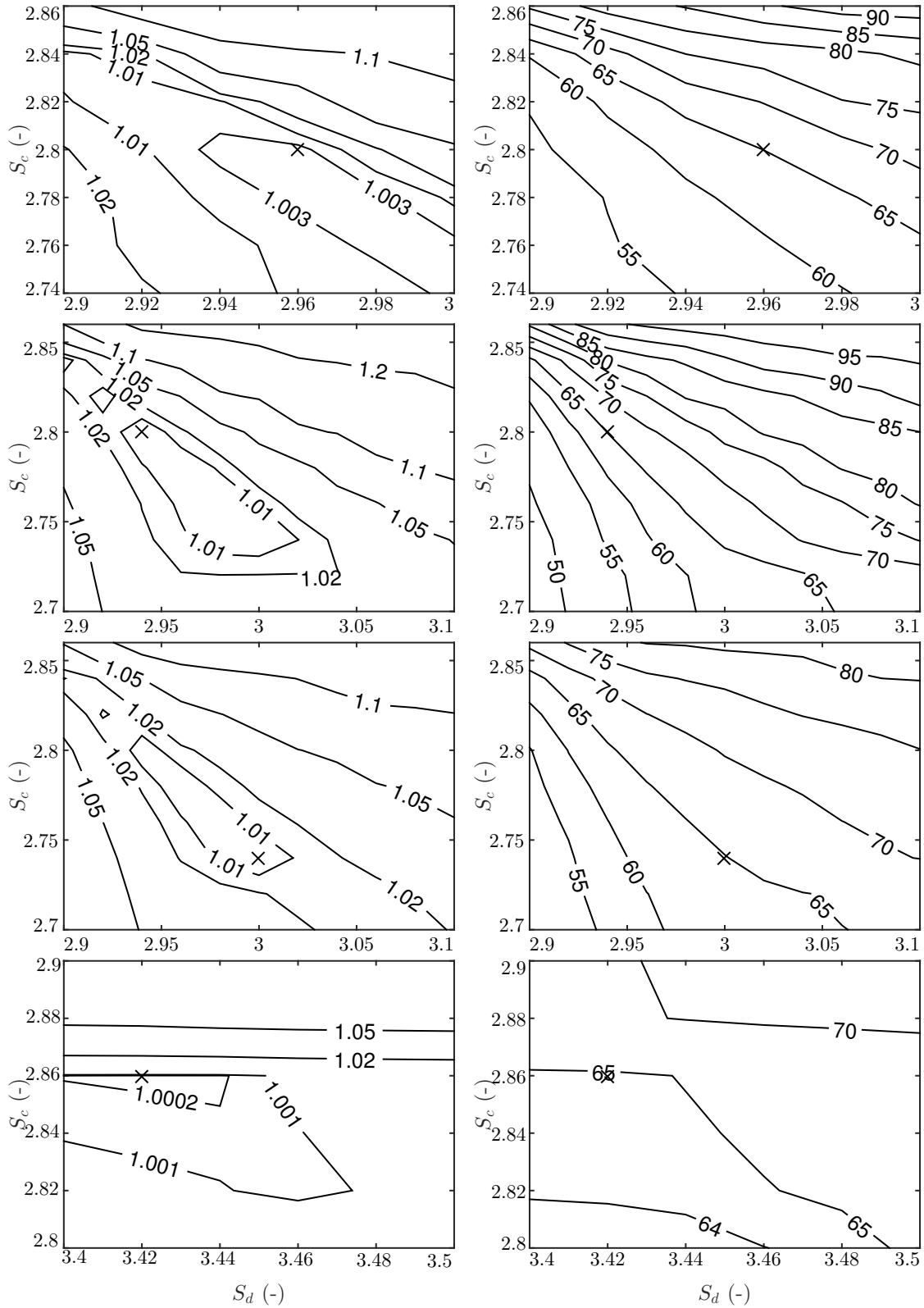

FIGURE 3.14: Normalized EFC M_{efc} (left) ($M_{efc} = 1$ is marked with a cross) and final SOC (right) for varying S_d and S_c coarsely when driving WL-L, WL-M, WL-H and WL-E (from top to bottom) with GECMS.

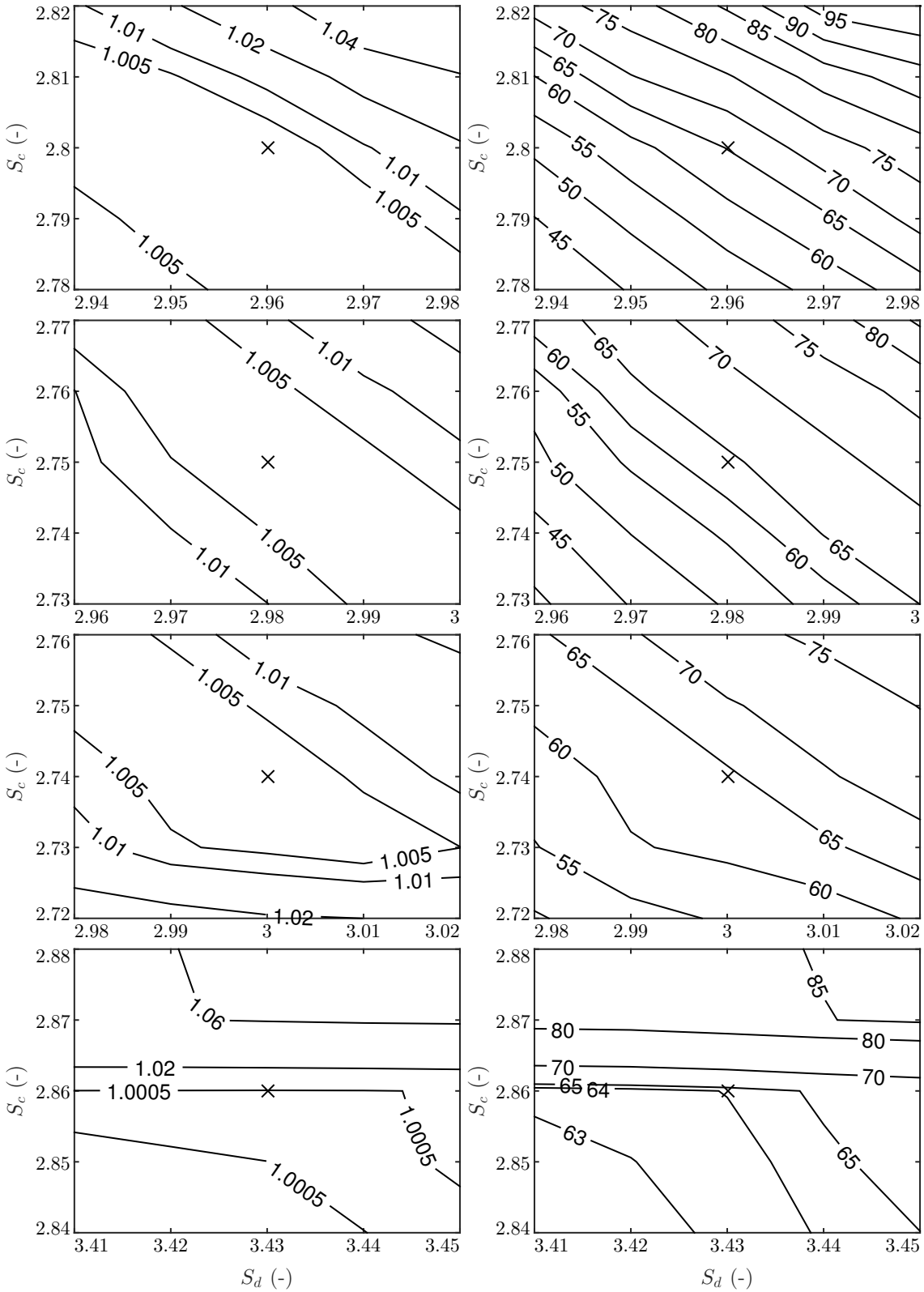

FIGURE 3.15: Normalized EFC M_{efc} (left) ($M_{efc} = 1$ is marked with a cross) and final SOC (right) for varying S_d and S_c when driving WL-L, WL-M, WL-H and WL-E (from top to bottom) with GECMS.

drop in fuel economy for WL-M), although the approximate optimal values (marked by the cross) are often found in close proximity to each other, in particular for the three first driving cycles. Furthermore, by comparing each set of subplots, it appears that each approximate optimal solution appears nearby the $SOC_{final} = SOC_{initial}$ line (where $SOC_{initial} = 65\%$). This is a desirable trait, as it tends towards making the GECMS CS. However, it is worth noting that this behavior is not inherent to the ECMS alone, but relies on appropriately defined S_d, efc and S_c, efc when evaluating the EFC m_{efc} (as discussed in Section 2.6.2). A badly defined EFC would not have the GECMS exhibit these CS tendencies.

Now further simulations can be run (for the full number of iterations of the driving cycles and with intervals of 0.01) in the proximity of the obtained approximate equivalence factors. The fuel economy results for these tests, together with final SOC values, are shown in Fig. 3.15.

At this precision level, it becomes apparent that the fuel economy is less sensitive than the final SOC to the equivalence factors (the fuel economy is still more sensitive for the GECMS than for the TCS or PFCS). In fact, this feature can be exploited to design a real-time ECMS. By tuning the equivalence factors in real-time based on the SOC, the real-time ECMS will remain CS for any driving cycle and achieve a fuel economy comparable to the GECMS. Although a real-time ECMS has not been implemented, this concept will be used in the next chapter.

The equivalence factor values obtained from this optimization process for the four driving cycles are given in Table 3.3 and the resulting optimal control maps are shown in Fig. 3.16. In all four cases it can be seen that the strategy includes a pure electric operation at low powers, which should be expected considering that the PS doesn't perform very efficiently at low loads. Equally, once the PS is turned on, it delivers more power than the required load and thus ends up charging the SS. This is followed by generally hybrid operation for higher power loads. The mix of $u < 1$ and $u > 1$ operation allows driving to be more CS than only relying on regenerative braking. These are all insights that will be used in designing further control strategies in the coming chapters.

The GECMS is implemented into the vehicle model in Simulink through a simple look-up table that uses the produced map (shown in Fig. 3.16) and the requested P_{PL} to select the optimal power share factor, that is then multiplied by P_{PL} to provide

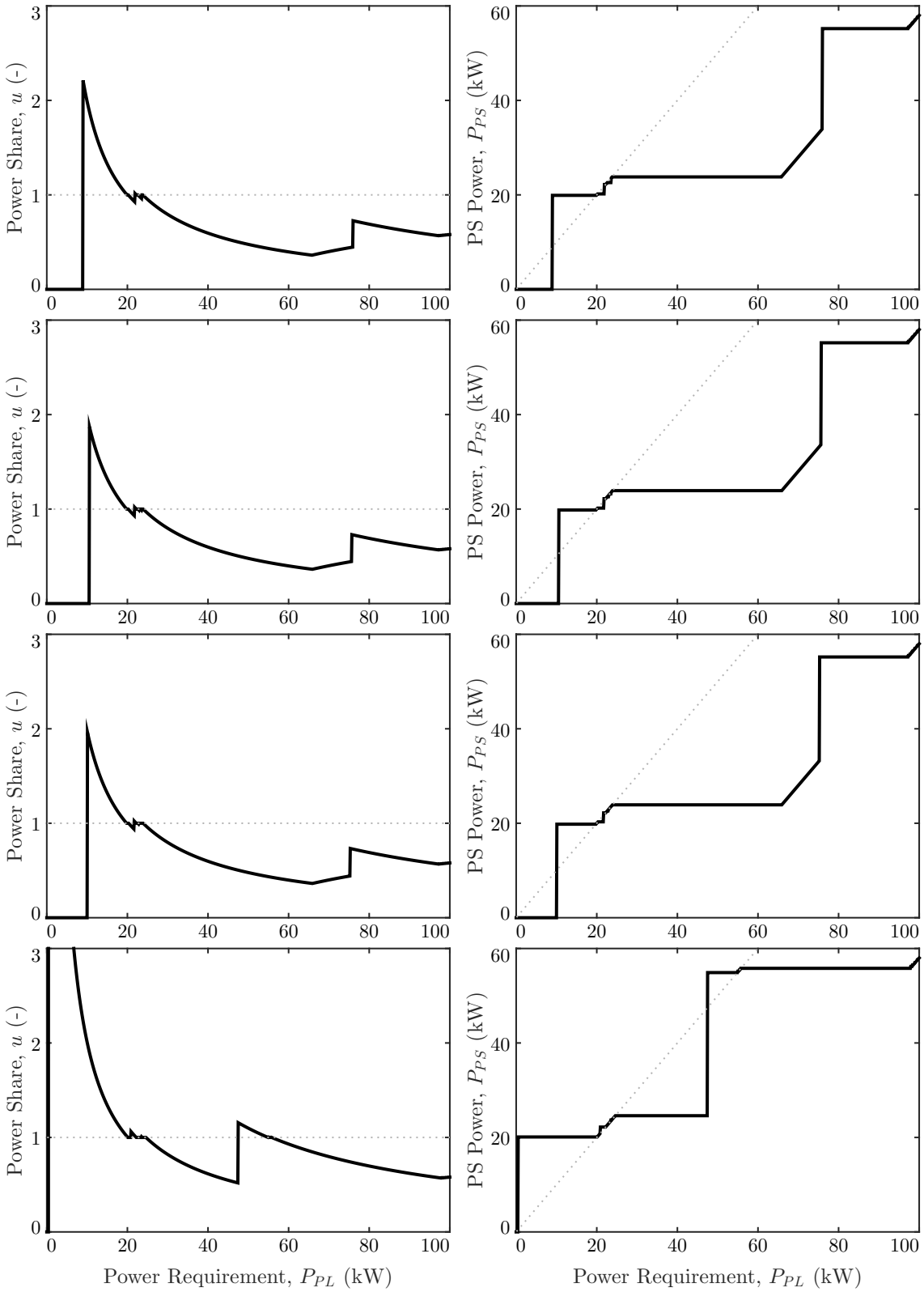

FIGURE 3.16: Power share factor and PS power for varying power requirements, for WL-L, WL-M, WL-H and WL-E (from top to bottom) with GECMS.

TABLE 3.3: Optimal equivalence factor values

Driving cycle	S_d	S_c
WL-L	2.96	2.80
WL-M	2.98	2.75
WL-H	3.00	2.74
WL-E	3.43	2.86

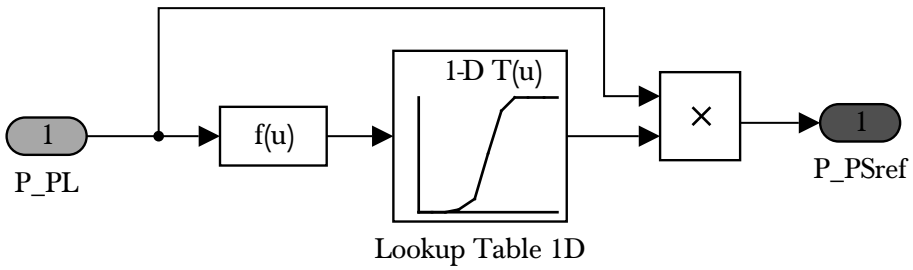

FIGURE 3.17: Implementation of the GECMS in Simulink.

the optimal P_{PSref}. This implementation is shown in Fig. 3.17. An alternative implementation would be to generate a power share ratio profile $u(t)$ for each driving cycle and implement it without any input from the model. However, such a method is less robust for changes in vehicle operation and requires more pre-simulation processing time (to generate the power share profile). Lastly, and maybe the most common method of implementation, would be to compute the power share ratio u (using globally tuned, pre-computed equivalence factors) at each sample time. Although this process is feasible in real time, it would result in increased simulation time and is thus not preferred.

3.4.3 Operation

The implemented GECMS, with optimally tuned S_d and S_c values, has been simulated and the resulting power profiles are shown in Fig. 3.18 for the four driving cycles. As the GECMS is state-independent, it operates exactly the same way for every iteration of the driving cycles. Therefore, only the first iteration is presented here.

For WL-L and WL-M, the control can be characterized by its frequent switching of the PS. It is not used more than 20 s continuously. It is consequently much more responsive to changes in required load, as compared to the TCS or PFCS that could

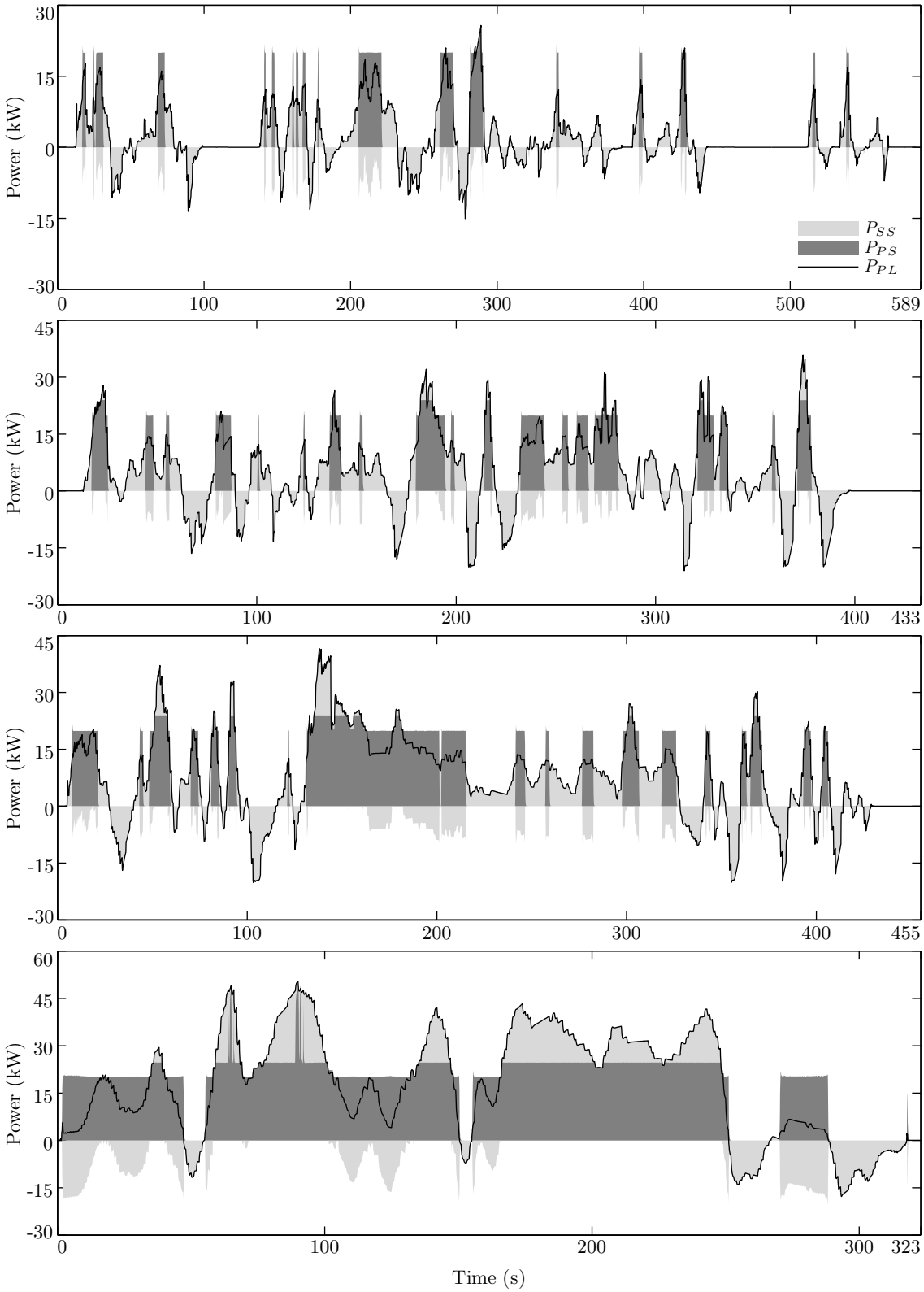

FIGURE 3.18: Power time histories for PS, SS and PL for the first iteration of driving WL-L, WL-M, WL-H and WL-E (top to bottom) with the GECMS.

keep on operating the SS close to its maximum limit rather than turn on the PS. In fact, while the TCS and PFCS would switch on the PS twice each during WL-L, the GECMS does it 144 times (corresponding to one switch per 33 s). Although this incurs a penalty in fuel consumption, it is quite likely that the improved power share will more than compensate for this (as is shown later). The GECMS experiences somewhat more continuous operation for WL-H and WL-E. For the latter, the PS operates in some sense even steadier than the PFCS. The PS is operated between 20 and 25 kW with a few spikes for very high loads.

More generally, it can be seen that the GECMS is quite "blocky" and often operates the PS quite steadily, despite having the possibility to operate with much more variance. This also corresponds with the nature of the series powertrain, where the ability to operate the PS quite freely (to operate close to its optimal operating point) is seen as the biggest advantage. However, the nature of these "blocks" are different from the TCS or PFCS, in the sense that they are often of a very short duration. In fact, some of these switches are just for about a second, which are unlikely to be optimal. Such operation is not ideal and would not occur in a truly global optimal solution. It is these kinds of discrepancies that separate the solutions obtained by methods such as DP and a GECMS. However, as mentioned, works in the literature suggest that the fuel economy differences between these approaches are very small.

The fuel economy results for the four driving cycles are presented in Table 3.4. It is immediately apparent that the GECMS is able to maintain the SOC very close to $SOC_{initial} = 65\%$. The absolute EFC results are not of great importance yet, but these GECMS results will be used to benchmark all other strategies in this work (as was done for TCS and PFCS earlier in this chapter).

Table 3.4: Fuel economy results for GECMS

Driving Cycle	SOC_{final} (%)	m_f (kg)	m_{efc} (kg)	Δ_{GECMS} (%)
WL-L	65.17	0.7100	0.7083	+0
WL-M	64.34	1.1317	1.1388	+0
WL-H	64.18	0.9404	0.9503	+0
WL-E	64.05	1.5723	1.5853	+0

3.5 Summary

This chapter has introduced past work on control strategies for HEVs. This has included a review of both rule-based and optimization-based control strategies, with the latter further subdivided into real-time and global control strategies. An overview of these strategies from the literature is shown in Table 3.5.

Table 3.5: Overview of control strategies for series HEVs

Rule-based Strategies	Real-time Optimization -based Strategies	Global Optimization -based Strategies
TCS	ECMS	DP
PFCS	MPC	GECMS
MSP	SDP	GA
FLC	NN	GT
SMC		CO

The TCS and PFCS are the most conventional rule-based strategies for series HEVs, and have therefore been adopted as benchmarking strategies in this work. While the ECMS and DP are the most common approaches in optimization-based strategies, the GECMS was found to be most suitable. It enjoys the simplicity and effectiveness of the ECMS while achieving a fuel economy performance comparable to DP.

The implementation of a real-time ECMS would have been useful as another benchmark, but there is a wide range of approaches that would have achieved a wide range of results. Based on work in the literature, the real-time implementation is typically a few percentage points behind the GECMS (assuming no GPS or telematic information is used). DP, on the other hand, has not been pursued due to it being unfeasible for the used model. The approach of creating a significantly reduced model for the application of DP (the conventional approach in literature) does not appear worthwhile, as any benchmarking where the candidate strategies are tested on different vehicle models has questionable validity.

The chapter also included the design, implementation and operation of the TCS, PFCS and GECMS. The TCS takes a load leveling approach while the PFCS applies load following, but both their operation and fuel economy results were similar. The GECMS outperformed these with 14.35% and 13.55% respectively in terms of fuel economy, and demonstrated consistently CS operation. The GECMS will be acting as the fuel economy benchmark for the proposed strategies in the coming chapters.

Chapter 4

Efficiency Maximizing Map Strategies

This chapter will propose a set of novel efficiency maximizing map strategies (EMMS). These will include the EMMS0, EMMS1 and EMMS2 that are real-time control strategies, as well as the the Global EMMS (GEMMS), which is a globally tuned variant. The core idea behind each of these strategies is to utilize a thorough understanding of the powertrain efficiencies to maximize the fuel economy during driving with precomputed control maps.

The chapter will begin by laying out the design principles of the proposed control strategies, before thoroughly evaluating the powertrain efficiencies, with the objective to control the powertrain in upcoming sections. Efficiencies for both the PS and SS are derived before a total efficiency is expressed. Thereafter, the EMMS0, which we have published in [12–14], is presented. Some minor adjustments have been made to the control strategy as compared to these publications and new results are presented. This is developed further with the EMMS1 by including a more intuitive and effective method to accomplish CS operation, in addition to delivering improved fuel economy. The EMMS1 is modified and converted into the globally tuned strategy GEMMS (similar to the GECMS in the previous chapter). Lastly, the GEMMS will be modified into EMMS2 to allow real-time implementation. For each of the proposed control strategies, the tuning process, the resulting control maps, and representative power profiles of operation will be presented and discussed.

4.1 Design Principles

The control strategies discussed and presented in Chapter 3 included a mix of rule-based and optimization-based strategies. It was mentioned that the latter type tend to deliver better performance but at the expense of simplicity, robustness and ease of tuning. In particular, the ECMS was emphasized, as it is the most popular approach within the research community today.

However, the success of the ECMS is quite sensitive to the equivalence factors, converting between fuel and battery charge, that depend on driving cycle and other time-variant factors. An alternative approach to minimizing equivalent fuel consumption is to maximize the powertrain efficiency. This has the advantage of not only being more intuitive but also less sensitive to tuning, as the component efficiencies are often readily available unlike equivalence factors. Also, this method is more transparent in the sense that it can be understood where the various losses are occurring in the powertrain. Furthermore, this control method does not rely on future driving information but only on the instantaneous power demanded for the vehicle to follow any given speed profile, as well as the SOC of the battery. Therefore, it can be implemented in real-time at low computational cost.

Past work that has taken the approach of considering the powertrain efficiency has often focused on the optimization of the internal combustion engine (ICE) or the engine-generator set, as a vast majority of the powertrain losses occurs there. Consequently, this often results in the battery dynamics and losses being considered very crudely, if not neglected. Instead the battery is only considered when applying constraints on the control, typically to ensure the SOC remains between a defined upper and lower bound. Some work investigates the overall powertrain efficiency but uses it to derive heuristic control rules rather than an efficiency-maximizing objective function [114–116]. Other work studies the powertrain efficiency in depth to inform the control algorithm (without specifically optimizing efficiency) and then evaluates simulation results rigorously [117, 118].

The work proposed in this chapter takes a holistic approach and investigates the efficiency of the whole powertrain in depth before producing a control map such that the total efficiency is continuously locally maximized during driving (subject to SOC constraints). The implementation of SCSs using control maps has been done in the past as well [119]. These maps are easy to implement and can be read during

driving in real-time with very limited processing requirements. Also, as the maps are precomputed off-line, there is practically no time-constraint on the optimization algorithm to maximize the efficiency.

Particular attention is also given to charge sustaining mechanisms. Any optimization that solely focuses on optimizing the fuel economy will tend to deplete the battery quite rapidly (or overcharge in rare cases). It is therefore essential to balance short-term gains in fuel economy with long-term sustainability of such driving. The first two real-time strategies (EMMS0 and EMMS1) will take two distinct approaches to address this problem, while the GEMMS has the luxury of knowing its route in advance and is thus inherently designed to be CS. The permissible range of SOC will be the same as in Chapter 3 ($SOC_L = 50\%$ and $SOC_U = 80\%$) but further emphasis will exist on maintaining the SOC reasonably close to $SOC_{initial} = 65\%$. This differs vastly from the TCS and PFCS, which both are designed to reach their extreme points of SOC before alternating the operation such that the SOC drifts in the opposite direction. This type of driving has certain benefits in terms of robustness and lack of engine start-stop events, but is very inefficient and has detrimental effects on the battery.

Lastly, an effort has been made to keep the control strategies practical. There are always possibilities to include additional factors or corrections that add new tuning parameters. Such choices tend to make the control design a tuning exercise, and often render the control system impractical for any other vehicle design. Thus, each of the control strategies proposed have been limited to use only two tuning parameters. The approach also aims to be general enough to allow the same optimization process to be successfully applied to a different series HEV design.

4.2 Powertrain Efficiency

This section studies and identifies the efficiency of the powertrain with the objective to control it in upcoming sections. Efficiencies for both the PS and SS are presented before a total efficiency is expressed.

4.2.1 Primary Source

The study of the PS efficiency has already been partly presented as part of the overall PS operation description in Section 2.3.4. This subsection will therefore only briefly identify the component efficiencies of the engine, the generator and the rectifier before presenting the resulting combined PS efficiency η_{PS}.

The energy of the PS originates from the fuel powering the ICE, where the chemical energy is converted to mechanical energy. The efficiency of this process is defined by

$$\eta_{ICE} = \frac{T_{ICE}\omega_{ICE}}{\dot{m}_{fuel} \cdot Q_{LHV}}, \tag{4.1}$$

where T_{ICE} and ω_{ICE} are the torque and speed of the ICE respectively, $\dot{m}_{fuel}$ is the fuel mass flow rate and Q_{LHV} is the lower heating value of the fuel. The PS then uses the PMSG to convert the above to three-phase electrical energy, and the efficiency of this process is given by

$$\eta_g = \frac{\frac{3}{2}(v_{qg}i_{qg} + v_{dg}i_{dg})}{T_{ICE}\omega_{ICE}}, \tag{4.2}$$

where v_{dg}, i_{dg}, v_{qg} and i_{qg} represent *d-q* voltages and currents respectively corresponding to the three-phase output of the PMSG. Lastly, the energy flows through the rectifier to make the energy available as DC power, and its efficiency is defined as

$$\eta_{rec} = \frac{P_{PS}}{\frac{3}{2}(v_{qg}i_{qg} + v_{dg}i_{dg})}. \tag{4.3}$$

The overall energy of the PS is therefore defined as the product of these three efficiencies

$$\eta_{PS}(P_{PS}) = \frac{P_{PS}}{\dot{m}_{fuel}(P_{PS}) \cdot Q_{LHV}}. \tag{4.4}$$

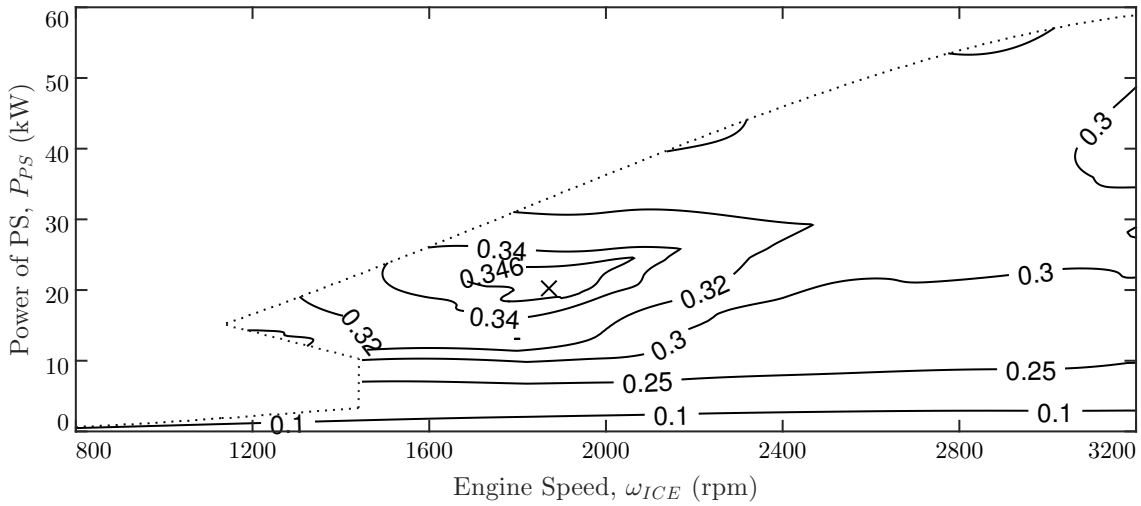

FIGURE 4.1: PS efficiency, η_{PS}, for varying PS power demand and engine speed.

Thus, for any given P_{PS} the efficiency η_{PS} can be determined by measuring the fuel rate $\dot{m}_{fuel}$, which will only depend on P_{PS} (as the optimal selection of engine speed ω_{ICE} is utilized as shown in Fig. 2.9). Based on the BSFC data from Section 2.3.4, the PS efficiency η_{PS} is presented in Fig. 4.1 as a function of P_{PS}. It demonstrates that the PS is generally more efficient at higher levels of power demand and medium speeds. As discussed in Section 2.3.4, the dotted border is defined by the operational limits of the ICE (due to feasibility or lack of validation). Note that the maximum efficiency is found at 20.1 kW at 1870 rpm and is marked with a cross in the chart.

4.2.2 Secondary Source

Strictly speaking, the SS is an energy buffer, rather than an energy source. It receives energy from the PS either directly (by charging) or indirectly (by regenerative braking). It is therefore not straightforward to express the efficiency as an instantaneous value. The conventional approach is to express it as the energy charge-discharge efficiency [41], defined as

$$\eta_{bat,c-d} = \frac{E_{discharge}}{E_{charge}}, \tag{4.5}$$

where the two energies are defined for the same SOC. Other alternatives include the expression of efficiency as the coulombic efficiency or the voltaic efficiency [120]. However, they all suffer from an inaccuracy: the underlying assumption of these types of efficiency is that the battery will be charged and discharged at the same

power level. Consequently, when evaluating the efficiency of the battery at a discharge of, e.g. 10 kW as compared to 20 kW, it is not the actual instantaneous efficiency being compared, but rather it is a comparison with two different assumptions being made for the two cases. The assumptions are that the battery was charged with 10 kW in the past if discharging at 10 kW, and 20 kW if discharging at 20 kW. Clearly the past charging should be already fixed, and not determined by present and future discharging levels. To address this, the efficiency is separated into charging efficiency and discharging efficiency, where the former is defined as

$$\eta_{bat,c} = \frac{P_{bat-charge}}{P_{bat-in}} = \frac{v_{bat,OC} \cdot i_{bat}}{v_{bat} \cdot i_{bat}} = \frac{v_{bat,OC}}{v_{bat}}, \tag{4.6}$$

in which $P_{bat-charge}$ is the power being stored in the battery. This power is obtained by multiplying the current, i_{bat}, with the open-circuit voltage of the battery, $v_{bat,OC}$. P_{bat-in} corresponds to the power sent to the battery at its ports, while v_{bat} is the voltage at the same ports. Similarly the discharging efficiency can be formulated as

$$\eta_{bat,d} = \frac{P_{bat-out}}{P_{bat-discharge}} = \frac{v_{bat} \cdot i_{bat}}{v_{bat,OC} \cdot i_{bat}} = \frac{v_{bat}}{v_{bat,OC}}, \tag{4.7}$$

where $P_{bat-out}$ is the power delivered by the battery at its ports, and $P_{bat-discharge}$ is the power consumed by the battery internally. The latter power is obtained by multiplying the current with the open-circuit voltage of the battery.

The efficiency of the DC-DC converter η_{dcdc} can now be included, which is defined through a look-up table (as given in Section 2.4.2). Thus the overall efficiency of the SS can be expressed as

$$\eta_{SS} = \begin{cases} \frac{v_{bat,OC}}{v_{bat}} \eta_{dcdc} & P_{SS} < 0 \\ \frac{v_{bat}}{v_{bat,OC}} \eta_{dcdc} & P_{SS} \geq 0 \end{cases}. \tag{4.8}$$

To allow simplification of Eq. 4.8 and make it more usable for the optimization in the next section, battery voltage can be substituted with current. The battery voltage is modeled to be a function of i_{bat} and SOC. However, $v_{bat,OC}$ has $i_{bat} = 0$ so we can determine that $v_{bat,OC} = f(SOC)$. Similarly, i_{bat} is a function of SOC

and v_{bat}, which can however be expressed as a function of P_{SS} as follows:

$$i_{bat} = \begin{cases} \frac{P_{SS} \cdot \eta_{dcdc}}{v_{bat}} & P_{SS} < 0 \\ \frac{P_{SS}}{v_{bat} \cdot \eta_{dcdc}} & P_{SS} \geq 0 \end{cases}. \tag{4.9}$$

Now, by considering Eqs. 4.8 and 4.9 the overall efficiency of the SS is given by

$$\eta_{SS}(P_{SS}, SOC, i_{bat}) = \begin{cases} \frac{v_{bat,OC} i_{bat}}{P_{SS}} & P_{SS} < 0 \\ \frac{P_{SS}}{v_{bat,OC} i_{bat}} & P_{SS} \geq 0 \end{cases}, \tag{4.10}$$

The defined SS efficiency can now be determined experimentally, analytically or through simulations. Both of the two latter methods have been performed and published in [12, 14], but only the analytical method will be presented in this thesis.

The battery model used is described in Section 2.4.1 where parameter values are also given. It has minor differences in dynamics between charging and discharging operation to account for differences in the polarization resistance. However, below only the discharging dynamics are presented, although the dynamics of each mode of operation were considered when performing the analysis and producing the efficiency map in this section. The key discharging dynamics of the battery model are given by Eqs. 2.25-2.29.

To make the efficiency model time-invariant, it is assumed that $i^*_{bat} = i_{bat}$, so that we obtain the efficiencies for steady-state operation. To obtain v_{bat-OC}, Eqs. 2.25 and 2.26 should be substituted with $i_{bat} = 0$ to create open circuit conditions. To express this as a function of SOC, we substitute with Eq. 2.29 to give

$$\begin{aligned} v_{bat,OC}(SOC) = E_0 - \frac{K_1 \cdot Q_{max}(1 - SOC)}{SOC} \\ + Ae^{-B \cdot Q_{max}(1-SOC)}. \end{aligned} \tag{4.11}$$

Lastly, i_{bat} can be determined by combining Eqs. 4.9, 2.25,2.26 and 2.29 to produce the following quadratic equation

$$aI^2_{bat} + bi_{bat} + c = 0, \tag{4.12}$$

where

$$a = \frac{K_2}{SOC} + R_{bat},$$
$$b = \frac{K_1 Q_{max}(1 - SOC)}{SOC} - E_0 - Ae^{-B \cdot Q_{max}(1-SOC)},$$
$$c = \frac{P_{SS}}{\eta_{dcdc}}.$$

Thus, we obtain the battery current as

$$i_{bat}(P_{SS}, SOC) = \frac{-b \pm \sqrt{b^2 - 4ac}}{2a}, \tag{4.13}$$

where it is only a function of P_{SS} and SOC. This allows the expression of Eq. 4.10 as follows:

$$\eta_{SS}(P_{SS}, SOC) = \begin{cases} \frac{v_{bat,OC} i_{bat}}{P_{SS}} & P_{SS} < 0 \\ \frac{P_{SS}}{v_{bat,OC} i_{bat}} & P_{SS} \geq 0 \end{cases}, \tag{4.14}$$

Equations 4.11 and 4.13 are then iteratively solved for $SOC \in [SOC_L, SOC_U]$ and $P_{SS} \in [P_{SSmin}, P_{SSmax}]$ in steps of 1% and 0.1 kW respectively before being substituted into Eq. 4.14 to provide the efficiency of the SS. The obtained results are presented in Fig. 4.2.

Battery efficiencies are typically high at low magnitudes of power and get gradually lower for higher loads. However, as the powertrain includes a DC-DC converter, the efficiency is very low at very low loads. These two features together result in an efficiency profile with a peak around 10 kW for discharging and -10 kW for charging. Furthermore, it is interesting to note that the charging becomes slightly more efficient at lower SOC levels, while discharging becomes slightly more efficient at higher SOC levels. Thus, if efficient operation is encouraged, CS is indirectly taking place to a limited extent.

4.2.3 Total Efficiency

Having obtained the efficiencies for both the PS and the SS in Eqs. 4.4 and 4.14 respectively, these can now be merged into a single expression. However, as we consider the complete powertrain, we need to make a correction to the SS efficiency. As mentioned, the battery is not a source of energy by itself but must ultimately

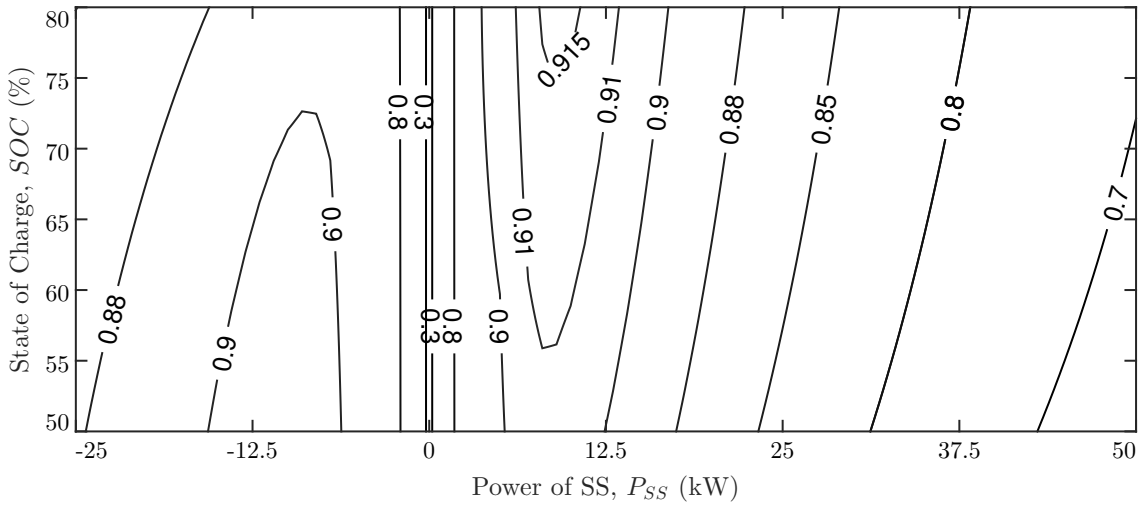

FIGURE 4.2: SS efficiency η_{SS} for varying charging (negative) and discharging (positive) SS power demand and SOC.

receive its energy through the PS. Therefore, a correction factor v is included to account for the PS losses involved in facilitating the SS to operate (the term is defined further in upcoming sections). Thus, the combined total efficiency (for $P_{PL} \geq 0$) can be expressed as

$$\eta_{tot}(P_{PS}, P_{SS}, SOC) = \frac{P_{PL}}{P_{in}} = \begin{cases} \frac{P_{PS}+P_{SS}}{\frac{P_{PS}}{\eta_{PS}}+\frac{P_{SS}\eta_{SS}}{v}} & P_{SS} < 0 \\ \frac{P_{PS}+P_{SS}}{\frac{P_{PS}}{\eta_{PS}}+\frac{P_{SS}}{v\eta_{SS}}} & P_{SS} \geq 0 \end{cases}, \tag{4.15}$$

As the SS efficiency (in Eq. 4.10) during discharging is the inverse of itself during charging, the expression can by simplified by using

$$\eta^*_{SS} = \begin{cases} 1/\eta_{SS} & P_{SS} < 0 \\ \eta_{SS} & P_{SS} \geq 0 \end{cases}. \tag{4.16}$$

Essentially, η^*_{SS} expresses the bi-directional efficiency as a single term. To simplify further, the individual powers of the sources can be expressed using the power share factor u, defined in Eq. 2.32, giving a single decision variable to determine both P_{PS} and P_{SS}. Thus the total efficiency can be formulated as

$$\eta_{tot}(u, P_{PL}, SOC) = \frac{\eta_{PS}\eta^*_{SS}v}{v\eta^*_{SS}u + \eta_{PS}(1-u)}. \tag{4.17}$$

4.3 Efficiency Maximizing Map Strategy 0

This section presents the general design of the EMMS approach as well as the specifics of the EMMS0. It begins by introducing the problem formulation and the control map approach that can be used to solve this. The fist attempt, the non-CS EMMS0, is presented before being improved further by including a mechanism to ensure CS operation, to produce the EMMS0. Lastly, the operation and performance is evaluated.

4.3.1 Control Approach

The fundamental principle of the EMMS is to operate the energy sources such that the efficiency η_{tot} is maximized. As it is clear from the definition of this variable in the previous section, it depends on two defined variables (P_{PL} and SOC) and one decision variable (u). The optimization problem can be expressed as the following local maximization problem:

$$P \begin{cases} \max\limits_{u} \eta_{tot}(t,u) \ \forall t \in [0,t_f] \\ 0 \leq u \leq \frac{P_{PSmax}}{P_{PL}} \end{cases} \tag{4.18}$$

However, the total efficiency at any time instant is determined by the power requested by the PL, the SOC and the power split between PS and SS, and therefore the optimization problem can be reformulated as:

$$P_{EMMS} \begin{cases} \max\limits_{u} \eta_{tot}(P_{PL}, SOC, u) \ \forall P_{PL} \in [0, P_{PLmax}], SOC \in [SOC_L, SOC_U] \\ 0 \leq u \leq \frac{P_{PSmax}}{P_{PL}} \end{cases} \tag{4.19}$$

where $P_{PLmax} = P_{PSmax} + P_{SSmax}$.

This reformulation has many benefits. It reduces the time to perform the optimization offline and allows the same control map to be used for different driving cycles. Furthermore, the memory used to store the maps is often reduced. However, the EMMS approach has some additional processing requirements during operation, as it needs to read the P_{PL} and SOC in real-time to select the appropriate operating point. However, this type of real-time feedback also makes the control more robust, should there be any unexpected variation in operating conditions.

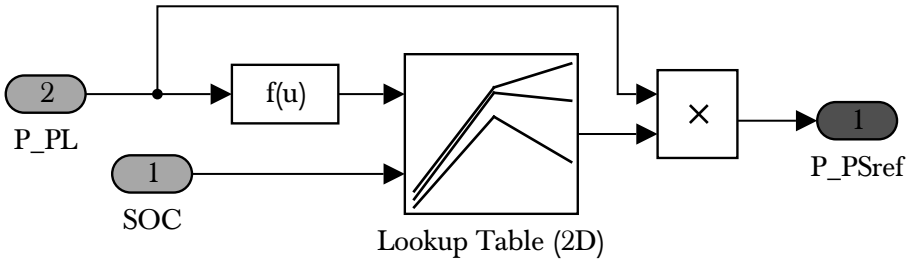

FIGURE 4.3: Implementation of the EMMS in Simulink.

The objective is thus to produce a map for the optimal decision variable given the defined variables, according to

$$u_{opt} = f(P_{PL}, SOC). \tag{4.20}$$

This control map is then implemented within the Simulink model as shown in Fig. 4.3. The SOC and load power P_{PL} signals are read into the map, which produces the optimal power share ratio that can simply be multiplied by the load power to generate a reference signal for the P_{PS}. Note that the $f(u)$ function block converts the input to the same precision as the generated control map.

The objective function can then be solved through a simple iterative process, within the search space of $SOC \in [SOC_L, SOC_U]$, $P_{SS} \in [P_{SSmin}, P_{SSmax}]$ and $P_{PS} \in [0, P_{PSmax}]$. Note that the search for ω_{ICE} is not needed due to the pre-computation of $\omega_{ICE,opt} = f(P_{PS})$ as shown in Fig. 2.9, thus significantly reducing computational time (which is not a significant issue though, as optimization is performed off-line). The efficiency is therefore computed for every feasible combination of values for the defined and the decision variables and the optimal u is selected in each case (the range of u is set by the P_{PL} of interest as $u \in [0, P_{PSmax}/P_{PL}]$ and is appropriately discretized). Once this optimization is performed, the efficiency maximizing control map is obtained.

4.3.2 Efficiency Maximizing Map

This first design attempt will only consider the efficiencies of the powertrain to produce the control map, without consideration for CS operation. To implement the control map it is first necessary to further define the total efficiency of the powertrain. As mentioned in the previous section, the SS efficiency needs to be

adjusted by a factor v to account for the PS losses incurred in the charging of the battery. The definition used in [14] is as follows:

$$v = \begin{cases} 1 & P_{SS} < 0 \\ \eta_{re} & P_{SS} \geq 0 \end{cases}. \tag{4.21}$$

where η_{re} is the replenishing efficiency. This term is applied only during discharging, and can be intuitively understood as a correction with consideration for the PS efficiency involved in replenishing the battery after it has been discharged. This can also be related to practically by considering the fact that the SS efficiency is often in the region of 90% while the PS efficiency is around 34%. Without any correction, the efficiency maximizing strategy would almost always operate using only the SS, ending up depleting the battery. By multiplying the SS discharging efficiency with the replenishing efficiency, the complete energy cycle involved in discharging the power from the battery is considered.

In reality, the replenishing efficiency is a variable that is dependent on both past and future operating conditions and is difficult to compute. However, as its dynamics can be considered very slow, it can be treated as a constant for a particular driving cycle without much loss in optimality. This is the approach taken in this work, and a unique control map can be produced for each selection of η_{re}.

The optimal power share factor u_{opt} for varying power demand is shown in Fig. 4.4 for $\eta_{re} = 34\%$, together with the realized efficiency η_{tot}. It can be seen that the SCS chooses to operate SS-only mode during low P_{PL} and almost PS-only mode during mid-range P_{PL}. For higher power requirements the non-CS EMMS0 uses a blended mode to drive the powertrain. It is worth noting that the dependence of u_{opt} on SOC-levels is quite limited, as could be expected from the efficiency plot of the SS in Fig. 4.2. The total efficiency η_{tot} that is realized by this selection of u is quite steady above 30% for most power requirements.

Simulations are run for the four different driving cycles to tune the replenishing efficiency $\eta_{re} \in [26, 36]\%$ to maximize the fuel economy. Results with normalized EFC and final SOC levels are presented in Fig. 4.5, and it can be seen that the optimal value is found as low as $\eta_{re} = 29\%$ for WL-E but higher than $\eta_{re} = 36\%$ for WL-L. Higher values for the replenishing efficiency were not tested as the battery SOC was dropping too low. However, by looking at the fuel economy of the four

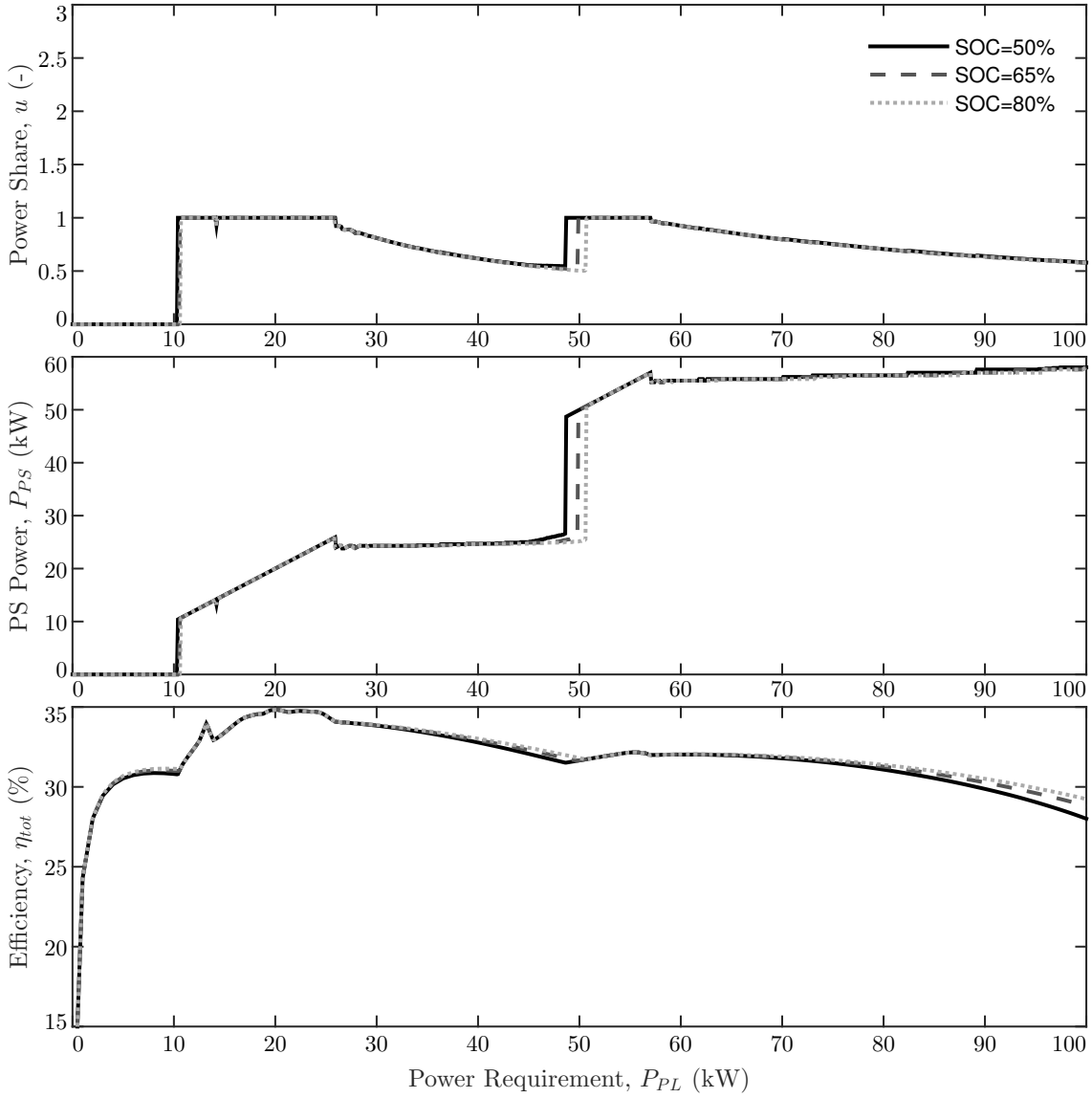

FIGURE 4.4: Optimal power share and PS power, and corresponding total efficiency for varying power requirements and SOC for $\eta_{re} = 34\%$ for non-CS EMMS0.

driving cycles combined, as shown in Fig. 4.6, it can be determined that $\eta_{re} = 34\%$ is the optimal selection. This corresponds to the typical efficiency of the PS, as shown in Fig. 4.1.

It is also evident that for all the driving cycles the SOC drops to low levels, and the control strategy is not CS. In fact, even for extremely low η_{re} values (which discourages the use of the SS), the final SOC is only higher than 70% for WL-M. This can be attributed to the unwillingness of the strategy to use the PS to charge the SS directly, and instead being overly reliant on regenerative braking.

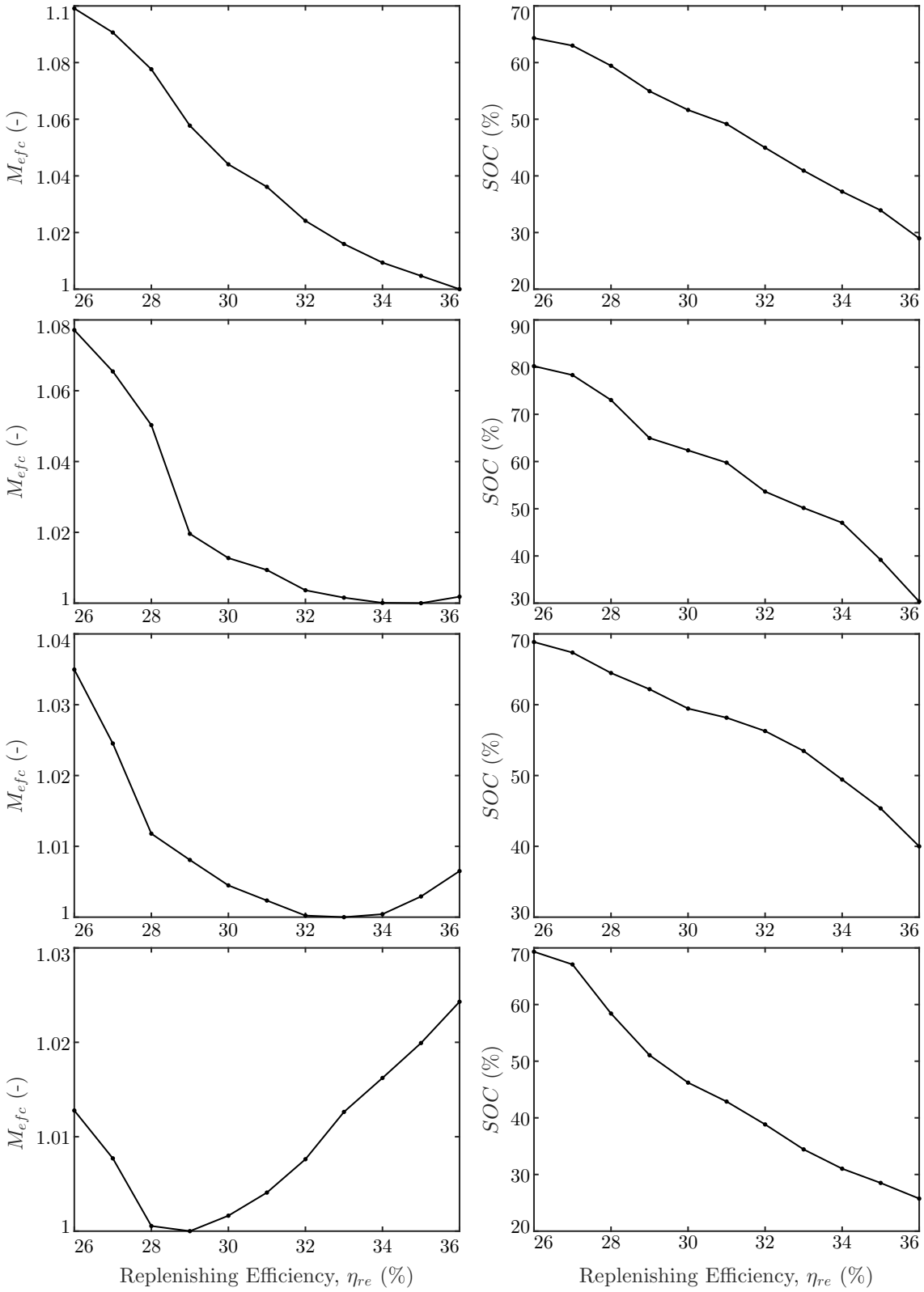

FIGURE 4.5: Normalized EFC (left) and final SOC (right) for varying η_{re} when driving WL-L, WL-M, WL-H and WL-E (from top to bottom) with non-CS EMMS0.

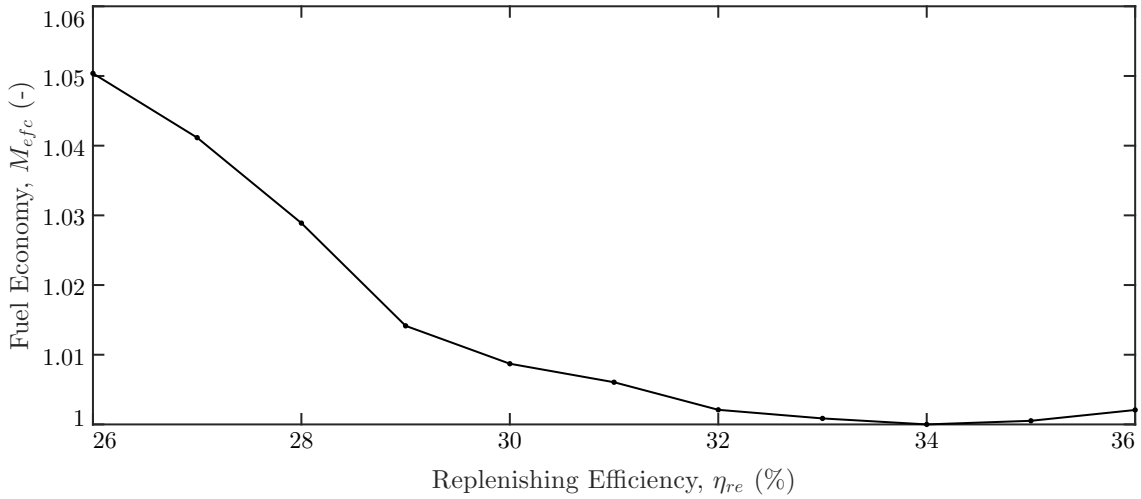

FIGURE 4.6: Normalized total EFC M_{tot} for varying η_{re} with non-CS EMMS0.

4.3.3 Charge Sustaining Operation

The non-CS EMMS0 has no inherent constraints in terms of SOC, so the battery could end up depleted or overcharged and permanently damaged. To address this, a CS function $k_{cs}(SOC)$ is included in the control design, which encourages the battery to be charged at low SOC values and discharged at high SOC values. This bias is introduced in the expression of total efficiency, by weighting the input power of the SS as follows:

$$\eta_{CS}(u, P_{PL}, SOC) = \frac{\eta_{PS}\eta_{SS}^{*}v}{v\eta_{SS}^{*}u + k_{cs}\eta_{PS}(1-u)}. \tag{4.22}$$

For $k_{cs} > 1$, the SS discharging power becomes heavier, causing it to be reduced by the optimization algorithm. Simultaneously the SS charging power becomes heavier, but since it is a negative quantity, this actually encourages further charging of the battery (as η_{CS} is always positive and we are aiming to minimize the denominator). Conversely, for smaller k_{cs} values, the discharging of the SS becomes more attractive and charging less desirable. The new objective is not only to maximize the efficiency but also to keep the SOC levels within a certain range. The upper and lower limits of SOC are the same as for TCS and PFCS (with $SOC_L = 50\%$ and $SOC_U = 80\%$). This allows a buffer for regenerative braking, as well as avoids very low or high SOC that accelerates degradation of the battery. Thus, the new optimization problem to

TABLE 4.1: Definition of CS function k_{cs}

$k_{cs}(SOC\%)$	Defined such that
$k_{cs}(80)$	$u = 0$ for $P_{PL} \leq P_{SSmax}$
$k_{cs}(75)$	$1 - (1 - k_{cs}(80))/K_{csi}$
$k_{cs}(70)$	No correction
$k_{cs}(60)$	No correction
$k_{cs}(55)$	$1 + (k_{cs}(50) - 1)/K_{csi}$
$k_{cs}(50)$	$u \geq 1$ for $0 < P_{PL} \leq P_{PSmax}$

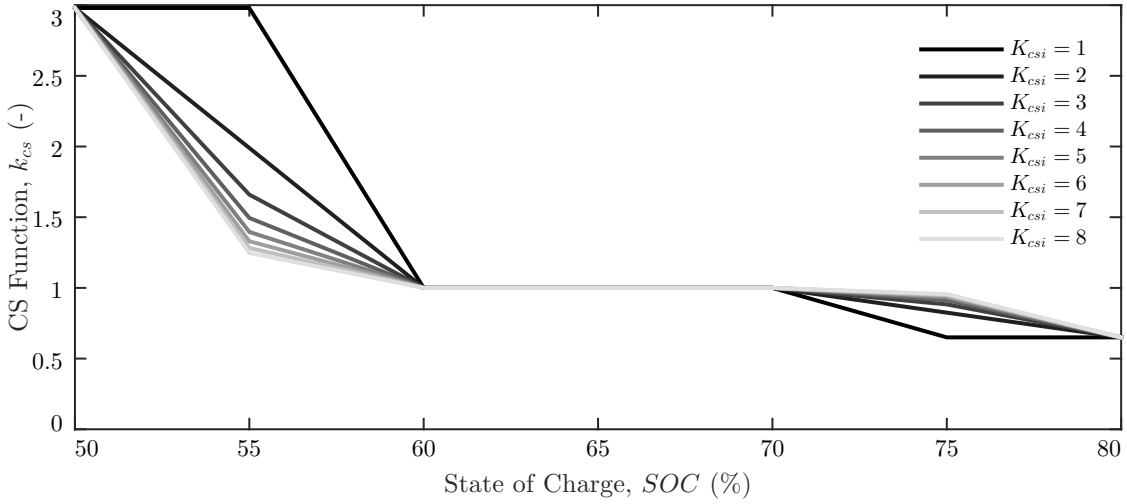

FIGURE 4.7: Charge sustaining function $k_{cs}(SOC)$ for various CSI factors K_{csi} for EMMS0.

be solved can be expressed as

$$P_{EMMS0} \begin{cases} \max\limits_{u} \eta_{CS}(P_{PL}, SOC, u) \; \forall P_{PL} \in [0, P_{PLmax}], SOC \in [SOC_L, SOC_U] \\ 0 \leq u \leq \frac{P_{PSmax}}{P_{PL}} \\ SOC_L \leq SOC \leq SOC_U \end{cases} \tag{4.23}$$

To ensure operation within this SOC range the CS function k_{cs} is shaped according to the rules presented in Table 4.1. During operation at high SOC, the PS is used to a minimal extent while at lower SOC the PS is often charging the SS. The resultant profile for the charge sustaining factor k_{cs} is shown in Fig. 4.7. It can be seen that the lower values of SOC are associated with a high k_{cs} value, encouraging the SCS to charge the battery, as discussed above. Similarly, at high SOC values, the k_{cs} value is low and thus encourages the battery to be discharged. There is a flat region between 60% and 70% where no modification is desired. The intensity of the charge

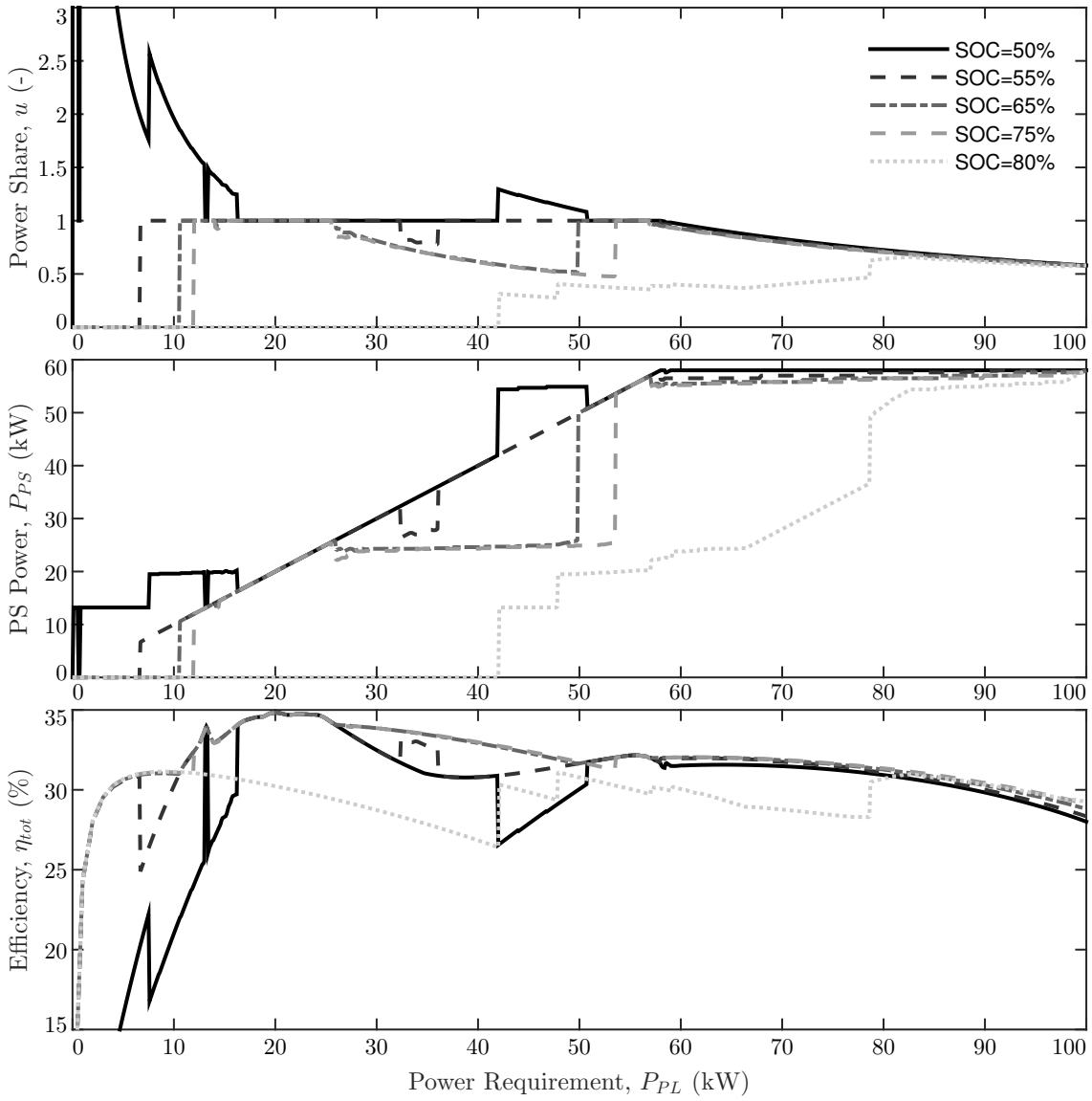

FIGURE 4.8: Optimal power share and PS power, and corresponding total efficiency for varying power requirements and SOC with $\eta_{re} = 34\%$ and $K_{csi} = 8$ for EMMS0.

sustaining modification at moderately low or high SOC levels is adjusted by the charge sustaining intensity factor K_{csi}. When published in [14], $K_{csi} = 4$ was used without any thorough tuning, but for the purpose of completion, and consistency with other control strategies being evaluated, it should be a tunable parameter as there is no intrinsic reason to choose any particular value.

As an example, the CS function is implemented for $\eta_{re} = 34\%$ and $K_{csi} = 8$, and new maps are produced for optimal power share factor and total efficiency in Fig. 4.8. Clearly the power share factor is consistently higher for lower SOC (often larger

than one) and quite low (often zero) for higher SOC. The charge sustaining factor thus seems successful in maintaining the SOC within the desired thresholds and the resulting power share is in accordance with the rules defined in Table 4.1. However, it is clear from Fig. 4.8 that this charge sustaining correction comes at the expense of efficiency in the case of extreme SOC values. Arguably, it is better to suffer some reduced efficiency immediately rather than damaging the battery or for that matter suffer heavy inefficiency later. Thus, over longer periods of driving, the EMMS0 could be more efficient.

With the CS function included, new power share maps are produced for each combination of values of $\eta_{re} \in [26, 36]\%$ and $K_{csi} \in [1, 8]$ in steps of 1% and 1 unit respectively. Each of these are then tested for the four driving cycles to tune the parameters to maximize the fuel economy. Results with normalized EFC and final SOC levels are presented in Fig. 4.9, and it can be seen that the optimal value is still found around 34% or lower, similar to the non-charge sustaining results of Fig. 4.5. However, it can be seen that the simulation results, for all η_{re} values, are within the defined SOC limits (between 50% and 80%) for each driving cycle. The CS function $k_{cs}(SOC)$ thus appears successful in its objective to maintain $SOC_L \leq SOC \leq SOC_U$.

To determine the optimal selection overall, the total fuel economy for the four driving cycles is evaluated and is presented in Fig. 4.10. It can be seen that the optimal selection is found to be $\eta_{re} = 34\%$ (which coincides with the optimal from the non-CS EMMS0) and $K_{csi} = 8$ (the maximum tested). As the CSI factor K_{csi} is increased, the effects of the CS function $k_{cs}(SOC)$ are reduced, thus resulting in a lower final SOC. As a consequence, the fuel economy is generally improved by the increasing K_{csi}, as the $k_{cs}(SOC)$ interferes less with the control decision. There is thus a trade-off between fuel economy and CS ability.

There is a case to be made for choosing a more CS set of tuning parameters, at the expense of half a percent of fuel economy. However, for the purposes of this work it is most useful to pursue the strategy that yields a higher fuel economy while delivering an acceptable CS ability. The EMMS0 will therefore be using $\eta_{re} = 34\%$ and $K_{csi} = 8$ for all result from here onwards.

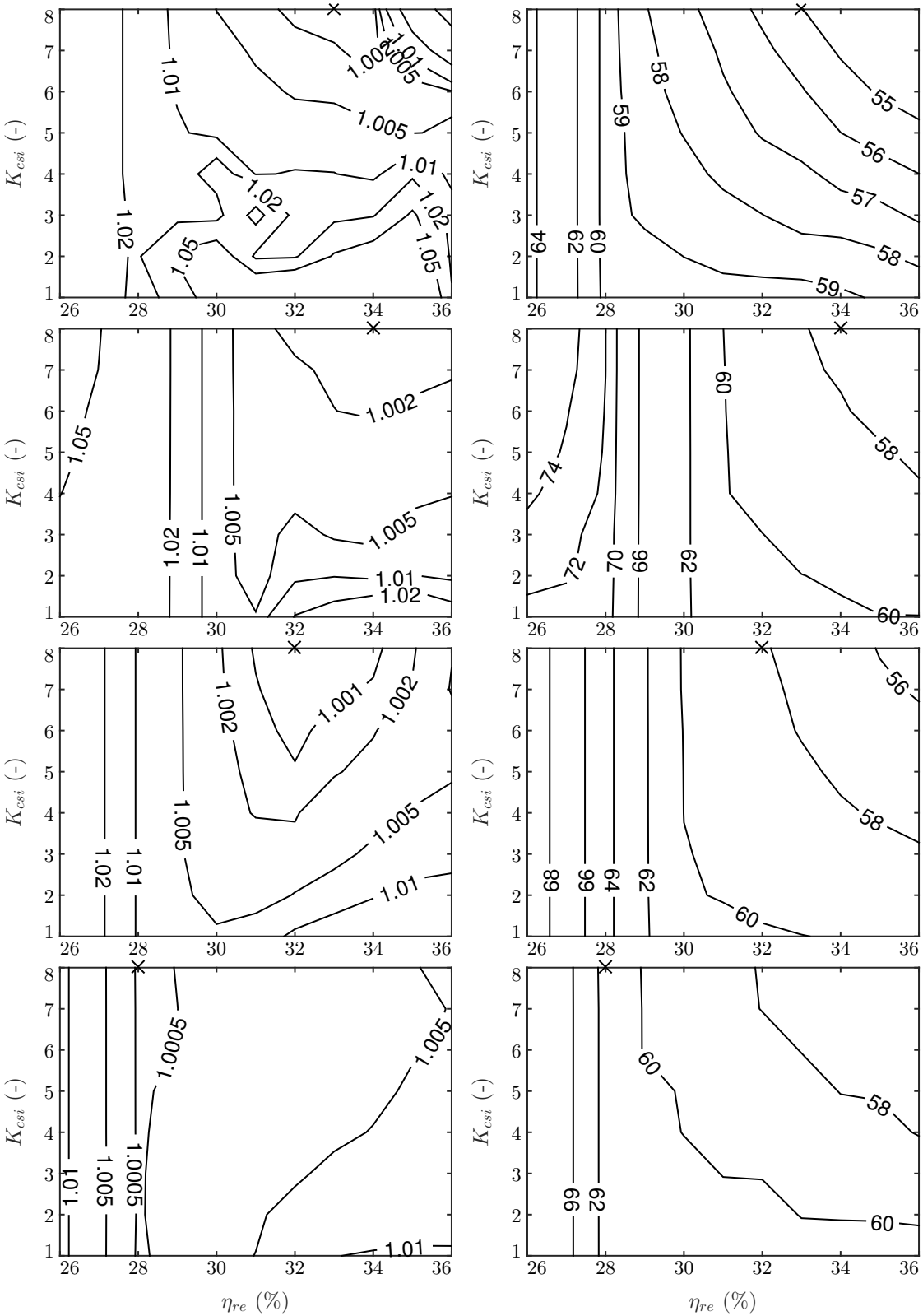

FIGURE 4.9: Normalized EFC M_{efc} (left) ($M_{efc} = 1$ is marked with a cross) and final SOC (right) for varying η_{re} and K_{csi} when driving WL-L, WL-M, WL-H and WL-E (from top to bottom) with EMMS0.

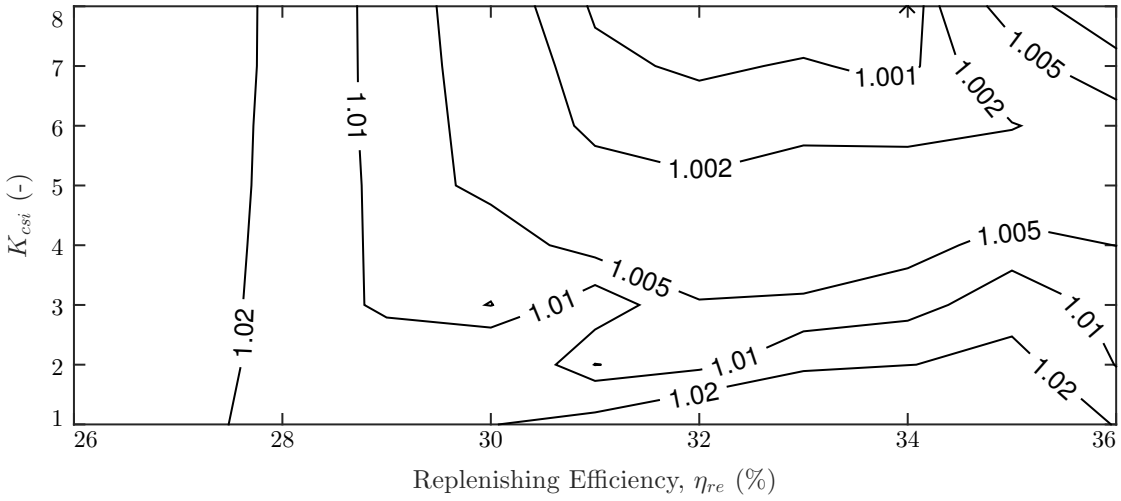

FIGURE 4.10: Normalized total EFC M_{tot} for varying η_{re} and K_{csi} with EMMS0.

4.3.4 Operation

The power profiles of the operation corresponding to this selection are presented for the first and final iterations of the tested driving cycles in Fig. 4.11 and Fig. 4.12 respectively. Note that final iterations correspond 8^{th}, 8^{th}, 4^{th} and 4^{th} iteration for WL-L, WL-M, WL-H and WL-E respectively.

For the first iteration of WL-L and WL-M, the operation of the EMMS0 is quite similar to the GECMS in when the PS is active. However, the difference is that the EMMS0 will often follow the load at these times rather than operate the PS as steadily as the GECMS. Nevertheless, resembling the GECMS rather than TCS or PFCS should be reassuring for the EMMS0, based on the fuel economy results from the previous chapter. It is also worth noticing that the SS is practically only recharged through regenerative braking. This is clear from the figure, as the SS is never charged (light shading that is negative) unless the vehicle is experiencing regenerative braking ($P_{PL} < 0$). Also, although the power share is normally either $u = 0$ (only SS delivering load) or $u = 1$ (only PS delivering load) there are a few times (when the load is somewhat high) when the SS and PS act together. This hybrid type of operation becomes more prevalent for WL-H and WL-E, as the load level is generally higher. However, even for these driving cycles, the PS is often switched on and off to adapt to the changing loads.

For the final iteration of each of these driving cycles the operation is quite different as the EMMS0 is *SOC* dependent, unlike the GECMS. Most visibly, the PS is used

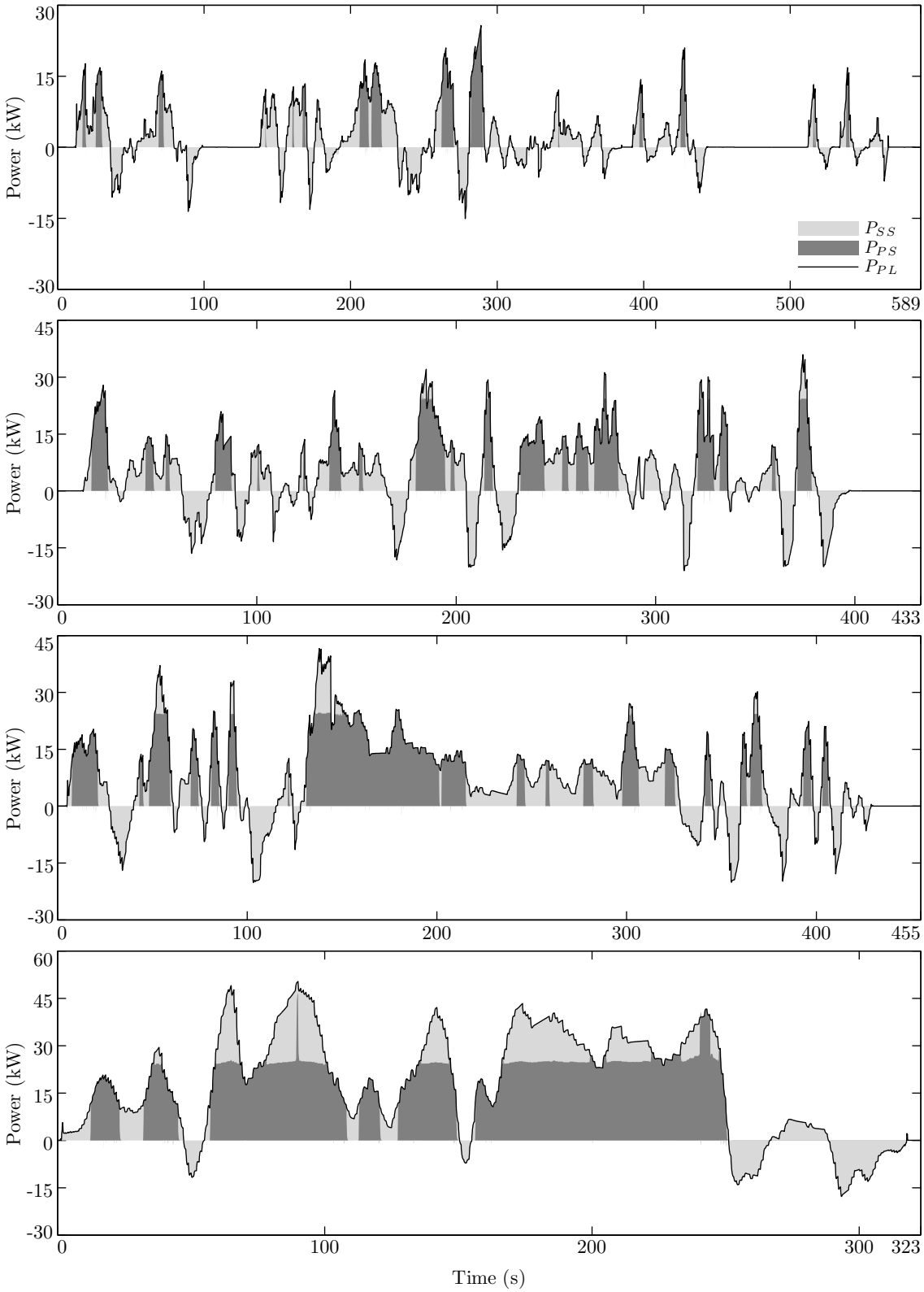

FIGURE 4.11: Power time histories for PS, SS and PL for the first iteration of driving WL-L, WL-M, WL-H and WL-E (top to bottom) with EMMS0.

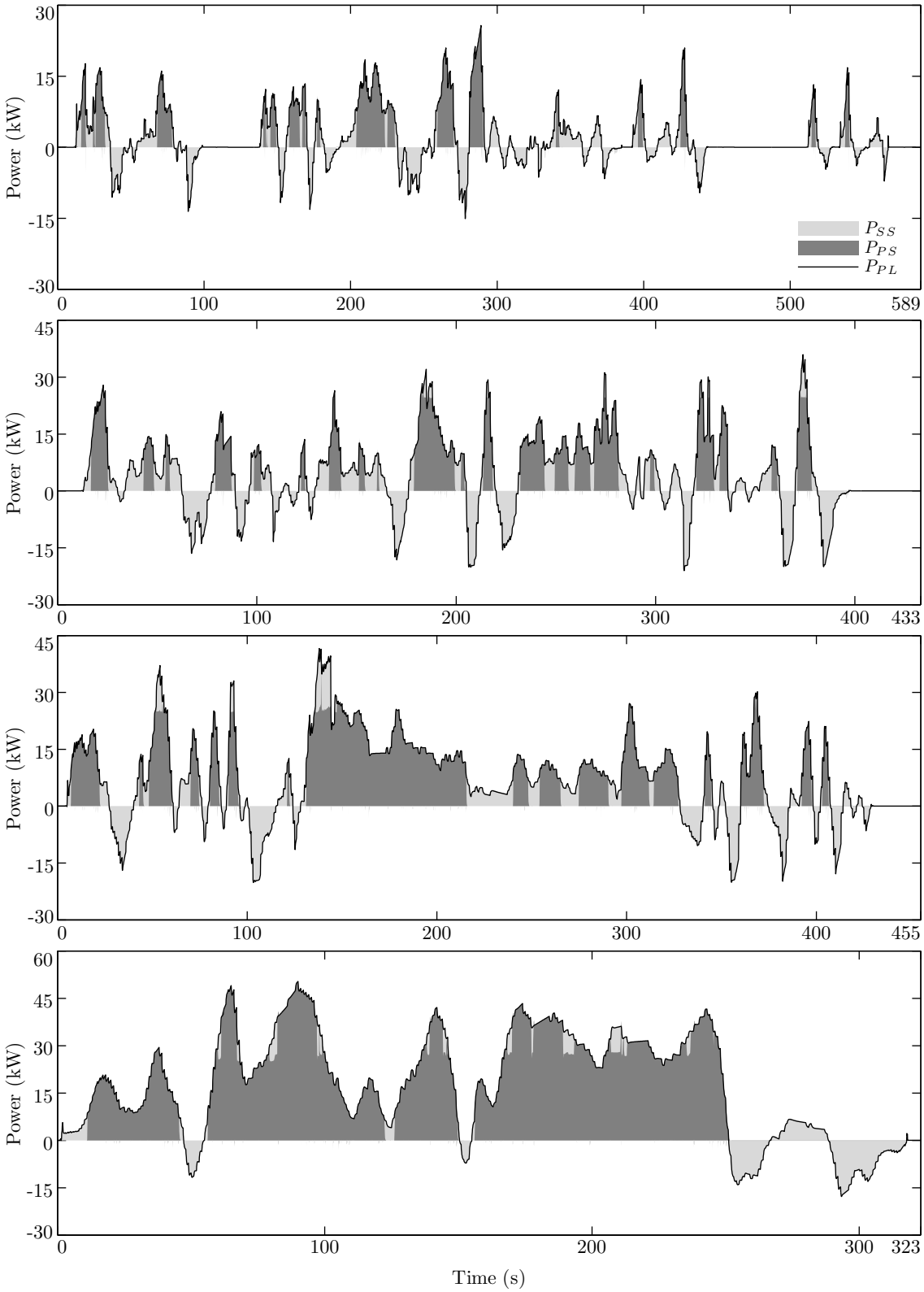

FIGURE 4.12: Power time histories for PS, SS and PL for the final iteration of driving WL-L, WL-M, WL-H and WL-E (top to bottom) with EMMS0.

to a much larger extent for each of the driving cycles. This can be attributed to the drop in SOC that has occurred over the repeated iterations of driving. The EMMS0 is now actively discouraging the use of SS and the driving is thus dominated by PS operation. There is however still no direct charging by the PS of the SS, as the SOC has not dropped low enough to trigger this type of operation (as seen in Fig. 4.8). This is probably an area for improvement.

Finally, the fuel economy of the EMMS0 is given in Table 4.2 for the four driving cycles. The actual fuel consumption of the engine m_f of the vehicle is actually much lower than the GECMS for each driving cycle. This is a result of significant driving with the SS, which is why it is followed by a significant drop in SOC (but still within the constraints). Looking at the fuel economy comprehensively, the EFC of the EMMS0 is consistently outperformed by the GECMS, with margins between 4 and 11%. The total fuel economy for the driving cycles combined (as defined for M_{tot}) has the EMMS0 5.68% behind the GECMS. This is a significant improvement on the TCS and PFCS, which were lagging the GECMS by 14.35% and 13.55% respectively. However, the urban driving is still a significant issue for EMMS0, as it needs to be able to use the SS more effectively.

Table 4.2: Fuel economy results for EMMS0

Driving Cycle	SOC_{final} (%)	m_f (kg)	m_{efc} (kg)	Δ_{GECMS} (%)
WL-L	54.54	0.6700	0.7835	+10.61
WL-M	57.25	1.1128	1.1963	+5.04
WL-H	56.67	0.8901	0.9897	+4.15
WL-E	55.97	1.5254	1.6492	+4.03

4.4 Efficiency Maximizing Map Strategy 1

This section presents the non-CS EMMS1, which is an evolution of the non-CS EMMS0 discussed in the previous section. The strategy is then further developed into the EMMS1 that accomplishes charge sustaining operation more intuitively and effectively, in addition to delivering improved fuel economy.

4.4.1 Modified Efficiency Maximizing Map

The non-CS EMMS0 employs the efficiency expressed in Eq. 4.17 to produce the control map shown in Fig. 4.4. It can be observed that for all power requirements, we always have $u \leq 1$, meaning that the PS is never used to charge the SS. Consequently, the powertrain is limited to operate the SS with only as much energy as is recuperated through regenerative braking. This works out reasonably well, as the SS is particularly useful in urban settings (where proportion of regenerative braking is high) and less important when cruising at highways (where a limited amount of regenerative braking is applied). However, considering the heavy investment in electrifying the powertrain, it makes sense to have the ability to utilize the SS to a larger extent and accomplish an even greater fuel economy.

The reason why the non-EMMS0 never opts for the "charging mode" (PS charging the SS directly) can be attributed to the severe drop in efficiency due to increased usage of the PS, which is the least efficient component in the powertrain. To illustrate the impact that the mode of operation has on efficiency, it is worth looking at a simplified example (values do not correspond exactly to the vehicle model being used). If the powertrain has to deliver 20 kW, we can explore three different modes of operation: PS only (PS mode); PS operation with SS supplementing (hybrid mode); or PS operation with the SS simultaneously being charged (charging mode). In this example we are using η_{PS}(15 kW)= η_{PS}(20 kW)= η_{PS}(25 kW)=33%, η_{SS}(-5 kW)= η_{SS}(5 kW)= 90% and $\eta_{re} = 33\%$.

The powertrain efficiency (as given in Eq. 4.15) can be simplified for PS mode and computed for $P_{PS} = 20$ kW as follows:

$$\eta_{tot} = \frac{P_{PS} + P_{SS}}{\frac{P_{PS}}{\eta_{PS}} + \frac{P_{SS}}{v\eta_{SS}}} = \frac{20}{\frac{20}{\eta_{PS}} + \frac{0}{\eta_{SS}\eta_{re}}} = \frac{20}{60 + 0} = 33\%. \tag{4.24}$$

The expression is reduced to $\eta_{tot} = \eta_{PS}$, which is obvious as we are only using the PS. For hybrid mode, the efficiency in the case of $P_{PS} = 15$ kW and $P_{SS} = 5$ kW is expressed and computed as:

$$\eta_{tot} = \frac{P_{PS} + P_{SS}}{\frac{P_{PS}}{\eta_{PS}} + \frac{P_{SS}}{v\eta_{SS}}} = \frac{20}{\frac{15}{\eta_{PS}} + \frac{5}{\eta_{SS}\eta_{re}}} = \frac{20}{45 + 16.67} = 32.43\%. \tag{4.25}$$

The chosen format is used to emphasize the PS and SS components of the input power (denominator). It can be seen that any increase in contribution from the SS will slightly decrease the total efficiency. However, it can be imagined that in a case where $\eta_{PS}(15 \text{ kW}) > \eta_{PS}(20 \text{ kW})$ there would be scope for the hybrid mode to be more efficient than PS only mode. Lastly, the efficiency for the charging mode in the case of P_{PS} =25 kW and P_{SS} =-5 kW is expressed and computed as:

$$\eta_{tot} = \frac{P_{PS} + P_{SS}}{\frac{P_{PS}}{\eta_{PS}} + \frac{P_{SS}\eta_{SS}}{v}} = \frac{20}{\frac{25}{\eta_{PS}} - 5 \cdot \eta_{SS}} = \frac{20}{75 - 4.5} = 28.37\%. \tag{4.26}$$

The charging mode clearly has a dramatically lower efficiency as compared to the two former modes. In particular, it can be seen that the input power of the PS (the first term in the denominator) has increased significantly with only a limited amount of power being absorbed by the SS (the second term in the denominator). This explains why this mode is seldom used for the non-CS EMMS0.

However, although the above efficiency expression might be true locally in real-time, it doesn't yield the maximum efficiency over a longer period of driving. An alternative understanding of the SS efficiency during charging would be to include a correction factor in the same way the replenishing efficiency η_{re} is applied during discharging. Similar to how the discharging efficiency of the battery needs to be penalized with the efficiency of the PS involved in replenishing the battery, any charging should be "rewarded" for offsetting future needs to be replenished. To include this consideration, the correction factor v from Eq. 4.21 needs to be modified to:

$$v = \eta_{re}. \tag{4.27}$$

This new formulation yields a different efficiency for the charging mode case with $P_{PS} = 25$ kW and $P_{SS} = -5$ kW:

$$\eta_{tot} = \frac{P_{PS} + P_{SS}}{\frac{P_{PS}}{\eta_{PS}} + \frac{P_{SS}\eta_{SS}}{v}} = \frac{20}{\frac{25}{\eta_{PS}} - \frac{5 \cdot \eta_{SS}}{\eta_{re}}} = \frac{20}{75 - 13.5} = 32.52\%. \tag{4.28}$$

It can be seen that the magnitude of the second term in the denominator is increased such that the overall impact of charging the battery is amplified. Consequently, the obtained efficiency is now comparable to that of the hybrid mode, and it can similarly be imagined that in a case of efficient use of the PS, the charging mode could outperform the other two modes of operation and end up being the optimal solution.

Based on the new efficiency expression, the optimization problem can be formulated in the same way as for the non-CS EMMS0 (in Eq. 4.19) with the updated correction factor v. The process to solve this problem is identical as well (described in Subsection 4.3.1), allowing the formation of the EMMS1 control map.

The optimal power share factor u_{opt} for varying power demand is shown in Fig. 4.13 together with the realized efficiency η_{tot}. It can be seen that the SCS chooses to operate SS-only mode during low P_{PL}, similar to the non-CS EMMS0. However, once the PS starts to be used, it is used at $u > 1$ (charging mode), which would not occur previously. Thereafter, at lower mid-range P_{PL}, a lot of the operation is almost PS-only mode. For higher power requirements the map uses hybrid mode to drive the powertrain. It is worth noting that the dependence of u_{opt} on SOC-levels is still quite limited, although the added charging mode operation can be expected to impact the SOC profile of the resulting driving. The total efficiency η_{tot} that is realized by this selection of u is slightly higher during the charging mode compared to the non-CS EMMS0, but this can currently only be attributed to the efficiency being redefined as opposed to superior performance.

Simulations are run for the four different driving cycles to tune the replenishing efficiency to maximize the fuel economy. Results with normalized EFC and final SOC levels are presented in Fig. 4.14. Simulations were run for the same range of η_{re} as non-CS EMMS0, but only $\eta_{re} \in [33, 36]\%$ were successfully completed. As can be seen from the results, the final SOC is extremely sensitive to the replenishing efficiency with variations from 100% to around 40% for WL-L, WL-M and WL-H. Even the WL-E sees significant changes in SOC_{final} for varying η_{re}.

It can be seen that the optimal value is often found around $\eta_{re} = 35\%$, and this is confirmed by looking at the normalized total EFC in Fig. 4.15. The data is quite sparse but the optimal value for η_{re} is likely to be in close proximity to $\eta_{re} = 35\%$. However, these results are sufficiently precise to realize that there is a need

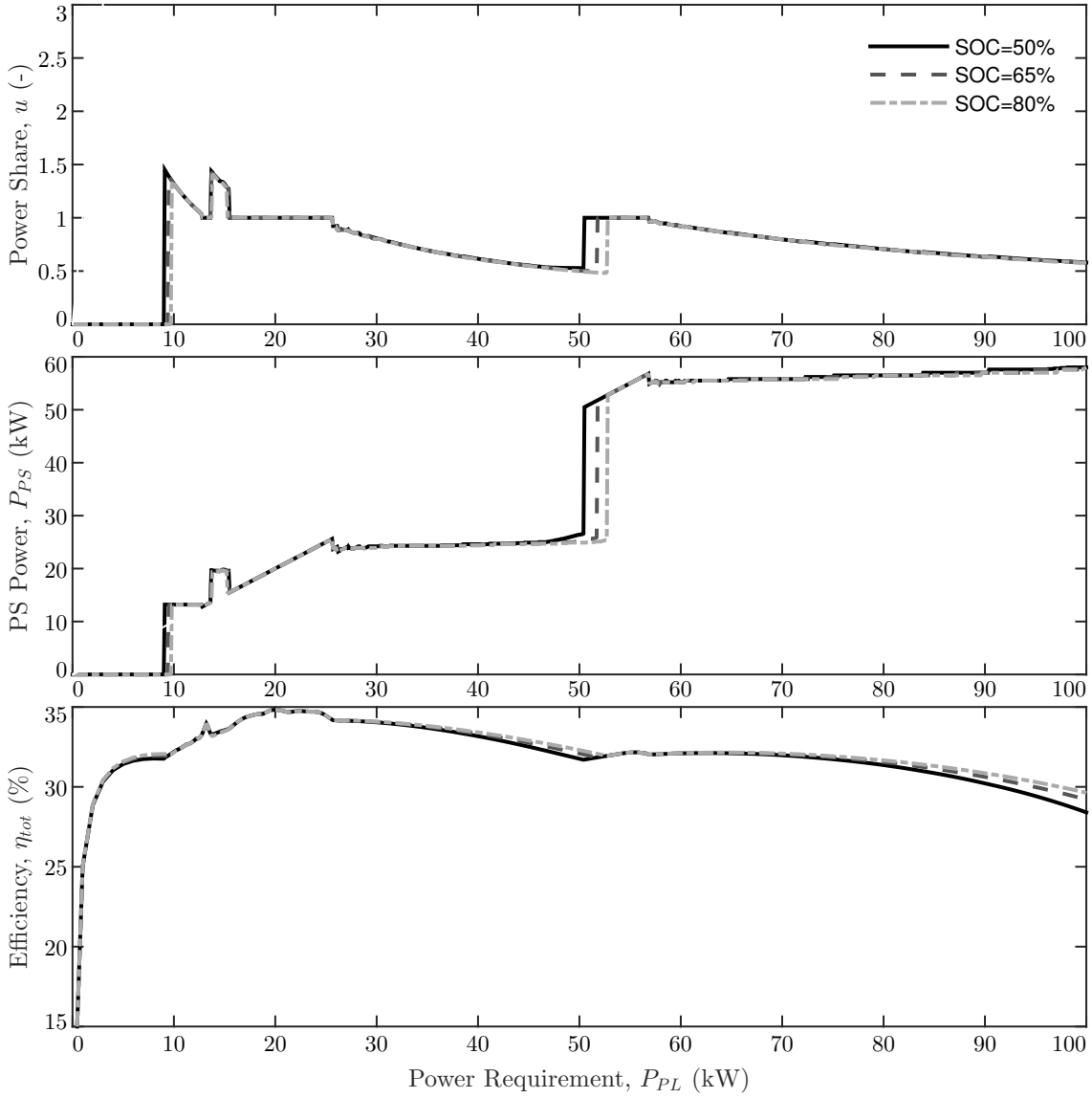

FIGURE 4.13: Optimal power share and PS power, and corresponding total efficiency for varying power requirements and SOC for $\eta_{re} = 35\%$ for non-CS EMMS1.

to improve upon this control strategy by designing a charge sustaining mechanism. The SOC_{final} values for $\eta_{re} = 35\%$ are 50%, 60%, 62% and 34% for the four driving cycles. Thus, similar to the non-CS EMMS0, the non-CS EMMS1 will require some modification to ensure CS operation. However, the non-CS EMMS1 might be in a better position to do so.

As mentioned, the SOC range of the non-CS EMMS1 stretches from very high to very low with a very limited range of η_{re}, while the non-CS EMMS0 can not even match the same SOC range with five times the range for η_{re}. This difference can

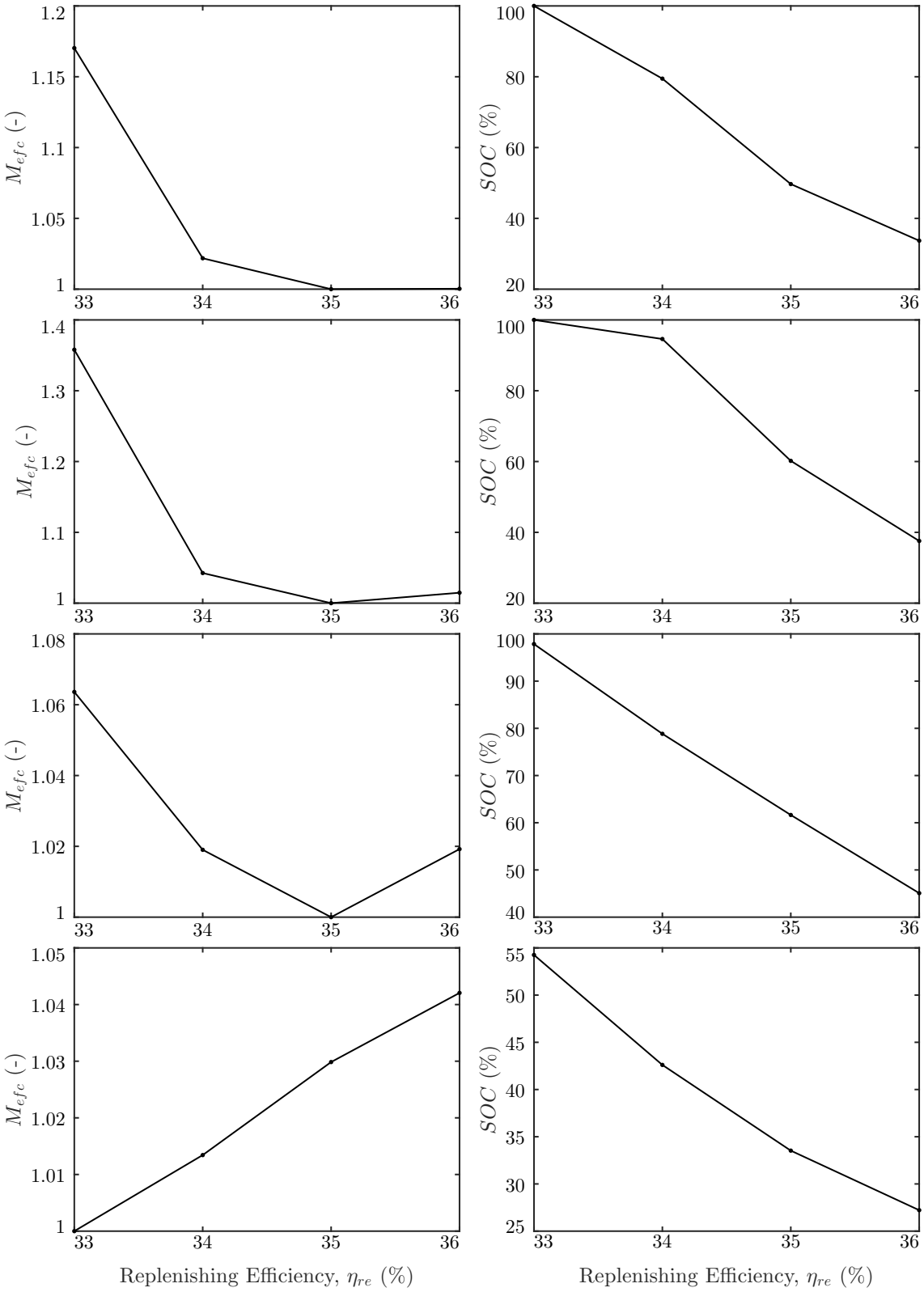

FIGURE 4.14: Normalized EFC (left) and final SOC (right) for varying η_{re} when driving WL-L, WL-M, WL-H and WL-E (from top to bottom) with non-CS EMMS1.

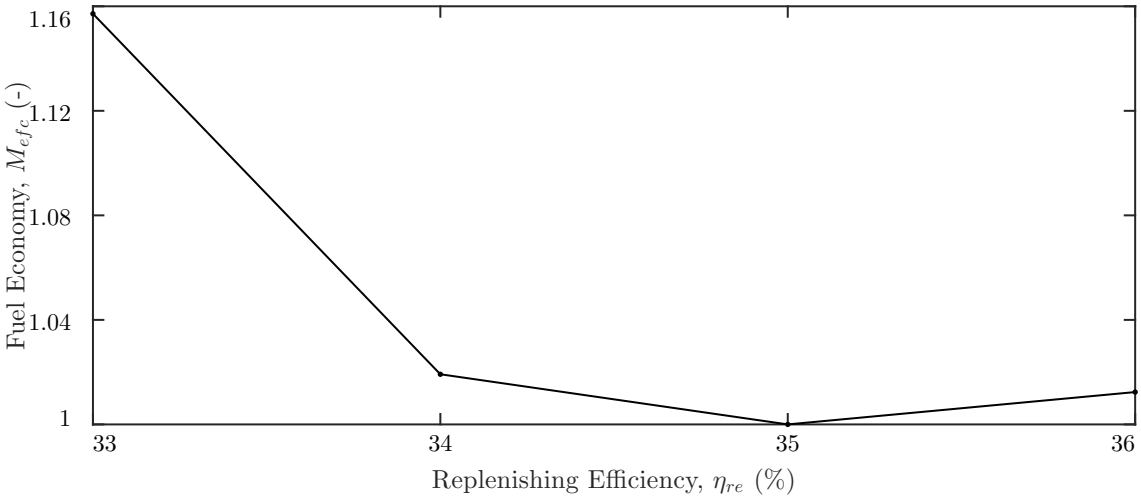

FIGURE 4.15: Normalized total EFC M_{tot} for varying η_{re} with non-CS EMMS1.

be attributed to the modification of the correction factor v which now encourages charging mode operation. Although the achievement of high final SOC comes at the expense of the fuel economy, it is a great characteristic that can be utilized to make the control strategy CS without designing an external function to perform this function.

4.4.2 Charge Sustaining Operation

As has been shown in Fig. 4.14, the non-CS EMMS1 is capable of controlling the final SOC over a wide range by simply adjusting the replenishing efficiency η_{re} for the control strategy. As η_{re} is reduced, the final SOC is increased, and a higher η_{re} results in a drop for the final SOC. Thus, if the control strategy is designed such that a low η_{re} is employed when the SOC is low (to increase the SOC) and a high η_{re} is used when the SOC is high (to decrease the SOC), then the control strategy would be inherently CS. Designing such an SOC-dependent η_{re} function is very simple, as a linear relationship would be sufficient for our purposes. Some possible designs, with varying CSI factors D_{csi}, are presented in Fig. 4.16 (where the optimal $\eta_{re,opt}$ is chosen to be 35%).

Each line represents a unique design that intersects with the optimal solution of $\eta_{re,opt}$ at $SOC = SOC_{initial}$. The CSI factor D_{csi} determines the deviation from the optimal $\eta_{re,opt}$. For example, with $\eta_{re,opt} = 34\%$ and $D_{csi} = 4$, the extreme points of SOC_L and SOC_U will correspond to $\eta_{re}(50\%) = 34\% - 4\% = 30\%$ and

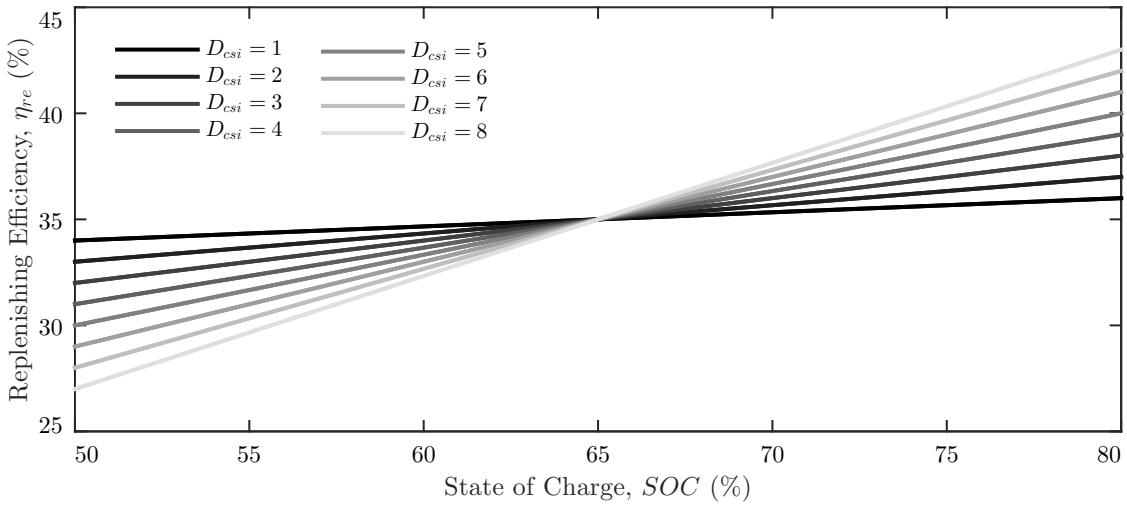

FIGURE 4.16: Replenishing efficiency $\eta_{re}(SOC)$ for various values of CSI factor D_{csi} with $\eta_{re,opt} = 35\%$.

$\eta_{re}(80\%) = 34\% + 4\% = 38\%$ respectively. This is expressed analytically as

$$\eta_{re} = \eta_{re,opt} + \frac{SOC - SOC_{mid}}{SOC_{range}} D_{csi} \tag{4.29}$$

where

$$SOC_{mid} = \frac{SOC_U + SOC_L}{2} = 65\% \tag{4.30}$$

and

$$SOC_{range} = \frac{SOC_U - SOC_L}{2} = 15\%. \tag{4.31}$$

Thus, D_{csi} determines how intensely CS operation should be pursued.

The SOC-dependent η_{re} is then considered to produce new control maps, using the same approach as taken in the previous section for EMMS0. The generated map for optimal power share is presented in Fig. 4.17 together with the corresponding power-train efficiencies. It can clearly be seen that the control strategy is relying heavily on the PS during low SOC, with significant amount of charging mode operation as well. Conversely, for higher SOC, the SS is used much more significantly. The contrast is less extreme compared to EMMS0 in Fig. 4.8, as it is beyond practical necessity to require complete SS mode for high SOC. It is worth noting that the operation for the cases of $SOC = 55\%$ and $SOC = 75\%$ are quite close to the operation of $SOC = 50\%$ and $SOC = 80\%$ respectively. This is in contrast to the EMMS0 where even these very low and high values of SOC would result in operation only marginally different from the $SOC = 65\%$ case. Thus, a more aggressive charge

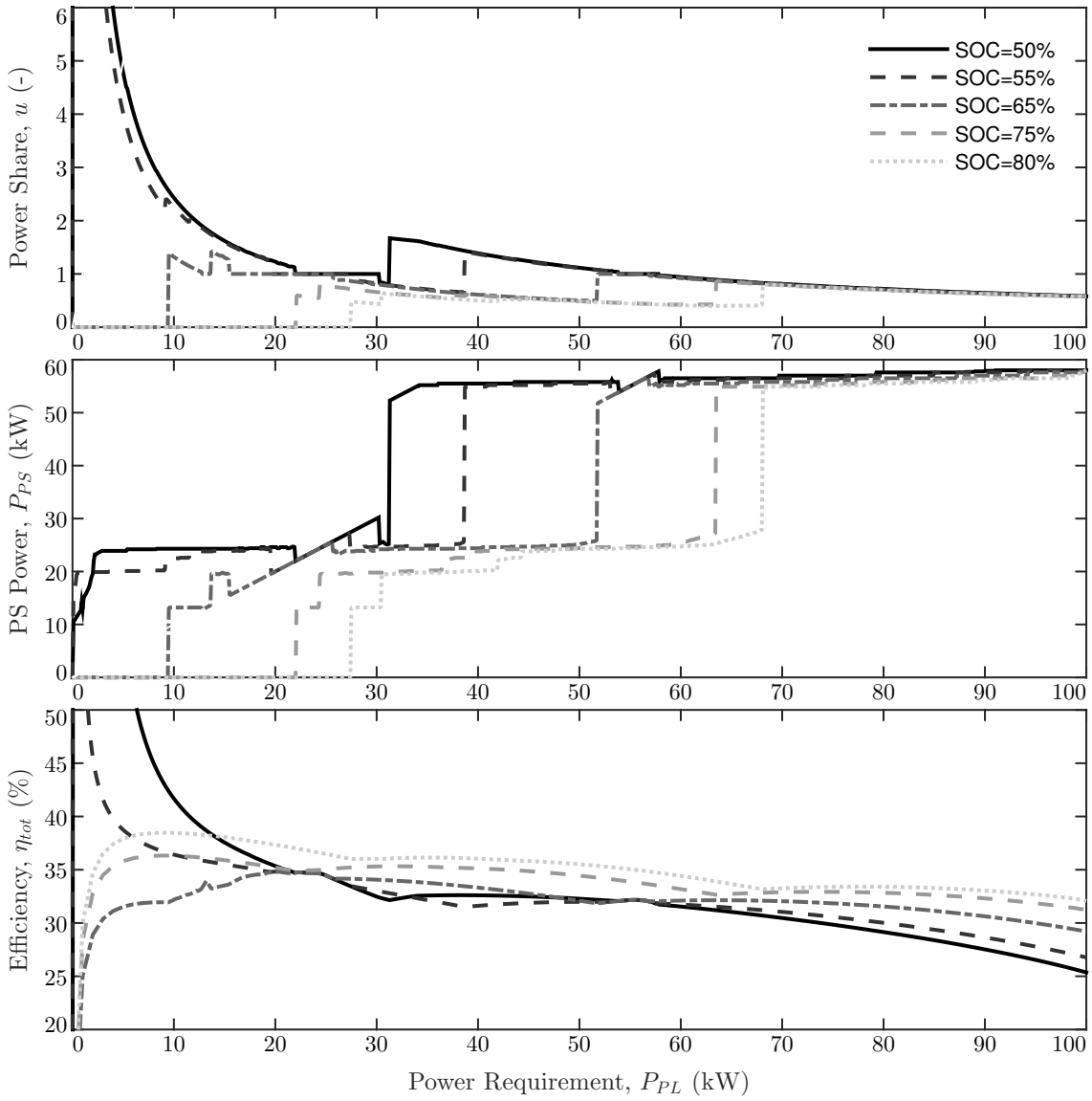

FIGURE 4.17: Optimal power share and PS power, and corresponding total efficiency for varying power requirements and SOC for $\eta_{re} = 35\%$ and $D_{csi} = 7$ for EMMS1.

sustaining operation can be expected. Also, the EMMS1 utilizes the charging mode not only for low power requirements but also at higher levels, where the EMMS0 would use hybrid mode.

The resulting efficiency is even more different. The inclusion of the replenishing efficiency for charging, which boosts the SS efficiency term, allows very high efficiency values to be achieved. This is particularly visible at very low power requirements where the use of charging mode results in efficiencies higher than the peak PS efficiency (around 35%), which has often been the upper limit for previous control

strategies. However, it is problematic to compare the efficiencies of each control strategy, as although the EMMS1 is still using the total powertrain efficiency η_{tot} as defined in Eq. 4.15 earlier in this chapter, the meaning is quite different. The definition of the total efficiency has changed as we use a new understanding of the replenishing efficiency η_{re} (within the correction factor v) which is now SOC-dependent rather than a constant and both boosts and penalizes the SS efficiencies during charging and discharging respectively. Consequently, this new efficiency for the EMMS1 does not relate to the instantaneous physical efficiency of the powertrain, but it allows the optimization process to identify suitable operating points for longer durations of driving.

To test the EMMS1 with its CS features, new power share maps are produced for each combination of values of $\eta_{re,opt} \in [34, 36]\%$ and $D_{csi} \in [1, 9]\%$ in steps of 0.2% and 1% respectively. Each of these are then tested for the four driving cycles to tune the parameters such that the fuel economy is maximized. Results with normalized EFC and final SOC levels are presented in Fig. 4.18.

The optimal selection of $\eta_{re,opt}$ and D_{csi} varies considerably between driving cycles, and is in fact typically outside the investigated region (thus appearing on the edge of the plots). However, it can be seen for the first three driving cycles that the final SOC is found to be sustained best within the investigated range (in particular just below $\eta_{re,opt} = 35\%$ where $SOC_{final} \approx SOC_{initial}$). Also, an overall evaluation of M_{tot}, as shown in Fig. 4.19, gives $\eta_{re,opt} = 35\%$ and $D_{csi} = 7\%$ as the optimal selection. This selection was manually favored over an alternative solution at $\eta_{re,opt} = 36\%$ and $D_{csi} = 8\%$ as it yields practically identical fuel economy results (<0.02% difference) but delivers improved CS ability.

As the investigated range of the tuning parameters is quite narrow, relative to the EMMS0, it might be thought that this control strategy is highly sensitive to precise tuning. However, there are two reasons why this is not true. Firstly, even though the optimal tuning parameters for various driving cycles are very different, the resulting fuel economy for varying tuning parameters are quite similar. Secondly, and most importantly, due to the nature of the charge sustaining mechanism, the control strategy will often tend to drift towards the optimal η_{re} value for the particular type of driving. For example, as was shown in Fig. 4.14, the WL-E driving cycle performs optimally for $\eta_{re} = 33\%$ while the other driving cycles prefer operation closer to $\eta_{re} = 35\%$. With the EMMS1, it can be seen that the optimal selection (of

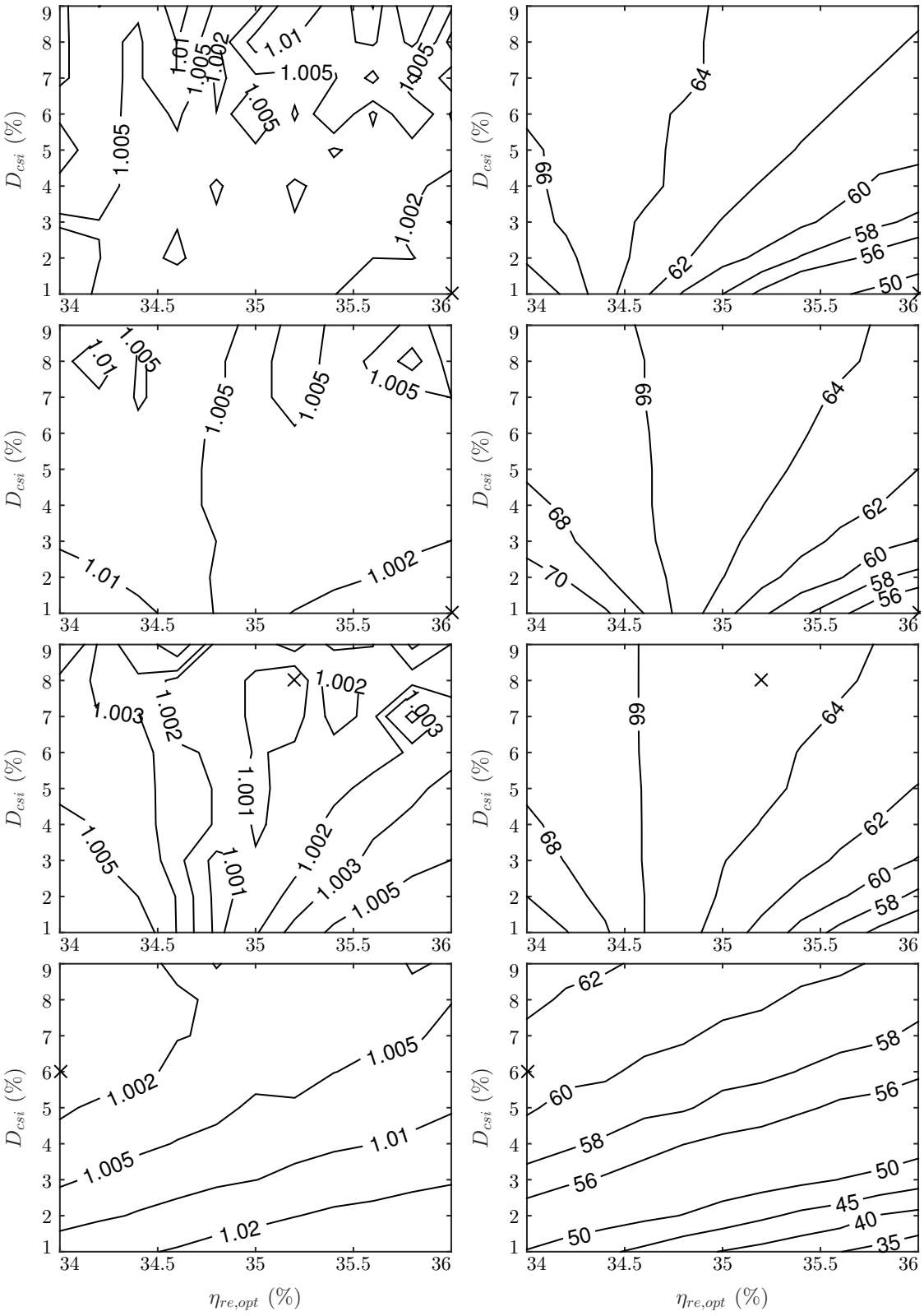

FIGURE 4.18: Normalized EFC M_{efc} (left) ($M_{efc} = 1$ is marked with a cross) and final SOC (right) for varying $\eta_{re,opt}$ and D_{csi} when driving WL-L, WL-M, WL-H and WL-E (from top to bottom) with EMMS1.

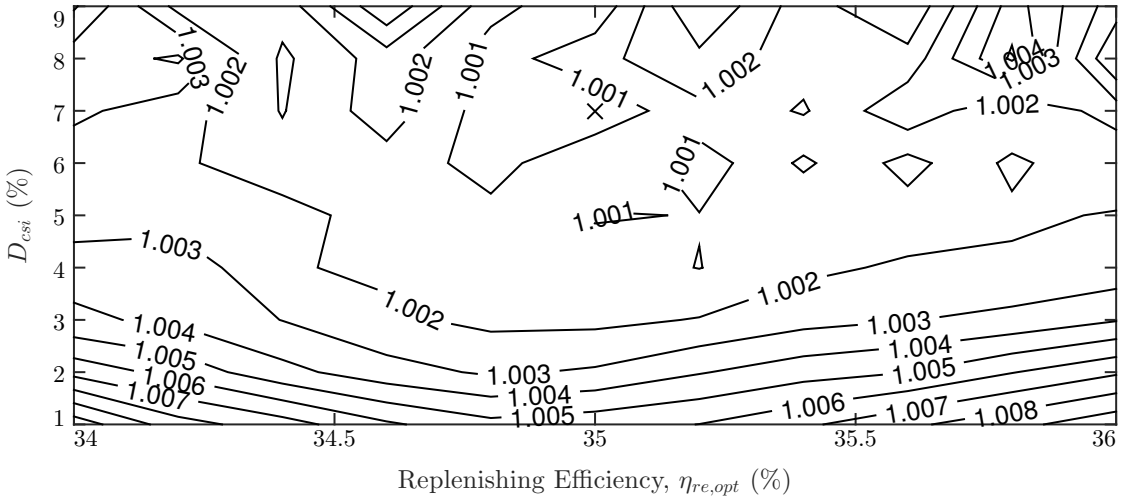

FIGURE 4.19: Normalized total EFC M_{tot} for varying $\eta_{re,opt}$ and D_{csi} with EMMS1.

$\eta_{re,opt} = 35\%$ and $D_{csi} = 7\%$) will result in a final SOC of 60% for WL-E. By using Eq. 4.29 we can calculate that this corresponds to operation with $\eta_{re} = 32.7\%$. Thus, for most types of driving, the SOC will often drift and become reasonably steady close to the point that yields the best η_{re} value such that the fuel economy is maximized.

It is also worth noting that for the first three driving cycles the final SOC is close to $SOC_{initial} = 65\%$. This has several benefits. Firstly, this mean that the SOC will rarely deviate significantly from the base SOC value. This reduced depth of discharge leads to improved battery health. Secondly, the limited need to apply CS adjustments speaks to the effective design of the core control strategy that is applicable to a wide range of driving cycles. Thirdly, the control strategy is quickly able to reach the optimal η_{re} value to maximize the fuel economy for the given driving cycle. If a particular driving cycle had its optimal operation with $\eta_{re} = 28\%$, the EMMS1 would need to drive sub-optimally for quite a while until the SOC drops down to 50% (as given by Eq. 4.29) to make the control strategy effectively operate with $\eta_{re} = 28\%$. Thus, the closer the final steady SOC value for a driving cycle is to $SOC_{initial}$, the faster it will reach its ideal fuel economy.

4.4.3 Operation

The power profiles resulting from the operation of EMMS1 with $\eta_{re,opt} = 35\%$ and $D_{csi} = 7\%$ are presented in Fig. 4.20 and Fig. 4.21, for the first and final iteration

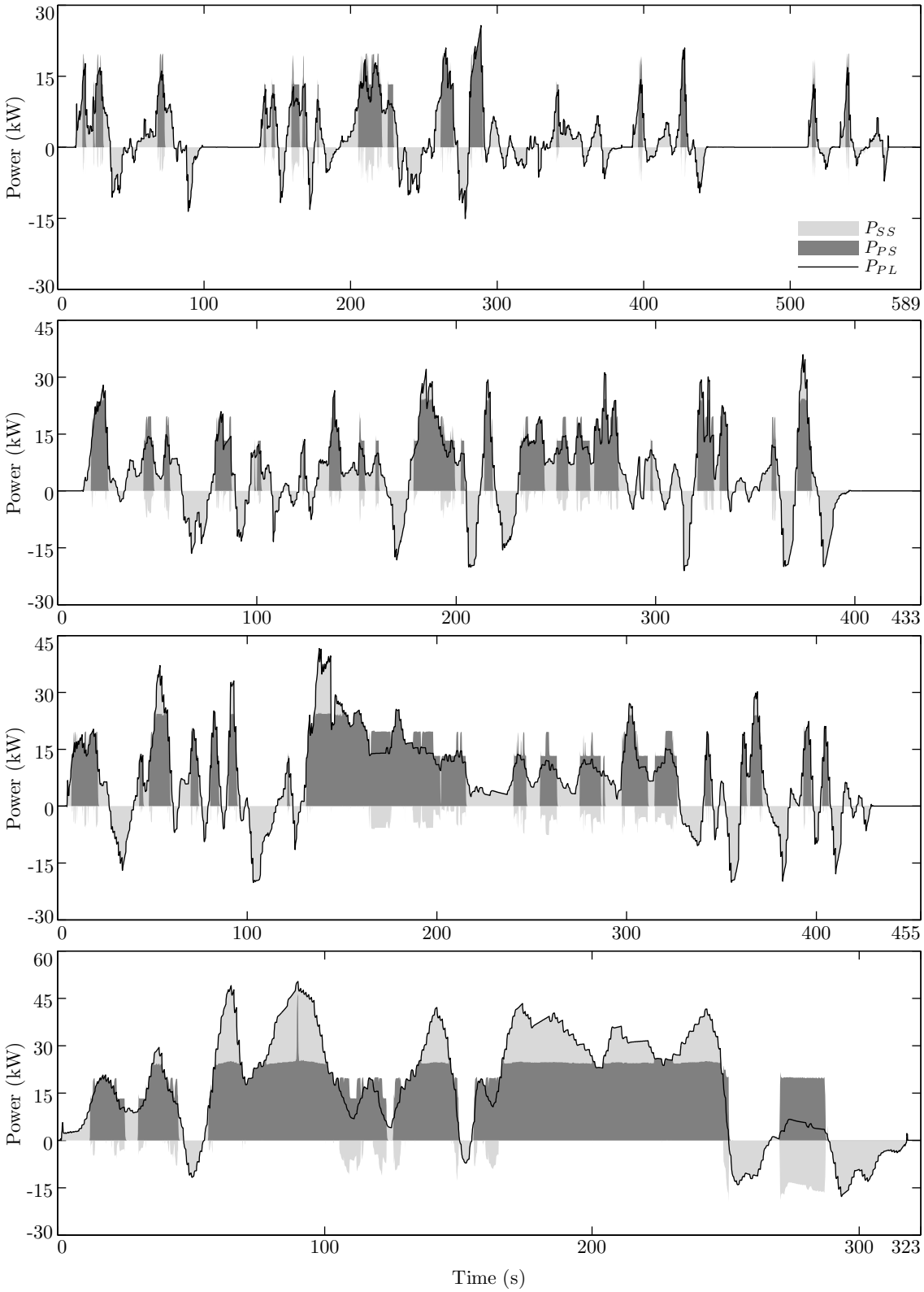

FIGURE 4.20: Power time histories for PS, SS and PL for the first iteration of driving WL-L, WL-M, WL-H and WL-E (top to bottom) with the EMMS1.

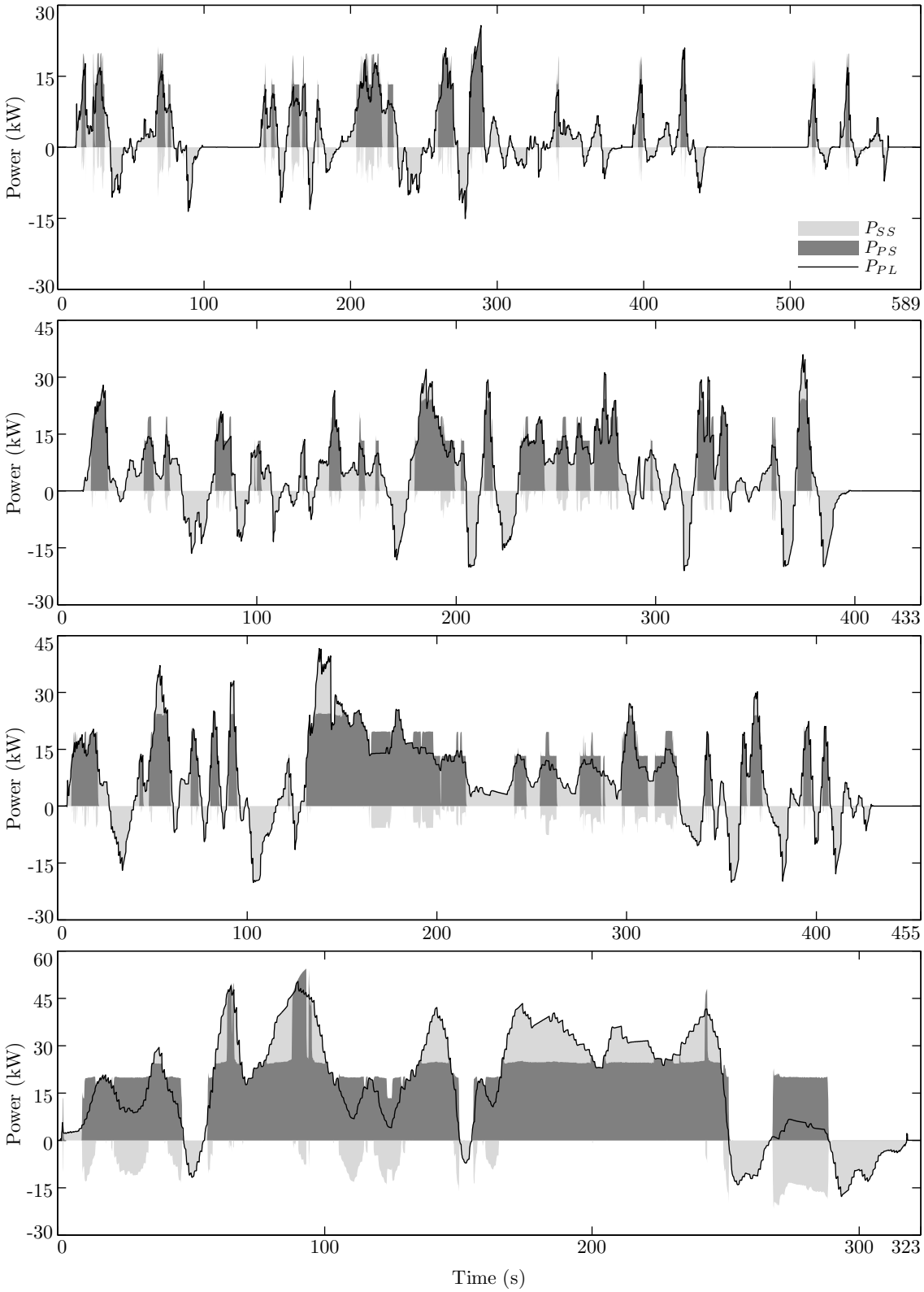

FIGURE 4.21: Power time histories for PS, SS and PL for the final iteration of driving WL-L, WL-M, WL-H and WL-E (top to bottom) with the EMMS1.

of the driving cycles respectively. There are three major differences between the operation of EMMS0 and EMMS1: the use of charging mode operation; the amount of PS operation; and the differences between the first and final iteration.

Firstly, it is quite clear from the EMMS1 results that the SS is quite often charged directly by the PS (shown as light shading in the negative region, while P_{PL} is positive). This occurs frequently for every single driving cycle, normally in quite small magnitudes. However, as is seen towards the end of WL-E, the EMMS1 even opts to charge the SS at about 15 kW during driving. This not only boosts the SOC but also allows the PS to operate at a more efficient power level. Consequently, the power share can be seen to exhibit a mix of load following and load leveling characteristics.

Secondly, the PS is used more frequently for the EMMS1. There are many instances where the SS on its own is more efficient than the PS on its own. However, in many of these cases an even more preferred option is to have the PS deliver power in excess of the required load and thus charge the SS. As this is allowed by the EMMS1, it can be seen that the PS is used to deliver reasonably low loads. The operation around $t = 120$ s for WL-E can be compared with the operation of EMMS0 in Fig. 4.11. The two valleys in P_{PL} are operated by the SS in EMMS0, while the EMMS1 decides to use the PS to deliver power (efficiently) in excess of the required load and thus charge the SS at the same time.

Thirdly, it can be seen that the difference between the first and final iteration for EMMS1 for each driving cycle is relatively low. The differences for WL-L, WL-M and WL-H are barely noticeable, while the WL-E clearly has more PS usage. Nevertheless, the differences are much smaller than EMMS0. This can be explained by the previous two differences mentioned, which both result in a higher SOC. As the EMMS0 struggled to maintain its SOC (having final SOC values around 55% for each driving cycle), it needed to apply control decisions that deviated significantly from its base operation (at $SOC = SOC_{initial}$). EMMS1 on the other hand maintains $SOC \approx SOC_{initial}$ for most of its driving and does thus not need to deviate from its operation. In fact, the limited deviation that does occur is desirable, as this is the mechanism that allows the EMMS1 to identify the ideal control policy for the particular driving conditions.

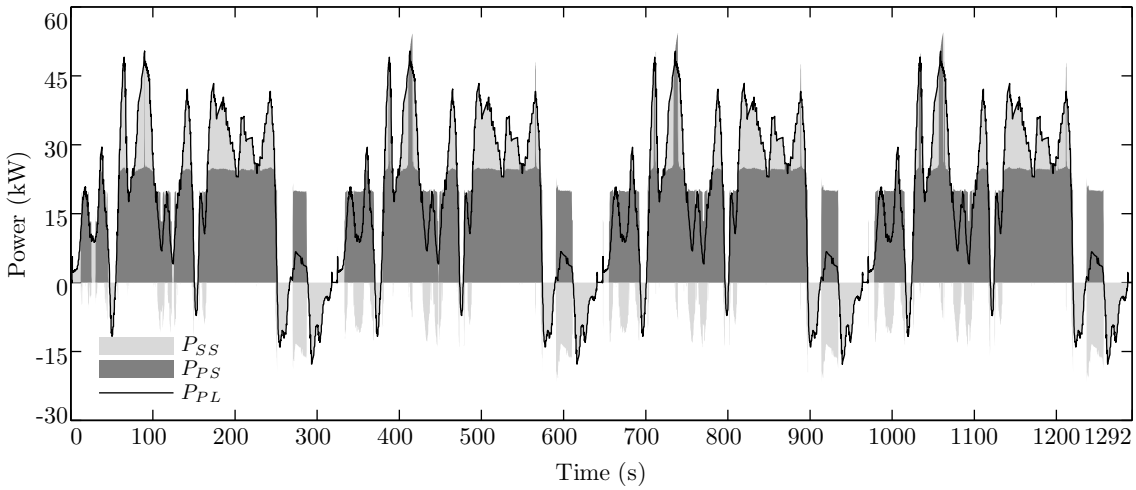

FIGURE 4.22: Power time histories for PS, SS and PL for all four iterations of driving WL-E with the EMMS1.

The WL-E is the only driving cycle where the SOC_{final} drops by more than 1.5%, which is why it has some clearly visible differences between the first and final iteration. It is however worth emphasizing that the EMMS1 operates quite steadily even for WL-E. To demonstrate this further, the power profiles for all four of the WL-E iterations are shown in Fig. 4.22. It is quite clear that the control strategy is quick to learn about the driving conditions, and adapts already by the second iteration. The differences in control between the second and fourth iteration are very small. Thus, it can be understood that the EMMS1 will "find" the preferred mode of operation within a short time frame and then settle into consistent operation.

The fuel economy results corresponding to these driving cycles are shown in Table 4.3. As observed and mentioned earlier, the EMMS1 is quite successful in maintaining its SOC (in contrast to the EMMS0). The EFC results are quite impressive as they are at worst less than 5% behind the GECMS, and at best less than 1% behind. Overall, for all driving cycles considered together, the GECMS outperforms the EMMS1 by only 2.34%, which essentially cuts the margin to EMMS0 by half.

TABLE 4.3: Fuel economy results for EMMS1

Driving Cycle	SOC_{final} (%)	m_f (kg)	m_{efc} (kg)	Δ_{GECMS} (%)
WL-L	63.63	0.7258	0.7406	+4.57
WL-M	65.18	1.1701	1.1684	+2.59
WL-H	65.30	0.9679	0.9651	+1.56
WL-E	59.60	1.5257	1.5997	+0.91

4.5 Global Efficiency Maximizing Map Strategy

As the EMMS framework is delivering good performance, it is of interest to produce a globally tuned variant that is comparable to the GECMS. This section will present such a control in the form of the GEMMS, which will be designed, tuned and studied, as well as compared to the GECMS.

4.5.1 Global Design

The GEMMS is a globally tuned EMMS (similar to the relationship between the GECMS and ECMS). However, the GEMMS not only tunes the EMMS1 optimally with prior knowledge of the driving cycle, it also refines the definition of the objective function. The EMMS1 refined the total efficiency expression used by the EMMS0, to include a correction to the battery charging operation as well (the EMMS0 only corrected discharging operation), and also made the correction factor SOC-dependent (rather than being a constant). However, the correction factors are the same for charging and discharging operation. Although this is a good approximation, the replenishing efficiency η_{re} is not identical for charging and discharging operation and a more precise expression can be obtained by modifying the correction factor v from Eq. 4.27 to:

$$v = \begin{cases} \eta_{re,c} & P_{SS} < 0 \\ \eta_{re,d} & P_{SS} \geq 0 \end{cases} \tag{4.32}$$

where $\eta_{re,c}$ and $\eta_{re,d}$ are the replenishing efficiencies for charging and discharging respectively.

Based on the new efficiency expression, the optimization problem can be formulated as the local maximization problem given in Eq. 4.19. However, for the GEMMS the correction factor v can be globally tuned for each driving cycle. Thus, for any given positive power requirement P_{PL}, an optimal power share factor u_{opt} can be defined for each set of replenishing efficiencies $\eta_{re,c}$ and $\eta_{re,d}$. Using the efficiency maps for the PS and SS, a sweep can be performed for Eq. 4.15 with $u \in [0, \frac{P_{PSmax}}{P_{PL}}]$, $P_{PL} \in [0, P_{PLmax}]$ and $SOC \in [SOC_L, SOC_U]$ to produce an optimal control map. This process is repeated for each candidate set of $\eta_{re,c}$ and $\eta_{re,d}$.

Table 4.4: Optimal replenishing efficiency values for GEMMS

Driving cycle	$\eta_{re,d}$ (%)	$\eta_{re,c}$ (%)
WL-L	37.7	31.9
WL-M	37.9	31.9
WL-H	36.7	32.8
WL-E	34.7	31.0

This optimization process is now applied to produce power share maps for each combination of values of $\eta_{re,c} \in [31.5, 33]\%$ and $\eta_{re,d} \in [36.5, 38]\%$ (the WL-E solution was however later found by studying $\eta_{re,c} \in [30, 32]\%$ and $\eta_{re,d} \in [34, 36]\%$) in steps of 0.1% for each. Each of these are then tested for the four driving cycles to tune the parameters to maximize the fuel economy. Results with normalized EFC and final SOC levels are presented in Fig. 4.23. The optimal selection of replenishing efficiencies for each of the four driving cycles is presented in Table 4.4.

The optimal selections of replenishing efficiency values are unique for each driving cycle, but they are very similar for the first three of them. In fact, using $\eta_{re,d} = 37.7\%$ and $\eta_{re,c} = 31.9\%$ yields fuel economies that are less than 0.2% inferior to the optimal solution for these three driving cycles. The GEMMS is thus less sensitive to varying driving cycles when compared to the GECMS. So despite that the optimal set of tuning parameters for WL-H is found at $\eta_{re,d} = 36.7\%$ and $\eta_{re,c} = 32.8\%$, which is far from the values mentioned above, the performance is negligibly small. In general, for each of the driving cycles, the performance of the control strategy is strongest along the $SOC_{final} = SOC_{initial}$ line of operation (similar to GECMS).

However, it can be seen that the optimal value for WL-L and WL-M is not very close to $SOC_{final} = SOC_{initial} = 65\%$, which can be expected from a global optimal solution. This can be attributed to the limited precision of the tuning. For example, for WL-L at $\eta_{re,d} = 37.6\%$ and $\eta_{re,c} = 31.8\%$ the fuel economy is only worsened by <0.04%, while achieving $SOC_{final} = 65.67\%$. It is quite likely that there is another solution in between these that achieves a better fuel economy (with very small margin) while approaching $SOC_{final} = SOC_{initial}$ even more. When a similar situation appeared for the EMMS1, the more charge sustaining option was selected, as it was the preferred solution for a real-time control strategy (that is expected to operate well for varying driving conditions). However, for the GEMMS the solution with the better fuel economy will be selected, as the priority is to minimize EFC such that it can be used as benchmark of what is realizable.

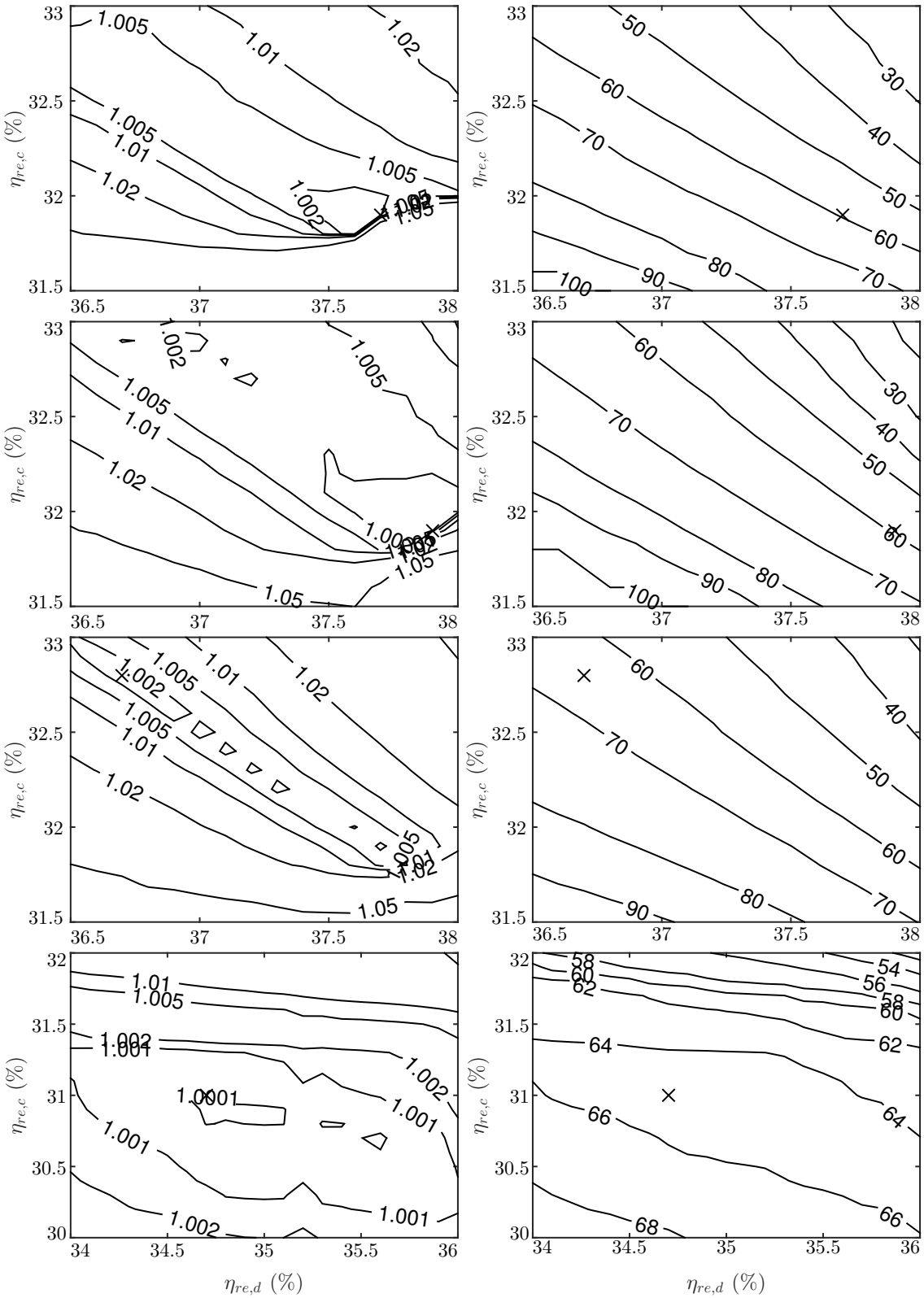

FIGURE 4.23: Normalized EFC M_{efc} (left) ($M_{efc} = 1$ is marked with a cross) and final SOC (right) for varying $\eta_{re,c}$ and $\eta_{re,d}$ when driving WL-L, WL-M, WL-H and WL-E (from top to bottom) with GEMMS.

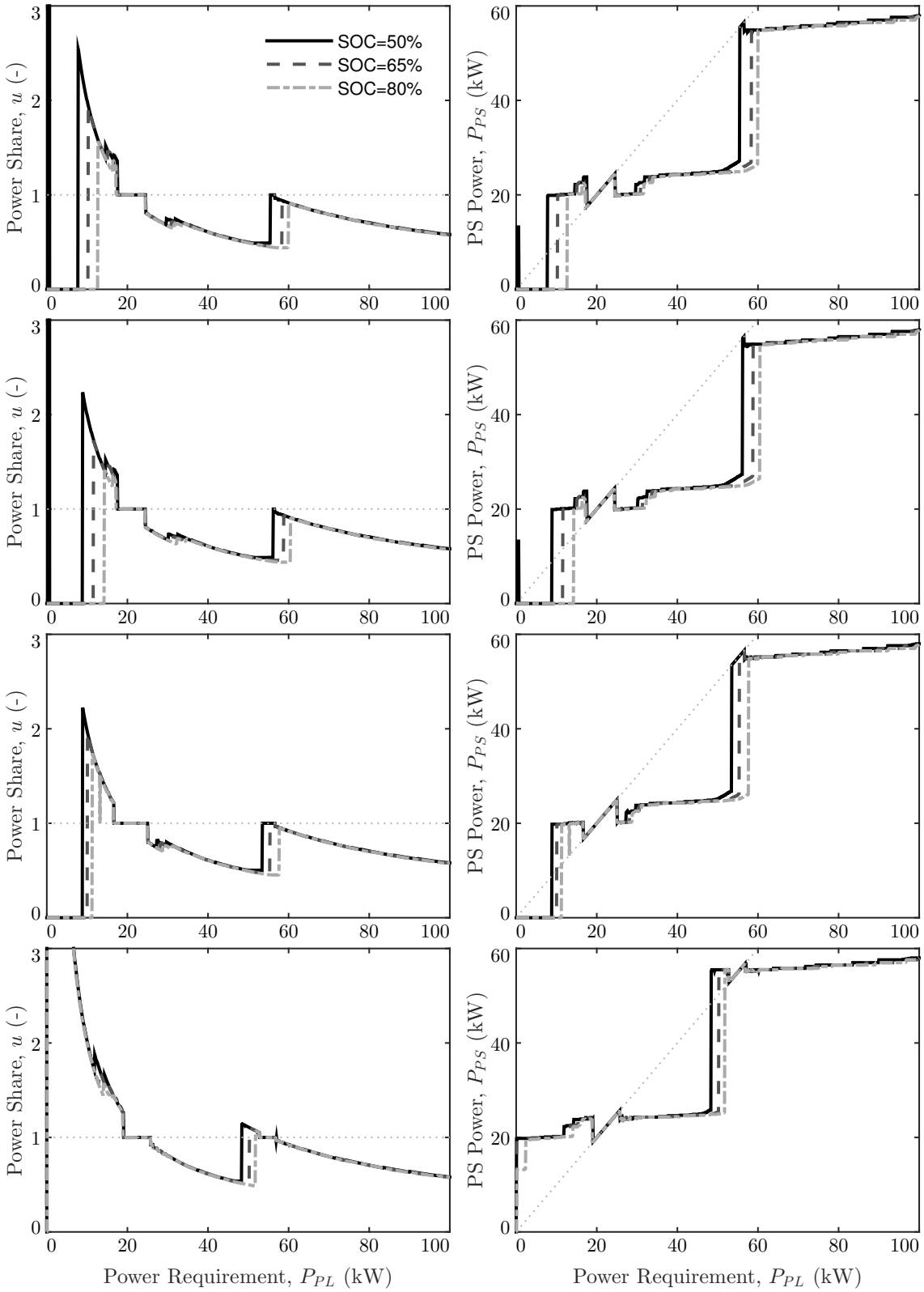

FIGURE 4.24: Optimal power share and PS power for varying power requirements and SOC for WL-L, WL-M, WL-H and WL-E (top to bottom) with GEMMS.

The optimal set of replenishing efficiencies for each of the four driving cycles, correspond to the control maps presented in Fig. 4.24. As can be seen, the optimal power share u_{opt} has similar trends to most of the previous optimization-based control strategies in this work: pure PS operation at very low power requirements; charging mode operation at mid-low power requirements; and hybrid operation for medium and high power requirements. However it differs from the previous control strategies in key respects. Firstly, it is interesting that the general shape of the GEMMS control map is more similar to the GECMS than it is to the EMMS1. The flexibility offered by having two tuning parameters allows both the GEMMS and GECMS to adopt more precisely the truly optimal power share. However, in terms of its SOC dependence, the GEMMS is more similar to the EMMS1 than the GECMS. Note that the spike in power share around $P_{PL} = 0.5$ kW, is an effect of the extremely low DC-DC converter efficiency. However, this spike is not implemented in the real control.

4.5.2 Operation

The operation based on the globally tuned parameter values is presented further in Fig. 4.25 and Fig. 4.26, showing the power profiles for the first and final iterations of the driving cycles respectively.

The operation for WL-L and WL-M is very similar to the GECMS. However, it can be seen that the GEMMS experiences fewer false starts, i.e. the PS being switched on for a brief moment before being switched off. This is particularly visible for the WL-L, where the GECMS suffers from a large quantity of false starts. However, rather than being a particular trait of the GEMMS, it has most likely been fortunate with the driving conditions and its own rules at these particular times. The GEMMS is using the PS to a lesser extent (as evidenced by the drop in final SOC discussed earlier) and fewer false starts would be a consequence for these driving cycles with low loads. Another difference between the GEMMS and GECMS, which is clearer in WL-M and WL-E, is that the GEMMS is using the PS much more flexibly. As was remarked earlier, the GECMS operates in a quite “blocky” manner, with the PS often operating quite steadily. In contrast, the PS operation of the GEMMS is much more uneven as it adapts to the changing load.

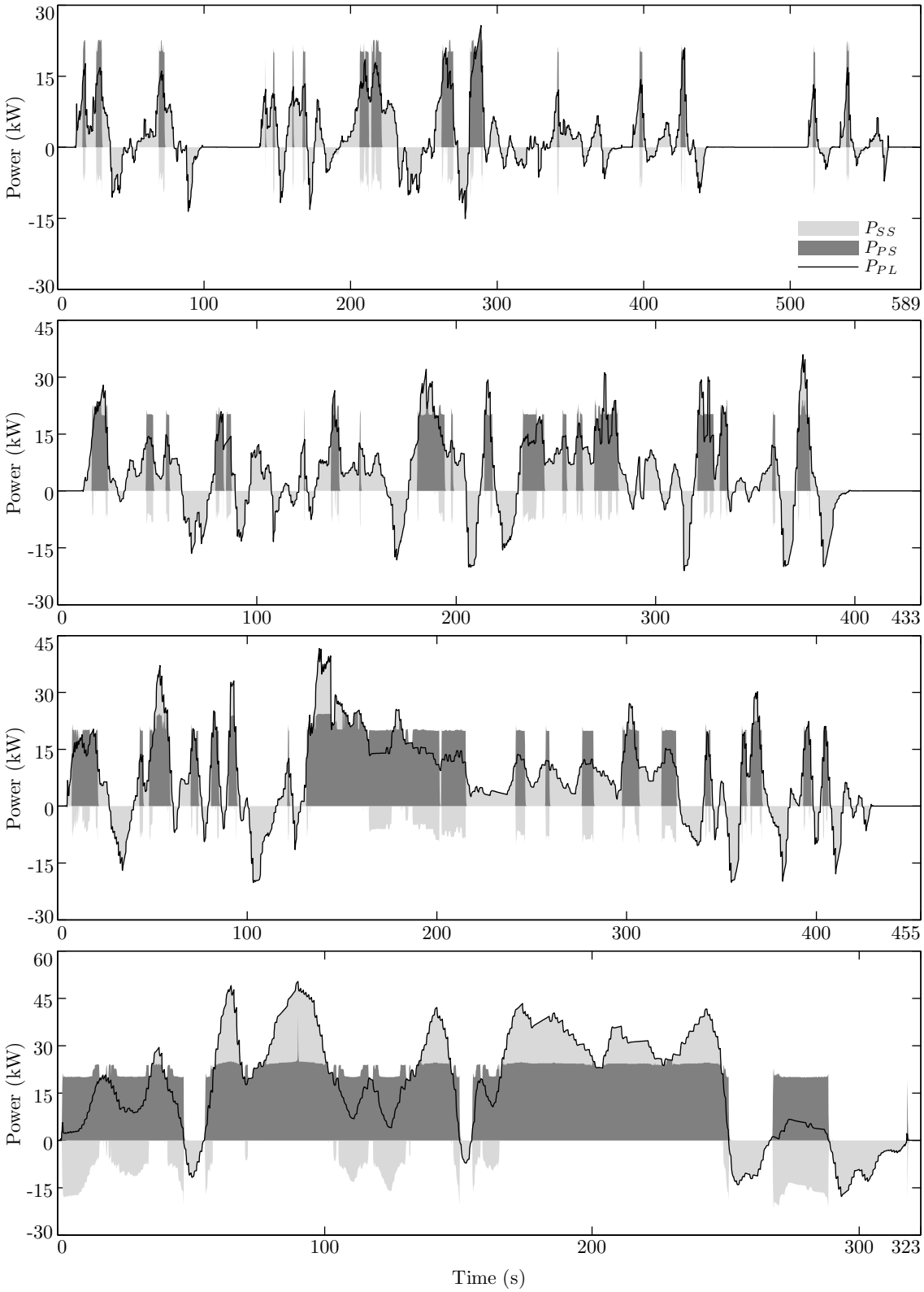

FIGURE 4.25: Power time histories for PS, SS and PL for the first iteration of driving WL-L, WL-M, WL-H and WL-E (top to bottom) with the GEMMS.

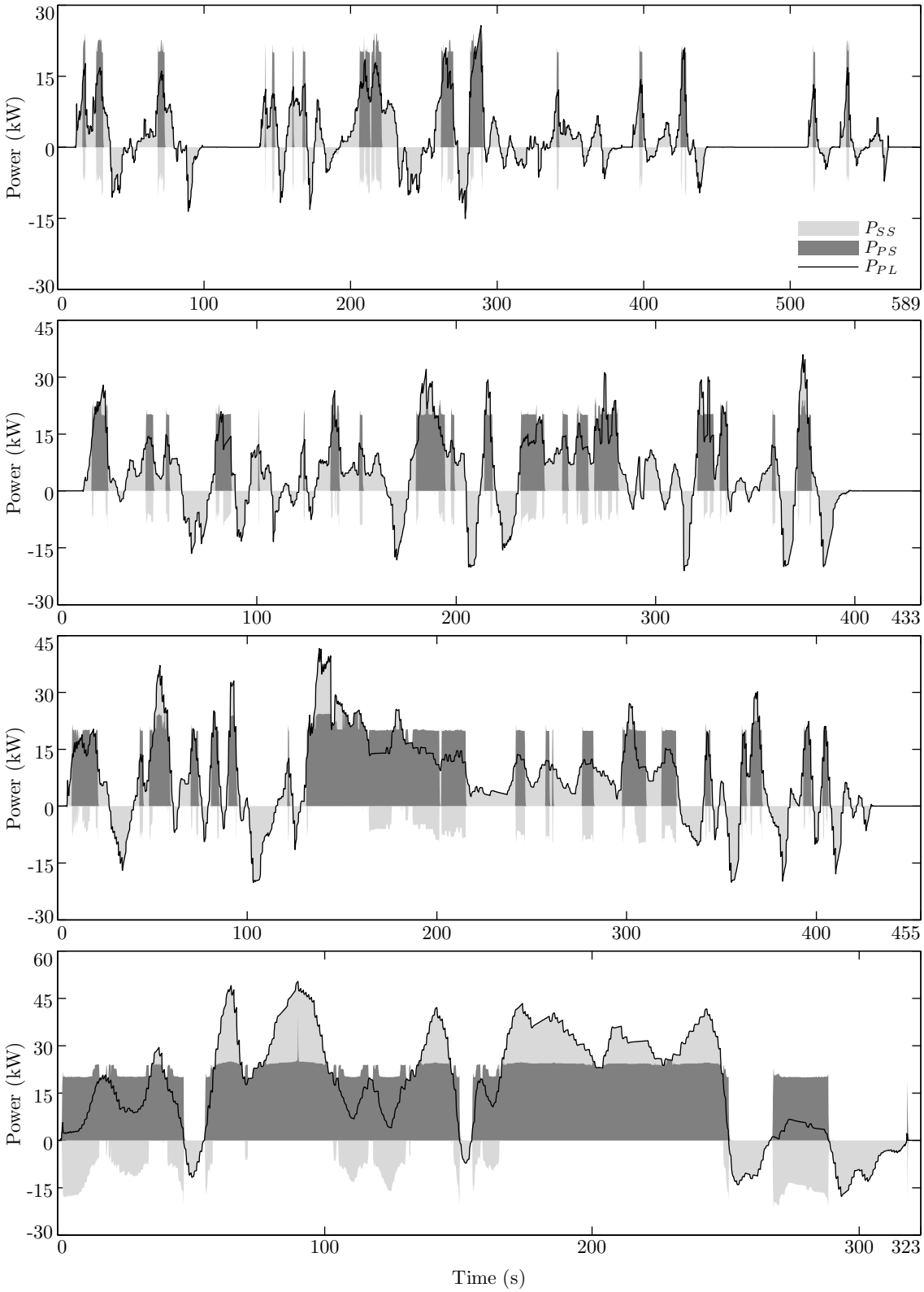

FIGURE 4.26: Power time histories for PS, SS and PL for the final iteration of driving WL-L, WL-M, WL-H and WL-E (top to bottom) with the GEMMS.

With regards to the GEMMS performance for the first and final iterations of the driving cycles, it can be seen that the PS is used to a larger extent for WL-L and WL-M (and WL-H to a limited extent). This can be attributed to the drop in SOC that was noted earlier that causes the SS efficiency to drop, making the PS the preferred energy source more often. This results in an indirect form of CS operation. The WL-E, on the other hand practically operates identically for all iterations.

It is worth noting that there is a significantly larger amount of charging mode operation when compared to the EMMS1 (in Fig. 4.21). The frequency or duration of charging mode operation is comparable but the magnitude is much higher with the GEMMS. This can be attributed to the fact that the EMMS1 has $\eta_{re,c} = \eta_{re,d}$, and is thus unable to include intense charging mode operation without detrimental impact on the optimization of the balance during hybrid mode operation. Thus, the ability to tune the replenishing efficiencies of charging and discharging separately makes the GEMMS much more nuanced in making its decisions.

Finally, the fuel economy results for the GEMMS are presented in Table 4.5. As mentioned earlier, the focus of the GEMMS is on minimizing EFC and thus the lower final SOC is less relevant. It can be seen that the GEMMS has outperformed the GECMS for every single driving cycle, with margins of 0.06-0.38%. For the driving cycles combined, the net improvement is 0.2%. Considering the additional analysis of the powertrain that was done to be able to implement this strategy, these gains can be considered quite modest. The GECMS has a simple implementation stage, and also results in relatively simple operation of the PS, which is operated quite steadily. In fact, maybe the GECMS performed well because of its simplicity rather than despite it. This will be explored further in Chapter 6.

Nevertheless, as the objective of both the GECMS and GEMMS is to act as benchmarks, representing approximate global optimal solutions, the 0.2% improvement is significant.

Table 4.5: Fuel economy results for GEMMS

Driving Cycle	SOC_{final} (%)	m_f (kg)	m_{efc} (kg)	Δ_{GECMS} (%)
WL-L	59.36	0.6451	0.7063	-0.28
WL-M	59.13	1.0750	1.1382	-0.06
WL-H	64.82	0.9465	0.9487	-0.17
WL-E	64.96	1.5788	1.5793	-0.38

4.5.3 Relation to GECMS

It might be apparent from the comparisons between the GEMMS and GECMS in this section that the two control strategies are similar. By looking closer at the objective function of each of these control strategies, their connection can be further understood.

The objective of the GEMMS (as given in Eq. 4.19) is to maximize the total powertrain efficiency for each possible power requirement. However, as the output power for a particular driving cycle is fixed, the problem can be reformulated as a minimization of the input power of the powertrain instead, giving:

$$P_{GEMMS}\begin{cases} \min\limits_{u} P_{in}(P_{PL}, SOC, u)\ \forall P_{PL} \in [0, P_{PLmax}], SOC \in [SOC_L, SOC_U] \\ 0 \leq u \leq \frac{P_{PSmax}}{P_{PL}} \\ SOC_L \leq SOC \leq SOC_U \end{cases} \tag{4.33}$$

where

$$P_{in} = \frac{P_{PS}}{\eta_{PS}} + \frac{P_{SS}}{\eta^*_{SS}} = \begin{cases} \frac{P_{PS}}{\eta_{PS}} + \frac{\eta_{SS}}{\eta_{re,c}} P_{SS} & P_{SS} < 0 \\ \frac{P_{PS}}{\eta_{PS}} + \frac{1}{\eta_{re,d}\eta_{SS}} P_{SS} & P_{SS} \geq 0 \end{cases}, \tag{4.34}$$

which corresponds to the denominator of the efficiency expression in Eq. 4.15. This can then be expressed in terms of fuel consumption using

$$P_{PS} = \dot{m}_f Q_{LHV} \eta_{PS} \tag{4.35}$$

which yields

$$\frac{P_{in}}{Q_{LHV}} = \begin{cases} \dot{m}_f + \frac{\eta_{SS}}{\eta_{re,c}} \frac{P_{SS}}{Q_{LHV}} & P_{SS} < 0 \\ \dot{m}_f + \frac{1}{\eta_{re,d}\eta_{SS}} \frac{P_{SS}}{Q_{LHV}} & P_{SS} \geq 0 \end{cases}. \tag{4.36}$$

This is equivalent to the GECMS cost function (in Eq. 3.14), with the equivalent factors as P_{SS} and SOC sensitive variables, rather than constants, as follows:

$$S_c(P_{PL}, u, SOC) = \frac{\eta_{SS}(P_{PL}, u, SOC)}{\eta_{re,c}} \tag{4.37}$$

$$S_d(P_{PL}, u, SOC) = \frac{1}{\eta_{re,d}\eta_{SS}(P_{PL}, u, SOC)} \tag{4.38}$$

The GEMMS can thus, in some sense, be considered equivalent to the GECMS, even though this was not the original intention.

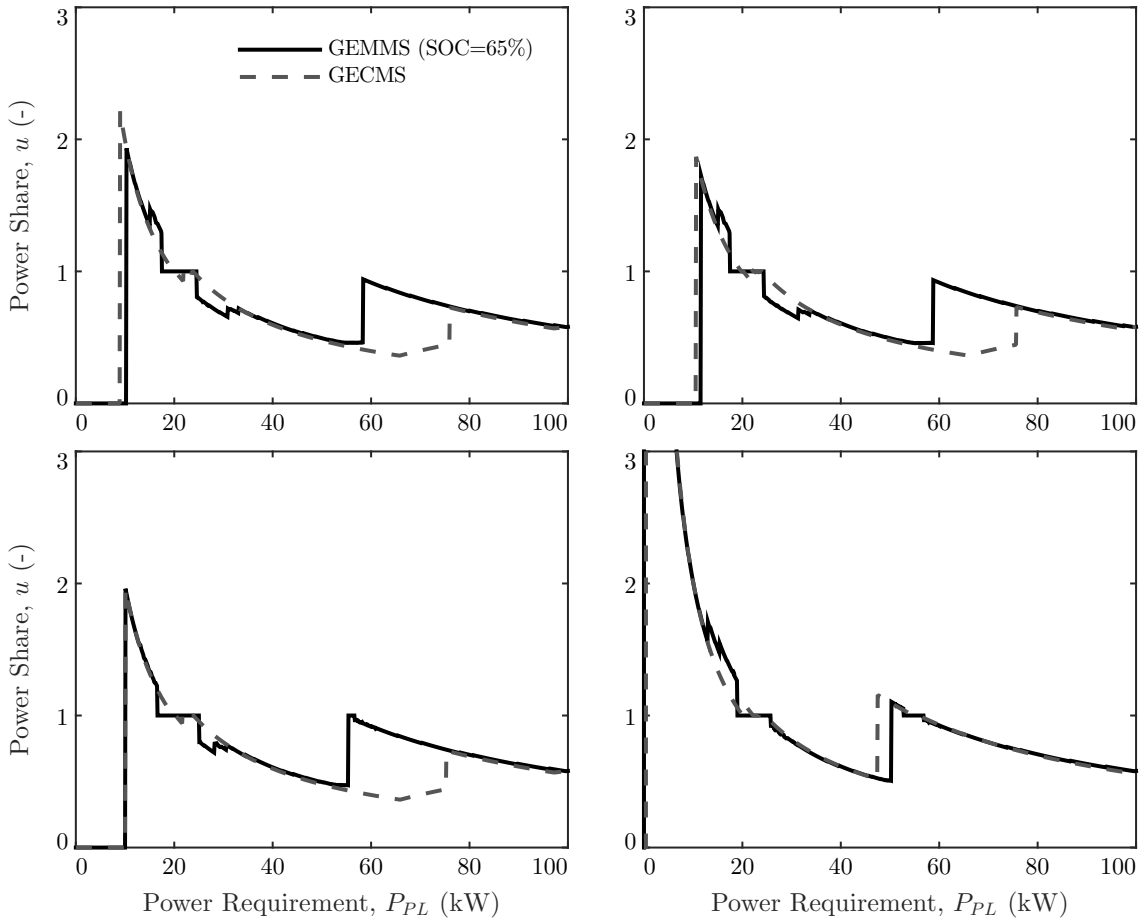

FIGURE 4.27: Comparison of optimal power share profiles for GECMS and GEMMS (for $SOC = 65\%$) for WL-L, WL-M, WL-H and WL-E (left to right, top to bottom).

However, note that the traditional GECMS, which pre-computes the control input, would find it difficult to solve above cost function as it would struggle to deal with the SOC dependence. However, any implementation that pre-computers tools (like the control maps of the GEMMS) rather than control inputs, would be able to solve the problem as the driving and state conditions are available at each time instance.

It is interesting to compare the GECMS control maps from Fig. 3.16 directly with GEMMS. This has been done in Fig. 4.27, where the GECMS is compared to the GEMMS with $SOC = 65\%$. It can be seen that the two control strategies produce similar control maps in general, but the GEMMS is less smooth. This can be attributed to the inclusion of the SS efficiency in the evaluation, due to the inefficient region of operation at very low SS power levels, resulting in sudden changes in power share. Also, at mid-high power requirements, the GEMMS is more inclined to use the PS, exhibiting another clear difference between the control strategies.

4.6 Efficiency Maximizing Map Strategy 2

This section presents the fourth and final EMMS. It aims to emulate the GEMMS operation, but with the constraint of being real-time realizable. It will therefore use the efficiency definition (and its tuned parameters) of GEMMS together with the CS mechanism of the EMMS1 to produce the EMMS2.

4.6.1 Real-time Adaption of GEMMS

The developed GEMMS is great at delivering excellent fuel economy, and is probably close to the global optimal solution as it outperformed the GECMS, but it is not realizable in real time and thus mainly serves as a great benchmark. However, it is possible to make use of the globally tuned selections of $\eta_{re,c}$ and $\eta_{re,d}$ of the GEMMS to produce a real-time version based on the EMMS process.

Similar to EMMS1, it will be necessary to make the the replenishing efficiencies SOC-dependent as $\eta_{re,c}(SOC)$ and $\eta_{re,d}(SOC)$ to allow the powertrain management to adjust depending on operating conditions. For the EMMS1 there was only one factor to be defined (in Eq. 4.29) while the EMMS2 will require the definition of two replenishing efficiencies as

$$\eta_{re,c} = \eta_{re,c,opt} + \frac{SOC - SOC_{mid}}{SOC_{range}} D_{csi,c} \tag{4.39}$$

$$\eta_{re,d} = \eta_{re,d,opt} + \frac{SOC - SOC_{mid}}{SOC_{range}} D_{csi,d} \tag{4.40}$$

where $\eta_{re,c,opt}$ and $\eta_{re,d,opt}$ are optimal base values for the charging and discharging replenishing efficiencies respectively, while $D_{csi,c}$ and $D_{csi,d}$ determine how intensely CS operation should be pursued for each respectively.

Having four different tuning parameters might make this control strategy appear excessively laborious. Investigating a range of 10 values for each parameter would require 10,000 simulations to determine the optimal combination, which would be prohibitively time-consuming. However, half the tuning is completed indirectly by producing the GEMMS where the optimal replenishing factors are given for each driving cycle in Table 4.4. Rather than selecting the values for a particular driving cycle, $\eta_{re,c,opt}$ and $\eta_{re,d,opt}$ were selected such that the deviation from optimality is

minimized. It was found that $\eta_{re,c,opt} = 31.9\%$ and $\eta_{re,d,opt} = 37.7\%$ delivered fuel economies that were within 0.2% of the optimal solution for the first three driving cycles and are therefore chosen. An alternative method to determine $\eta_{re,c,opt}$ and $\eta_{re,d,opt}$ would be to define them as the set of values that optimizes the total fuel economy of all four driving cycles together, or that minimizes the total distance to all preferred solutions. The EMMS2 therefore only has to tune $D_{csi,c}$ and $D_{csi,d}$.

Combinations of tuning parameters in the range of $D_{csi,c} \in [0, 1]\%$ and $D_{csi,d} \in [0, 5]\%$ in steps of 0.1% are used to produce control maps, based on the process described in Section 4.3.1. Each of these are then tested for the four driving cycles to tune the parameters such that the fuel economy is maximized. Results with normalized EFC and final SOC levels are presented in Fig. 4.28.

The most striking feature is the straight lines of the profiles of the fuel economy and SOC results for the first three driving cycles. This can attributed to the discretization process where the realized $\eta_{re,c,opt}$ and $\eta_{re,d,opt}$ values are implemented in 0.1% intervals. Thus, for example, there would be no change in $\eta_{re,d,opt}$ with $D_{csi,d} = 3\%$, for any changes in $SOC \in [64.5, 65.5)$ (as this would yield values of $\eta_{re,d,opt} \in [37.65, 37.75)\%$, which would be rounded to $\eta_{re,d,opt} = 37.7\%$). Thus, for the first three driving cycles which operate within a very narrow band of SOC, the effects of discretization are very prominent, unlike the WL-E where the operation over a wider range of SOC conceals this effect.

In general, the results have low sensitivity to changes in CSI factors $D_{csi,c}$ and $D_{csi,d}$. This is an expected outcome, if we consider the results of Fig. 4.23 for the GEMMS. The selected $\eta_{re,c,opt}$ and $\eta_{re,d,opt}$ values do not only yield close to optimal fuel economy results for the first three driving cycles, but also very close to $SOC_{final} = SOC_{initial}$. Consequently, these driving cycles are immediately operated in a close to optimal strategy such that the SOC remains steady. The $D_{csi,c}$ and $D_{csi,d}$ factors mainly influence the control behavior at low and high SOC values and are thus barely needed for the three mentioned driving cycles.

In contrast, the WL-E relies heavily on the CSI factors $D_{csi,c}$ and $D_{csi,d}$ to achieve its optimal fuel economy. In fact, it would prefer a very high $D_{csi,d}$ so that the $\eta_{re,d,opt} = 37.7\%$ can be adjusted to $\eta_{re,d} = 34.7\%$ (as given in Table 4.4) as quickly as possible. However, the $\eta_{re,c,opt} = 31.9\%$ needs to be adjusted to a lesser extent to reach its preferred $\eta_{re,c} = 31.0\%$, which is why a small $D_{csi,c}$ factor will suffice.

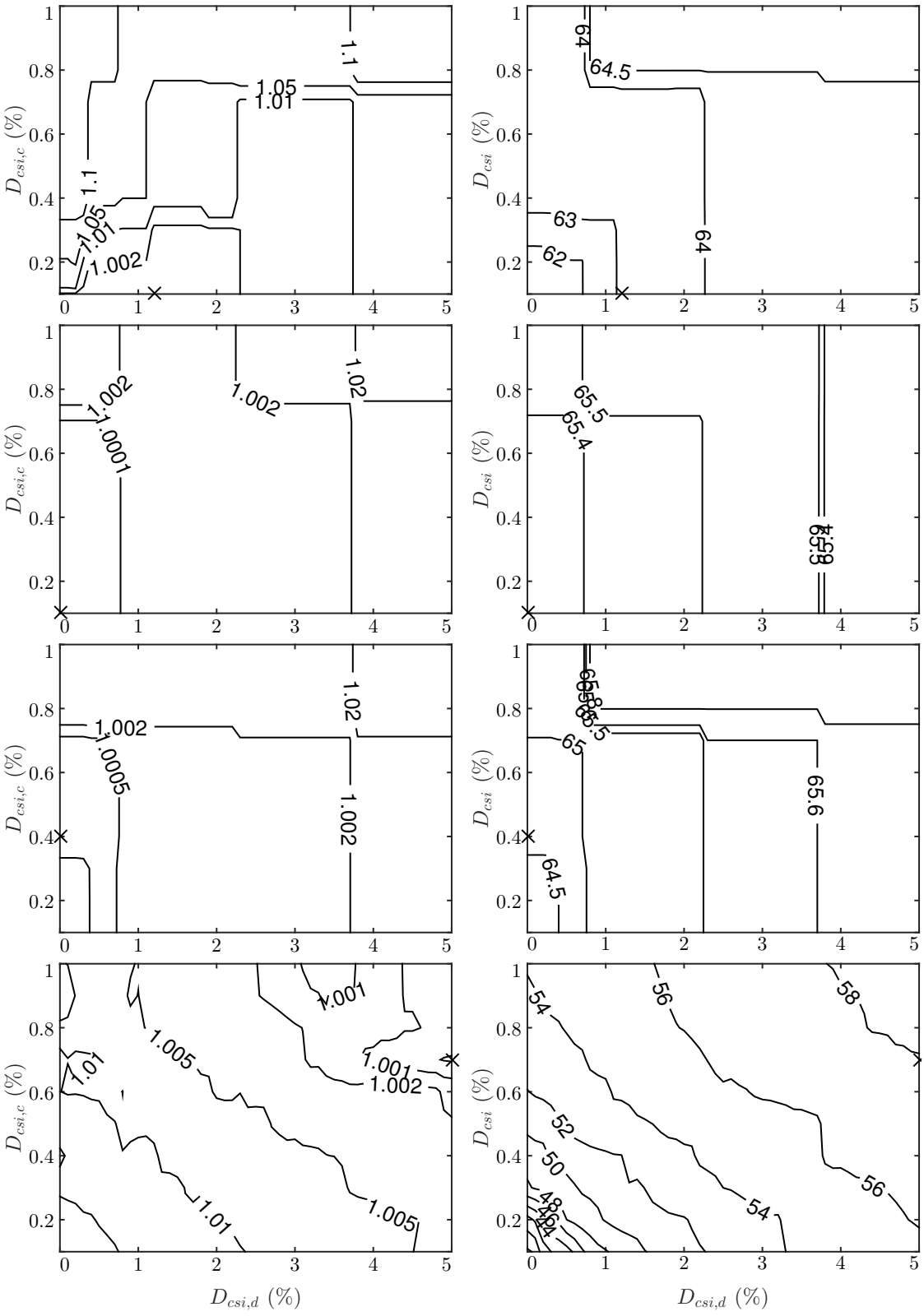

FIGURE 4.28: Normalized EFC M_{efc} (left) ($M_{efc} = 1$ is marked with a cross) and final SOC (right) for varying $\eta_{re,c}$ and $\eta_{re,d}$ when driving WL-L, WL-M, WL-H and WL-E (from top to bottom) with EMMS2.

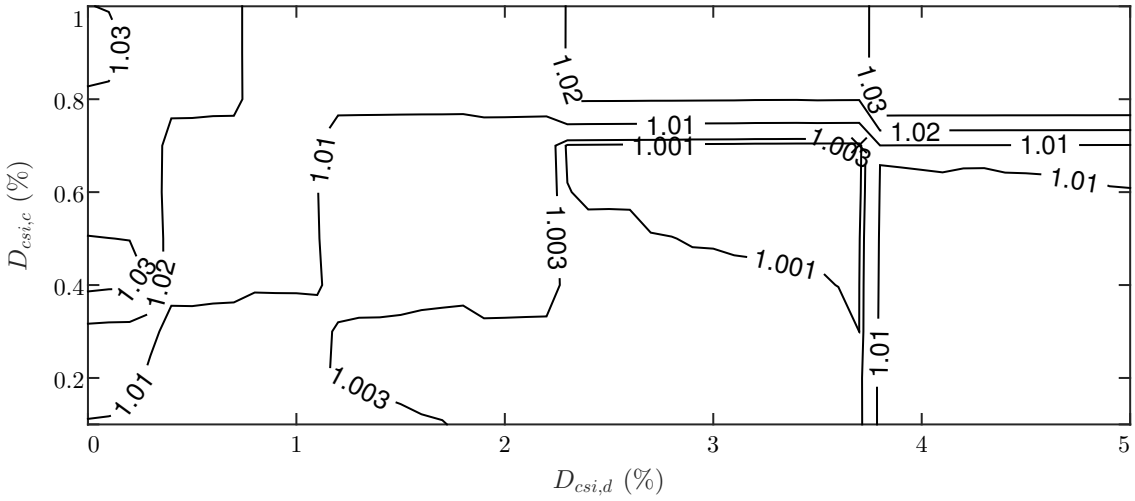

FIGURE 4.29: Normalized total EFC M_{tot} for varying $D_{csi,c}$ and $D_{csi,d}$ with EMMS2.

As can be seen, the ideal selection of the CSI factors for the WL-E would compromise the fuel economies of the remaining three driving cycles. Therefore, the total normalized EFC M_{tot} is found and is shown in Fig. 4.29. The optimal selection, such that the overall fuel economy of all driving cycles together is optimized, is delivered with the selection $D_{csi,c} = 0.7\%$ and $D_{csi,d} = 3.7\%$.

The resulting control map of optimal power share (and corresponding efficiency) for the case of $D_{csi,c} = 0.7\%$ and $D_{csi,d} = 3.7\%$ is shown in Fig. 4.30. It can be seen that the power share at medium SOC is very similar to the GEMMS for WL-L, WL-M and WL-H. Also, at lower SOC, the power share is similar to the GEMMS for WL-E. This control can therefore be expected to perform close to the optimal fuel economy solution. It also clearly resembles the EMMS1 with regards to its SOC dependence, although it is less aggressive in its CS pursuits. This is most evident at medium-high load levels, where charging mode would be enabled already at around $P_{PL} = 32$ kW for $SOC = 50\%$ with EMMS1 but at around $P_{PL} = 47$ kW with EMMS2. The gentler CS intensity means less diversion from the optimal power share.

4.6.2 Operation

The resulting power profiles from this selection are presented in Fig. 4.31 and Fig. 4.32 for the first and final iterations of the driving cycles respectively. For WL-L, the operation in the final iteration is very similar to the first iteration, suggesting

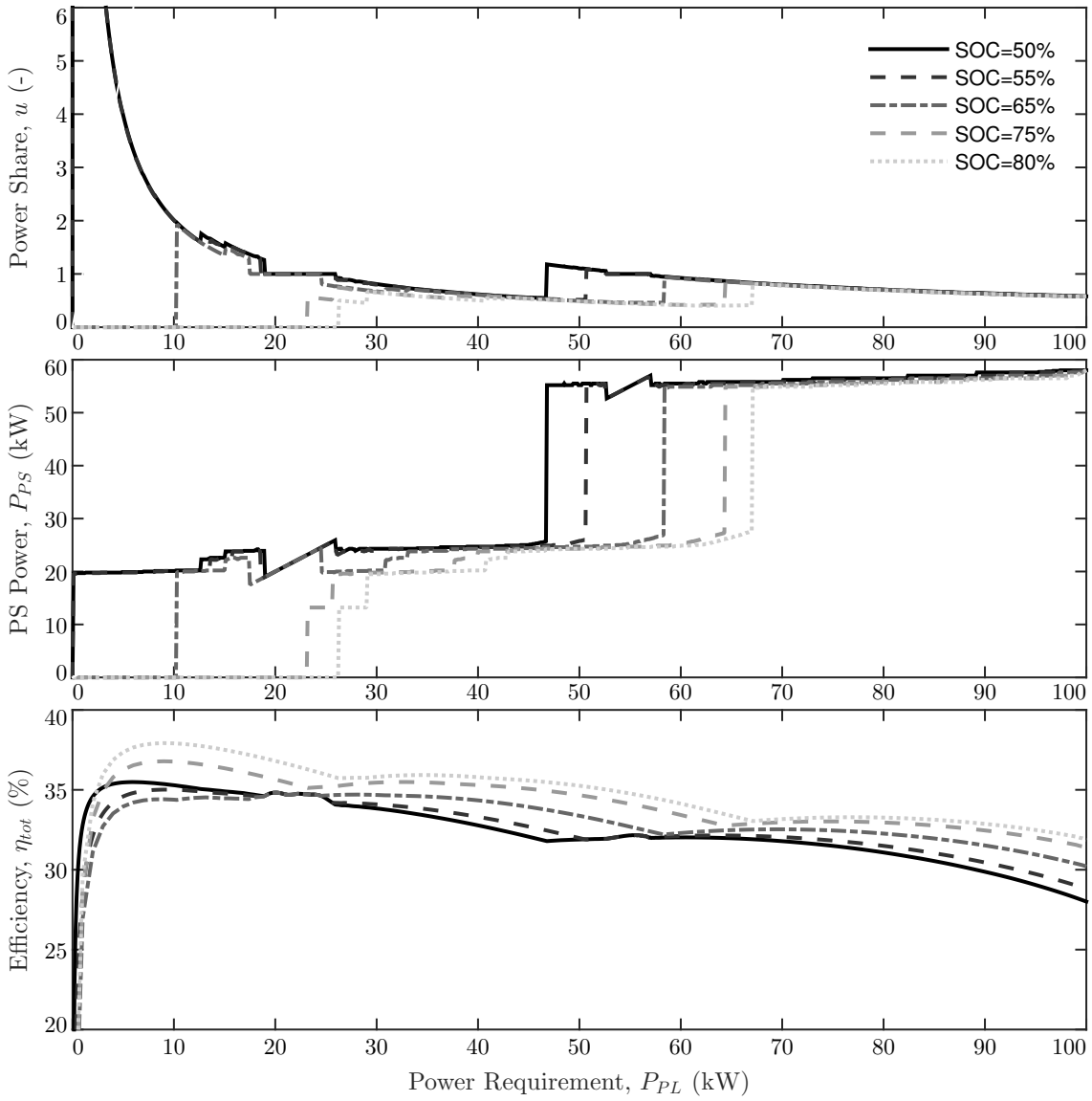

FIGURE 4.30: Optimal power share and PS power, and corresponding total efficiency for varying power requirements and SOC for $\eta_{re,c,opt} = 31.9\%$, $\eta_{re,d,opt} = 37.7\%$, $D_{csi,c} = 0.7\%$ and $D_{csi,d} = 3.7\%$ for EMMS2.

that the control finds its stride quickly and operates quite consistently. Furthermore, by comparing to the GEMMS results in Fig. 4.25 and Fig. 4.26, it can be seen that the operation is very similar. The EMMS2 is thus successful in adopting the approximate global optimal solution in real time and does it quickly and effectively.

For WL-M and WL-H, the EMMS2 delivers very similar operation for the first and final iterations of the driving cycles as well, as they both start and end around $SOC_{final} = SOC_{initial}$. When comparing with the GEMMS, the results are qutie similar, but there are some distinct differences as well. For both the WL-M and

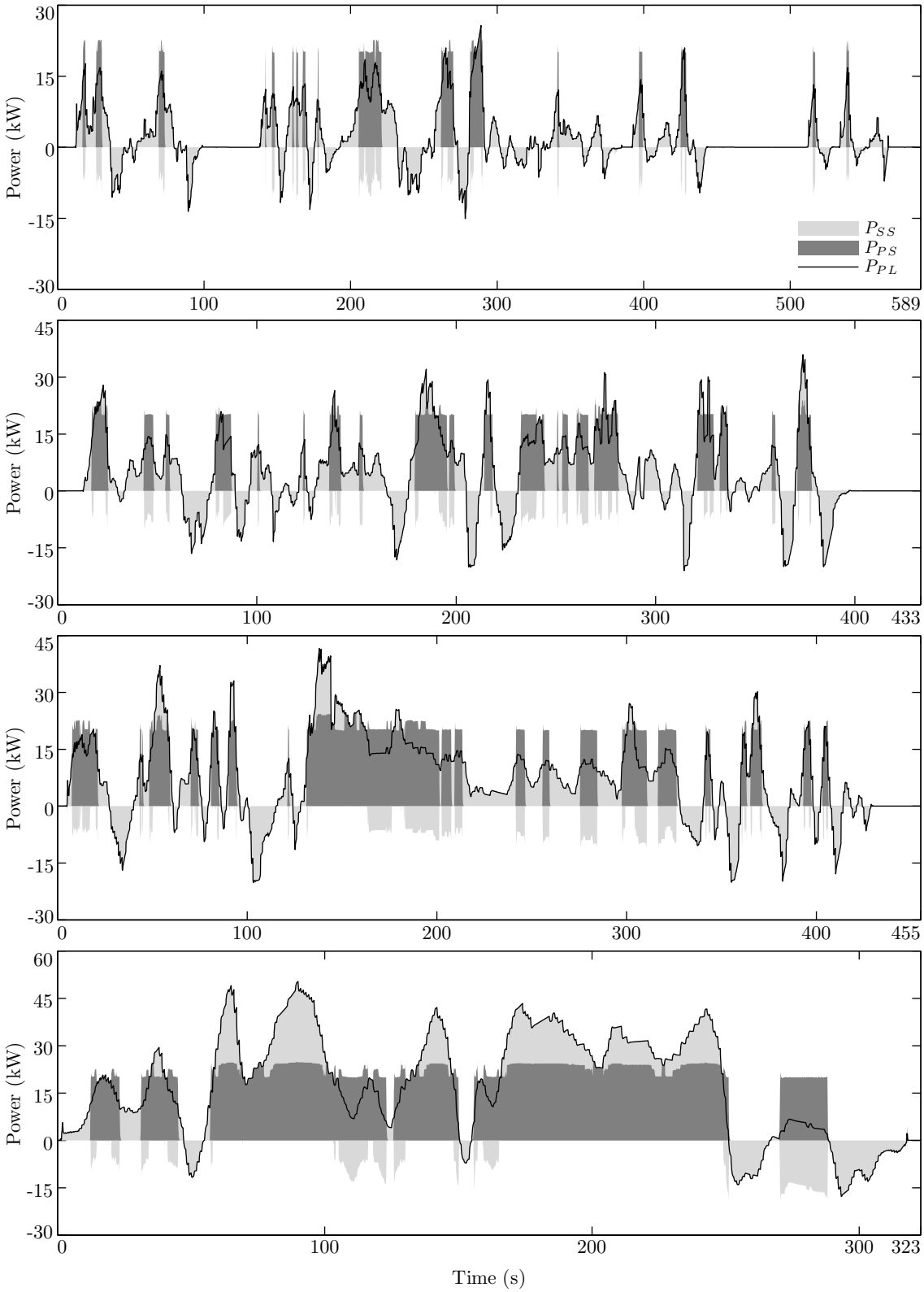

FIGURE 4.31: Power time histories for PS, SS and PL for the first iteration of driving WL-L, WL-M, WL-H and WL-E (top to bottom) with the EMMS2.

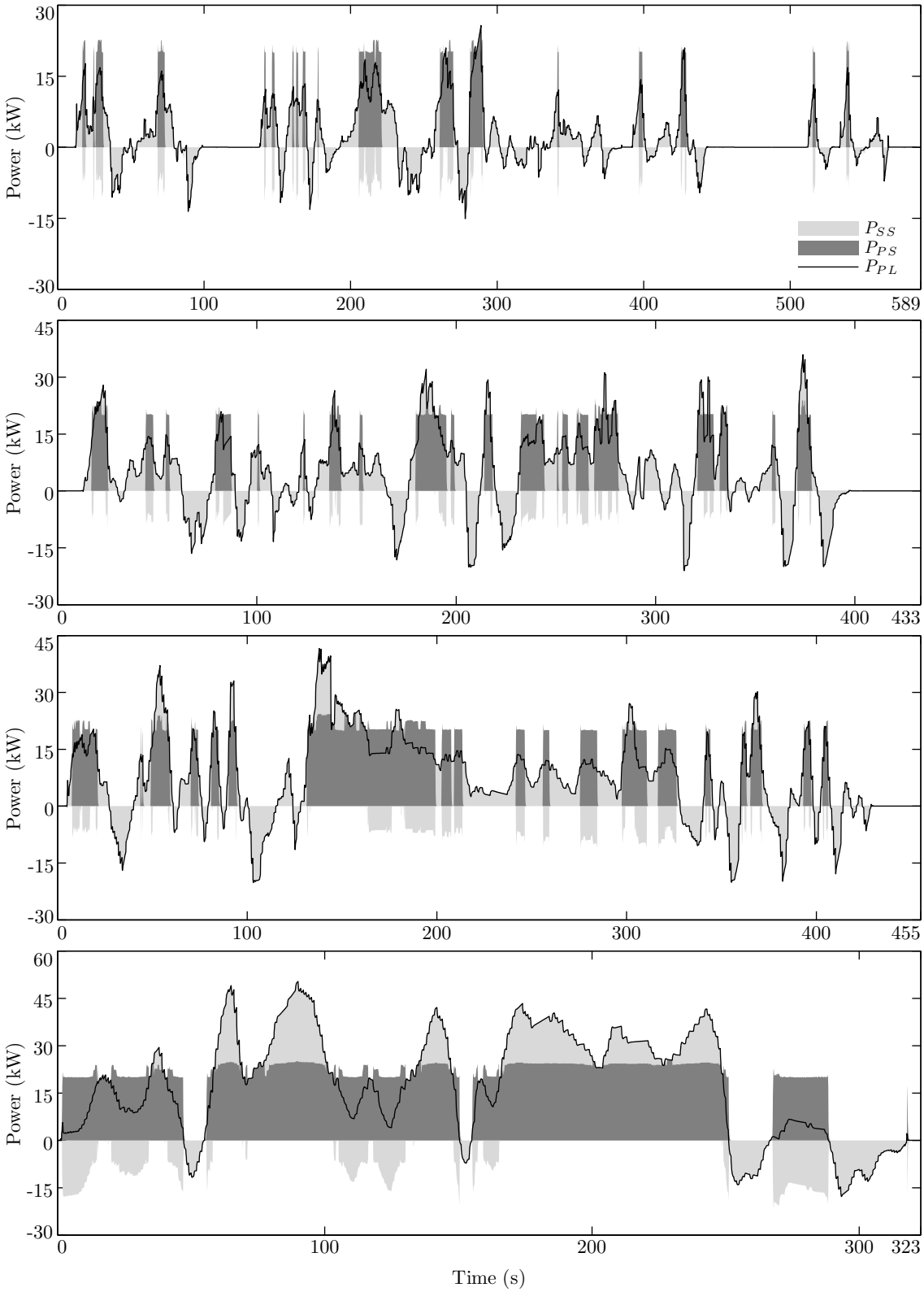

FIGURE 4.32: Power time histories for PS, SS and PL for the final iteration of driving WL-L, WL-M, WL-H and WL-E (top to bottom) with the EMMS2.

WL-H, the PS is active more often for the EMMS2 than for the GEMMS. However, when used, the PS is generally used in a similar manner as the GEMMS (although there is some additional charging mode operation with the PS in WL-H).

Lastly, for the WL-E, the EMMS2 operation is quite different for the first and final iterations of the driving cycle. The base operation (corresponding to $SOC = 65\%$) of the EMMS2 uses the SS a lot, before its SOC drop and it needs to react by adopting a more rural type of driving. As the SOC drops further, it adapts further and takes on a more highway type of operation. Thus, it can be seen that the final iteration uses the PS more frequently and often uses it to a larger extent. This type of operation is expected, as the principle of the EMMS2 is that it should seek its way to an optimal manner of operation. Comparing its operation to the GEMMS, it can be seen that their first iterations are quite different. However, their final iterations are very similar, with the EMMS2 applying just a bit more charging mode operation.

The ability of the EMMS2 to realize operation that is quite similar to the GEMMS suggests that it should achieve great fuel economy results. To look at this further, the fuel economy results for the four driving cycles are presented in Table 4.6. It can be seen that the EMMS2 performs very similarly to the GECMS, despite being a real-time control strategy. In fact, it outperforms the GECMS for two of the driving cycles. Comparing to the GEMMS instead, EMMS2 results for WL-L, WL-M and WL-H are only behind by 0.11%, 0.17% and 0.15% respectively. A better choice of $\eta_{re,c,opt}$ and $\eta_{re,c,opt}$ might have delivered even better results.

The WL-E results are slightly worse. Considering the fact that the EMMS2 needed to spend some time to find the desired control policy, and thus had to operate in an inefficient way for a while, the results are quite impressive. The final SOC is somewhat low, but this is by design, as the EMMS2 essentially needed to locate the control policy that matched the WL-E type of driving. Overall, for all driving cycles considered together, the EMMS2 results were 0.18% behind the GECMS.

Table 4.6: Fuel economy results for EMMS2

Driving Cycle	SOC_{final} (%)	m_f (kg)	m_{efc} (kg)	Δ_{GECMS} (%)
WL-L	64.24	0.6988	0.7071	-0.17
WL-M	65.53	1.1452	1.1402	+0.12
WL-H	65.60	0.9558	0.9501	-0.02
WL-E	57.16	1.4909	1.5983	+0.83

4.7 Comparison of Optimization-based Strategies

Having developed the four EMMS (EMMS0, EMMS1, EMMS2 and GEMMS) it is of interest to compare them internally, as well as with the GECMS from Section 3.4. This section will compare their operation by studying their SOC profiles as well as compare their fuel economy results.

The SOC profiles for each of the five optimization-based strategies are presented in Fig. 4.33 for the four driving cycles. It can be seen that a majority of the control strategies maintain their SOC quite steady around $SOC_{initial}$ across the driving cycles. This could have been expected based on the SOC_{final} values that have been presented for each SCS earlier in this chapter. However the EMMS0 does stand out from this pattern, as it can be seen to experience a fall in SOC before steadying, resulting in final values lower than 60%. Interestingly enough, it is joined by the GEMMS for the WL-L and WL-M, where the SOC drops and steadies. As mentioned earlier, this is not typical for a global optimization strategy, but it did yield the best fuel economy among the tested parameters.

In addition, it is worth noting that the operation of all five strategies is generally smooth, as opposed to the oscillatory operation (where SOC oscillates between SOC_L and SOC_U) that is associated with conventional strategies like TCS and PFCS. This is a result of each of these strategies operating with a single state. There is however an element of repetition in the profiles, which is a result of the repeated iterations for each driving cycle.

This general pattern of dropping and steadying applies to all the presented control strategies here, apart from GECMS. All the EMMS strategies have a charge sustaining element such that they will tend to flatten their SOC profile as they deviate from $SOC_{initial}$. This is not true for the GECMS though, for which the error will accumulate and get progressively worse. This is not very visible in the present chart as the SOC deviation is very small for each driving cycle. Nevertheless it can be seen for WL-H and WL-E in particular that the GECMS keeps dropping in SOC relative to other strategies with a steady SOC.

The GECMS and GEMMS are the only strategies that remain close to $SOC_{initial}$ for the WL-E. This is easily understood as an effect of their global tuning. The EMMS0 drops and steadies, due to the charge sustaining factor K_{CSI}, but would

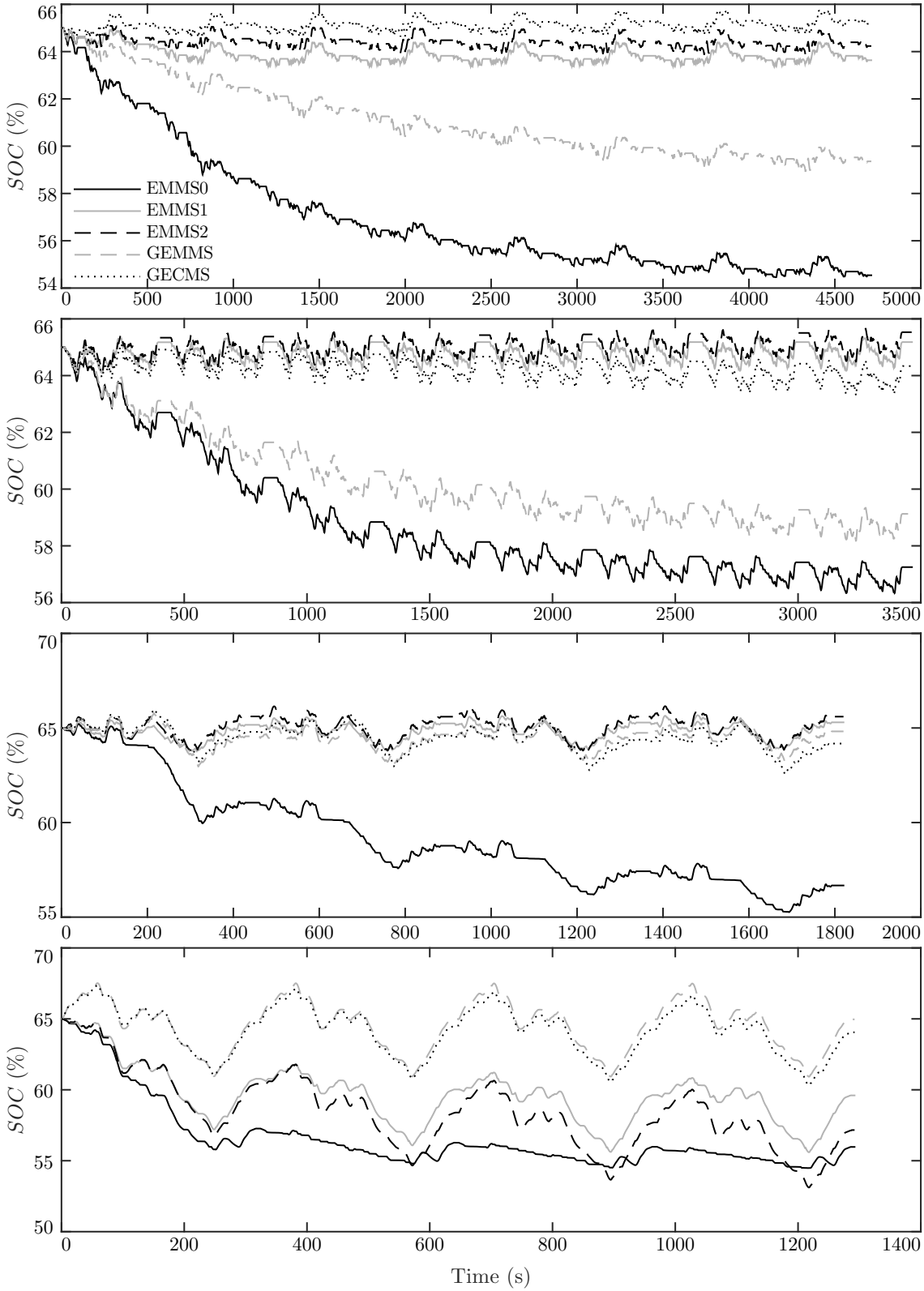

FIGURE 4.33: SOC profiles for EMMS0, EMMS1, EMMS2, GEMMS and GECMS when driving WL-L, WL-M, WL-H and WL-E.

have preferred to operate close to $SOC \approx SOC_{initial}$. However, the other real-time control strategies, EMMS1 and EMMS2, have both mechanisms that encourage the SOC to drop such that it can reach control rules that are more suited for the WL-E type of driving. The drop in SOC for these SCSs is thus not a failure, but rather a tool that is actively employed to seek the optimal type of operation and to deliver great fuel economy.

It is also worth noting that all of these control strategies have either kept a flat SOC profile, or have dropped. Considering the fact that the SOC band between $SOC_L = 50\%$ and $SOC_U = 80\%$ is at the disposal of the control strategies, none of them make use of the upper half of this band. This could possibly have been due to badly tuned equivalence factors $S_{d,efc}$ and $S_{c,efc}$, such that any stored charged by the end of a driving cycle is not proportionally rewarded, compared to the penalty of having a net discharge. However, apart from the fact that the process for obtaining these equivalence factors was rigorous, it can also be observed that the fuel economy results for the tuning process of most control strategies have been quite symmetrical about the $SOC_{final} = SOC_{initial}$ lines (e.g. the GEMMS tuning results in Fig. 4.23).

A more plausible explanation might be that the repetitive and short nature of the driving cycles biases the results to be more short-term oriented. Although it would in reality be ideal for a medium-speed rural driving cycle to charge the SS while driving, such that more SS energy is available at a later date for either a lot of low-speed urban driving or high-speed highway driving, the simulations results do not consider this. Instead, the optimization process is about a single cycle being repeated. The use of the equivalence factors is supposed to address this, but it considers the average case for each driving cycle separately, so the benefits of having a well-charged battery for WL-E is not considered in the EFC calculation for the WL-L.

An additional consideration is that the general approach of HEV operation is to use the SS as much as it will allow sustainably (this is even more true for PHEVs). Most control strategies are greedy in the sense that "sustainably" is seen to mean "without depleting or damaging the battery". Such an approach is inherently biased towards either discharging or maintaining the battery SOC.

Finally, the fuel economy performance relative to the GECMS (Δ_{GECMS}) for all these strategies is presented in Fig. 4.34. It can clearly be seen that the EMMS0

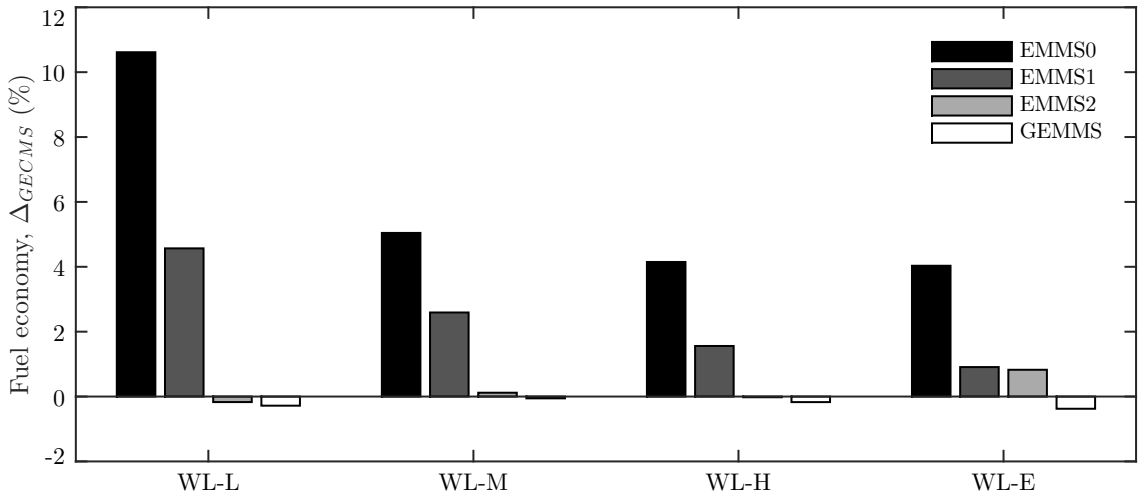

FIGURE 4.34: Comparison of fuel economy for EMMS0, EMMS1, EMMS2 and GEMMS against GECMS when driving WL-L, WL-M, WL-H and WL-E.

is the least impressive among these. Its results are consistently behind the other strategies. The same can not be said for the EMMS1 as it becomes progressively better for driving cycles with higher loads. In fact it is comparable to the EMMS2 for WL-E. The EMMS2 is however the most impressive, as it is able to outperform the GECMS on WL-L and WL-H (and is not far behind on the other strategies), despite being a real-time control strategy.

The performance should however be considered in relation to the complexity of the strategy. The GEMMS is somewhat more difficult to implement than the GECMS (as it requires the powertrain analysis) but achieves a marginal improvement. However, for any solution that claims to approximate the global optimal solution, improvements in the order of 0.38% (as for WL-E) are quite significant. Between the real-time strategies the performance is, as expected, improved gradually from EMMS0 to EMMS1 to EMMS2. Considering the minor change in complexity from EMMS0 to EMMS1, and the major difference in fuel economy performance, the EMMS0 is not a worthwhile alternative (at least for the vehicle design for the model in this work). However, in contrast, there is a significant increase in complexity from EMMS1 to EMMS2, with more modest differences in fuel economy (in particular for driving cycles with higher load). Therefore, the EMMS1 serves a function as an easier implementation with decent performance.

4.8 Summary

This chapter has presented a family of novel control strategies based on the objective of maximizing the powertrain efficiency, which was determined by studying each component comprising the powertrain sources: ICE, PMSG and rectifier for the PS, and battery and DC-DC converter for the SS. In addition, a correction factor v was considered to account for the losses involved in replenishing the battery after it is discharged (or the gains involved in avoiding future replenishing after being charged). The four control strategies EMMS0, EMMS1, GEMMS and EMMS2 used this correction factor differently and a summary is provided in Table 4.7.

Table 4.7: Choice of correction factor v

Correction factor v	EMMS0	EMMS1	GEMMS	EMMS2
For $P_{SS} < 0$	1	$\eta_{re}(SOC)$	$\eta_{re,c}$	$\eta_{re,c}(SOC)$
For $P_{SS} \geq 0$	η_{re}	$\eta_{re}(SOC)$	$\eta_{re,d}$	$\eta_{re,d}(SOC)$

Each of the control strategies was implemented through a control map, which provides the optimal power share u_{opt} as a function of the operating conditions (SOC and P_{PL}). This method is not only simple and computationally light, but it also easily allows effective use of state dynamics (such as SOC) that are difficult to assess offline for global control strategies. The fuel economy became progressively better from the EMMS0, EMMS1 to the EMMS2 as the correction factor became more nuanced and effective. The EMMS0 adopted a CS function $k_{cs}(SOC)$ to penalize and reward the use of the SS, while the EMMS1 (and EMMS2) made the replenishing efficiency η_{re} (and $\eta_{re,c}$ and $\eta_{re,d}$) a function of SOC to achieve CS operation. The GEMMS achieved the same inherently through global tuning, which required no modification to its optimization procedure. Interestingly, the GEMMS was found to be equivalent to a SOC dependent GECMS with consideration for SS efficiency.

In terms of fuel economy, the GEMMS was found to outperform the GECMS consistently (by 0.2% overall), while the real-time EMMS2 was better than the GECMS for half the driving cycles (but was 0.18% worse overall). The results demonstrate how a more detailed understanding of the powertrain can contribute toward better performance by the control strategies. Nevertheless, the GECMS has compared quite favorably despite its simplicity (or maybe because of it).

Chapter 5

Heuristic Strategies

This chapter will propose two novel heuristic strategies: the exclusive operation strategy (XOS) and the optimal primary source strategy (OPSS). Each of these makes use of insights from previous chapters to deliver good performance with very simple rule-based control. In some sense, these two strategies can be considered to be improved versions of the TCS and PFCS from Chapter 3. The XOS presented in this thesis has been partly modified since being published in [15], but has the same essence (differences will be discussed within the chapter).

Although it is increasingly easier to make use of optimization-based strategies in real HEVs, it is still useful to produce effective rule-based strategies. Not only are these appropriate for prototypes and preliminary studies of powertrains (evaluating architecture choice or component sizing), but they can also be the preferred choice when simple and intuitive operation is a higher priority than an optimized fuel economy. In fact, most commercial HEVs so far have opted to use heuristic energy management strategies [55, 63].

The chapter will first explore the design principles that have been derived through insights from previous chapters and discuss their applicability in designing heuristic strategies for series HEVs. Thereafter, the XOS will be introduced in the context of discussed design principles. This will be followed by the presentation of the OPSS. For both the proposed control strategies the implementation, the tuning process, representative power profiles of operation, and the fuel economy are presented and discussed. Finally, the performance of the XOS and OPSS will be compared to the conventional heuristic strategies.

5.1 Design Principles

The essence of heuristic strategies is to apply design rules based on knowledge of and experience with the system to be controlled. For the series HEV that is the subject of this work, several insights have been gained over the past two chapters that will here be condensed into a handful of such rules.

5.1.1 Fuel Economy Optimizing Mechanisms

There are three distinct approaches to determine the power share within the powertrain to achieve fuel efficient driving: load leveling, load following and load blending.

Load leveling refers to the strategy of operating the PS steadily and using the SS to "level" the load as a buffer, as

$$P_{PS}(t) = P_{PS,cop} \tag{5.1}$$

$$P_{SS}(t) = P_{PL}(t) - P_{PS,cop} \tag{5.2}$$

where $P_{PS,cop}$ is a constant operating point of the PS. This is most clearly applied in the TCS where the PS is operated at its optimal point of operation ($P_{PS,cop} = P_{PSopt}$) and the SS takes care of the difference between the PS and the propulsion load. This approach typically optimizes the PS efficiency but suffers higher SS losses. The general shape of the control input, both in terms of power share and PS power, is presented in Fig. 5.1 (with $P_{PS,cop} = 20$ kW).

This technique is also partly used by the GEMMS and GECMS, where it can partly be seen in the smooth curves (corresponding to constant P_{PS} levels) of the power share charts in 4.27. However, it is more clearly visible in the operational power profiles where the PS can be seen to operate quite steadily around 20 kW whenever it is used in Fig. 3.18 and 4.25.

Load following on the other hand takes the opposite approach. It uses the PS to "follow" the load power while the SS is ideally used at zero power levels, as

$$P_{PS}(t) = P_{PL}(t), \tag{5.3}$$

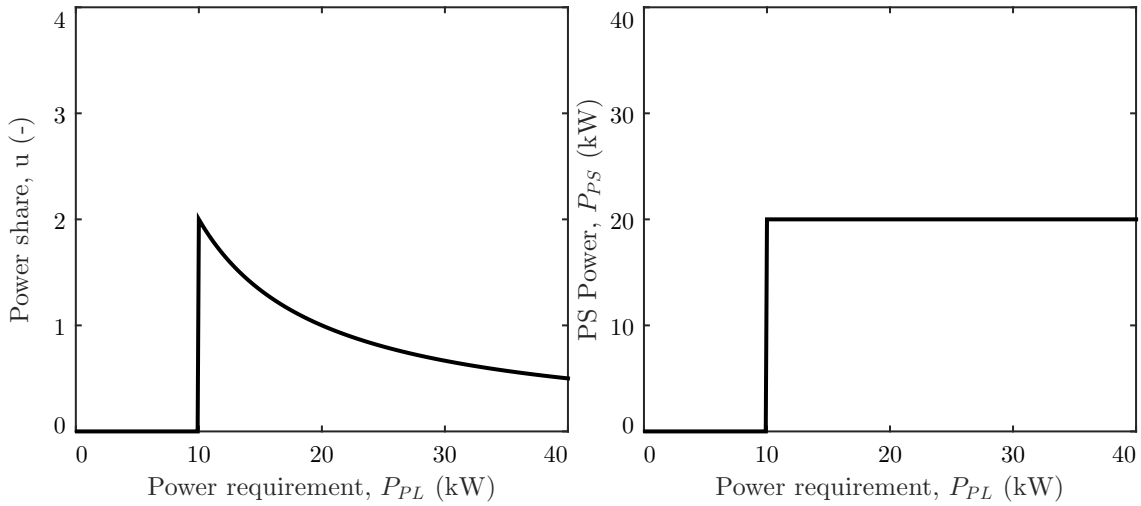

FIGURE 5.1: Power share and PS power for varying load for a load leveling strategy.

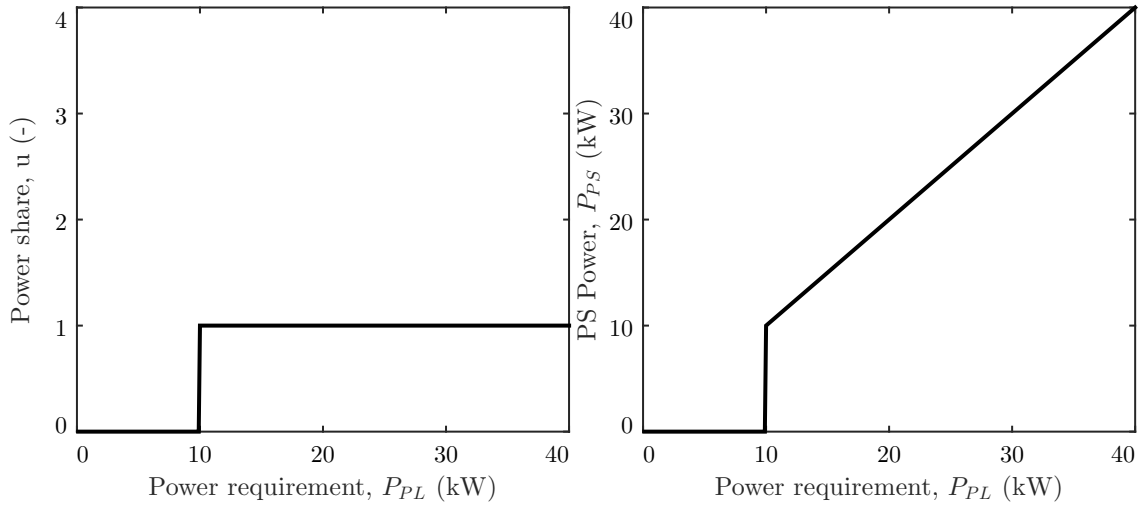

FIGURE 5.2: Power share and PS power for varying load for a load following strategy.

$$P_{SS}(t) = 0. \tag{5.4}$$

This is the core approach behind the PFCS, where the above expression holds exactly true for $SOC = SOC_{initial}$. However, to ensure charge sustaining operation, the PFCS deviates from strict load following operation and instead allows the SS to charge or discharge in proportion to its SOC deviation. Having the SS operate at low power levels ensures higher SS efficiencies but this leaves the PS efficiency to be determined by the varying load. The resulting control input, both in terms of power share and PS power, is illustrated in Fig. 5.2.

This type of operation is also apparent in non-CS EMMS0 where the strategy often uses $u = 1$ in Fig. 4.4. To a lesser extent the same technique can also be seen within

non-CS EMMS1 in Fig. 4.13 (during $P_{PL} \in [17, 28]$ kW and $P_{PL} \in [50, 57]$ kW.

Lastly, the load blending mode of operation concerns itself with optimizing both the power source branches of the powertrain. The operation is thus not as clearly defined as the load leveling and load following modes, but instead encompasses all techniques that blend the use of the PS and SS such that the overall performance of the powertrain is benefited. This would clearly include the EMMS strategies of the previous chapter that display a varied choice of operation with consideration of both the PS and SS. For example, the EMMS2 in Fig. 4.30 has elements that would fit either of the load leveling and load following modes, as well as some power share choices that would fit neither. This approach is typically required to achieve global optimal solutions, but it does not lend itself to be expressed as simple rules.

As shown, each of the fuel economy optimizing mechanisms discussed has been employed in various control strategies within this work. However, as was just mentioned, the load blending operation does not easily translate into a rule-based control strategy. Therefore, this chapter will aim to deliver one strategy based on load following and another on load leveling.

5.1.2 Charge Sustaining Mechanisms

From the presented work, four approaches have emerged to make control strategies charge sustaining: state changing, threshold changing, power changing and emergency handling.

The state changing approach does not have inherently CS rules, but rather switches between two (or more) sets of rules depending on the SOC. These changes in state are often triggered as the SOC reaches its lower (SOC_L) or upper (SOC_U) limit, with a hysteresis area in between, as

$$S(t) = \begin{cases} 0 & SOC(t) \geq SOC_U \\ 1 & SOC(t) \leq SOC_L \\ S(t^-) & SOC_L < SOC(t) < SOC_U \end{cases}, \tag{5.5}$$

where $S(t^-)$ is the state in the previous time instance. This approach is followed precisely with the TCS (as defined in Eq. 3.7) and is implemented with some additional conditions with the PFCS (as defined in Eq. 3.8). These changing states

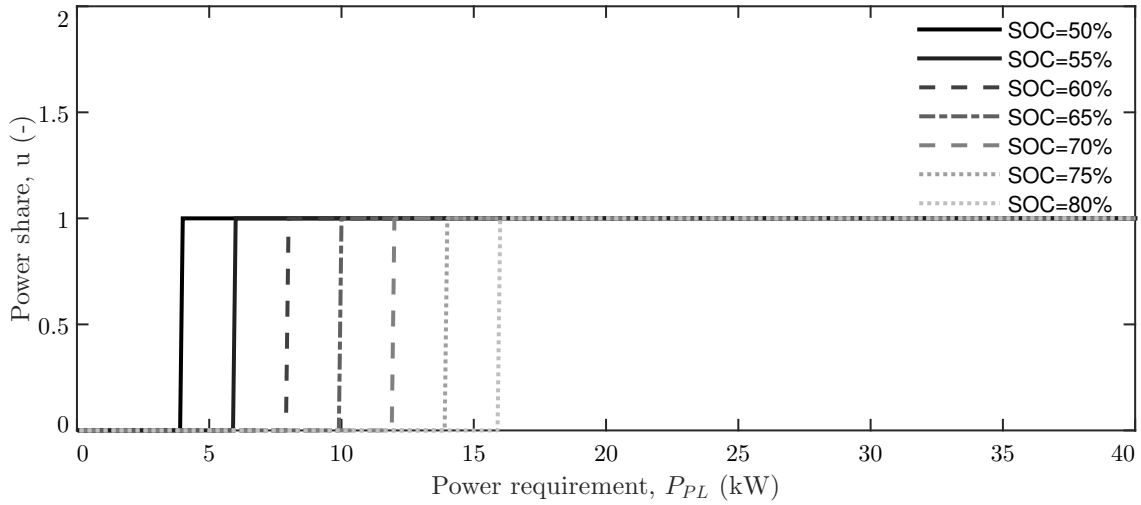

FIGURE 5.3: Optimal power share for varying power requirements and SOC when employing the threshold changing mechanism to encourage charge sustaining operation.

are often relatively easy to define and none of them need to be CS in themselves. In fact, the only necessary constraint is that at least one of the states is charge depleting and at least one is charge increasing. Furthermore, these changes in states can easily be connected to whether the PS is active or not (as is done for both TCS and PFCS), such that the engine is only turned on or off when there is a change in state. This reduces the number of start-stop events of the engine.

Threshold changing refers to the definition of a SOC dependent threshold to govern whether the PS is active or not. Such a lower limit of the PS can be defined as

$$P_{PSmin}(SOC) = P_{th} + P_{csi}\left(\frac{SOC - SOC_{mid}}{SOC_{range}}\right) \tag{5.6}$$

where P_{th} is the base power threshold and P_{csi} (which does not necessarily need to be a constant) regulates the CSI of the strategy by defining the range as $P_{PSmin}(SOC) \in [P_{th} - P_{csi}, P_{th} + P_{csi}]$. This is shown in Fig. 5.3 with an illustrative example. It can be seen that the threshold operates such that the PS is activated at lower load levels (and thus more frequently) if the SOC is low and is activated at higher load levels if the SOC is high. This encourages the use of the SS when the SOC is high, and discourages it when the SOC is low, thus tending towards making the operation CS. It is however essential that the threshold and its range is defined appropriately to ensure CS operation in all kinds of realistic operation.

The use of threshold changing operation is very clearly visible in EMMS0 (Fig. 4.8),

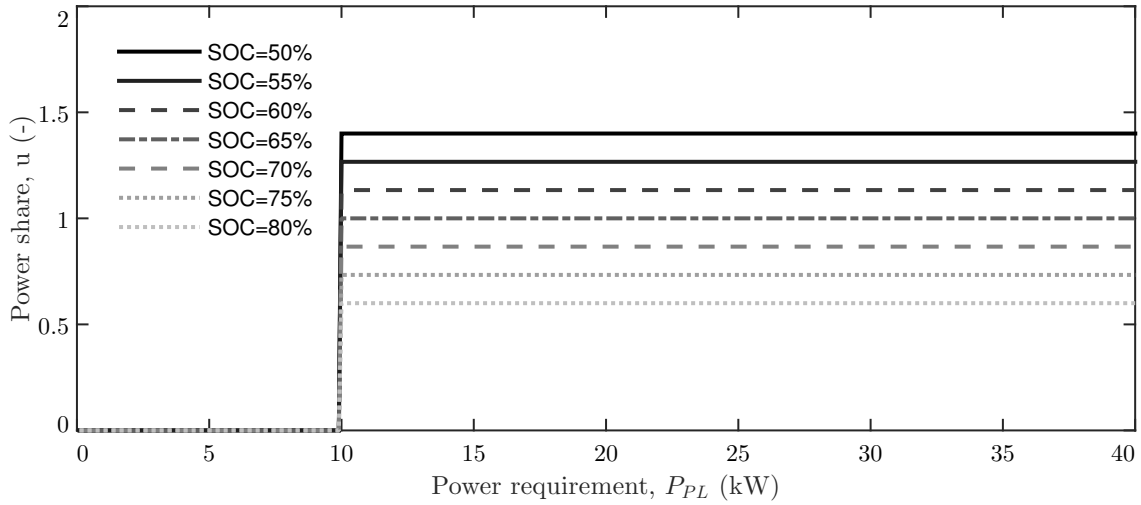

FIGURE 5.4: Optimal power share for varying power requirement and SOC when employing the power changing mechanism to encourage charge sustaining operation.

EMMS1 (Fig. 4.17) and EMMS2 (Fig. 4.30), with a wide range for the threshold. In all of these cases the range of the threshold stretches all the way down to $P_{PL} = 0$ kW which guarantees that the SOC will not drop below SOC_L. This mechanism is present to a limited extent in the GEMMS as well due to the SOC sensitive efficiency expression (as shown in Fig. 4.24) but the range is very limited.

The power changing approach modifies the PS operating point to be SOC dependent. This can be applied to a load leveling strategy as

$$P_{PS,op}(SOC) = P_{cop} - P_{csi}\left(\frac{SOC - SOC_{mid}}{SOC_{range}}\right) \tag{5.7}$$

where $P_{PS,op}$ is the operating point of the PS and is defined in the range of $P_{PS,op} \in [P_{cop} - P_{csi}, P_{cop} + P_{csi}]$. Alternatively, the power changing mechanism can be applied to a load following strategy as

$$P_{PS,op}(P_{PL}, SOC) = P_{PL} - P_{csi}\left(\frac{SOC - SOC_{mid}}{SOC_{range}}\right). \tag{5.8}$$

The power changing mechanism is shown visually in Fig. 5.4 for the load following case (where $u = 1$ corresponds to exact power following operation).

The PFCS uses the power changing method (with the load following alternative) to bias operation in favor of maintaining the SOC close to SOC_{mid}, as expressed in Eq. 3.10. The EMMS on the other hand can be considered to employ a blended version

of the power changing mechanism. For example, in Fig. 4.30 for EMMS2, it can be seen that a higher power share is selected in general for lower SOC cases, and lower power share for higher SOC. In fact, typically $u > 1$ (charging mode) is used for very low SOC values, thus encouraging charge sustaining operation.

However, this particular CS mechanism has a few vulnerabilities. If the power changing mechanism is applied all the way down to $P_{PL} = 0$ kW, the PS will have to be operated at very low power levels which would be highly inefficient. The solution could be to use a threshold above which the power changing (together with load following or load leveling) is active. However, even in this case, if the powertrain is operated at a low load level where the PS is not active, the fact that the PS power levels at higher load levels are being adjusted by the power changing mechanism as the SOC decreases will have no CS effect. Thus, this CS mechanism is generally insufficient by itself.

Finally, as a last resort, it is useful to include emergency handling. These are rules that are activated only if the SOC bounds are violated. These can in some sense be considered a subset of the state changes discussed earlier, with the difference that the emergency handling rules are only active while the SOC bounds are violated, and normal mode is restored as soon as $SOC_L < SOC < SOC_U$. However, note that the TCS does not make use of emergency handling rules, as Eq. 3.7 does not provide separate instructions for how to operate if the SOC constraints are continuously transgressed. This is later demonstrated in Fig. 5.20, where the SOC profile for the TCS when driving the WL-E can be seen to fall to $SOC = 45\%$ before recovering. In contrast, the PFCS clearly has defined emergency handling rules in Eq. 3.9 in case the SOC limits are exceeded. The emergency handling rules need to be CS at the very least, or possibly charge increasing for $SOC < SOC_L$ and charge depleting for $SOC > SOC_U$. It is however important to emphasize that the emergency handling rules are typically not very fuel efficient. Thus, if the main CS mechanism employed is badly designed, the benefits of the main fuel economy optimization mechanism will be lost.

From these charge sustaining techniques, the threshold changing mechanism is considered to be the most suitable one for a modern series HEV. The state changing approach has many attractive features (e.g. its simplicity and lack of engine start-stop events), but these are increasingly less relevant today. As modern HEVs use very efficient start-stop systems (SSSs), the cost of turning the engine on is very low,

compared with a decade ago. The objective of minimizing the number of start-stop events is thus much less of a priority (although it still matters to some extent for the purposes of drivability). Furthermore, computational power is easily available in any modern HEV and the automotive companies have the resources to develop and test more advanced strategies (although robustness remains imperative). The threshold changing approach on the other hand is the primary benefactor of the more efficient SSSs, and can be expected to sustain the charge without compromising the fuel economy too much. However, it will be sensible to include some emergency handling rules nevertheless to handle exceptional driving circumstances.

Thus, the rule-based strategies presented in this chapter will mainly make use of a threshold changing approach together with some emergency handling rules.

5.1.3 Implementation Mechanisms

Two different real-time implementation mechanisms have been used in the control strategies presented so far: state machines and control maps. The GECMS can also use precomputed control inputs to implement its strategy but this option is only available for global strategies with prior knowledge of the driving route and is thus not an option for the rule based strategies being considered in this chapter. However, an additional approach that has not been considered so far is the algebraic implementation with logic gates.

The state machines are particularly suitable for state changing strategies, as they naturally involve multiple states with varying rules. This would include the TCS and PFCS. In these cases a state-machine implementation is almost unavoidable. However, for other rule based strategies with a single set of rules, the state machine can be used by treating various operating conditions (such as low and high load powers, or low and high SOC) as different states. However, this often requires certain rules to be repeated in multiple states, making the expression of some strategies less concise. Also, it often comes with a higher computational load (which is quite negligible anyway).

The control maps on the other hand are look-up tables that are essentially flexible enough to express any type of rules or optimizations. These were used for all the EMMS and have also been implemented for the GECMS. They are also easy to

design and have the benefit of being easily visualized. Although they are particularly suitable for single-state strategies, it is possible to implement multiple-states strategies like the TCS and PFCS using multiple control maps. However, the control maps don't shine when used to express simple rules. The precision of the control is only as good as its sampling interval. Thus, a simple logical or algebraic relation (or a state machine) could follow the intended strategy perfectly while the control map has to compromise based on the imperfect precision arising from the finite size of the map.

The third approach, which hasn't been presented so far is the algebraic implementation with logic gates. Most rule-based controllers rely on simple arithmetical and logical relations between inputs and outputs. These relations can be directly expressed by equations and logic blocks in Simulink and most other design environments. Not only is this approach computationally efficient and easy to design, it also delivers perfect precision when interpreting the intended strategy. For these reasons, the algebraic implementation will be used for the rule-based strategies presented in this chapter.

5.2 Exclusive Operation Strategy

The exclusive operation strategy (XOS) is based on the load following technique and uses the threshold changing mechanism to ensure CS operation. This design uses insights gained from the PFCS and EMMS0 in particular, but also attempts to emulate parts of the operation of the global strategies GECMS and GEMMS.

5.2.1 Design

Investigation of the power-split between the PS and SS in a powertrain shows that the optimal selection is often to operate with the SS at lower powers and the PS at higher load requirements. This agrees roughly with previously developed control systems [14] as well as the GECMS and GEMMS presented here. Thus, the principle of XOS is quite simple: operate with only SS at low load requirements (or if $SOC > SOC_U$), and operate with only PS at medium loads. The two energy sources are only used together if the load power exceeds the maximum rating of the source in operation (or $SOC < SOC_L$, in which the SS is charged). These rules are shown visually in Fig. 5.5.

The XOS is inspired by the PFCS as can be seen by its "power following" behavior during PS-only mode. However, the XOS does not adjust PS power to correct SOC deviation as done by P_m with the PFCS in Eq. 3.10. Such a deviation tends to use the SS at very low powers, which is quite inefficient due to the high amount of

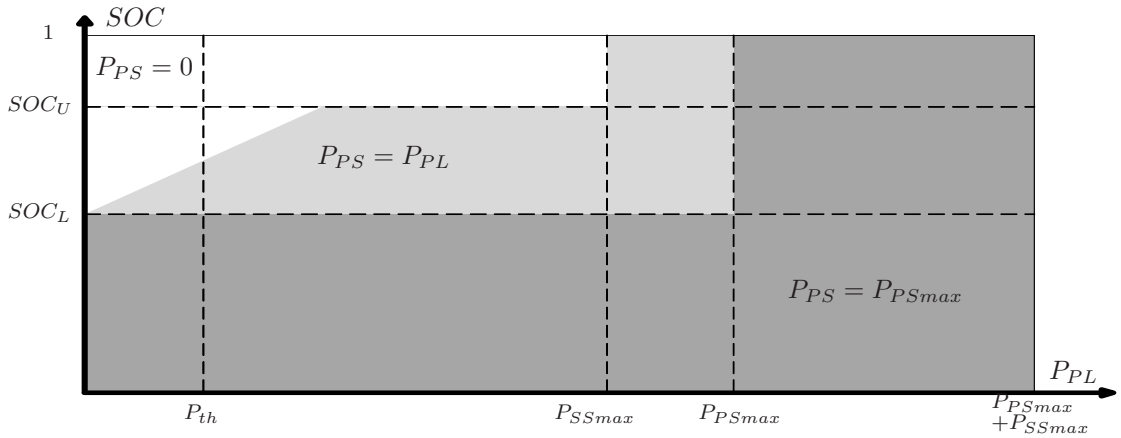

FIGURE 5.5: The XOS operates in three distinct ways depending on given SOC and P_{PL}: SS-only (white), PS-only (light gray) and hybrid operation (dark gray).

DC-DC converter losses at these operating points. Instead the SOC correction is performed by using the threshold changing approach discussed in Section 5.1.2.

The XOS requires three parameters: $P_{PSmin}(SOC)$, P_{PSmax} and P_{SSmax}. The two latter are readily available for any powertrain, but the former needs some further attention. The threshold $P_{PSmin}(SOC)$ is the load at which the SCS switches from using the SS to PS, and is defined as Eq. 5.6. However, it is preferable to consider the case of $P_{csi} = P_{th}$. Not only does this eliminate one tuning parameter from the control strategy, but it also ensures that the strategy is CS for continuous operation at low power levels. For example, if $P_{csi} < P_{th}$, then a low persistent load $P_{PL} > 0$ will gradually drain the battery until the emergency handling rules are activated at $SOC = SOC_L$. However, if $P_{csi} = P_{th}$, then the PS will always be activated before $SOC = SOC_L$, practically always avoiding the need to trigger the emergency handling rules. Therefore, the following PS activation threshold is used instead:

$$P_{PSmin}(SOC) = P_{th} + P_{th}\left(\frac{SOC - SOC_{initial}}{SOC_{range}}\right). \tag{5.9}$$

To determine the optimal value for P_{th}, the efficiencies of the SS and PS could be compared. However, as the SS efficiency by itself does not consider the PS losses required to replenish the SS, the replenishing efficiency $\eta_{re} = 35\%$ (based on the findings for EMMS1 in Section 4.4.2) is also included. Figure 5.6 shows a comparison of PS and SS efficiencies based on the components used in this work, but similar shapes would be found for most series HEVs. As expected, the SS efficiency is high at low loads and drops for higher loads, while the PS starts with a lower efficiency and moves towards a higher efficiency (peaking at $P_{PSopt} = 20.1$ kW). Thus the threshold at which the PS becomes more efficient than the SS is found to be between 11.1 and 11.5 kW depending on SOC. In this work, P_{th} values of between 10.4 and 15.0 kW are found to deliver optimal fuel economy results for tested driving cycles.

A particular benefit of driving with each energy source exclusively is the linear correlation between PL power request and PS power supply. Drivers have developed a sense of intuition with regards to the speed and acceleration of the vehicle based on auditory cues from the ICE in a conventional car. The unfamiliar, and sometimes counterintuitive, cues provided by a hybrid powertrain remain a significant challenge in terms of drivability for adopters of HEVs. The XOS addresses this particular

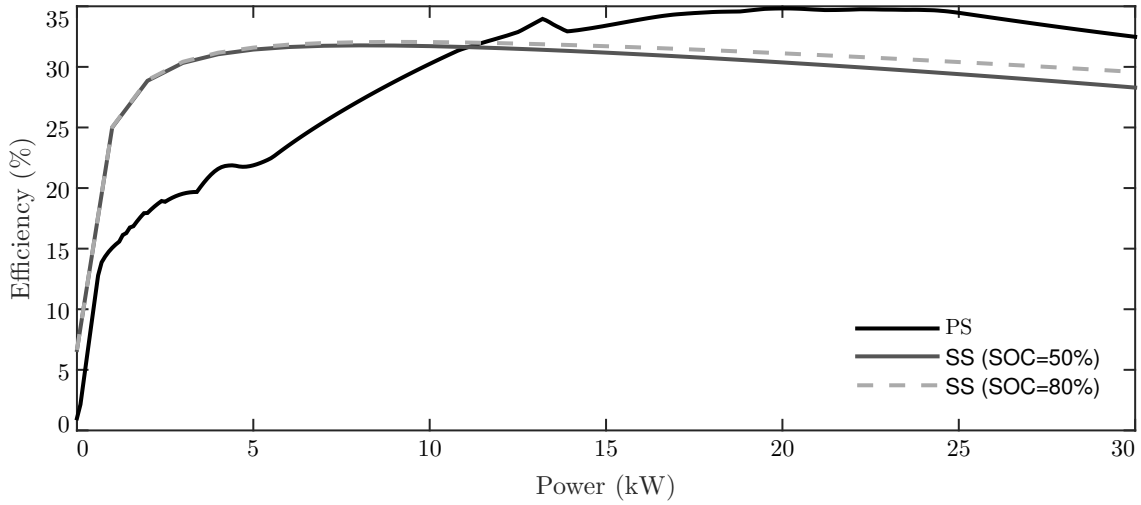

FIGURE 5.6: Efficiency profiles for PS and SS (corrected by $\eta_{re} = 35\%$). The intersection between the profiles can be considered as P_{th}.

issue, but the switching between PS and SS mode, as the engine is switched on and off, remains a challenge in terms of drivability. However, drivers are increasingly becoming familiar with this sensation as SSSs are introduced in conventional vehicles or mild hybrids. The XOS therefore helps in making the driver experience for a HEV more similar to a conventional vehicle.

It is interesting to compare and contrast the operation of the GECMS and the XOS. Each SCS has the same task: to determine the optimal power split of the load request between the PS and SS. This task is reduced to the selection of the power share factor u, as shown for the GECMS and GEMMS in Fig. 4.27. The equivalent chart for XOS is presented in Fig. 5.7, for operation with $SOC_L \leq SOC \leq SOC_U$.

It can be seen that the XOS has three simple stages of operation: the first stage (low P_{PL} and medium or high SOC) is SS-only; the second stage (medium P_{PL}) is PS-only; and the third stage (high P_{PL}) is hybrid mode with the PS delivering maximum power. The transition between the first and second stage is dependent upon the SOC, such that battery use is encouraged at high SOC and discouraged at low SOC. This type of transition is also visible for the GEMMS and GECMS in Fig. 4.27 to a lesser extent. Although the latter is not sensitive to SOC directly, it can be seen that the transition occurs at higher P_{PL} for WL-L to encourage the use of the SS during urban driving, while the transition is at lower P_{PL} for WL-E where PS operation is preferred for highway driving. In the second stage, where XOS applies $u = 1$, the GECMS and GEMMS are somewhat higher towards the

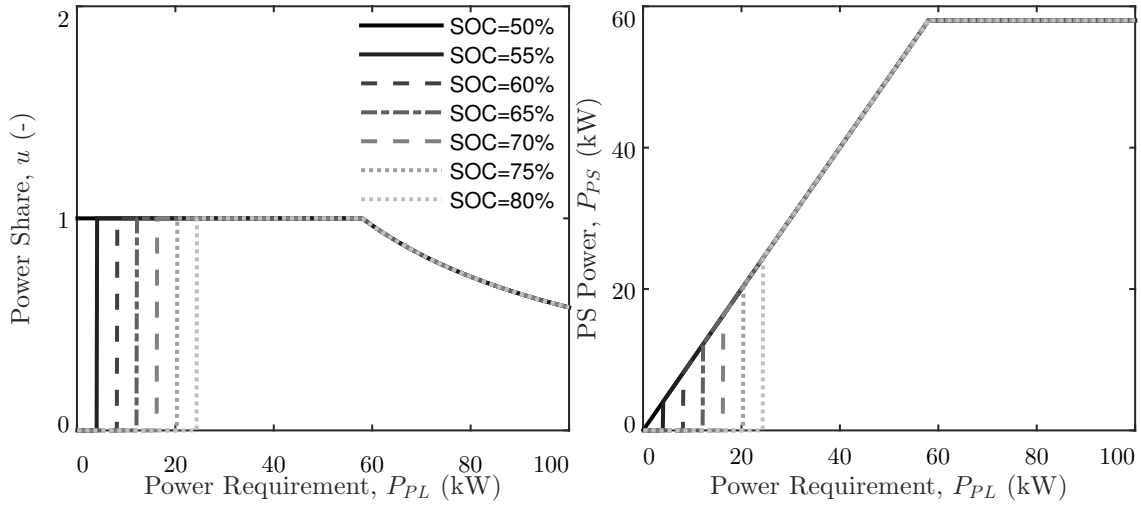

FIGURE 5.7: Power share factor and PS power for varying load and SOC (with $P_{th} = 12.2$ kW) for XOS.

start of this stage, and somewhat lower towards the end of the stage. Operation above the $u = 1$ line is charge increasing operation while operation below this line is charge depleting. Thus, the operation of XOS can be considered a smoothened version of the GECMS and GEMMS operation, to balance out charging and charge depleting operations. Although not optimal, the simplified control policy of XOS roughly reflects the general behavior of the GECMS and GEMMS, and can thus be expected to perform well.

Unlike the TCS and PFCS that operate in two distinct states, and are thus implemented with state machines, the XOS has a single state of operation and can be implemented algebraically with the use of logic gates. The Simulink implementation of the XOS is shown in Fig. 5.8. It can be seen that only simple arithmetic and logic blocks are required for this implementation.

5.2.2 Tuning

The only tuning parameter for the XOS is the base threshold P_{th}. It is varied in the range of $P_{th} \in [10, 17]$ kW in steps of 0.2 kW. Each of these values are then tested for the four driving cycles to tune the parameters such that the fuel economy is maximized. Results with normalized equivalent fuel consumption and final SOC levels are shown in Fig. 5.9.

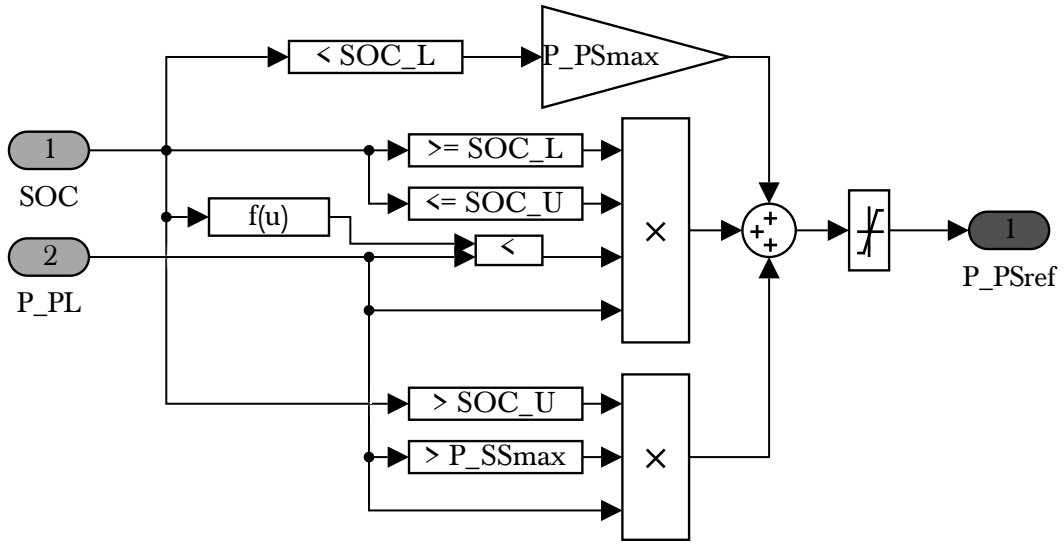

FIGURE 5.8: Implementation of the XOS in Simulink. Note that $f(u)$ implements Eq. 5.9 to define $P_{PSmin}(SOC)$.

As can be seen, each of the driving cycles have different thresholds P_{th} (the optimal threshold P_{th} for WL-L, WL-M, WL-H and WL-E are 15.0 kW, 12.6 kW, 11.6 kW and 10.4 kW respectively). The pattern of having higher thresholds for WL-L (often low loads) and lower thresholds for WL-E (often high loads) is consistent with previously presented strategies, including the GECMS and GEMMS presented in Fig. 4.27. However, for all of those previous strategies, low-medium loads meant charging of the SS and medium-high loads meant discharging of the SS. Thus, driving cycles that often operate at medium-high loads would need to have a lower transition threshold to ensure CS operation. However, this explanation is not valid for the XOS. When the PS is active, whether at low-medium or medium-high load, the SS is neither charged nor discharged. Thus, the driving cycles with low loads are discharging the SS the most, and are thus in most need of a lower transition threshold.

This apparent contradiction can be resolved by understanding the inverse relationship between the propulsion load and the need to apply CS correction. As the SOC drifts over the duration of the driving cycle, the effective transition threshold P_{PSmin} tends to be quite different from the base threshold P_{th}. It is therefore more useful to consider the $P_{PSmin}(SOC_{final})$ (by using the optimal values of P_{th} and SOC_{final} from Fig. 5.9 and use with Eq. 5.9) which yields values of 6.5 kW, 8.4 kW, 7.8 kW and 10.5 kW for the four driving cycles. These agree better with the mentioned expectations.

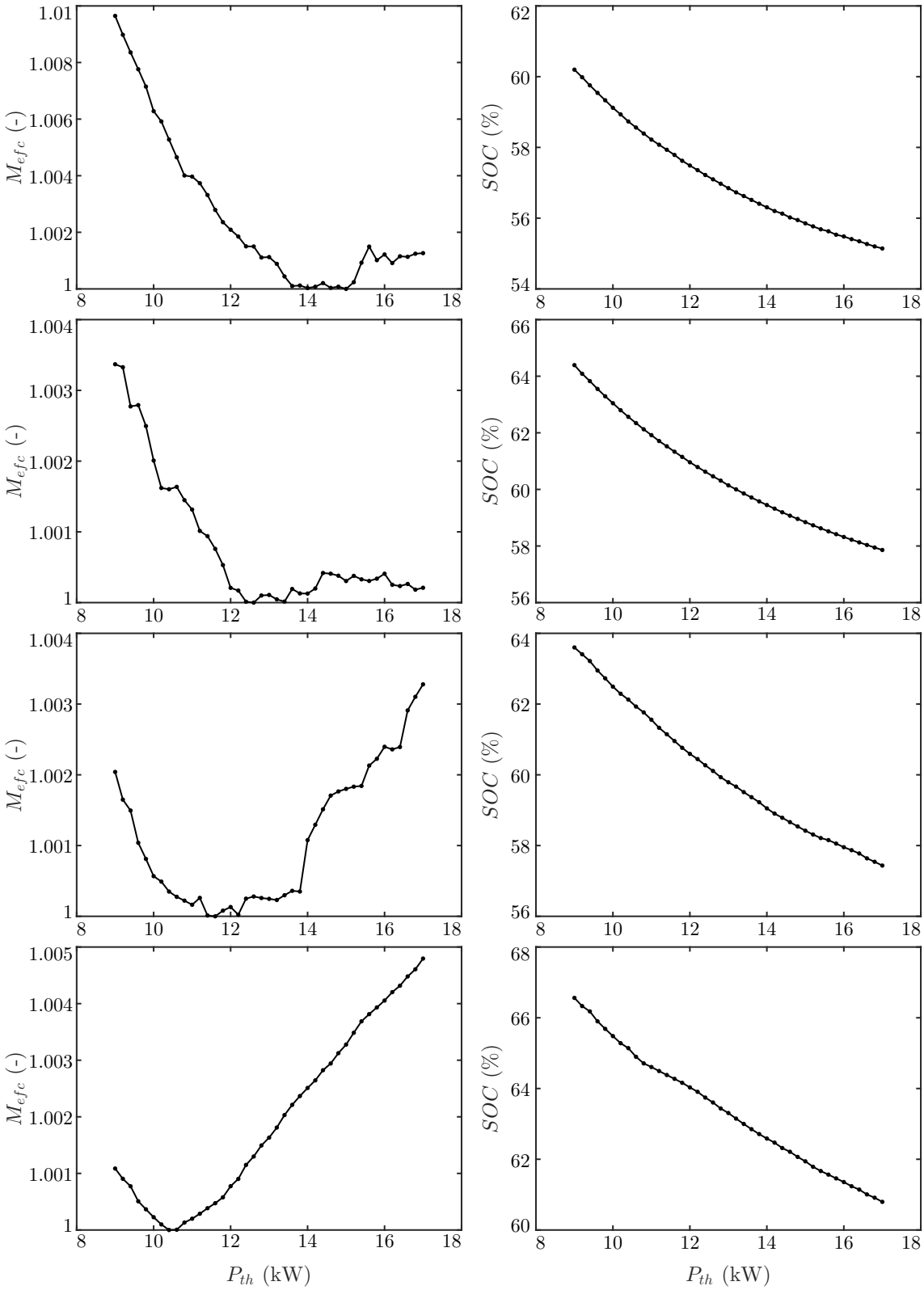

FIGURE 5.9: Normalized EFC (left) and final SOC (right) for varying P_{th} when driving WL-L, WL-M, WL-H and WL-E (from top to bottom) with XOS.

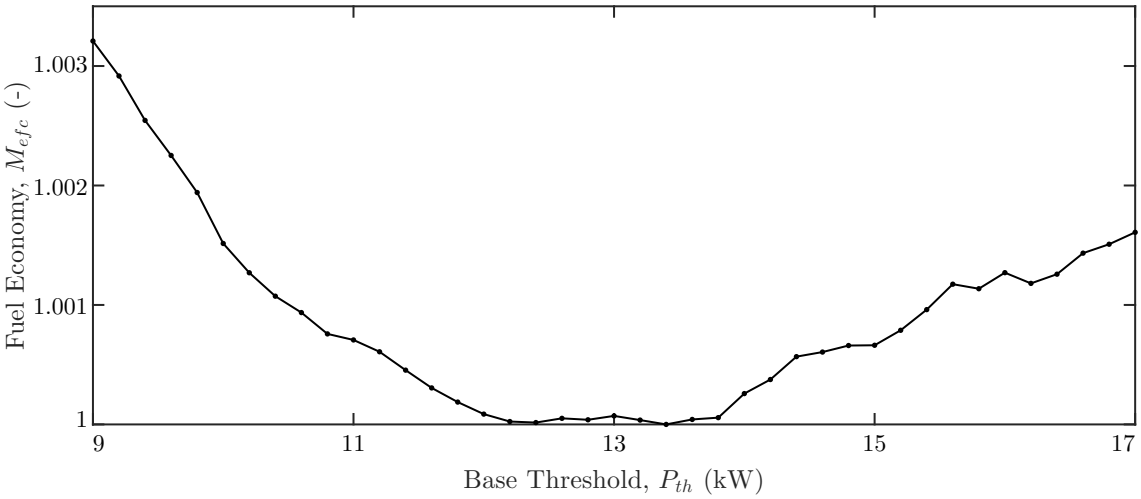

FIGURE 5.10: Normalized total EFC M_{tot} for varying P_{th} with XOS.

Despite the variations in threshold across the driving cycles, it can be noted that the compromise in fuel economy for a badly tuned threshold is lower than 1% in each case. It is also worth noting that the final SOC values are typically quite lower than $SOC_{initial}$, even for quite low thresholds. This control strategy has the same limitations as the EMMS0 with regards to being overly reliant on regenerative braking to recharge the SS. Nevertheless, the operation is well within the *SOC* bounds of the vehicle.

To identify the optimal base threshold P_{th} with consideration for the varying results for the different driving cycles, the EFC of each driving cycle is combined (as discussed in Section 2.6.2) and normalized, and is presented in Fig. 5.10. As can be seen, there is a very flat region for $P_{th} \in [12, 14]$ kW, but the optimal value is found at $P_{th} = 13.4$ kW. However, as it is possible to choose a lower threshold value at negligible impact to fuel economy, while realizing a higher final SOC (a lower base threshold translates to a high final SOC, as shown in Fig. 5.9), this is preferred. Thus, for the purposes of this work, $P_{th} = 12.2$ kW is selected instead (sacrificing 0.0024% in fuel economy relative to the optimal selection). The overall fuel economy is only affected by about 0.2% for changes of 25% in P_{th}. With such a low tuning sensitivity, the realized fuel economy can not be expected to be comparable to the EMMS, but the aim is to keep the XOS extremely simple and still deliver superior fuel economies to the conventional heuristic strategies.

5.2.3 Operation

Using the selected base threshold value, the power profiles for the XOS when driving the first and final iteration of the driving cycles are presented in Fig. 5.11 and Fig. 5.12 respectively. The operation is clearly applying the load following mechanism, as the PS, when used, is always matching the load requirement P_{PL} precisely. However rather than resembling the PFCS, which would use the PS persistently at P_{min} at low loads and operate the PS much more steadily, the operation is more similar to the EMMS0 in Fig. 4.11 and 4.12. It is also evident that the PS and SS are never used together, but rather used exclusively (as the name suggests). This has, as mentioned, great benefits for drivability as the auditory cues of the engine are more intuitive and comparable to conventional vehicles. However, as a result there is no direct charging of the SS, which has to rely on regenerative braking to increase its charge.

The operation for WL-L is almost exactly like the EMMS0, for both the first and final iteration, as the load is generally low and the threshold at when to activate the PS is the main decision. For WL-M and WL-H, there are some differences at higher loads. Whenever the load increases beyond about 25 kW, the EMMS0 will supplement the PS with the SS in hybrid mode, while the XOS persists in using PS only operation. Interestingly, the changes that occur from the first to the final iteration of driving with the XOS are very similar to the changes that occur for the EMMS0, as both of these strategies see the SOC gradually decrease before steadying.

The differences are most clear for the first iteration for the WL-E, where the EMMS0 will rarely use the PS beyond 25 kW, while the XOS is operating the PS close to 50 kW. There is a significant difference in operation here, and it might be unclear which operation should be preferred. However, by looking at the final iteration of the WL-E driving, it can be seen that even the EMMS0 adopts the same approach as the XOS and uses the PS at much higher power levels (as high as 50 kW). Essentially, the EMMS0 needed to operate for quite a while (until SOC had dropped significantly) before it recognized what type of operation was desirable and sustainable, while the XOS figured this out much faster. However, even the XOS will be using the PS to a larger extent for all driving cycles in the final iteration, as its SOC has dropped somewhat.

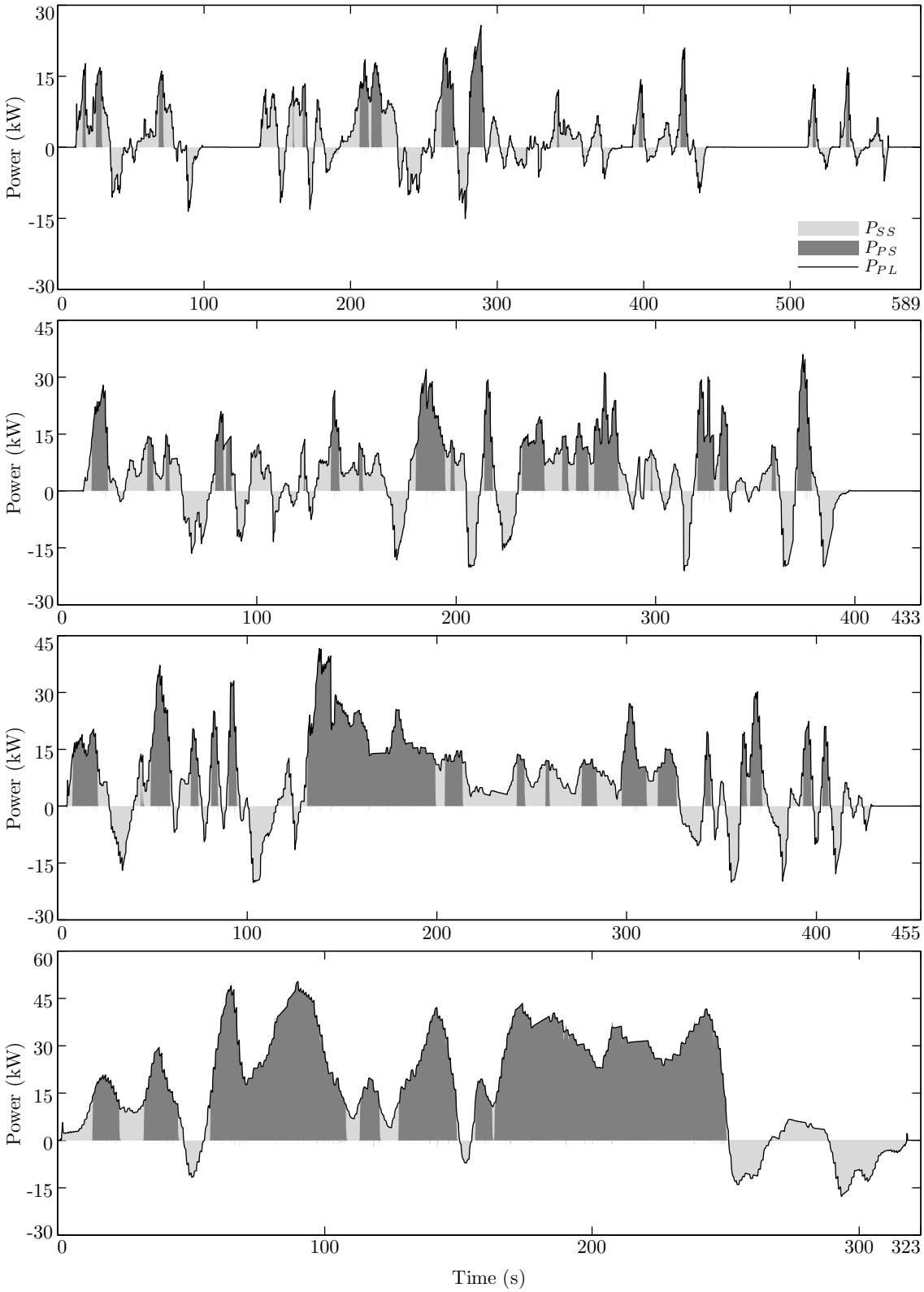

FIGURE 5.11: Power time histories for PS, SS and PL for the first iteration of driving WL-L, WL-M, WL-H and WL-E (top to bottom) with the XOS.

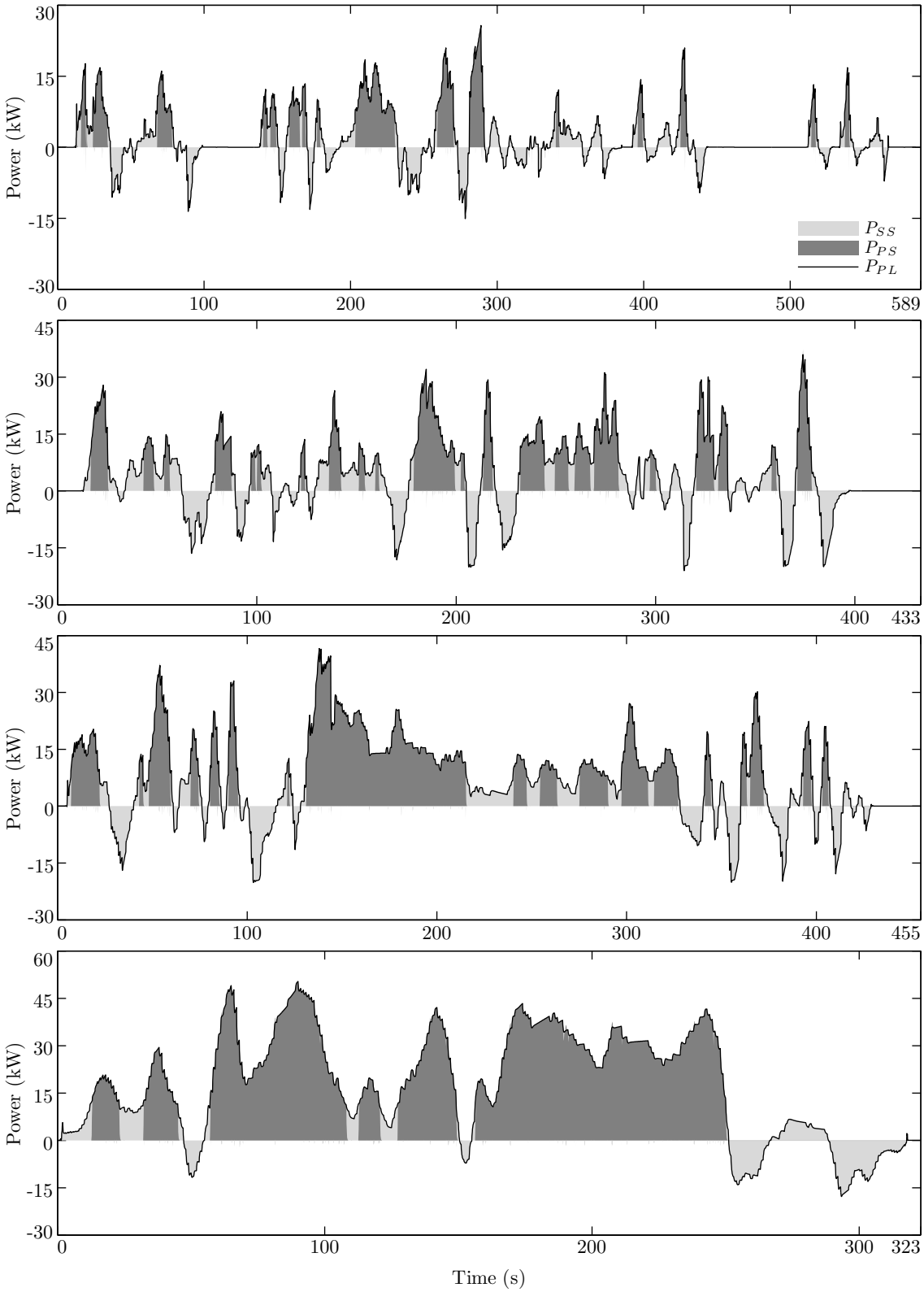

FIGURE 5.12: Power time histories for PS, SS and PL for the final iteration of driving WL-L, WL-M, WL-H and WL-E (top to bottom) with the XOS.

Lastly, the fuel economy of the XOS is evaluated in Table 5.1 for the four different driving cycles. Although the charge has been sustained in each case (with good margins between SOC_{final} and SOC_L or SOC_U), the XOS is unable to maintain the SOC steady at $SOC_{final} \approx SOC_{initial}$ for any of the driving cycles. Also, the inability to actively adjust the SOC by charging the SS clearly reduces the flexibility of the strategy to operate efficiently without compromising the CS operation. The resulting EFC is thus not great, but lags the GECMS results by 4.45-11.53%, with a combined difference (for all four driving cycles together) of 6.29%.

This is however quite favorable if compared to the TCS and PFCS, which were outperformed by the GECMS by 14.35% and 13.72% respectively. The results are particularly good for high-speed driving cycles, where the regenerative braking is sufficient to balance the SS load over the driving cycles. Also, as another benchmark, the XOS performs almost as well the EMMS0 (which is 5.68% behind the GECMS) while using simpler rules and implementation.

Table 5.1: Fuel economy results for XOS

Driving Cycle	SOC_{final} (%)	m_f (kg)	m_{efc} (kg)	Δ_{GECMS} (%)
WL-L	57.36	0.7070	0.7899	+11.53
WL-M	60.79	1.1568	1.2022	+5.56
WL-H	60.44	0.9414	0.9959	+4.80
WL-E	63.91	1.6409	1.6559	+4.45

5.3 Optimal Primary Source Strategy

The OPSS employs the load leveling approach for the powertrain management and operates the PS at its optimal operating point (in terms of efficiency), like the conventional TCS. However, rather than using the state changing technique like the TCS, the OPSS uses the threshold changing mechanism to ensure that charge is sustained. This type of operation is strongly inspired by the global solutions found through GECMS and GEMMS.

5.3.1 Design

One of the key characteristics of the series HEV is the ability to operate the engine-generator set independent of the wheel speed, thus allowing continuously optimal operation if desired. Although such an optimization strategy neglects the SS losses, it is worth considering that all energy delivered by the SS ultimately originates from the PS through either regenerative braking or direct charging. Thus, even the SS, when considered holistically, is greatly benefited by operating the PS optimally. Furthermore, this could enable further optimization of the engine and generator design, sizing, coupling and control to perform optimally at a single point of operation, as opposed to the more complex consideration of all the various possible operating points in a load following strategy.

Although the name of the OPSS makes emphasis on the optimal operation of the PS, the TCS does not. The key characteristic of the TCS is the "thermostat" type of operation, oscillating between charge increasing and charge depleting operation through a hysteresis mechanism. As mentioned earlier in this chapter in Section 5.1.2, this state changing approach allows the number of start-stop events of the engine to be minimized. However, within a modern HEV the cost of start-stop events is much lower than it used to be, and it is therefore possible to reduce SS losses (by switching off the PS at appropriate times) such that they outweigh the cost of the start-stop events involved. The OPSS therefore uses the threshold changing mechanism to not only ensure CS operation, but also to reduce the typical magnitude of the charging and discharging operation of the SS. The implementation of the threshold changing mechanism is the same as for the XOS, as given in Eq. 5.9 (and described in Section 5.1.2).

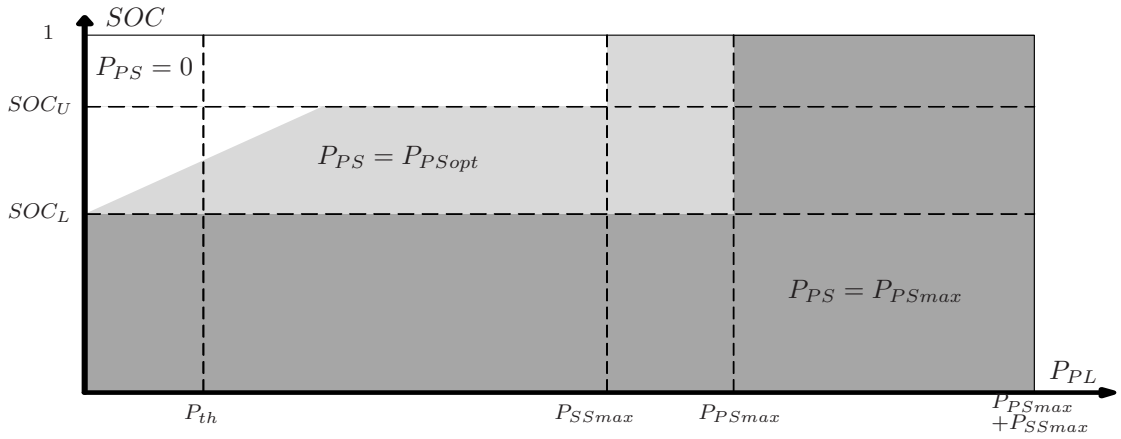

FIGURE 5.13: The OPSS operates in three modes depending on given SOC and P_{PL}: SS mode (white), optimal PS mode (light gray) and maximum PS mode (dark gray).

The complete set of rules governing the OPSS is best illustrated graphically, as shown in Fig. 5.13, where the assigned PS power is shown for various operating conditions (varying load power and SOC). It can be seen that the "shell" of the strategy, in the form of its emergency handling rules (for $SOC < SOC_L$ or $SOC > SOC_U$), is practically identical to the XOS (in Fig. 5.5). The simple difference exists only in the center of the chart, where the PS power is defined as $P_{PS} = P_{PSopt}$.

It is also useful to compare the simple nature of these rules to the setup of the TCS and PFCS (in Section 3.2.1 and Section 3.3.1 respectively). The TCS arguably has the simplest rules, followed by the XOS, OPSS and PFCS in this particular order. The TCS has a single tunable parameter $P_{PS,cop}$ that can readily be estimated as $P_{PS,opt}$, while both the XOS and OPSS have to tune the base threshold P_{th} with some guidance. The PFCS on the other hand has two tunable parameters in P_{ch} and P_{min}. However, the TCS and PFCS have two states of operation as opposed to the single-state operation of the XOS and OPSS. Furthermore, there are significantly fewer rules and modes of operation within the XOS and OPSS as compared to the PFCS.

To further clarify the design of the OPSS, the resulting power share has been presented in Fig. 5.14 (with $P_{PSopt} = 20$ kW) in the same form as previously presented strategies. The strategy uses only SS at low powers but turns on the PS to its optimal operating point once it passes the threshold P_{PSmin}. Only as the load reaches the maximum power of the PS P_{PSmax} does the PS begin to contribute more power (in fact its maximum power) to meet the load.

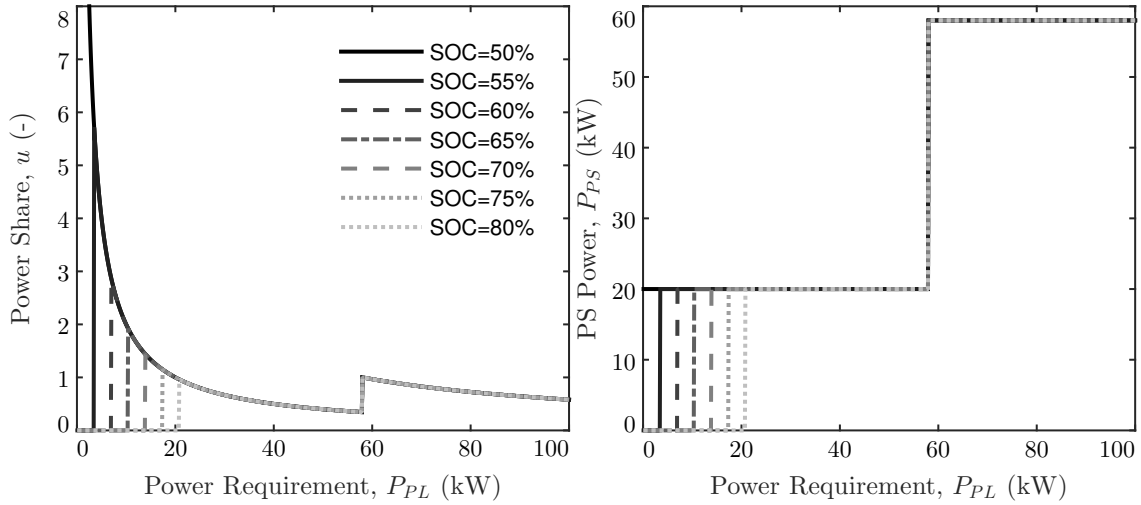

FIGURE 5.14: Power share factor and PS power for varying load P_{PL} and SOC (with $P_{th} = 10.4$ kW) for OPSS.

Comparing these profiles to those of the GECMS and GEMMS in Fig. 4.27, it can be seen that they are almost identical up until about $P_{PL} = 50$ kW (for $SOC = 65\%$). The main exception is a small region around $P_{PL} = 20$ kW where $u = 1$ is used instead (like the XOS). This deviation is expected, as the GECMS and GEMMS have considered the extremely low DC-DC converter efficiency at low SS power levels and have opted to use $P_{SS} = 0$, rather than $P_{SS} = 1$ kW or $P_{SS} = -1$ kW. Such consideration or nuance does not exist for the OPSS which persistently uses the PS at P_{PSopt}. The implementation of the OPSS is practically the same as the XOS, as might be expected from the similarities between the control schematics in Fig. 5.5 and Fig. 5.13. Figure 5.15 shows the OPSS Simulink implementation, where the second of the three terms being added is now a constant (P_{PSopt}), unlike the XOS.

5.3.2 Tuning

To tune the OPSS, the threshold power is varied in the range of $P_{th} \in [4, 15]$ kW in steps of 0.2 kW. Each of the values is then tested for the four driving cycles to tune the parameter such that the fuel economy is maximized. Results with normalized EFC and final SOC levels are shown in Fig. 5.16.

The optimal threshold P_{th} varies for each of the driving cycles. The fuel economy is maximized when P_{th} is defined as 9.2 kW, 10.2 kW and 10.4 kW for WL-L, WL-M and WL-H respectively (although not very clear from the figure). The ideal

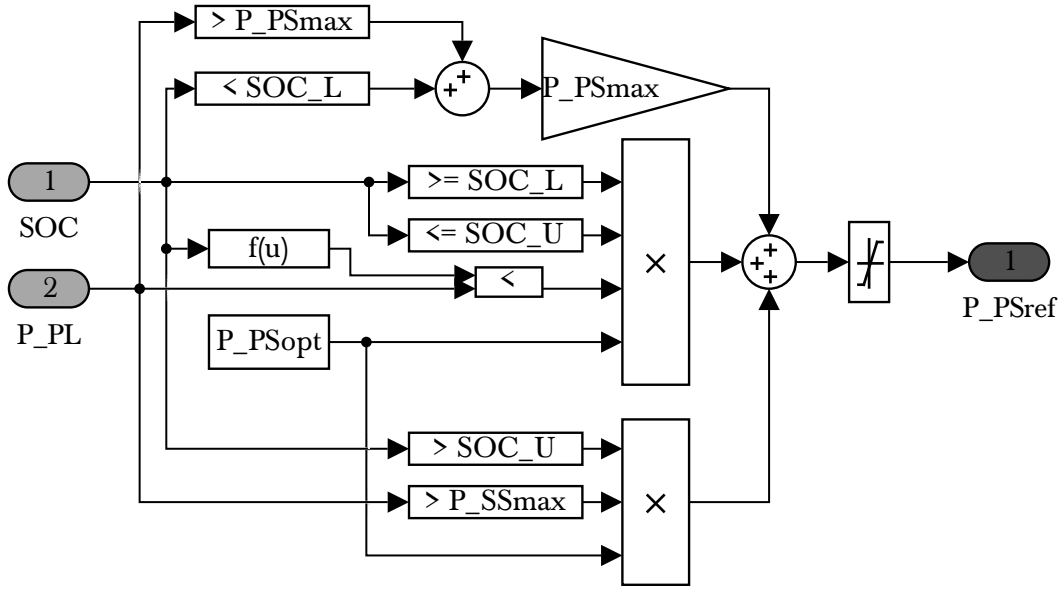

FIGURE 5.15: Implementation of the OPSS in Simulink. Note that $f(u)$ implements Eq. 5.9 to define $P_{PSmin}(SOC)$.

threshold for WL-E is outside the investigated region (the minimum at $P_{th} = 5.4$ kW is just a local minimum), but is found separately to be at -0.8 kW. Similar to the EMMS and GECMS, the threshold is higher for the driving cycles with lower load (e.g. WL-L) and lower for higher loads (e.g. WL-E). The exception of the XOS results in Section 5.2.2, is thus not applicable as the OPSS operation is more similar to optimization-based strategies in the sense that the SS is charged at medium-low loads and discharged at medium-high loads (the SS is neither charged or discharged in either of these cases for the XOS). Furthermore, the distinction between the base threshold P_{th} and the effective transition threshold P_{PSmin} is less relevant for the OPSS results as there is barely any SOC deviation ($SOC_{final} \approx SOC_{initial}$), giving $P_{PSmin}(SOC_{final})$ (as given by Eq. 5.9) values of 9.02 kW, 10.26 kW, 10.47 kW and 1.00 kW for WL-L, WL-M, WL-H and WL-E respectively (with SOC_{final} values of 64.81%, 65.06%, 65.08% and 53.64%).

It is also interesting to contrast the final SOC values of the OPSS results with those of the XOS. As the XOS relied solely on regenerative braking to charge the SS, the strategy was essentially only able to reduce the discharging of the SS to maintain CS operation. The OPSS, on the other hand, is able to actively charge the SS more by reducing the power threshold P_{th}. Consequently it can be seen that the SOC reaches its upper limit $SOC_U = 80\%$ for the first three driving cycles at low values of P_{th}. Such threshold selections cause the emergency handling rules, as displayed

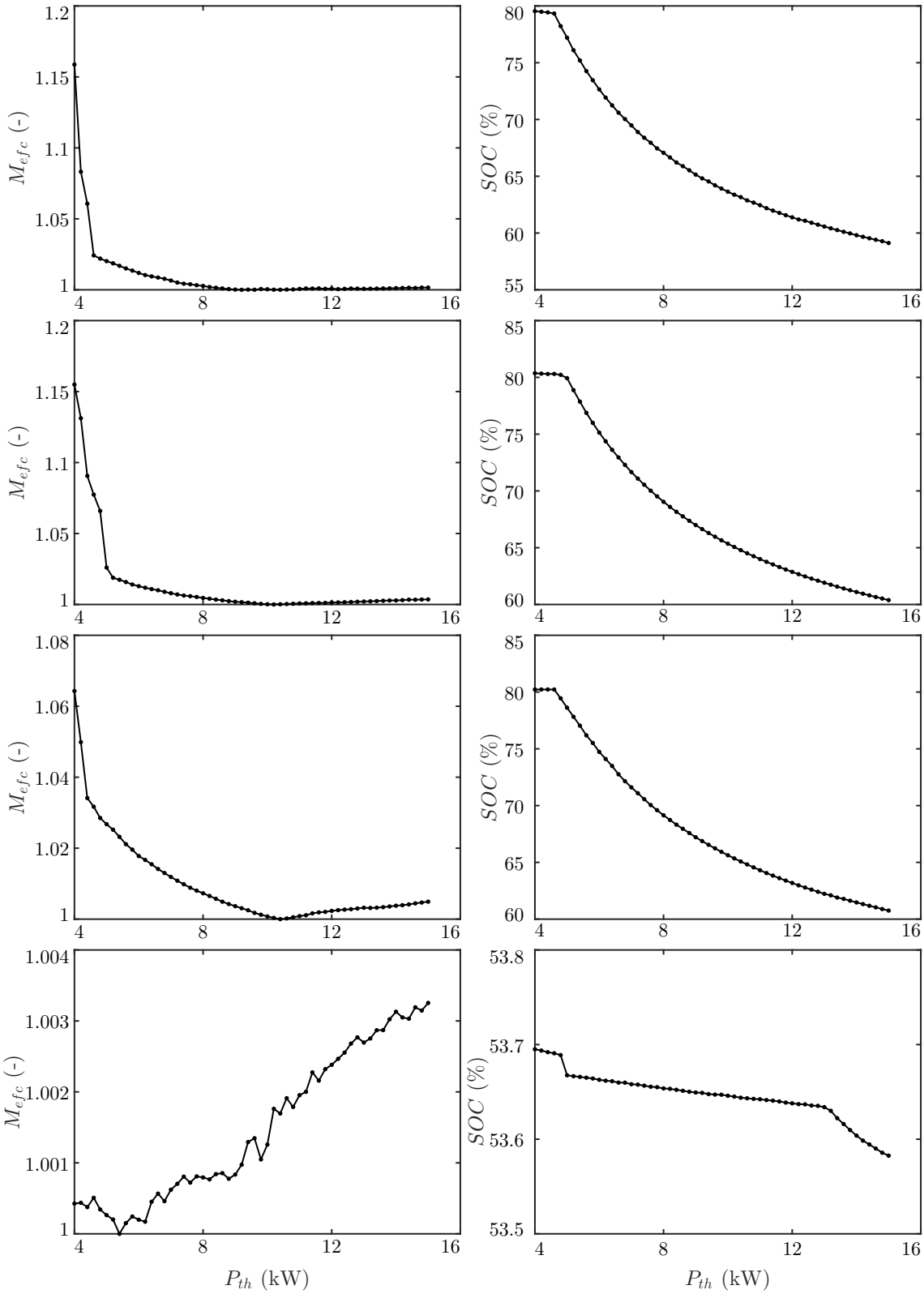

FIGURE 5.16: Normalized EFC (left) and final SOC (right) for varying P_{th} when driving WL-L, WL-M, WL-H and WL-E (from top to bottom) with OPSS.

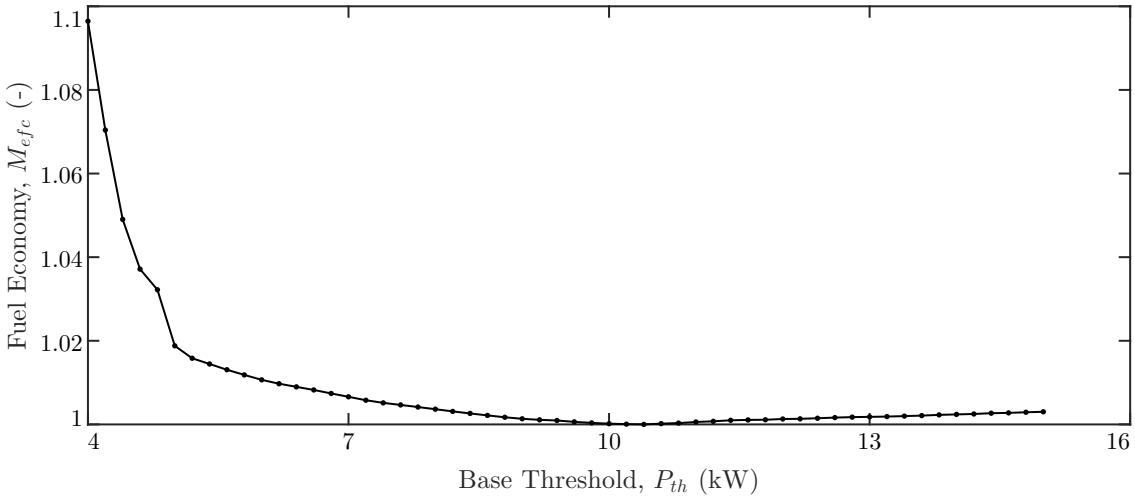

FIGURE 5.17: Normalized total EFC M_{tot} for varying P_{th} with OPSS.

in Fig. 5.13, to intervene to prevent the SOC from increasing further. However, this intervention comes at the expense of fuel economy, where a clear spike is visible, in particular for WL-L and WL-M. It is thus clearly desirable to set an appropriate value for P_{th} to avoid the emergency handling rules on the upper range of SOC.

The consequences of triggering the emergency handling rules in the lower SOC range are quite different. The case of the WL-E shows the SOC flattening off around $SOC = 54\%$, which still has a decent gap to $SOC_L = 50\%$. However, as will be shown later in Fig. 5.20, the SOC actually reaches this lower threshold during the driving cycle, before recovering somewhat by the end of the cycle to yield $SOC_{final} = 54\%$. Most importantly, it can be seen that the fuel economy also flattens out around $P_{th} = 10$ kW. Thus, the fuel economy in some sense benefits by triggering the emergency handling rules, as it prevents the operation from becoming even more suboptimal. This is the ideal type of emergency handling rules. However, for this work the emergency handling rules at higher SOC have prioritized simplicity, which is why a spike in fuel economy can be observed for badly tuned threshold values.

To determine the optimal tuning of the OPSS, the overall fuel economy is evaluated for the four driving cycles combined. The normalized results are presented in Fig. 5.17. The optimal power threshold is found at $P_{th} = 10.4$ kW, which is very close to the ideal selection for WL-M and WL-H (which arguably represents the most common type of driving). Although the OPSS is more sensitive to tuning than the XOS, even if the P_{th} is off by 25%, it would only affect the fuel economy by less than 0.4%.

5.3.3 Operation

The resulting power profiles are shown in Fig. 5.18 and Fig. 5.19, for the first and final iteration of the driving cycles respectively. It is clear that the OPSS is relying on the load leveling approach as the PS, whenever used, is always used at $P_{PSopt} = 20$ kW. Although this approach might sound or even look primitive, it is worth comparing the resulting power profiles to the GECMS and GEMMS in Fig. 4.27.

The operation for WL-L is very similar to the GECMS, which operates the PS with slightly more variation. However, both the GEMMS and GECMS generally use the PS for the same durations as the OPSS. These variations in power levels for the PS by the GECMS and GEMMS become larger for the WL-M and WL-H, while the OPSS maintains its steady operation, but generally uses the PS at the same occasions. It is also worth noting that the OPSS is operating almost identically in its first and final iteration, suggesting that its operation is charge sustaining from the very beginning.

The same can not be said for the WL-E, where the OPSS uses the SS more often at high magnitudes, as compared to the GECMS and GEMMS. As can be expected, this results in a lower SOC and the operation in the final iteration is therefore quite different. Apart from generally having the PS on at all times (except during regenerative braking), the OPSS experiences some extreme oscillatory behavior towards the second half of the final iteration of WL-E. Essentially the SOC drops below SOC_L, requiring the emergency handling rules to be kicked in. This results in the PS being requested to deliver its maximum rated power (as illustrated in Fig. 5.13), causing the PS load to exceed the required load, thus charging the SS and increasing the SOC. This in turn, results in the OPSS returning to normal mode (i.e. exiting emergency handling rules), causing the PS to return to delivering P_{PSopt} and the SS supplementing the difference to the load as the SOC drops again. This causes high-speed oscillations in the operation of the PS such that it on average follows the load ($P_{PS} = P_{PL}$). Although this operation is sensible, these oscillations are highly undesirable. They can however be removed by either redefining the emergency handling rules or by including a hysteresis effect between the emergency handling rules to prevent the oscillations. This will be done in the next version of this control strategy.

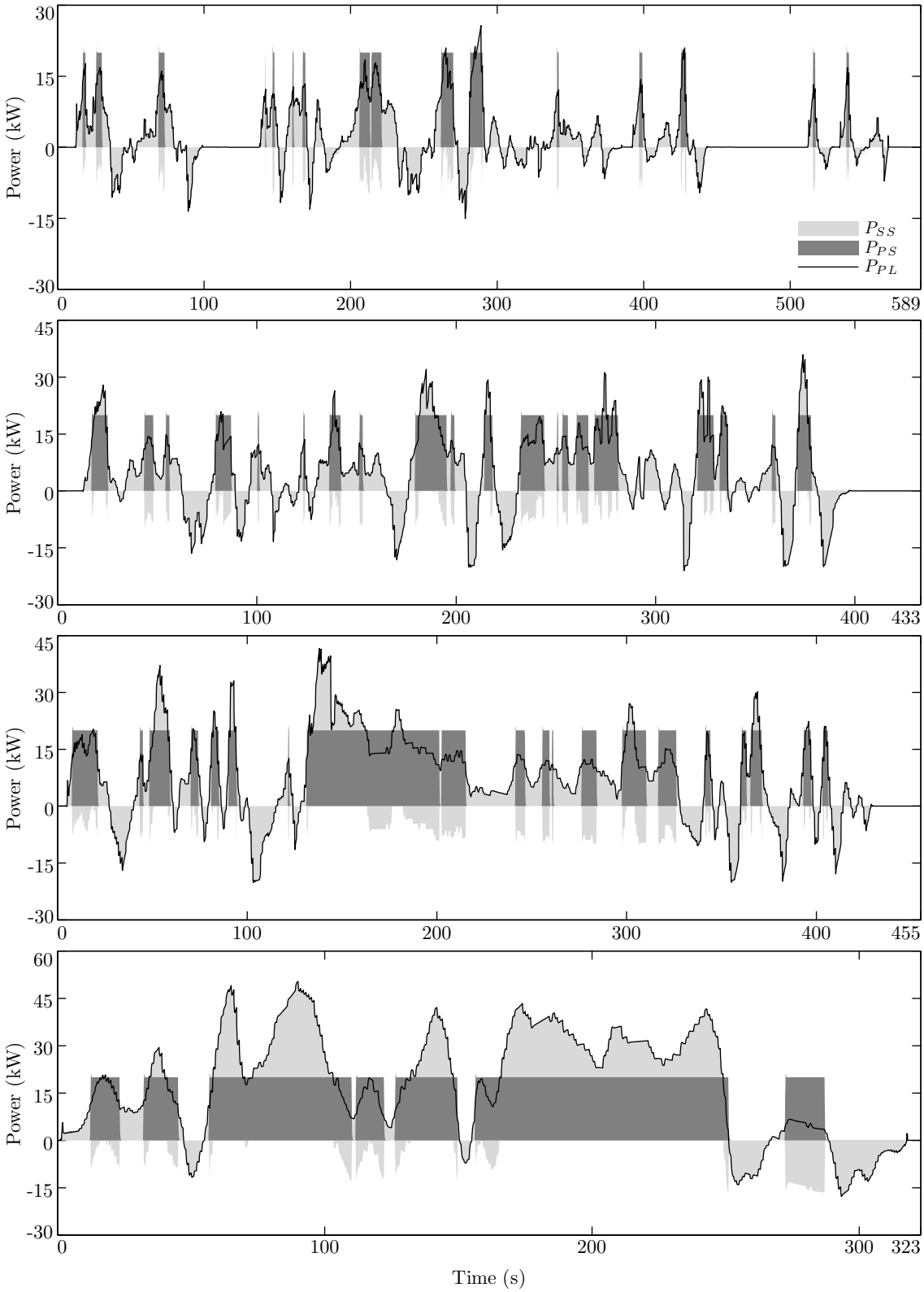

FIGURE 5.18: Power time histories for PS, SS and PL for the first iteration of driving WL-L, WL-M, WL-H and WL-E (top to bottom) with the OPSS.

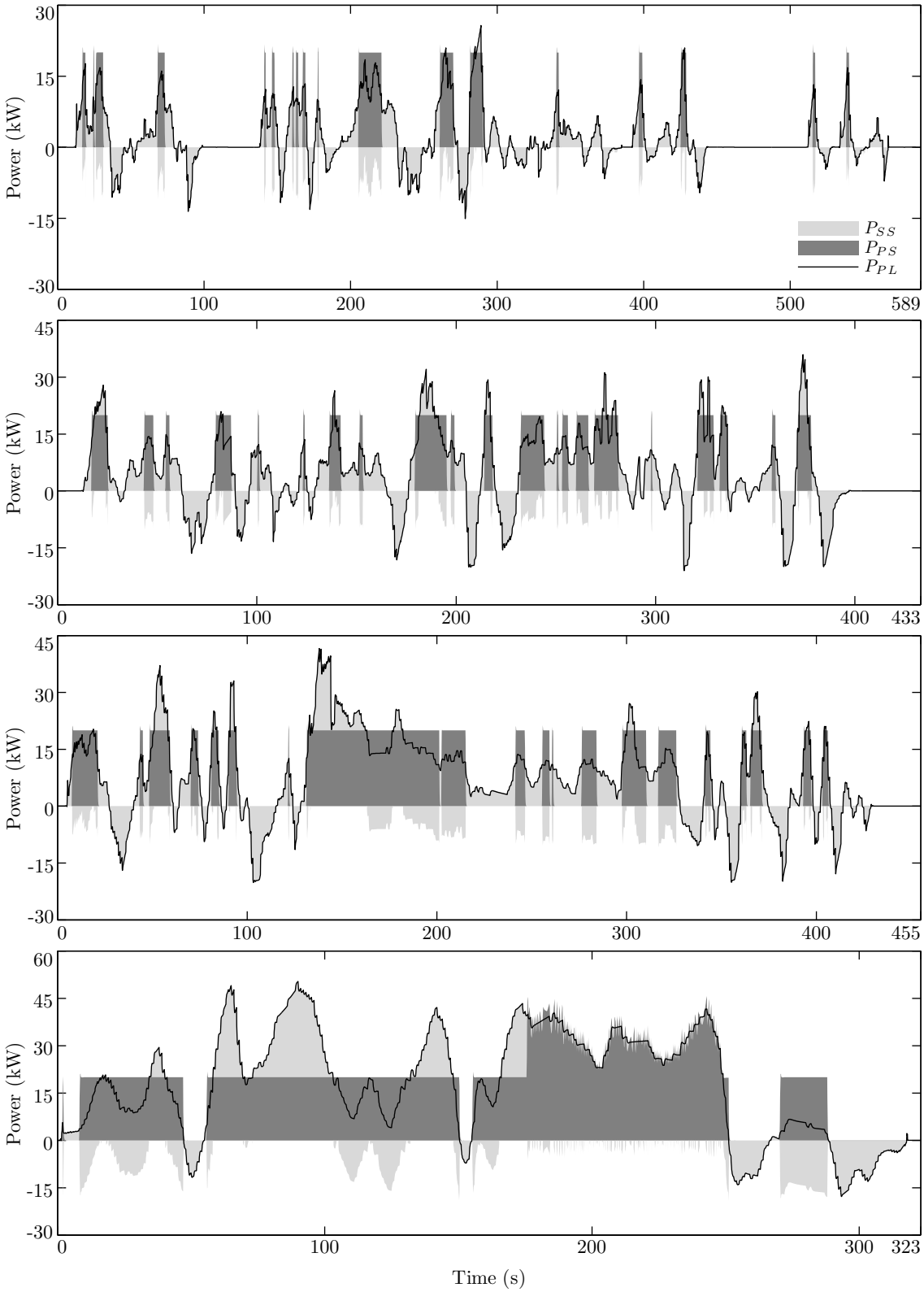

FIGURE 5.19: Power time histories for PS, SS and PL for the final iteration of driving WL-L, WL-M, WL-H and WL-E (top to bottom) with the OPSS.

Finally, the fuel economy of the OPSS is evaluated in Table 5.2 for the four different driving cycles. It can be seen that the SOC has been closely sustained ($SOC_{final} \approx SOC_{initial}$) for the first three of the studied driving cycles, while it has dropped significantly for WL-E×4. Considering the simplicity of the rules, this CS ability is very impressive. The achieved fuel economy is equally impressive, being only 0.00-3.52% behind the GECMS (the GECMS outperforms the OPSS with 0.0042% for WL-L). If the four driving cycles are considered together (as calculated for M_{tot}), the difference is 0.95%. Considering the analytical effort invested in the GECMS, the OPSS delivers exceptional utility in terms of results per effort.

TABLE 5.2: Fuel economy results for OPSS

Driving Cycle	SOC_{final} (%)	m_f (kg)	m_{efc} (kg)	Δ_{GECMS} (%)
WL-L	63.16	0.6884	0.7083	+0.00
WL-M	64.78	1.1404	1.1428	+0.34
WL-H	65.08	0.9532	0.9525	+0.23
WL-E	53.64	1.4853	1.6410	+3.52

5.4 Comparison of Heuristic Strategies

Having presented the XOS and OPSS, and their individual designs and performances, it is interesting to compare their operation to the two conventional heuristic strategies: the TCS and PFCS. Results of the GECMS are also included as a reference point.

The SOC profiles for each of the four heuristic strategies are presented in Fig. 5.20 for the four driving cycles. It should be noted that the selection of tuning parameters for the PFCS in Section 3.3.1 makes this strategy operate quite similarly to the TCS for $P_{PL} \leq P_{PSopt}$. As this is often true for WL-L (and somewhat true for WL-M and WL-H), the SOC profiles of the PFCS and TCS are very similar (and somewhat similar for WL-M and WL-H) in the presented results. This similarity is also visible in comparing the power profiles of TCS and PFCS in Fig. 3.5 and Fig. 3.11. The difference of 3 kW between $P_{PS,cop} = 19.8$ kW and $P_{min} = 16.8$ kW results essentially in a change in period for the SOC profiles.

There is also a distinct difference between the operational pattern between the state changing strategies (TCS and PFCS) and threshold changing strategies (XOS and OPSS). The former can be seen to oscillate between the lower and upper SOC limits, alternating between charge depleting and charge replenishing modes of operation. This is also true for WL-E, although the oscillations occur at the limits rather than between them.

The TCS can be seen to discharge quite sharply at the start of the driving cycle, but even as the operation changes to charging mode, the charge keeps depleting for some further time. This occurs due to the high level of load for the WL-E, such that $P_{PL} \geq P_{PSopt}$, meaning that the SS has to supplement the PS to meet the load power. Thus the SOC drops to 42.65% before beginning to recover. The TCS then remains in charging mode (with the SS occasionally entering discharging mode) for the rest of the driving cycle as the progress of increasing SOC towards the upper limit of SOC is essentially flat due to the generally high load power. However, if the $P_{PS,cop}$ was slightly higher, the SOC would reach its upper limit and the TCS would enter the charge depleting mode again. This operation is consistent with the observation that the period of the state changes (T_{tcs}) for the TCS is proportional to the average load power of the driving cycle ($\bar{P}_{dc}$). As shown in Table 2.6, we have

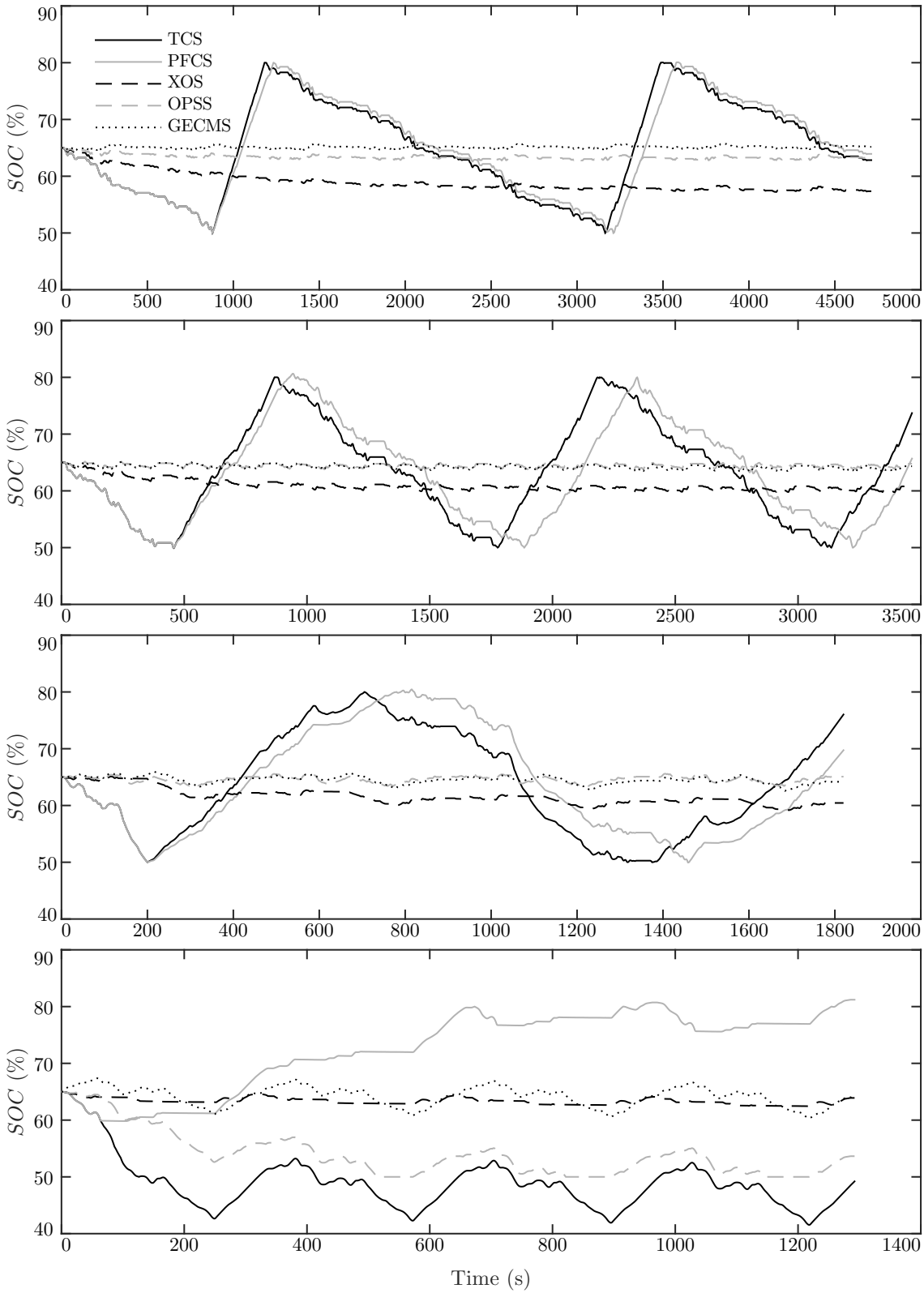

FIGURE 5.20: SOC profiles for XOS, PFCS, OPSS, TCS and GECMS when driving WL-L, WL-M, WL-H and WL-E. Note that the TCS and PFCS profiles often overlap.

$\bar{P}_{WL-L} < \bar{P}_{WL-M} < \bar{P}_{WL-H} < \bar{P}_{WL-E}$. Thus, it follows (and matches the results in Fig. 5.20) that $T_{WL-L} < T_{WL-M} < T_{WL-H} < T_{WL-E}$.

The PFCS operation is however quite different for WL-E. While the TCS can only change its mode by having the SOC reach its lower or upper limits, the PFCS has some additional possibilities, as shown in Eq. 3.8. The PFCS will also activate the charging mode operation if the load power exceeds the maximum SS power ($P_{PL} > P_{SSmax}$), which occurs quite frequently for the WL-E. Thus, it can be seen that the PFCS enters charging mode operation already around $t = 60$ s, without needing to operate the SS at very high loads (as TCS has do). Thereafter, the PFCS often operates in a load following manner but ends up charging the SS during low loads (and regenerative braking). The SOC is thus gradually increased, before reaching its upper limit around $t = 670$ s As the PFCS switches mode to operate with SS only, the SOC begins dropping. However, quite soon the load power briefly exceeds the maximum SS power ($P_{PL} > P_{SSmax}$), making the strategy return to its load following mode. As a result, the PFCS keeps on operating at a quite high SOC, oscillating between around $SOC = 81\%$ and $SOC = 76\%$.

In contrast, both XOS and OPSS operate much more steadily, quite similarly to the GECMS. In fact, the OPSS is always operating within the following SOC bands for WL-L, WL-M and WL-H: 62.75-65%, 63.76-65.15% and 63.39-65.59% respectively. Such a limited depth-of-discharge (DOD), as opposed to the 50-80% cycles of TCS and PFCS, is not only beneficial for the fuel economy of the vehicle, but also helps to reduce battery degradation. Similarly, the XOS also has a small DOD, but operates within a band of SOC that has deviated further from $SOC_{initial}$. It can be seen that it takes the XOS less than a quarter of the simulated driving cycles to reach its steady and CS operation, while the OPSS is very well positioned from the very start. However, the simulation results for WL-E demonstrate the opposite relation. Here, the XOS is operating within the SOC band of 62.43-64.33%, which is very close to $SOC_{initial}$, while the OPSS is operating at 49.99-55.06%. In fact, the OPSS is briefly activating the emergency handling rules to remain within the SOC bounds.

As the operation of both XOS and OPSS (and in particular the latter) is very similar to the GECMS, which significantly outperformed the TCS and PFCS in Chapter 3, it is not surprising to have these new heuristic strategies achieve better fuel economies than the conventional heuristic strategies. The relative fuel economy performance is shown in Fig. 5.21 for the four driving cycles. It can be seen that the

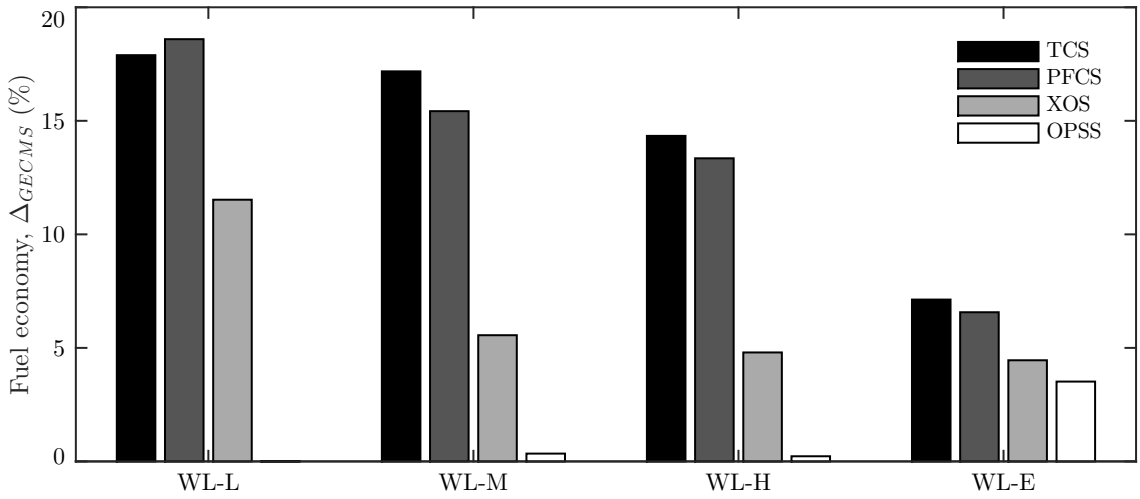

FIGURE 5.21: Comparison of fuel economy for PFCS, TCS, XOS and OPSS, relative to the performance of the GECMS, when driving WL-L, WL-M, WL-H and WL-E.

novel proposed heuristic strategies are consistently outperforming the conventional ones. It is also clear that the XOS tends to perform better for higher loads, while the OPSS performs at its best at lower loads (note that that OPSS bar for WL-L is at $\Delta_{GECMS} = 0$ so is not visible).

It is useful to compare the load following and load leveling strategies internally. The XOS reduces the EFC by 6.83% relative to the PFCS for the four driving cycles considered together, while the OPSS improves the fuel economy by 13.28% relative to the TCS for the four driving cycles combined. These results demonstrate the ineffective nature of the state changing mechanism for modern HEVs for which the frequent, but intelligent, use of a SSS for the ICE is essential to achieve great fuel economy. Although the XOS is a significant improvement over the conventional heuristic strategies, it is the OPSS that is the most impressive one, achieving fuel economy comparable (in fact identical for WL-L) to the GECMS.

The fact that the OPSS only has made use of a single tunable parameter and is matching the fuel economy of the GECMS, raises some new questions. How much further can the fuel economy of heuristic strategies be pushed? How close to the truly global optimal solution are these strategies operating? These questions will be discussed further in Chapter 6.

5.5 Summary

This chapter has discussed insights gained from past chapters that can serve as design principles for heuristic control strategies. These have been formulated as distinct design principles, which are summarized in Table 5.3.

Table 5.3: Possible design principles for control of HEVs

Fuel Economy Optimizing Mechanisms	Charge Sustaining Mechanisms	Implementation Mechanisms
Load leveling	State changing	State machine
Load following	Threshold changing	Control map
Load blending	Power changing	Algebraic
	Emergency handling	

The XOS used the load following technique together with a threshold changing mechanism. It thus operated as: SS-only mode at low load power; PS-only mode at medium load; and hybrid mode at higher loads. This generally exclusive operation of each power source allows more intuitive auditory feedback for the driver, and makes the experience more similar to driving a conventional vehicle. The XOS outperformed the PFCS (the conventional implementation of load following) by 6.83%. However, the fuel economy results were still lagging the GECMS by 6.29%.

The OPSS, on the other hand, used the load leveling technique together with a threshold changing mechanism. The resulting strategy operated as follows: SS-only mode at low load power; PS operating at its optimal level at medium load; and PS operating at its maximum level at higher loads. This type of operation is very similar to the operation of GECMS and GEMMS, and thus the performance of the OPSS was very impressive. It lags the GECMS by only about 1.4%, and consequently outperformed the TCS (the conventional implementation of load leveling) by 12.7%.

The dramatic improvements of XOS and OPSS, over PFCS and TCS respectively, clearly demonstrated the advantage that threshold changing has over state changing mechanisms to enable charge sustaining operation in a modern HEV. The benefit of fewer ICE start-stop events that the state changing mechanism enjoys, is less relevant if an efficient SSS is installed. This result would translate to modern HEVs with parallel architecture as well. However, the extraordinary performance of the OPSS, with its load leveling strategy, can only be expected to be effective for series HEVs where the ICE can be operated independently of the vehicle speed.

Chapter 6

Global Optimality

This work has proposed several novel control strategies, including both optimization-based (EMMS0, EMMS1 and EMMS2) and rule-based strategies (XOS and OPSS). Their performance relative to conventional control (TCS and PFCS) strategies has been impressive and the results have often approached the performance of GECMS, which supposedly is close to the global optimal solution [75, 78, 79, 104]. The fact that GEMMS narrowly outperformed the GECMS might support this claim, as the room for improvement seems quite limited. However, the extraordinary performance of the OPSS, albeit inferior to GECMS, suggests that there might be a global optimal solution out there that has not been considered in the search space of the investigated control strategies so far.

To investigate this possibility, ideally a DP or brute force approach should be applied to explore the control space more exhaustively. However, the previously mentioned computational issues make any such attempt unfeasible. The best practical choice is thus to take a "brute force light" approach, where a suitable heuristic control structure is setup with multiple tunable parameters. This chapter will thus design a global heuristic strategy (GHS) with the aim to outperform the GECMS and GEMMS. The larger the margin, the less validity can be asserted to the claim that the GECMS is practically identical to the DP solution.

This chapter will begin by introducing the design of the GHS, followed by a demonstration of its operation and analysis of its fuel economy. Thereafter the results will be discussed in the context of claims of global optimality among other control strategies.

6.1 Global Heuristic Strategy

6.1.1 Design

The objective of the GHS is to apply heuristic rules that can be globally tuned to achieve fuel economy results that are superior to GECMS with as large a margin as possible. There are a wide range of heuristic insights that can be considered, including those mentioned in the Design Principles section in Section 5.1. However, rather than investigating new heuristic rules it makes sense to apply the OPSS rules, which were shown to deliver fuel economies comparable to the GECMS results in Section 5.3.3. This tried and tested approach will thus be further improved in this section by allowing for a significantly larger amount of tuning.

Firstly, the tuning process will be made driving cycle specific. The global nature of the control allows it access to the whole driving cycle in advance, so that it can be tuned separately for each driving cycle, as has been the case for the GECMS and GEMMS. This allows the control strategy to perform at its optimum rather than needing to have a compromised nature of policies that are not excellent on any one driving cycle but are instead good at all of them.

Secondly, a few additional tuning parameters are included. Rather than just tuning the power threshold P_{th}, like the OPSS, the GHS will also tune P_{csi} and $P_{PS,cop}$ (previously defined as $P_{csi} = P_{th}$ and $P_{PS,cop} = P_{PSopt} = 20$ kW for OPSS). This wide range of tuning will result in control policies that have not been tested before, and have not been replicated by the GECMS or GEMMS either. It is expected that this somewhat blind tuning process will yield improvements on OPSS (unless $P_{csi} = P_{th}$ and $P_{PS,cop} = P_{PSopt}$ happen to be the truly optimal tuning). The actual implementation of the GHS is identical to the OPSS (as shown in Fig. 5.15).

However, result from the tuning process show that the initial selection for $P_{csi} = P_{th}$ is already selected quite well, and the potential gains in fuel economy are smaller than 0.05%. Therefore, this chapter will not describe the tuning of this variable further, focusing instead on $P_{PS,cop}$. This also makes the presentation of the tuning results more readable. It should be noted that the use of only two tuning parameters is quite restrictive, and the ideal approach would be to consider at least three or four variables.

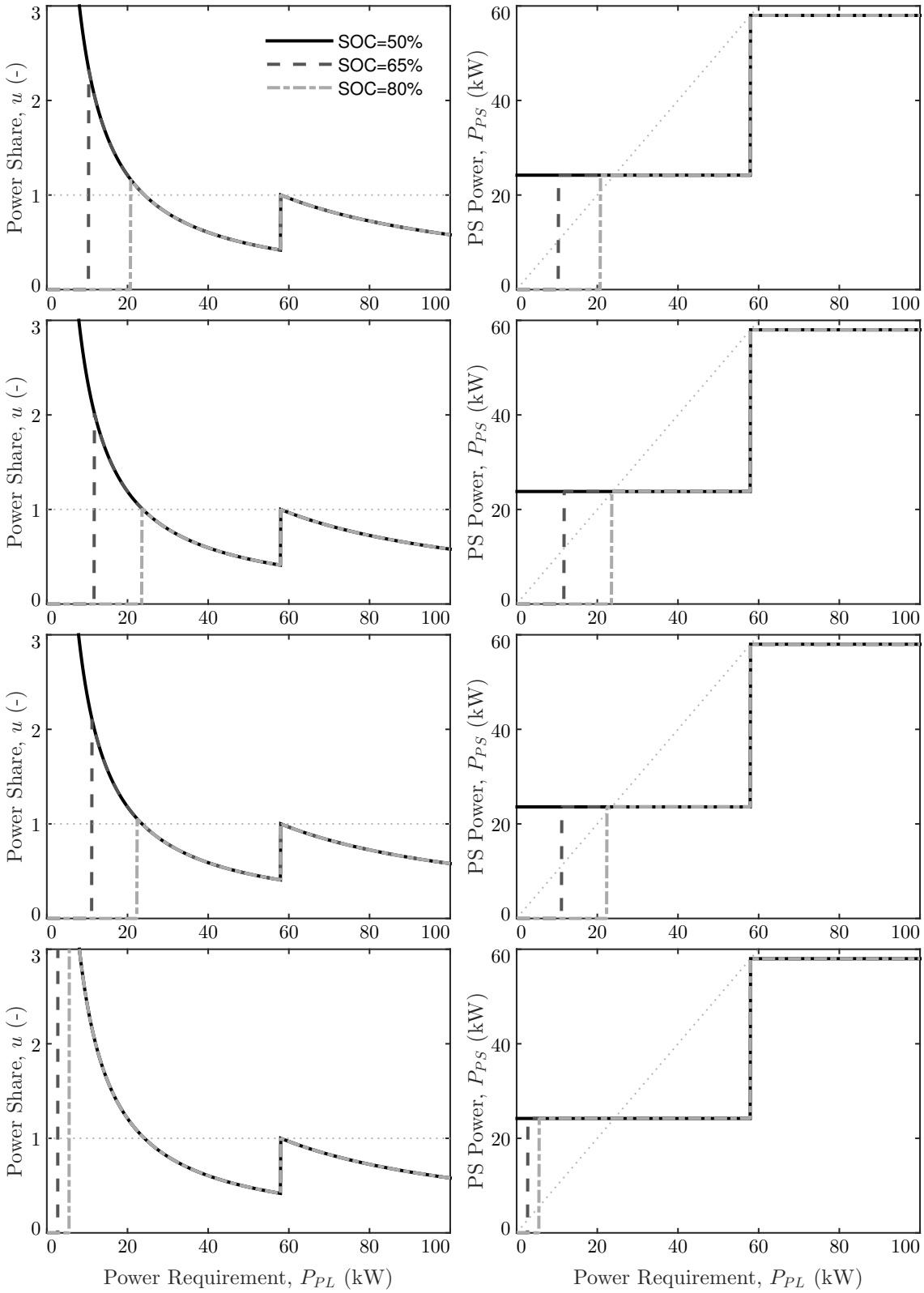

FIGURE 6.1: Optimal power share and PS power for varying power requirements and SOC for WL-L, WL-M, WL-H and WL-E (from top to bottom) for GHS.

The resulting control policy (based on the tuning process described in the upcoming subsection) for each of the four driving cycles is shown in Fig 6.1. This corresponds to: $P_{th} = 10.4$ kW and $P_{PS,cop} = 24.2$ kW for WL-L; $P_{th} = 11.8$ kW and $P_{PS,cop} = 23.8$ kW for WL-M; $P_{th} = 11.2$ kW and $P_{PS,cop} = 23.6$ kW for WL-H; and $P_{th} = 2.8$ kW and $P_{PS,cop} = 24.2$ kW for WL-E. The control policy can generally be considered a vertical shift of the OPSS control from Fig. 5.14, while maintaining close resemblance to the GECMS and GEMMS in Fig. 4.27.

6.1.2 Operation

The tuning process for the GHS involves simulating the control strategy with a wide range of P_{th} and $P_{PS,cop}$ for the four driving cycles. The presented tuning result for the three first driving cycles will be in the range $P_{th} \in [10, 12]$ kW and $P_{PS,cop} \in [22, 25]$ kW in intervals of 0.2 kW. However, the optimal tuning parameter for WL-E was found elsewhere and the tuning results are presented for $P_{th} \in [1, 4]$ kW and $P_{PS,cop} \in [22, 25]$ kW in intervals of 0.2 kW. The resulting tuning graphs for all driving cycles are presented in Fig. 6.2 with normalized EFC and final SOC values.

It can be seen that none of the optimal power levels are found at $P_{PS,cop} = 20$ kW, as was assumed for OPSS. Instead the ideal power levels are found at 24.2 kW, 23.8 kW, 23.6 kW and 24.2 kW for the four driving cycles. By noting that the final SOC for each driving cycle is very close to $SOC_{final} = SOC_{initial} = 65\%$, it can be understood that the GHS can use the PS constant operating point $P_{PS,cop}$ to affect the charge sustaining ability of the control strategy. The ideal base thresholds are found at 10.4 kW, 11.8 kW, 11.2 kW and 2.8 kW. Each of these has seen an increase compared to the OPSS (which had optimal thresholds at 9.2 kW, 10.2 kW, 10.4 kW and 5.4 kW), with the exception of WL-E. This final driving cycle didn't finish with $SOC_{final} = SOC_{initial}$ for OPSS, and should therefore be corrected by Eq. 5.9 to find P_{PSmin}. This value for OPSS if found to be at 1.32 kW. Thus, for each driving cycle, the effective threshold P_{PSmin} was increased for GHS, and the power level $P_{PS,cop}$ was increased as well.

While the OPSS determines the $P_{PS,cop} = P_{PSopt}$ with the aim to operate the PS efficiently and tunes the base threshold P_{th} to make the control strategy charge sustaining, the GHS uses both parameters to make the strategy charge sustaining and to improve overall powertrain efficiency. By having a higher $P_{PS,cop}$ level, the

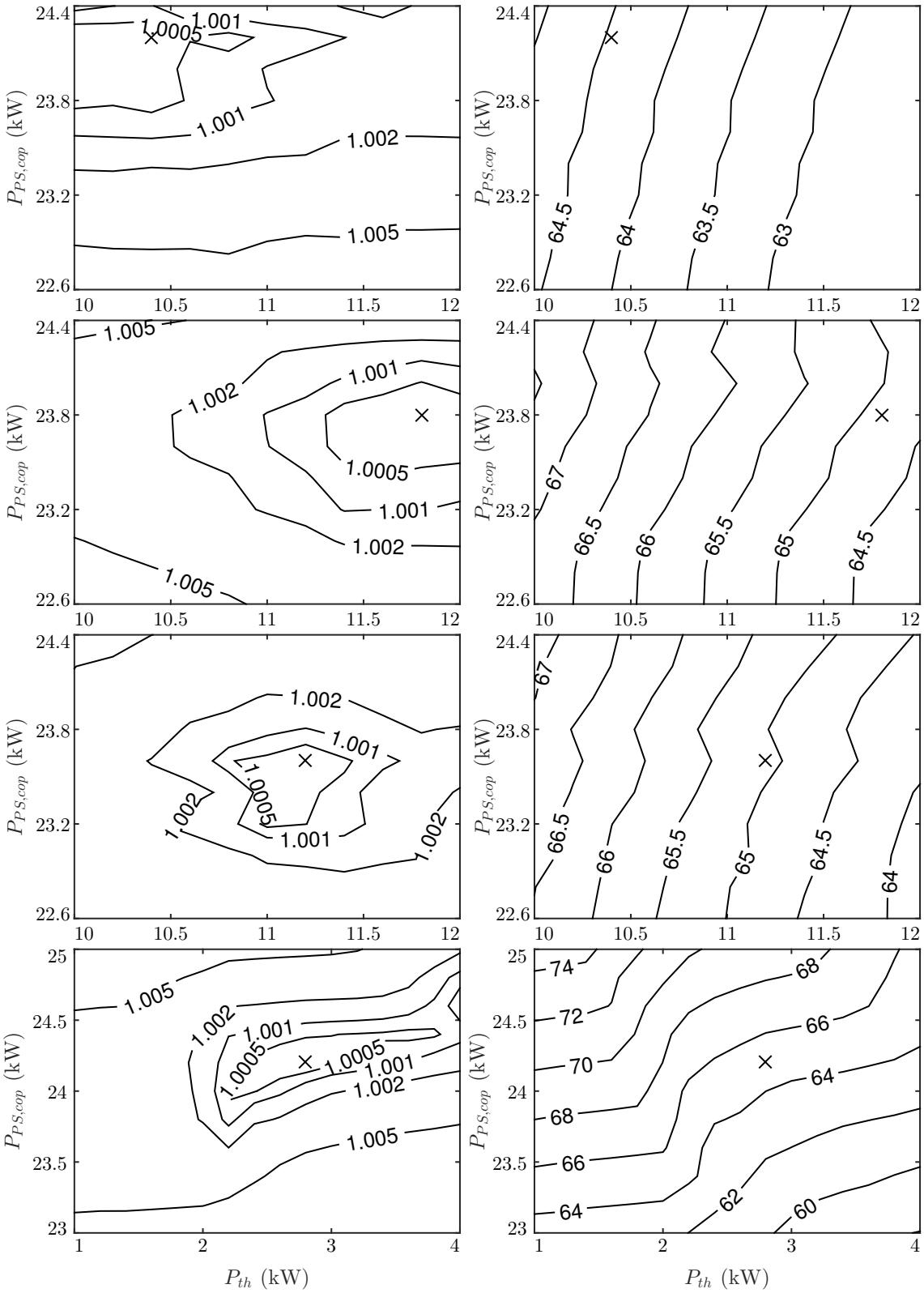

FIGURE 6.2: Normalized EFC M_{efc} (left) ($M_{efc} = 1$ is marked with a cross) and final SOC (right) for varying P_{th} and $P_{PS,cop}$ when driving WL-L, WL-M, WL-H and WL-E (top to bottom) with GHS.

base threshold level can be kept higher without compromising the charge sustaining ability. This allows the SS to be used to a larger extent.

Despite the global nature of tuning, the fuel economy is not very sensitive (relative to the sensitivities of the optimization-based strategies) to the tuning parameters. Even the final SOC values are very close to $SOC_{final} = SOC_{initial}$ for the first three driving cycles for practically the whole investigated search space. This speaks to the general robustness that often comes with heuristic strategies, and is further discussed in the next chapter.

It is also worth noting that the generally vertical nature of the SOC profiles (meaning that the SOC_{final} is not very dependent on $P_{PS,cop}$) for the first three driving cycles explains why the OPSS is able to achieve $SOC_{final} = SOC_{initial}$ without an optimal selection of tuning parameters. In these cases the base threshold P_{th} is the critical tuning parameter. However, for WL-E the SOC profiles are more horizontal (or diagonal), meaning that the SOC_{final} is quite dependent on $P_{PS,cop}$. Thus, for WL-E, the OPSS is not able to achieve $SOC_{final} = SOC_{initial}$.

To study the operation of the GHS, the power profiles for the first and final iterations of the driving cycles are shown in Fig. 6.3 and Fig. 6.4 respectively. The operation clearly resembles the OPSS operation, but with more intense use of the PS, and somewhat less frequent. It is also remarkable how similar the first and final iteration is for every single driving cycle: they are practically identical. This suggests that the GHS enters its efficient stride from the very start and is able to perform well through all the iterations, and is able to maintain a steady SOC. Nevertheless, the control and operation looks deceptively simple.

It is not until the fuel economy results are studied, that the performance of the GHS is appreciated. The fuel economy of the GHS is presented in Table 6.1 for the four different driving cycles. As can be seen, this control strategy has outperformed the GECMS for every single driving cycle, while maintaining the SOC sustained ($SOC_{final} \approx SOC_{initial}$). The GHS is particularly successful at slower driving cycles, but keeps an edge even at the highway. There is quite likely an alternative heuristic strategy that could serve as the core structure for another GHS that would excel for highway driving only. Overall, if the four driving cycles are considered together, the GHS improves the fuel economy by 0.83% compared to GECMS (and 0.58% compared to GEMMS).

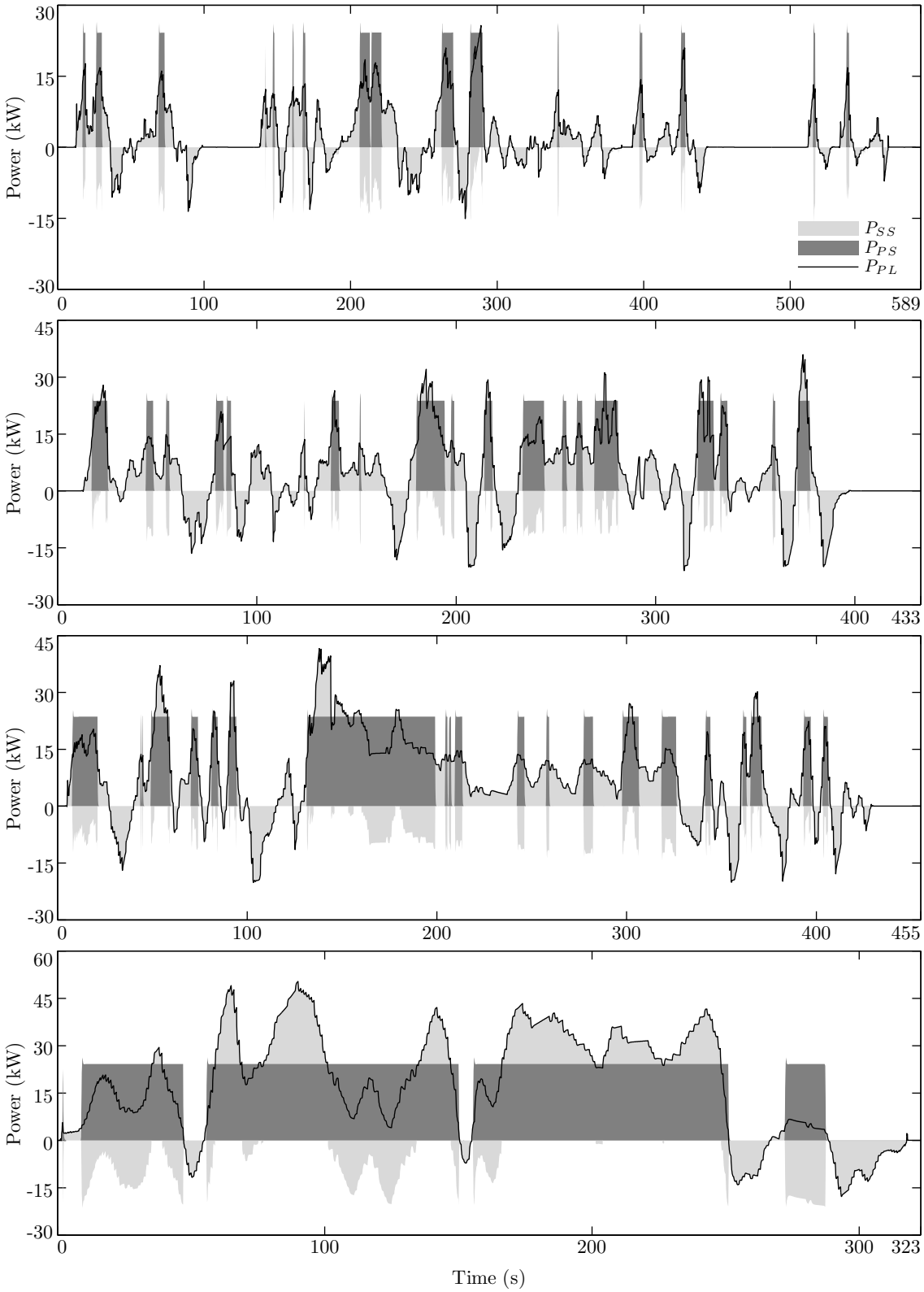

FIGURE 6.3: Power time histories for PS, SS and PL for the first iteration of driving WL-L, WL-M, WL-H and WL-E (top to bottom) with the GHS.

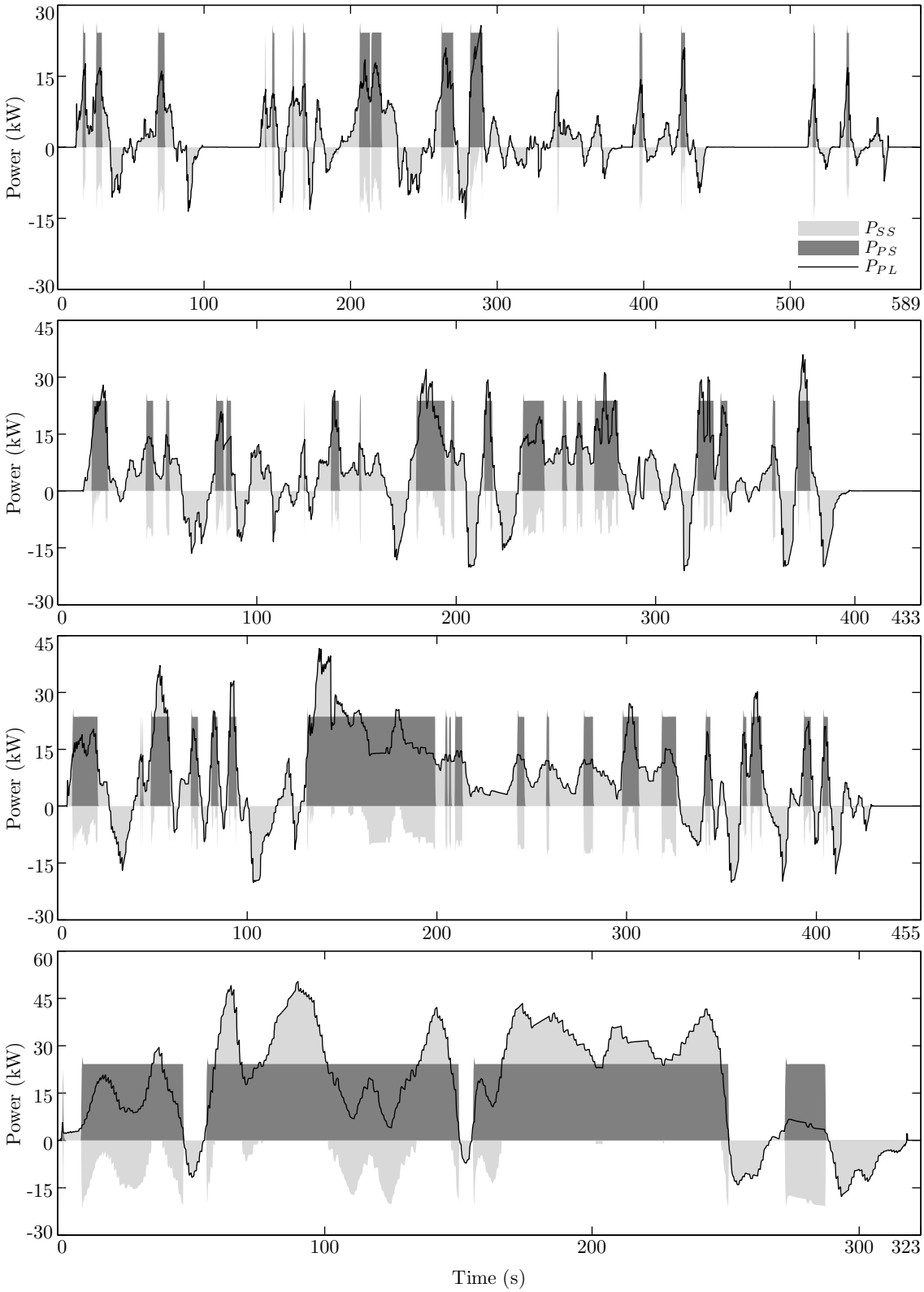

FIGURE 6.4: Power time histories for PS, SS and PL for the final iteration of driving WL-L, WL-M, WL-H and WL-E (top to bottom) with the GHS.

This impressive performance has been achieved with very simple rules and quite limited tuning. As the GECMS is outperformed by up to 1.8%, it suggests that the GECMS might not be as close to the global optimal solution as originally thought.

Table 6.1: Fuel economy results for GHS

Driving Cycle	SOC_{final} (%)	m_f (kg)	m_{efc} (kg)	Δ_{GECMS} (%)
WL-L	64.45	0.6895	0.6954	-1.82
WL-M	64.87	1.1227	1.1241	-1.34
WL-H	65.11	0.9453	0.9442	-0.64
WL-E	64.94	1.5826	1.5834	-0.12

6.2 Discussion

This section will discuss the findings of the previous section, where the GHS was found to outperform the GECMS and GEMMS. It will begin by exploring various causes for this unexpected result, before discussing the impact and conclusions for the wider body of work.

6.2.1 Causes

Precision of Implementation

The first possible, but trivial, suspect for the cause of the GECMS and GEMMS being outperformed by the GHS is the precision of implementation. Both of these strategies were implemented with three significant digits. However, these control strategies are very sensitive to changes in the equivalence factors, where a change of 0.3% (roughly double the error margin of three significant digits) in just one of the equivalence factors can change the SOC_{final} with more than 2%. However, by studying the tuning plots for both the GECMS and GEMMS, it can be seen that the general area around the optimal policy selection in terms of fuel economy is quite flat, and any hidden solution between the studied points is unlikely to be more than a 0.1% improvement.

However, there are a few additional imprecisions. The whole process of designing these strategies has involved discretizing each space. The PS fuel consumption and efficiency has been measured for engine speeds and power levels that have been discretized in 10 rpm and 0.1 kW intervals respectively. The SS efficiency has been determined for SOC and power levels that have been discretized in 1% and 0.1 kW intervals respectively. Also, the input for the control system, the load power P_{PL} is discretized in 0.1 kW intervals before being processed. Altogether, these minor imprecisions can be accumulated into a somewhat larger error. Nevertheless, these imprecisions are unlikely to account for the whole difference between the GHS and the studied global strategies. Also, the discretization in this work has been quite narrow, relative to other work and implementations in the literature.

Limited Search Space

There are many limitations in the search space for the proposed global strategies in this work. A DP solution allows for the controller to apply different control inputs for two instances t_1 and t_2 where the load requirement and vehicle states are identical. This is not possible for GECMS or GEMMS, for which the control input is essentially a mapping between load power P_{PL} (and SOC for GEMMS) and the control input. Thus, at any two instances t_1 and t_2, where the load power is identical (as well as the SOC for GEMMS), the power share ratio u as determined by the GECMS and GEMMS will always be identical, independent of where in the driving cycle these two instances are.

It is also important to understand the role of the equivalence factors in determining the control policy for the GECMS (and replenishing efficiencies for GEMMS). Each GECMS control policy assumes a constant S_d and S_c for the duration of the driving cycle. Furthermore, the same set of equivalence factors are considered for a particular policy for all power requirements. Thus, an optimal policy, such that it requires different equivalence factors at different power levels, would never be able to be discovered by the GECMS. This can be visually understood as follows. As the equivalence factors are tuned, every single point of the control map in Fig. 3.16 is adjusted. For the ideal selection of equivalence factors, certain parts of the control policy match the optimal policy. Any further tuning would make some additional points match up with the optimal policy but a larger number of points would fall out of alignment with the optimal policy, with a net negative impact on fuel economy. Thus, despite the tens of thousands of control policies that were tested for GECMS and GEMMS, none of these matched the better control policies that GHS produced.

To quantify some of these limitations, we can look at the number of control decisions that are designed. For the GECMS, a control decision is defined for each load power $P_{PL} \in [0, 100]$ kW in increments of 0.1 kW. In each case, the PS can take on a value of $P_{PSref} \in [0, 58]$ kW in increments of 0.1 kW, although this will be restricted in many cases due to the limited ability of the SS to be charged. For simplicity, 300 different possible control decisions can be considered. Thus, 1001 scenarios are considered with 300 possible decisions in each case. A brute force approach would allow 300^{1001} different control policies, while the GECMS would at most have tested 100×100 (assuming 100 values each of S_d and S_c are trialled). This constitutes a

negligible part of the control space (which is mostly junk). In the case of GEMMS, the SOC is also considered as $SOC \in [50, 80]\%$ in 1% increments, resulting in a total of 31,031 control scenarios, and thus $300^{31,031}$ different control policies. Of course, any intelligent approach to optimization would not consider each of these cases, but the necessary computational time would become prohibitive long before we can consider additional factors such as engine temperatures or battery voltage.

Complexity of Model

The fallibility of the global optimal benchmark has not been considered an issue in previous work, where a simplified and reduced model is used to apply DP to identify the global optimal solution. This solution has been found by exhaustively searching the feasible points of operation, and truly represents the global optimal solution of that particular model. Thus, in the case of an ECMS (or any other real-time strategy) being tested on a quite simple model and the DP on a very simple model, the benchmarking can be considered quite valid. This explains why in general the DP results are marginally better than the real-time control strategies, as should be expected. However, in the case of a real-time control strategy being applied to detailed dynamic model, and being compared to a DP solution on a very simple model, the results can't be considered valid.

In fact, considering a normal distribution of any systematic deviation between the full and simplified model, it should be expected that the DP is outperformed by an excellent real-time control strategy almost half the times. There are some reported cases of the DP being outperformed, but these have typically been attributed to numerical errors. Also, such negative results might be held back from publication. However, considering that most real-time strategies are at least 1-2% inferior to the DP, any results with a simplified model that produces fuel economy errors (relative to the full model) within $\pm 1\%$ would produce results consistent with the expectation of DP beating the real-time strategy. However, the accuracy of the simplified models are never disclosed in the published works.

Apart from the inaccuracy of the simplified model, it is worth recognizing the inaccuracy of the full models as well. These are very often vehicle models with a handful of states (maybe some of SOC, engine speed, transmission gear and vehicle speed). However, a real vehicle would be greatly affected by many more states and would

experience transient behavior that can't be modeled. This discrepancy can easily be observed in any work that publishes experimental data together with simulation data. The error in the full model is typically larger than the 1-2% that were previously mentioned for the simplified model. The vehicle model in this particular work has been modeled in greater detail than most previously published work, and includes states and transients that give a better representation of a real vehicle. Thus, the greatly simplified analysis of GECMS (assuming constant component efficiencies, steady state fuel consumption, instantaneous engine speed changes, etc.) is not as successful as it would be on a simpler model.

6.2.2 Impact

Simulation vs Reality

In the published body of work on SCSs, the vast majority of proposed control strategies have been demonstrated on vehicle simulations only. This is reasonable enough, considering the costs involved in real vehicle validation. However, it is important to recognize the compromise in accuracy when dealing with simulation results.

Based on the findings in this work, as well as some experience with other vehicle models, it could be claimed that the complexity of the ideal control policy is inversely proportional to the complexity of the vehicle model. A very simple model can make use of optimization techniques such as DP to obtain the optimal control policy. A medium-level model wouldn't allow DP solutions, but has simple enough dynamics to be analyzed to design an optimization-based control strategy that would perform very well. A high fidelity vehicle model or a real vehicle would only allow the optimization-based control strategy to analyze a fraction of the vehicle and component dynamics and would thus design a competent control strategy (recognizing that most of the assumptions going into the design would not hold during actual operation), which might be comparable to a well-designed heuristic strategy.

However, at this point the distinction between an optimization-based and a heuristic strategy becomes somewhat blurred. The ideal heuristic strategy could be derived either by brute force tuning (similar to numerical optimization approaches like DP or GA) or by heuristics derived from analysis of the powertrain (similar to ECMS or EMMS). Nevertheless, as it is not feasible to execute an extensive tuning process on

a real vehicle, and quite difficult for a high fidelity model, the best approach might be to use the analysis behind optimization-based strategies to inform the control structure for the heuristic strategy, which can then be tuned on a high-fidelity model, with further minor adjustments by tests on a real vehicle.

A final example of this point can be made by considering the optimal engine speed map that was produced in Section 2.3.4. The standard method to design this map is to determine the most efficient engine speed for each possible load requirement, and use the corresponding point of operation for each given load during driving. However, recognizing that the change in engine speed is not instantaneous in our model, or in reality, it was found that the vehicle performed better if a smoother engine speed map was implemented, although this would result in suboptimal points of operation. Essentially, it was preferable to operate on a slightly suboptimal engine speed consistently, rather than have significant changes in engine speed every second in the pursuit of achieving the "optimal" engine speed, as defined by its steady state efficiency. This illustrates how simplistic analysis that performs well on simpler models might be bad for high fidelity model and real vehicles.

Better benchmarking practices

As discussed, the validity of DP solutions executed on a simplified model is questionable. The application of theoretically sound analysis on a bad model of reality will not yield sound control policies or good benchmarking results. There is thus a need to develop tools that allow the determination of the global optimal performance, or at least an approximate solution, for high-fidelity models for benchmarking purposes. There are many possible paths towards this, but based on this work, it is probably a good idea to be open-minded about what the balance should be between pre-design analysis and tuning. The former might be more rigorous, elegant and transferable (to be applied on other powertrains), but the value of a richer and more vast search space might be useful. This is not to argue for a brute force method, but possibly something like the GHS, where a competent heuristic strategy is defined and then multiple aspects are opened up for tuning. Any such tuning will explore control space that would have been ignored by optimization-based strategies.

A variation of this approach could be to further tune the control policy of the GECMS. Having found the ideal set of equivalence factors, further control space

can be explored by strategically increasing or decreasing the power share ratio for various power requirements. The easiest approach might be to smoothen the control policy and remove occurrences of very low SS power being charged or discharged. Depending on computational load, more advanced tuning could be done. The essential principle would be to treat the original GECMS control policy as a competent "initial guess" rather than as the actual optimal policy.

In fact, the objective of actually achieving a guaranteed global optimal policy might be impossible for a high-fidelity model or a real vehicle. Not only is the search space incredibly vast, but the complexity of the model, and the significant amount of interconnectivity between powertrain components, makes the system exhibit certain chaotic features. The effects of a particular control decision cannot be predicted well enough, despite the system being deterministic. This limits any analytical approach to the problem, thus prohibiting any rigorous proof of optimality. Thus, it might be more productive to determine a different benchmarking target; possibly defined by the searched control space. For example, a numerical optimization approach might be applied to obtain the optimal control policy such that the control decision u is defined for each load power P_{PL}. Thus, for any two time instances t_1 and t_2 where the load power P_{PL} is identical, the control decisions u_1 and u_2 will also be identical. Although this is a compromise on optimality, it would be a well-defined solution that would be more informative as a benchmark than a DP solution on a simplified model.

Powerful heuristic strategies

The findings of this work also emphasize the potential of heuristic strategies. The rule-based strategies are often overlooked as a simplistic approach that exist for historic reasons or are at best useful as baseline benchmarks. However, it is important to appreciate the significant value they offer. Not only are they very effective (assuming well designed rules), they are in fact remarkably robust against modeling inaccuracies. For example, Serrao et al. in [3] found that heuristic strategies outperformed ECMS if applied to models which included temperature dynamics for the engine. This advantage would be significantly stronger on a real vehicle where all kinds of additional dynamics come into play.

The most appropriate method for designing SCSs for real-time implementation might therefore be to produce good suboptimal control policies (preferably by previously mentioned method) and then extract simpler rules to produce a real-time control strategy. There have been some works in the literature taking this approach of converting DP solutions into rule-based strategies as well. This might be the best approach until more powerful tools exist to design optimization-based control strategies for high fidelity models. However, strong candidate methodologies for producing good suboptimal solutions would include the NN (neural network) approach, which is applied in [50]. It demonstrates many of the desired features, including the ability to deal with larger search spaces (considering state space, control space and decision space).

6.3 Summary

Based on the surprisingly impressive results of the previous chapter, this chapter has investigated the claim that the GECMS delivers results that are close to the global optimal solution. The most suitable approach was identified to be the global tuning of a heuristic strategy, producing the GHS, in an attempt to outperform the GECMS. The GHS in this work was based on the OPSS. Several control parameters were investigated, but finally only the power level was treated as a tunable parameter. This control strategy was found to outperform the GECMS by 0.83% (the improvement for WL-L was 1.82%), thereby discrediting the claim to approximate global optimality of the GECMS.

The causes for this failure of the GECMS are multiple, including the precision of implementation, the limited search space, and the complexity of the model. However, the latter might be most relevant. Optimization-based control strategies (and benchmark implementations like DP) have often been implemented on simple models, where they are most effective. The vehicle dynamics are simple enough to be analyzed and controlled effectively, and simple assumptions might either hold true for the model or affect the performance negligibly. However, a real vehicle, or a high-fidelity model as the one used in this work, will have significantly richer dynamics that are not as easy to analyze, and practically impossible to control optimally. Thus, the GECMS, which might perform close to the global optimal solution for a simple model, is less effective on the vehicle model in this work.

Consequently, it raises the importance of appreciating the differences between simulation results and reality. These differences can be partly reduced by using high-fidelity models. However, this in turn will require the development of better benchmarking practices to be applied to high-fidelity models, as the current benchmarking tools require excessive computational load. A potential solution could be in the form of a tunable heuristic strategy, like the GHS, but with a more robust method of tuning and defining the control space. Lastly, the point from the previous chapter was further strengthened: heuristic strategies (with inspiration from optimization-based strategies) might be the most suitable category of control strategies for commercial vehicles.

Chapter 7

Control Sensitivity Analysis

The past chapters have presented both conventional and novel control strategies, and have evaluated their results in terms of fuel economy. However, it is of interest to consider the performance of each control strategy more broadly. Other work in the literature may consider additional performance metrics, such as emissions, battery degradation or drivability, but there is a very limited body of work on the sensitivity of the strategies to various design or operating conditions. Ignorance of such considerations may lead to the design of control strategies that only perform well under very particular operating conditions (realized in a simulation setting), such as driving profile or initial battery SOC. A control strategy that excels on two driving cycles, but performs terribly at ten other driving cycles, might appear very impressive if only tested on the "right" set of driving cycles. Furthermore, the performance of control strategies might be significantly affected by technological developments, such as improvements in the performance of start stop systems (SSSs) or batteries. It is important to appreciate these sensitivities to determine how the optimal strategy might change with time.

This chapter will analyze and compare the sensitivities of the six presented real-time control strategies (TCS, PFCS, XOS, OPSS, EMMS1 and EMMS2) to four different factors: correct tuning of the control parameters; effectiveness of the SSS; initial conditions of the vehicle; and the driving cycles being tested. Each of these will be considered in a separate section. The objective of this study is to further understand the strengths and weaknesses of the different control strategies, so they can be selected more appropriately.

7.1 Tuning Parameters

This section compares the six real-time control strategies that have been presented in this work, in terms of the sensitivity of the fuel economy results to the tuning of the control parameters.

To make any such comparison possible, it is necessary to normalize the fuel economy results as well as the tuning parameters. The former can be dealt by the normalized EFC M_{efc} that has been used throughout this work already, with the distinction that each control strategy will be normalized separately. Thus, each control strategy will have $M_{efc} = 1$ at its optimal point. Also, the total fuel economy results are considered (for all four driving cycles together). This ensures $M_{efc} \geq 1$ at all points, and the results are more readable.

Normalizing the tuning parameters is less straightforward, but the most appropriate method was found as:

$$X_{tune} = \frac{x_{tune}}{x_{tune,opt}} \tag{7.1}$$

where x_{tune} is the tuning parameter for the SCS in question, and $x_{tune,opt}$ is the optimal value that yields the best fuel economy results. For control strategies with two tuning parameters (PFCS, EMMS1 and EMMS2), the more influential parameter is considered. For PFCS, the fuel economy results are mainly driven by P_{min}, whereas P_{ch} only has a minor role (in fact $P_{ch} = 0$ is used in this work). For EMMS1, the performance is governed primarily by η_{re}, while D_{csi} is for CS purposes. Lastly, for EMMS2 $D_{csi,d}$ and $D_{csi,c}$ (modifying $\eta_{re,d}$ and $\eta_{re,c}$ respectively) have equal conceptual influence. However, as the range of variation in $\eta_{re,d}$ for various driving cycles is much greater than $\eta_{re,c}$, the $D_{csi,d}$ parameter is found to be the most influential.

The tuning results for TCS, PFCS, XOS, OPSS, EMMS1 and EMMS2 from previous chapters are then processed and normalized as discussed, and are presented in Fig. 7.1. Here, the optimal results for each control strategy is found at $X_{tune} = 1$ (where $M_{efc} = 1$). The results are shown in the range $X_{tune} \in [0.6, 1.4]$, meaning that the tuning parameter is considered within $\pm 40\%$ of its optimal value.

It can be seen that the TCS and PFCS are most sensitive to the correct tuning of its control parameters, with the latter producing 1% inferior fuel economy for a 10% error in tuning. Both the XOS and OPSS are significantly less sensitive, with a 20% tuning error only compromising the fuel economy by about 0.2%. The XOS

in particular is impressive, allowing up to 40% tuning error while the fuel economy only drops by 0.2%. The EMMS1 results are defined within a narrow range (but represents the relevant tuning space) where the fuel economy is compromised 0.2-0.3% for bad tuning. EMMS2 is tuned for a much larger range, and show extremely low sensitivity for the lower range of the tuning parameter (less than 0.1% drop in fuel economy for tuning error of 35%), while there is a significant error for the higher range (1% drop in fuel economy for tuning error of 5%).

Many of the tuning sensitivity profiles are somewhat asymmetrical, meaning that the sign of the tuning error is relevant. In general, it can be seen that it is preferable to overestimate the value for the tuning parameters, rather than underestimate, with the EMMS2 being the only clear exception (and the TCS in very close range of the optimally tuned value). A larger set of control strategies would be needed though, to study such a bias further.

It can also be seen that the range for the various control strategies is different: the EMMS1 results are defined for roughly $X_{tune} \in [0.97, 1.03]$ (as $\eta_{re} \in [34, 36]$) while EMMS2 is defined for $X_{tune} \in [0, 1.37]$ (as $D_{csi,d} \in [0, 5]$). It can thus be seen that lower values of x_{tune} will produce relatively larger values of X_{tune} (e.g. $x_{tune} = 6$ and $x_{tune,opt} = 5$ will give $X_{tune} = 1.2$, while $x_{tune} = 51$ and $x_{tune,opt} = 50$ will give $X_{tune} = 1.02$). Thus, the X_{tune} parameter might mean quite different things for each control strategy. Nevertheless, this definition of X_{tune} together with the presented range (which gives an indication of the relevant search space), gives sufficient information to evaluate the sensitivity of the tuning process.

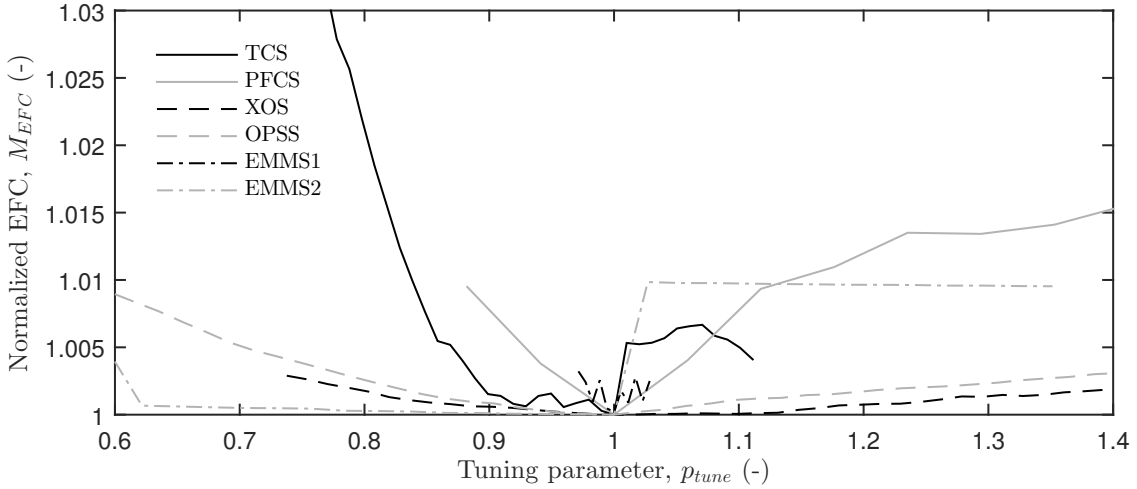

FIGURE 7.1: Fuel economy sensitivity profiles for the tuning of control strategies.

7.2 Start Stop System

This section investigates the SSS impact on the fuel economy results of the six real-time control strategies presented in this work. In particular, it looks at how effective each control strategy would have been for a SSS with a different turn-on penalty.

It has been suggested earlier in this work that the conventional heuristic SCSs, which aim to minimize the number of engine turn-on events, are based on outdated ideas of the tradeoff between engine idling and switching. In the 1980s, the rule-of-thumb used to be that the engine should be switched off if the vehicle is expected to idle for 30 seconds or more. This tradeoff has become updated with time, and it has been commonly advised in the past decade that the tradeoff is 10 seconds. However, as mentioned earlier in Section 2.5.3, modern HEVs use very efficient SSSs that have reduced this tradeoff to less than 1 second. The vehicle model in this work uses a SSS that penalizes each engine turn-on event by a fuel penalty m_{pen}, defined as

$$m_{pen} = T_{SSS} \cdot \dot{m}_{idling} \tag{7.2}$$

where T_{SSS} is the tradeoff time between switching off and idling, and $\dot{m}_{idle}$ is the rate of fuel consumption during idling operation. In this work $T_{SSS} = 1$ second has been used (corresponding to $m_{pen} = 0.00011$ kg).

It would be interesting to find how the fuel economies determined in the previous chapters would be affected by a different selection of T_{SSS}. To proceed with this analysis, the number of engine turn-on events $N_{turn-on}$ for each control strategy (when optimally tuned) are measured, and the overall fuel economy is defined as:

$$m_{efc} = m'_{efc} + N_{turn-on} \cdot m_{pen} \tag{7.3}$$

where m'_{efc} is the pre-correction value for the EFC (which can be calculated from the previously obtained results by computing $m'_{efc} = m_{efc} - N_{turn-on} \cdot 0.00011$). Furthermore, as the EMMS2 results are the best for each driving cycle, it is appropriate to normalize all the fuel economy values for the $m_{pen} = 0$ case of EMMS2 operation, as:

$$M_{efc} = \frac{m'_{efc} + N_{turn-on} \cdot m_{pen}}{m'_{efc,EMMS2}}. \tag{7.4}$$

This would give $M_{efc} \geq 1$ for all control strategies, for all positive values of T_{SSS}.

The normalized fuel economy results for $T_{SSS} \in [0, 30]$ seconds are presented in Fig. 7.2 for the four driving cycles. It is important to understand that the slope of the lines are proportional to $N_{turn-on}$. Thus, a control strategy with a low value for $N_{turn-on}$ would have a flat profile (like TCS and PFCS), whereas a higher $N_{turn-on}$ value would lead to an increasing profile. Also, as mentioned, the actual fuel economy results for the vehicle in this work are those that correspond with $T_{SSS} = 1$ second.

The most striking feature of these charts is the flat nature of the TCS and PFCS. As these control strategies make use of a state changing charge sustaining mechanism (as discussed in Section 5.1.2), the aim is to minimize the number of engine switching events. This used to be a sensible policy two decades ago when these control strategies were developed, but is clearly less effective today. As can be seen, the XOS outperforms the PFCS for $T_{SSS} < 4$, $T_{SSS} < 7.5$, $T_{SSS} < 11$ and $T_{SSS} < 17$ seconds, for the four driving cycles respectively. The other control strategies outperform the TCS and PFCS with an even more generous margin for T_{SSS}. This clearly suggests that the aim to minimize $N_{turn-on}$ should not be a priority once the SSSs are good enough to deliver about $T_{SSS} = 5$ seconds, which happened many years ago.

This largely explains why the XOS and OPSS have been able to outperform the conventional heuristic control strategies (TCS and PFCS) with very large margins (up to 20%). These novel control strategies are designed in a paradigm where significant engine switching is a necessary requirement to achieve good fuel economy results. In fact, it is interesting to observe that the optimization-based strategies (EMMS1 and EMMS2) typically have a higher slope (larger $N_{turn-on}$ values) than XOS and OPSS. Consequently, the EMMS are more sensitive to T_{SSS}, and are actually outperformed by the OPSS for high T_{SSS} values for most driving cycles. This is particularly pronounced for WL-E where the EMMS2 is the best strategy for $T_{SSS} = 0$ and the worst strategy for $T_{SSS} = 30$ seconds.

However, it is worth emphasizing that the reduction of $N_{turn-on}$ is not only a matter of fuel economy. Any such switching causes undesirable jerks in operation that need to be kept low for the comfort of the driver. Also, there might be considerations in terms of component degradation, as frequent engine switching has a negative impact on the engine life. However, most modern engines will fail for other reasons, long before the switching becomes a dominant influence. Thus, although extremely frequent engine switching might be undesirable, it is likely to become less of an issue with time.

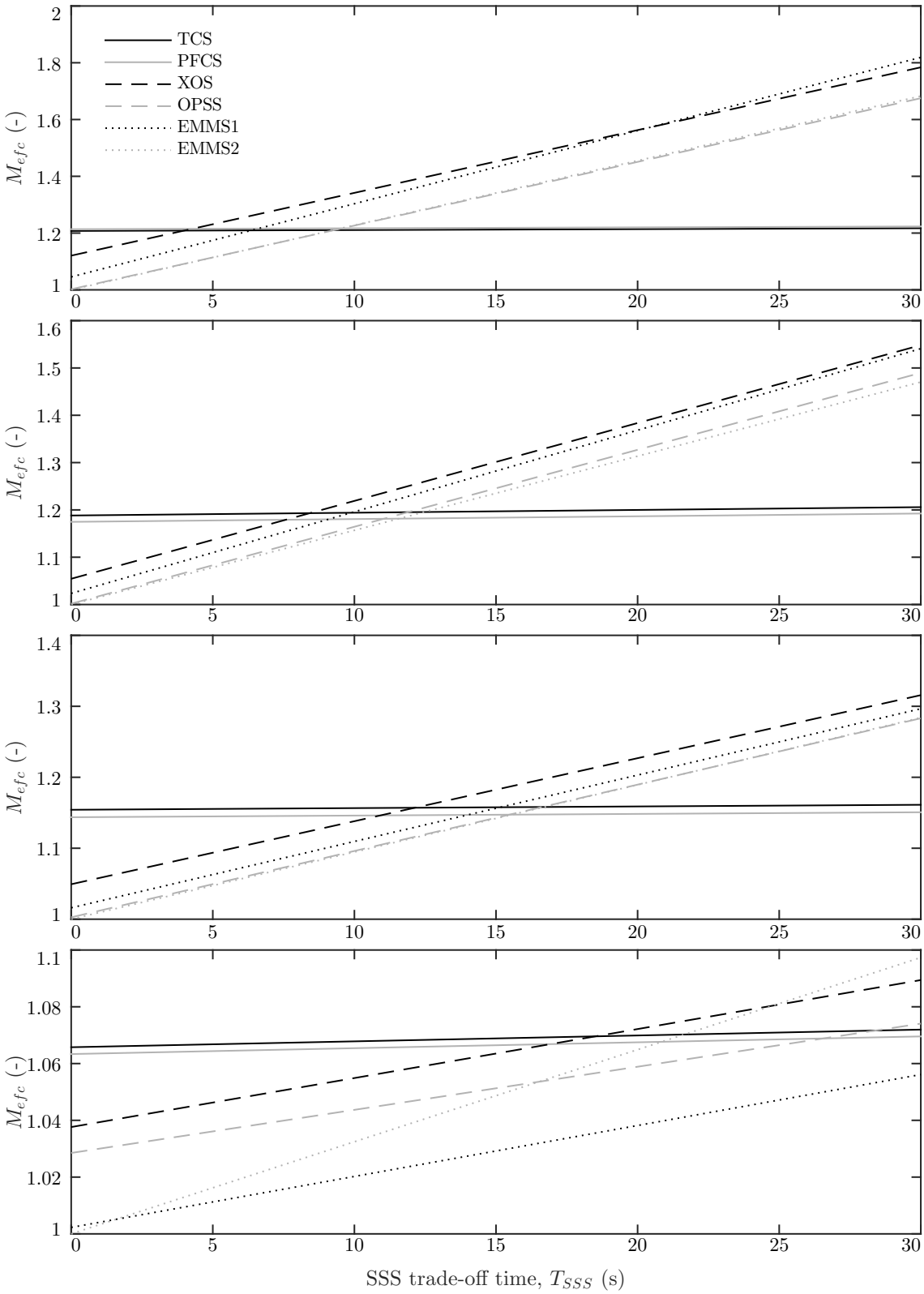

FIGURE 7.2: Normalized EFC M_{efc} for varying tradeoff time between engine switching and idling, when driving WL-L, WL-M, WL-H and WL-E (from top to bottom) with six different real-time control strategies.

7.3 Initial Conditions

This section investigates the influence of simulation initial conditions on the final state of the vehicle and its fuel economy. It focuses on determining how sensitive each of the presented real-time control strategies are to the setting of the initial SOC value, $SOC_{initial}$.

All the simulation results presented in this work so far have consistently used the same initial conditions. The state of the vehicle at the start of the simulation is identical for when testing each control strategy. This is essential to allow a fair comparison between various control strategies, which has been an essential part of this work. However, this comes with a few limitations. To measure the performance of the control strategies for the same initial conditions every time, might not be indicative of actual performance in a real vehicle, where initial conditions vary for every single journey. There are several initial conditions that could be considered. However, most states have quite fast dynamics and would quickly return to some reference value (e.g. DC Link voltage, battery voltage, etc.), so any variation in initial condition would have a negligible effect. Instead, it is more useful to consider states like ambient temperature, engine temperature and battery SOC, as these change more slowly and can impact simulation results to a larger extent.

In this chapter, only the battery SOC will be considered. The ambient temperature should affect both the battery and engine performance, but as the vehicle model in this work does not include battery temperature dynamics, the results of such a study would not be valid. A sensitivity study of engine temperature could be done, but considering that most real journeys, and most commercials tests, are done with a cold start of the engine, this is probably an appropriate assumption for all tests. The battery SOC, however, is distinct in the sense that it does not tend towards a reference or ambient value with time. As such, each journey with a real vehicle might start with any battery SOC value, depending on the past history of driving of the vehicle. Therefore, the influence of the initial setting of SOC on the fuel economy and final SOC for each journey will be studied.

To investigate this, new simulations are run for the optimal setting of the six real-time control strategies presented in this work, with the following three initial SOC values: $SOC_{initial} \in \{50, 65, 80\}\%$ (as $SOC_L = 50\%$ and $SOC_U = 80\%$). Results of normalized EFC and final SOC for the four driving cycles are shown in Fig. 7.3.

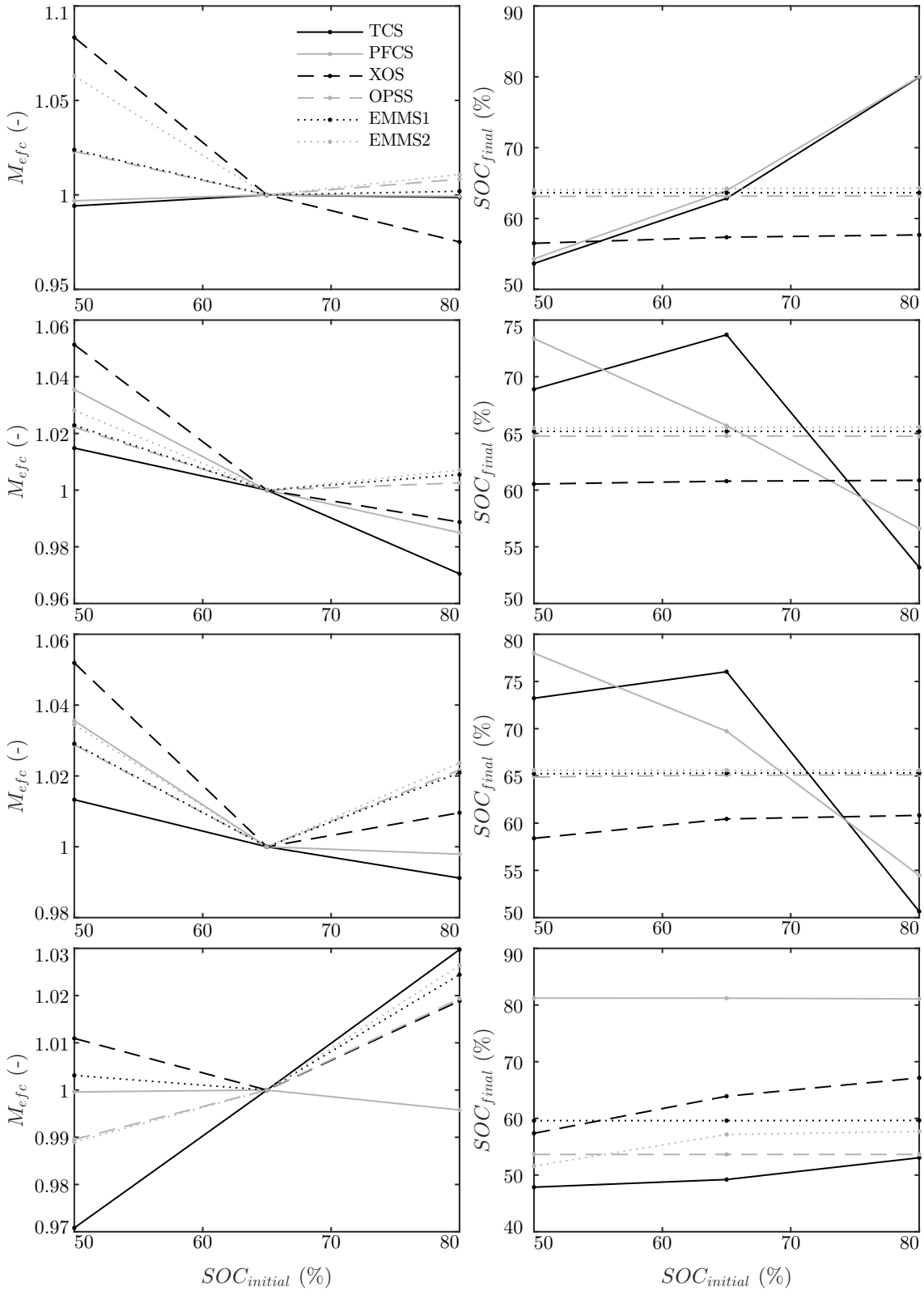

FIGURE 7.3: Normalized EFC M_{efc} and final SOC for varying values of initial SOC at the start of simulations when driving WL-L, WL-M, WL-H and WL-E (from top to bottom) with six different real-time control strategies.

Note that the EFC is calculated based on the new initial SOC values, and that the EFC of each control strategy has been normalized with respect to the EFC results corresponding to the case of $SOC_{initial} = 65\%$ of the same strategy:

$$M_{efc} = \frac{m_{efc}}{m_{efc,SOCinitial=65\%}}. \tag{7.5}$$

Also, note that the lines are based on only three values of $SOC_{initial}$ for each control strategy and line charts have been used to allow easier distinction between the strategies. Interpolating these results would not be valid (for TCS and PFCS in particular).

It can clearly be seen that the impact of varying $SOC_{initial}$ on the fuel economy of each control strategy is very significant, with fuel economy typically improving for higher $SOC_{initial}$ values. This is the expected result, as the battery gets more efficient for higher SOC levels. The conventional rule-based strategies TCS and PFCS are least affected, as their operation tend to by cyclical, and no particular SOC_{final} is preferred (as is clear from the SOC_{final} plots). However, WL-E is an exception as both the TCS and PFCS are forced to use their emergency handling rules and operate consistently around $SOC = 50\%$ and $SOC = 80\%$ respectively. In this case the TCS benefits from being able to operate in its steady mode as long as possible, and it thus has better fuel economy at lower SOC levels.

The EMMS1 and EMMS2 are slightly more sensitive to the initial SOC setting in terms of fuel economy, but it can be seen that the final SOC values remain consistent for all settings, for all driving cycles (apart from the drop for $SOC_{initial} = 50\%$ for WL-E for EMMS2). This is an effect of the charge sustaining mechanisms of these strategies, meaning that they will seek themselves towards $SOC_{final} = 65\%$, independent of the initial setting of $SOC_{initial}$. As a consequence, the fuel economy is compromised for any deviation from the $SOC_{initial} = 65\%$, as they have to struggle their way towards this operating point. Again, the WL-E is an exception as the EMMS strategies have their optimal operating point below $SOC = 65\%$ for this driving cycle, and thus the $SOC_{initial} = 50\%$ setting ends up being favorable, for EMMS2 in particular.

The OPSS performs quite similar to the EMMS, and is actually less sensitive than EMMS2 to $SOC_{initial}$ variations in terms of SOC_{final} values. But it is slightly less successful in keeping the SOC close to the $SOC_{final} = 65\%$. However, the XOS has

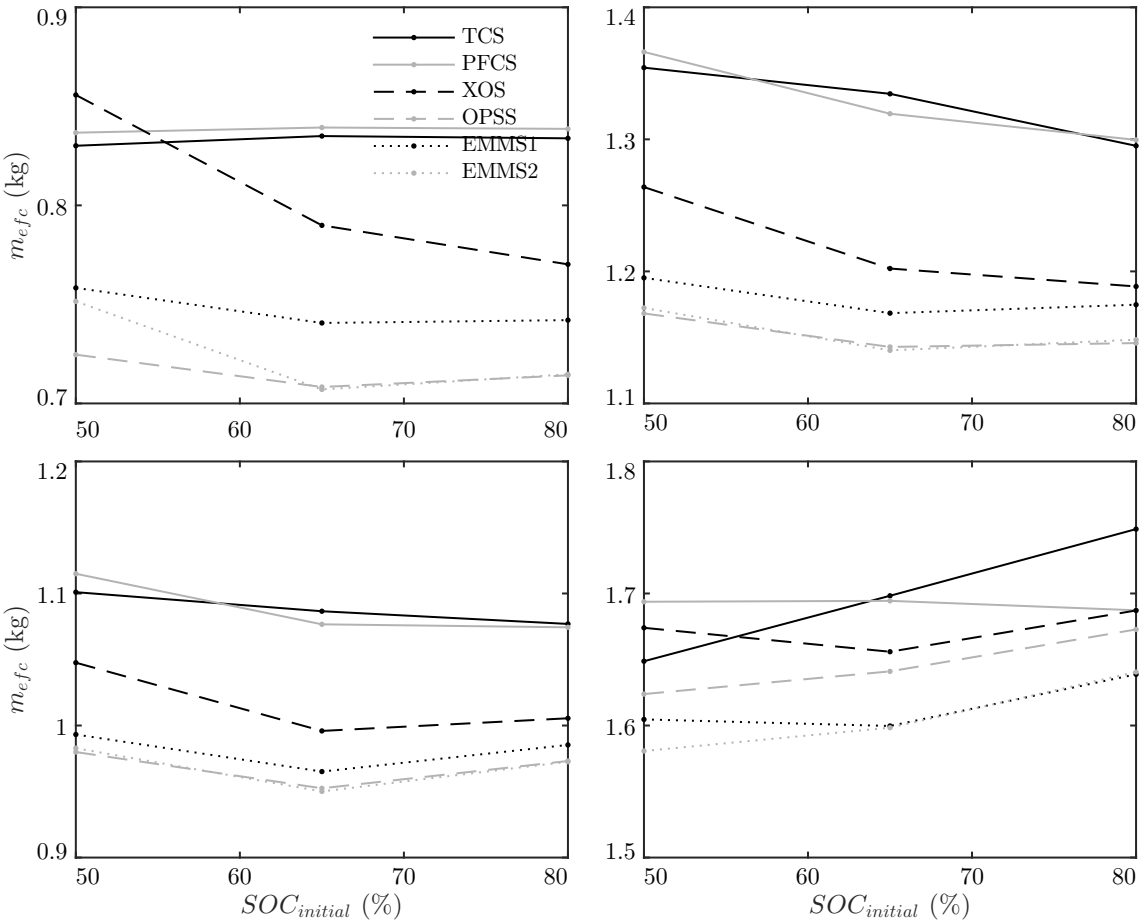

FIGURE 7.4: Equivalent fuel consumption m_{efc} for varying values of initial SOC at the start of simulations when driving WL-L (top left), WL-M (top right), WL-H (bottom left) and WL-E (bottom right) with six different real-time control strategies.

the most distinct profiles. In terms of fuel economy, it is the most sensitive to varying $SOC_{initial}$ values. This can easily by understood by its limited ability to control its SOC trajectory, as it is unable to recharge the battery directly and has to rely on regenerative braking to increase the SOC. Most importantly, the XOS is not ever supposed to operate at its extreme SOC limits, as its charge sustaining mechanism gets progressively more extreme from towards the boundaries. The operation at either end of the SOC band has quite extreme control decisions to push the SOC away from its limits and this will inevitably have a negative impact on the fuel economy.

To further study the impact on fuel economy, the sensitivity plot for the absolute values of m_{efc} are presented in Fig. 7.4 for the four driving cycles. It can be seen that, in general, each of the control strategies have somewhat similar sensitivity to

variations in $SOC_{initial}$, with the exception of the XOS. In fact, the effect on the XOS is so pronounced that it is actually outperformed by both the TCS and PFCS for WL-L, and it is outperformed by TCS and almost matched by the PFCS for WL-E.

This limitation of the XOS was not visible in previous simulation results in this work, but has been discovered in this sensitivity analysis. However, considering the design and performance of the XOS, it is quite unlikely that it would ever get itself into a position of $SOC_{initial} = 50\%$ in the first place (due to the mentioned progressively more extreme charge sustaining behavior towards the SOC limits). However, for example, a HEV that has not been used for a very long time might find the SOC dropping to these levels through natural charge leakage. Nevertheless, the variations in $SOC_{initial}$ that would occur for each journey in a real vehicle would affect the XOS and compromise its fuel economy (even if not to the extent to be outperformed by the TCS and PFCS).

7.4 Driving Cycles

This section will be testing the performance of the control strategies for a new set of driving cycles, that have not been part of the tuning process. The aim is to assess how sensitive each control strategy is to varying driving conditions.

It is quite common for SCSs presented in the literature to be developed and tested for two or three driving cycles. This always raises the question of how effective the SCS in question might be for alternative driving cycles. This work has actively sought to develop, design, tune and test the control strategies for a wide range of driving cycles, as discussed in Section 2.6.1, which is why the driving cycle segments of the WLTP were employed. This has allowed the testing of each control strategy on low-speed urban (WL-L), medium-speed urban (WL-M), rural (WL-H), and high-speed highway (WL-E) driving cycles.

To further test the developed control strategies, they will be used to simulate six additional driving cycles. These driving cycles consist of the NYCC, HWFET, FTP-75 and US06 that are the most standard American driving cycles, as well as the EUDC and the NEDC that are the most conventional European driving cycles. These will be run for multiple iterations to allow the study of SOC deviation and fuel economy over longer period of driving. However, the EFC equivalence factors $S_{d,efc}$ and $S_{c,efc}$ have not been evaluated for these new driving cycles. Therefore, as an approximate solution, the equivalence factors from WL-L, WL-M, WL-H and WL-E will be used and assigned based on which driving cycle is most similar. While this compromises the precision of the study to some extent, the results are still quite reliable due to the repeated iterations and the reasonably narrow range of SOC deviation (as shown later). A brief summary of the driving cycles are presented in Table 7.1.

Table 7.1: Additional driving cycles tested

Driving Cycle	Iterations	EFC factors from	Description
NYCC	8	WL-L	Low-speed urban
NEDC	4	WL-M	Low-speed urban and high-speed rural
FTP75	4	WL-M	Medium-speed urban
EUDC	8	WL-H	High-speed rural
HWFET	4	WL-H	Medium-speed highway
US06	4	WL-E	Aggressive highway

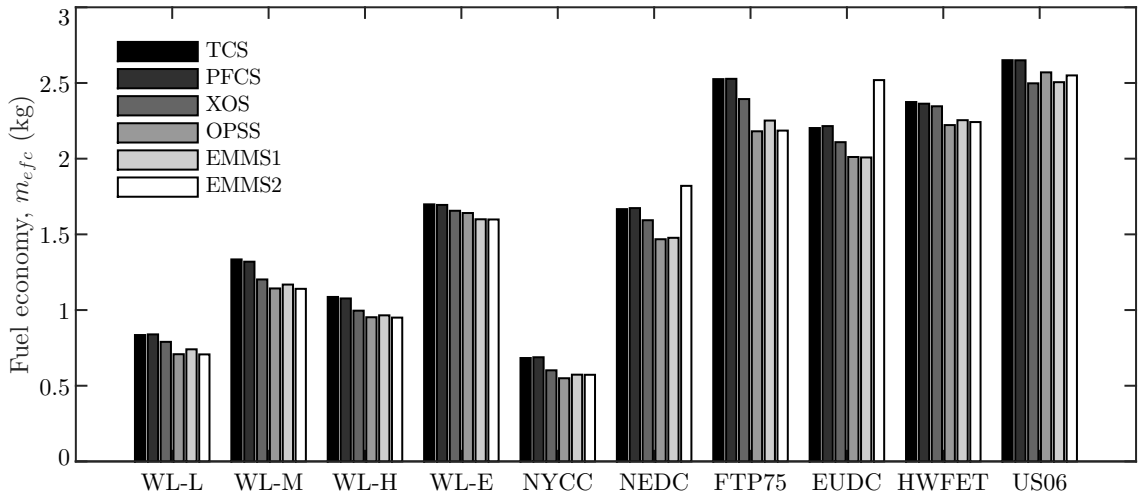

FIGURE 7.5: EFC m_{efc} for multiple iterations (see Table 7.1) of ten different driving cycles with six different real-time control strategies.

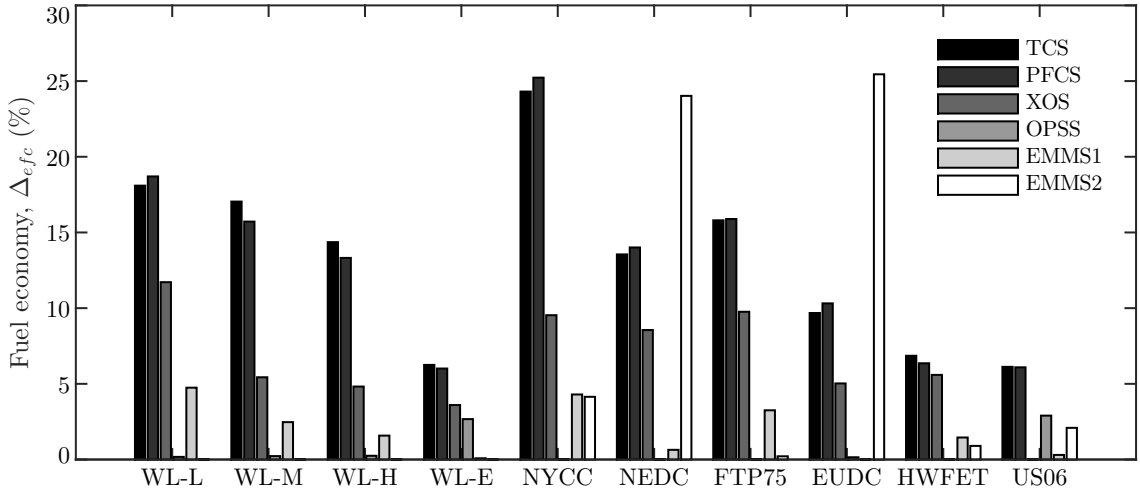

FIGURE 7.6: Relative EFC Δ_{efc} for multiple iterations (see Table 7.1) of ten different driving cycles with six different real-time control strategies.

Fuel economy results for the four WLTP driving cycles as well as the six additional driving cycles are presented in Fig. 7.5, where the absolute EFC results are given for each of the presented real-time control strategies, for each driving cycle. In addition, for further clarity, Fig. 7.6 shows the relative difference in EFC Δ_{efc} compared to the best strategy for that particular driving cycle. It can be seen for the first four sets of data (for WL-L, WL-M, WL-H and WL-E) that the results are reasonably consistent. The TCS and PFCS are the worst, followed by the XOS, followed by the OPSS and EMMS1, and finally the EMMS2 that yields the best fuel economy for each of these driving cycles.

However, the results for the additional six driving cycles are quite different. Quite remarkably, the EMMS2 is the worst-performing strategy for NEDC and EUDC. The results for the NEDC could have been expected, as it consists partly of low-speed urban driving and partly of high-speed rural driving. This prevents the EMMS2 from settling into an optimal mode of operation and it has to keep changing its desired mode of operation. However, the negative impact of such switching wouldn't have needed to be as high if the strategy had also considered the NEDC in the tuning process and the CSI factors had been chosen more appropriately. The weak results for the EUDC are somewhat more surprising, as the EMMS2 should have handled such repetitive driving cycles quite well. However, this result might be attributed to the distinct type of operation the EUDC exhibits, which is different from both WL-H and WL-E. Again, a better tuning process might have addressed this issue, but the point has been made: an optimization-based strategy will always be vulnerable to driving conditions that have not been part of the designing and tuning process.

It is also worth noting that the EMMS1 performance is much more reliable than the EMMS2. As the tuning process of EMMS1 is essentially based on powertrain analysis, its results are quite consistent. In contrast, the tuning of the EMMS2 is partly based on the global tuning of the GEMMS, which is much more susceptible to bias the control strategy based on the particular driving conditions for which it was tuned. Thus, EMMS1 not only performs consistently, but actually is the best control strategy for EUDC. This can partly be attributed to the artificially plain speed and acceleration profiling of the EUDC, which is always piecewise linear. Such operation allows plenty of steady state operation, allowing the EMMS1 to excel with its steady-state analysis of the powertrain efficiencies.

However, the most impressive results are achieved by the OPSS, which achieves the best results for four out of the six additional driving cycles being tested. Although the OPSS is also based on a tuning process involving only WL-L, WL-M, WL-H and WL-E, there is only a single tuning parameter and it is not very sensitive to driving conditions (apart from very aggressive driving). Consequently, the OPSS achieves excellent fuel economy results for all driving cycles apart from WL-E and US06 (where it still performs decently).

It is also worth noting that the XOS delivered the best results for the US06. In contrast to the OPSS, the XOS excels with aggressive driving, as it allows plenty of opportunities for regenerative braking and has a good balance between the use

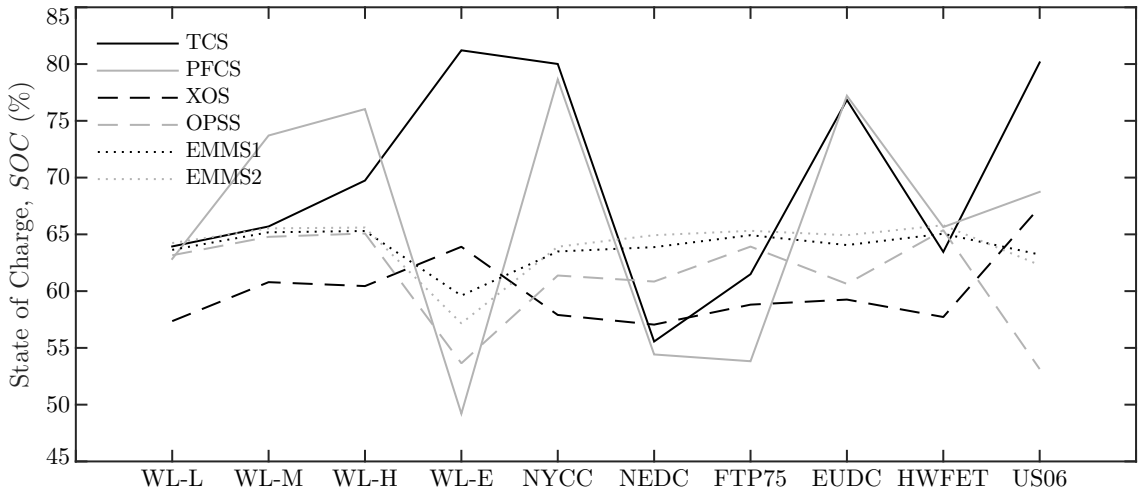

FIGURE 7.7: Final SOC values for multiple iterations (see Table 7.1) of ten different driving cycles with six different real-time control strategies.

of battery and engine. The latter is not true for urban driving with this particular vehicle model. The XOS can be expected to perform better for a powertrain where the battery power rating is more limited, such as in [15]. Nevertheless, even for all the other driving cycles, it always outperforms the conventional heuristic control strategies TCS and PFCS.

Finally, it is also of interest to check the charge sustaining ability of the control strategies under new driving conditions. The final SOC values from simulations with each of the control strategies are shown for each of the driving cycles in Fig. 7.7. It can be seen that the TCS and PFCS remain as erratic as ever, as they are based on state changing operation. Most of the other final SOC results are around 60-65%, which is quite good.

The EMMS strategies are the most capable ones in maintaining their SOC such that $SOC_{final} \approx SOC_{initial}$. The fact that the EMMS2 is able to do so, despite the poor performance for EUDC and NEDC, is somewhat surprising. The OPSS profile is more in line with expectations where the aggressive driving cycles WL-E and US06 are seeing a dip in SOC_{final}, but other results are more charge sustaining. Conversely, the XOS generally has a lower SOC_{final} value for most driving cycles, but is boosted for the aggressive driving cycles WL-E and US06, where it was shown to perform best. This chart, is quite effective in contrasting the nature of the XOS and OPSS, where the SOC will increase and decrease respectively for more aggressive driving.

7.5 Summary

This chapter has conducted a brief control sensitivity analysis of six real-time control strategies (TCS, PFCS, XOS, OPSS, EMMS1 and EMMS2), investigating the impact on changes in: tuning parameters; effectiveness of SSS; initial battery SOC; and selection of driving cycles.

It was found that the conventional heuristic strategies (TCS and PFCS) are most sensitive to correct tuning, with a 10% error causing a drop of 1% in fuel economy. This can be contrasted with the novel heuristic strategies (XOS and OPSS) which could suffer a 20% tuning error but only lose 0.2% in fuel economy. Thus, the novel heuristic strategies have more robust designs and might be easier to design.

The influence of the SSS on the preference among control strategies was found to be very significant. A poor SSS resulted in the conventional heuristic strategies being preferred, while a strong SSS overwhelmingly favored the novel heuristic strategies, as well as the EMMS. The results verified the earlier stated hypothesis that the TCS and PFCS are based on an outdated concept of the undesirability to switch the engine on or off. Thus, the control principles put forward with the XOS and OPSS can be expected to be successful in most modern HEVs.

By studying the impact of the initial battery SOC on the resulting fuel economy, it was found that the XOS in particular is more sensitive to deviations in initial conditions (in particular low supplies of charge). In fact, it is so sensitive that it was at times outperformed by the TCS and PFCS. The other novel strategies presented were not only quite robust in terms of fuel economy, but were also quite successful in returning the SOC to medium levels by the end of the driving cycles.

Lastly, the study of an additional six driving cycles exposed the strong sensitivity to driving conditions of the EMMS2 in particular. It failed miserably for two of the tested driving cycles, and was generally less effective when facing new types of driving. However, this could probably be addressed by better tuning. In contrast, the OPSS, for which the design is less tuning-dependent, excels at the new driving cycles (finishing top for four out of six).

Overall, the sensitivity analysis provided much deeper insights into the operation of each control strategy, and exposed limitations that were not visible in previous fuel economy results. In consideration of these results, the OPSS is the top performer.

Chapter 8

Conclusion

This thesis has gone though three distinct stages: Chapters 1 to 3 introduced the problem, the vehicle model and conventional control strategies; Chapters 4 and 5 presented several novel control strategies; and Chapters 6 and 7 have provided novel analysis and perspective of control strategies.

It has been found that the conventional control strategies are lacking in several regards. The heuristic strategies are based on outdated ideas of engine switching, making room for the novel heuristic strategies XOS and OPSS to outperform these conventional strategies by a good margin. As SSSs get better, this effect becomes more pronounced. The most established optimization-based strategy (ECMS) lacks knowledge about the powertrain it operates on. The design of the EMMS, based on a thorough understanding of the powertrain efficiencies, allowed the GEMMS to outperform the GECMS (suggesting that the EMMS2 would outperform the ECMS).

Also, overall, the optimization-based strategies have been found to be less effective than expected, due to the use of a high-fidelity model. The optimization-process often requires significant assumptions, which might hold true in a simple model, but not in a real vehicle. This was further aggravated when driving on fresh driving cycles, where heuristic strategies like the OPSS excelled.

This final chapter will not further summarize the findings of these past chapters, as it has been done quite concisely by the end of each chapter. Instead, the key contributions of this thesis will be listed. This will be followed and finished by an outlook on future research directions.

8.1 Contributions

This section will list the key contributions from each chapter of this work.

Chapters 2 and 3: Vehicle Model and Conventional Strategies

1. A high-fidelity model was further developed to enable more reliable study and design of control strategies.

2. A reduced model was developed to allow more than 50 times faster simulations at a very limited loss of precision. This enabled the implementation of control strategies with higher tuning requirements.

3. Conventional strategies (TCS, PFCS and GECMS) were implemented and tested for this high-fidelity model, providing new insights about their operation and effectiveness.

Chapter 4: Efficiency Maximizing Map Strategies

1. A framework for designing control strategies is proposed, such that the particular powertrain in question is optimized. Control objectives and cost functions are expressed in terms of component efficiencies, in an intuitive, measurable (replenishing efficiencies being the only non-measurable parameter), and comprehensive way (in contrast to the ECMS that typically assumes constant battery efficiency).

2. The concept of replenishing efficiency is proposed, that is not only more intuitive than equivalence factors, but also more compatible when dealing with battery efficiencies. Multiple uses of the replenishing efficiencies are considered (in EMMS0, EMMS1 and EMMS2), leading to varying advantages and disadvantages, which are explored.

3. Simulation results suggest that EMMS1 and EMMS2 are effective (but the latter will require more thorough tuning). The global version, the GEMMS, delivers superior performance than GECMS and is thus a better benchmark for future work.

Chapter 5: Heuristic Strategies

1. A useful classification is given for design principles for fuel economy optimizing, charge sustaining and implementation mechanisms. These can be mixed and matched to create a wide range of control strategies.
2. The XOS is proposed, which is found to deliver good fuel economy (7% improvement on PFCS), with very simple rules. Also, the exclusive operation of each power source allows intuitive auditory feedback from the engine, improving drivability, and reducing barriers to adoption of HEVs.
3. The OPSS is proposed, which is found to deliver excellent fuel economy (13% improvement on TCS), with very simple and intuitive rules. The results are found to be consistent across varying driving conditions.

Chapter 6: Global Optimality

1. The developed GHS outperforms the GECMS (with up to 1.82% margin), thus disproving the notion of approximate optimal solution for the GECMS.
2. Results, from both this work and literature, are used to make the case for the limited validity of designing advanced control strategies on simplistic models.
3. Alternative benchmarking methods and concepts are proposed, whereof only the GHS is implemented.

Chapter 7: Control Sensitivity Analysis

1. A sensitivity study of control strategies, the first of its kind, was conducted for: tuning parameters; effectiveness of SSSs; initial battery conditions; and varying driving cycles. This provided a deeper insight into each control strategy.
2. The superiority of the novel heuristic strategies (XOS and OPSS) over the conventional heuristic strategies (PFCS and TCS) is further shown by demonstrating more robustness to tuning errors.
3. The significant impact of the SSS on the fuel economy and the relative performance of control strategies is exposed. The results justify the superiority of the novel heuristic strategies for a modern HEV.

8.2 Future Research Direction

This section highlights some of the suggested future paths of research.

Chapter 2: Vehicle Model

1. Many components should be further refined, in particular the DC-DC converter and the CVT. The engine and battery models should be developed further, to allow the modeling of emissions and battery degradation.
2. Components with various power ratings should be modeled, allowing control strategies to be tested on different powertrains.
3. It would be useful to conduct hardware in the loop (HiL) simulations, or even implement control strategies in real vehicles.

Chapter 3: Conventional Strategies

1. A real-time ECMS should be implemented to act as a better benchmark for the EMMS, as well as to inform the discussion in Chapter 6.
2. Fuzzy logic controllers (FLCs) should be implemented to provide a fuller picture of the rule-based strategies.
3. More generally, wide types of strategies should be implemented for a large benchmarking exercise.

Chapter 4: Efficiency Maximizing Map Strategies

1. The concept of replenishing efficiency should be further refined, ideally allowing real-time estimation during driving in an intuitive way.
2. The strategies should be tuned more broadly (especially EMMS2), as exposed in Section 7.4. The base values for the replenishing efficiencies for EMMS2 should be selected more rigorously.
3. It would be interesting to try to use more dynamic expressions for the efficiencies rather than the steady state maps.

Chapter 5: Heuristic Strategies

1. Further heuristic strategies can be designed based on the design principles presented in Section 5.1. An exhaustive benchmarking exercise might be insightful.

2. The performance results of the XOS were not as impressive for the model used in this work, as compared to the previous results in [15]. The impact of powertrain sizing on control strategies would be a very useful study.

3. The use of fuzzy logic control (FLC) should be explored.

Chapter 6: Global Optimality

1. It would be useful if DP solutions on varying model complexities could be systematically compared to result of a high-fidelity model or a real vehicle.

2. A more powerful GHS (or alternative) should be designed to provide a better indication of how much the GECMS is lagging the global optimal solution.

3. New concepts of control space-constrained optimal solutions should be proposed (building on the brief discussion in Section 6.2.2), as they might be more valuable as benchmarks.

Chapter 7: Control Sensitivity Analysis

1. There are several other factors for which a sensitivity study would be of interest: component sizing, hybridization, or component temperatures.

2. The influence of the SSS on control strategies is dramatic, and definitely merits further study. This should also consider emissions and drivability though.

3. Sensitivity to driving conditions (including road slopes) should be studied further, including tests with mixed driving cycles, as opposed to repeating the same for multiple iterations. The EMMS2 performance on the NEDC in particular raises this flag.

Bibliography

[1] L. Glielmo, K. Butts, C. Canudas-de Wit, I. Kolmanovsky, B. Lohmann, and G. Stewart, "Automotive control," *The Impact of Control Technology*, 2011.

[2] A. Malikopoulos, "Supervisory power management control algorithms for hybrid electric vehicles: a survey," *IEEE Transactions on Intelligent Transportation Systems,*, vol. 15, no. 5, pp. 1869–1885, 2014.

[3] L. Serrao, A. Sciarretta, O. Grondin, A. Chasse, Y. Creff, D. Di Domenico, P. Pognant-Gros, C. Querel, and L. Thibault, "Open issues in supervisory control of hybrid electric vehicles: A unified approach using optimal control methods," *Oil & Gas Science and Technology–Rev. IFP Energies nouvelles*, vol. 68, no. 1, pp. 23–33, 2013.

[4] A. Shukla, *Modelling and Simulation of Hybrid Electric Vehicles*. PhD thesis, Imperial College London, 2012.

[5] S. A. Evangelou and A. Shukla, "Advances in the modelling and control of series hybrid electric vehicles," in *American Control Conference (ACC)*, pp. 527–534, IEEE, 2012.

[6] S. A. Evangelou and W. Shabbir, "Dynamic modeling platform for series hybrid electric vehicles," in *Advances in Automotive Control*, IFAC, in review.

[7] J. Meisel, W. Shabbir, and S. A. Evangelou, "A practical control methodology for parallel plug-in hybrid electric vehicle powertrains," in *Vehicle Power and Propulsion Conference (VPPC)*, pp. 1–6, IEEE, 2013.

[8] J. Meisel, W. Shabbir, and S. A. Evangelou, "Evaluation of the through-the-road architecture for plug-in hybrid electric vehicle powertrains," in *International Electric Vehicle Conference (IEVC)*, pp. 1–5, IEEE, 2013.

[9] J. Meisel, W. Shabbir, and S. A. Evangelou, "Control of PHEV and HEV parallel powertrains using a sequential linearization algorithm," tech. rep., SAE Technical Paper, 2015.

[10] M. Roche, W. Shabbir, and S. A. Evangelou, "Voltage control for enhanced power electronic efficiency in series hybrid electric vehicles," *IEEE Transactions on Vehicular Technology*, in review.

[11] W. Shabbir and S. A. Evangelou, "Efficiency analysis of a continuously variable transmission with linear control for a series hybrid electric vehicle," in *IFAC World Congress*, vol. 19, pp. 6264–6269, 2014.

[12] W. Shabbir, C. Arana, and S. A. Evangelou, "Series hybrid electric vehicle supervisory control based on off-line efficiency optimization," in *International Electric Vehicle Conference (IEVC)*, pp. 1–5, IEEE, 2012.

[13] W. Shabbir and S. A. Evangelou, "Efficiency maximizing and charge sustaining supervisory control for series hybrid electric vehicles," in *Conference on Decision and Control (CDC)*, pp. 6327–6332, IEEE, 2012.

[14] W. Shabbir and S. A. Evangelou, "Real-time control strategy to maximize hybrid electric vehicle powertrain efficiency," *Applied Energy*, vol. 135, pp. 512–522, 2014.

[15] W. Shabbir and S. A. Evangelou, "Exclusive operation strategy for the supervisory control of series hybrid electric vehicles," *IEEE Transactions on Control Systems Technology*, in review.

[16] M. Thommyppillai, S. Evangelou, and R. Sharp, "Advances in the development of a virtual car driver," *Multibody System Dynamics*, vol. 22, no. 3, pp. 245–267, 2009.

[17] H. B. Pacejka, *Tyre and Vehicle Dynamics*. Oxford: Butterworth Heinemann, 2002.

[18] Anon., *Autosim 2.5+ Reference Manual*. Mechanical Simulation Corporation, 709 West Huron, Ann Arbor MI, 1998. http://www.carsim.com.

[19] P. Pillay and R. Krishnan, "Modeling, simulation, and analysis of permanent-magnet motor drives. i. the permanent-magnet synchronous motor drive," *Industry Applications, IEEE Transactions on*, vol. 25, no. 2, pp. 265–273, 1989.

[20] EVO Electric Ltd., *AFM-140 Axial Flux Motor*, 2010.

[21] R. Burgos, P. Kshirsagar, A. Lidozzi, F. Wang, and D. Boroyevich, "Mathematical model and control design for sensorless vector control of permanent magnet synchronous machines," in *Workshops on Computers in Power Electronics*, pp. 76–82, IEEE, July 2006.

[22] C. Schauder and H. Mehta, "Vector analysis and control of advanced static var compensators," *Proc. Inst. Elect. Eng.*, vol. 140, pp. 299–306, 1993.

[23] M. Roche, "Parametric modelling, control and optimisation of hybrid vehicles," Master's thesis, Imperial College London, 2014.

[24] D. Graovac and M. Purschel, "IGBT power losses calculations using data-sheet parameters," tech. rep., Infineon Technologies, 2009.

[25] M. H. Bierhoff and F. W. Fuchs, "Semiconductor losses in voltage source and current source IGBT converters based on analytical derivation," in *Power Electronics Specialists Conference (PESC 04), IEEE 35th Annual*, vol. 4, pp. 2836–2842, 2004.

[26] Infineon Technologies AG, *Technical Information: FS150R12KT4*, 11 2013. Rev. 2.1.

[27] T. Kim and H. Kim, "Performance of integrated engine-cvt control considering powertrain loss and cvt response lag," *Proceedings of the Institution of Mechanical Engineers, Part D: Journal of Automobile Engineering*, vol. 216, pp. 545–553, 2002.

[28] R. P. G. Heath, "Seamless amt offers efficient alternative to CVT," *JSAE Annual Congress 314-20075013*, 2007.

[29] D. Gunji and H. Fujimoto, "Efficiency analysis of powertrain with toroidal continuously variable transmission for electric vehicles," in *Industrial Electronics Society, IECON 2013-39th Annual Conference of the IEEE*, pp. 6614–6619, IEEE, 2013.

[30] M. Delkhosh, M. S. Foumani, M. Boroushaki, M. Ekhtiari, and M. Dehghani, "Geometrical optimization of half toroidal continuously variable transmission using particle swarm optimization," *Scientia Iranica*, vol. 18, no. 5, pp. 1126 – 1132, 2011.

[31] C. Yildiz and T. M. Wasfy, "Time-accurate multibody dynamics model for toroidal traction drives," in *International Design Engineering Technical Conferences and Computers and Information in Engineering Conference*, pp. 257–265, ASME, 2011.

[32] C. M. Shepherd, "Design of primary and secondary cells - part 2. an equation describing battery discharge," *Journal of Electrochemical Society*, vol. 112, pp. 657–664, July 1965.

[33] O. Tremblay and L. A. Dessaint, "Experimental validation of a battery dynamic model for EV applications," *World Electric Vehicle Journal*, vol. 3, no. 1, pp. 1–10, 2009.

[34] Kokam Co., Ltd, *Cell Specification Data*.

[35] H. Li, F. Z. Peng, and J. Lawler, "A natural ZVS medium-power bidirectional DC-DC converter with minimum number of devices," *IEEE Transactions on Industry Applications*, vol. 39, 2003.

[36] F. Krismer and J. Kolar, "Efficiency-optimized high-current dual active bridge converter for automotive applications," *IEEE Transactions on Industrial Electronics*, vol. 59, pp. 2745–2760, 2012.

[37] R. Seyezhai, "Performance evaluation of modulation strategies for dual active bridge multiport DC-DC converters," *IOSR Journal of Engineering*, vol. I, pp. 077–083, 2011.

[38] Unknown, "Start/Stop technology reduces CO2 emissions and saves fuel," tech. rep., Robert Bosch GmbH, 08 2010.

[39] P. Mock, J. Kühlwein, U. Tietge, V. Franco, A. Bandivadekar, and J. German, "The wltp: How a new test procedure for cars will affect fuel consumption values in the eu," *International Council on Clean Transportation*, 2014.

[40] T. Katrašnik, "Analytical method to evaluate fuel consumption of hybrid electric vehicles at balanced energy content of the electric storage devices," *Applied Energy*, vol. 87, no. 11, pp. 3330–3339, 2010.

[41] L. Guzzella and A. Sciarretta, *Vehicle propulsion systems*. Springer, 2 ed., 2007.

[42] A. Sciarretta, M. Back, and L. Guzzella, "Optimal control of parallel hybrid electric vehicles," *IEEE Transactions on Control Systems Technology*, vol. 12, no. 3, pp. 352–363, 2004.

[43] S. Janisse, "Prof. Ferdinand Porsche created the first functional hybrid car." `http://press.porsche.com/news/release.php?id=642`. Accessed: 30-08-2015.

[44] A. Sciarretta and L. Guzzella, "Control of hybrid electric vehicles," *Control systems, IEEE*, vol. 27, no. 2, pp. 60–70, 2007.

[45] C. Anderson and E. Pettit, "The effects of apu characteristics on the design of hybrid control strategies for hybrid electric vehicles," tech. rep., SAE Technical Paper, 1995.

[46] C. G. Hochgraf, M. J. Ryan, and H. L. Wiegman, "Engine control strategy for a series hybrid electric vehicle incorporating load-leveling and computer controlled energy management," tech. rep., SAE Technical Paper, 1996.

[47] M. Ehsani, Y. Gao, and A. Emadi, *Modern electric, hybrid electric, and fuel cell vehicles: fundamentals, theory, and design*. CRC press, 2010.

[48] J. Gao, F. Sun, H. He, G. Zhu, and E. Strangas, "A comparative study of supervisory control strategies for a series hybrid electric vehicle," in *Asia-Pacific Power and Energy Engineering Conference (APPEEC)*, pp. 1–7, March 2009.

[49] K. Çagatay Bayindir, M. A. Gözüküçük, and A. Teke, "A comprehensive overview of hybrid electric vehicle: Powertrain configurations, powertrain control techniques and electronic control units," *Energy Conversion and Management*, vol. 52, no. 2, pp. 1305 – 1313, 2011.

[50] R. Johri and Z. Filipi, "Optimal energy management of a series hybrid vehicle with combined fuel economy and low-emission objectives," *Proceedings of the Institution of Mechanical Engineers, Part D: Journal of Automobile Engineering*, vol. 228, no. 12, pp. 1424–1439, 2014.

[51] M. R. Cuddy and K. B. Wipke, "Analysis of the fuel economy benefit of drivetrain hybridization," tech. rep., SAE Technical Paper, 1997.

[52] N. Jalil, N. A. Kheir, and M. Salman, "A rule-based energy management strategy for a series hybrid vehicle," in *American Control Conference (ACC)*, vol. 1, pp. 689–693, IEEE, 1997.

[53] J. Bumby and I. Forster, "Optimisation and control of a hybrid electric car," in *Control Theory and Applications, IEE Proceedings D*, vol. 134, pp. 373–387, IET, 1987.

[54] J. Gao, G. G. Zhu, E. G. Strangas, and F. Sun, "Equivalent fuel consumption optimal control of a series hybrid electric vehicle," *Proceedings of the Institution of Mechanical Engineers, Part D: Journal of Automobile Engineering*, vol. 223, no. 8, pp. 1003–1018, 2009.

[55] S. G. Wirasingha and A. Emadi, "Classification and review of control strategies for plug-in hybrid electric vehicles," *IEEE Transactions on Vehicular Technology*, vol. 60, no. 1, pp. 111–122, 2011.

[56] F. Salmasi, "Control strategies for hybrid electric vehicles: Evolution, classification, comparison, and future trends," *IEEE Transactions on Vehicular Technology*, vol. 56, pp. 2393–2404, Sept 2007.

[57] M. Kim, D. Jung, and K. Min, "Hybrid thermostat strategy for enhancing fuel economy of series hybrid intracity bus," *IEEE Transactions on Vehicular Technology*, vol. 63, no. 8, pp. 3569–3579, 2014.

[58] Y. Ko, J. Lee, and H. Lee, "A supervisory control algorithm for a series hybrid vehicle with multiple energy sources," *Transactions on Vehicular Technology*, 2015.

[59] X. Zhang, C. C. Mi, and C. Yin, "Active-charging based powertrain control in series hybrid electric vehicles for efficiency improvement and battery lifetime extension," *Journal of Power Sources*, vol. 245, pp. 292–300, 2014.

[60] M. Hajimiri and F. Salmasi, "A fuzzy energy management strategy for series hybrid electric vehicle with predictive control and durability extension of the battery," in *Conference on Electric and Hybrid Vehicles (ICEHV)*, pp. 1–5, IEEE, 2006.

[61] S. G. Li, S. Sharkh, F. C. Walsh, and C.-N. Zhang, "Energy and battery management of a plug-in series hybrid electric vehicle using fuzzy logic," *IEEE Transactions on Vehicular Technology*, vol. 60, no. 8, pp. 3571–3585, 2011.

[62] A. M. Phillips, M. Jankovic, and K. E. Bailey, "Vehicle system controller design for a hybrid electric vehicle," in *International Conference on Control Applications*, pp. 297–302, IEEE, 2000.

[63] D. Crolla, Q. Ren, S. ElDemerdash, and F. Yu, "Controller design for hybrid vehicles - state of the art review," in *Vehicle Power and Propulsion Conference (VPPC)*, pp. 1–6, Sept 2008.

[64] S. Jeon, S. Jo, Y. Park, and J. Lee, "Multi-mode driving control of a parallel hybrid electric vehicle using driving pattern recognition," *Journal of dynamic systems, measurement, and control*, vol. 124, no. 1, pp. 141–149, 2002.

[65] Y. Zhu, Y. Chen, G. Tian, H. Wu, and Q. Chen, "A four-step method to design an energy management strategy for hybrid vehicles," in *American Control Conference (ACC)*, vol. 1, pp. 156–161, IEEE, 2004.

[66] J.-S. Won, R. Langari, and M. Ehsani, "An energy management and charge sustaining strategy for a parallel hybrid vehicle with cvt," *Control Systems Technology, IEEE Transactions on*, vol. 13, no. 2, pp. 313–320, 2005.

[67] C. Kim, E. NamGoong, S. Lee, T. Kim, and H. Kim, "Fuel economy optimization for parallel hybrid vehicles with cvt," tech. rep., SAE Technical Paper, 1999.

[68] G. Paganelli, T. Guerra, S. Delprat, J. Santin, M. Delhom, and E. Combes, "Simulation and assessment of power control strategies for a parallel hybrid car," *Proceedings of the Institution of Mechanical Engineers, Part D: Journal of Automobile Engineering*, vol. 214, no. 7, pp. 705–717, 2000.

[69] G. Paganelli, G. Ercole, A. Brahma, Y. Guezennec, and G. Rizzoni, "General supervisory control policy for the energy optimization of charge-sustaining hybrid electric vehicles," *JSAE review*, vol. 22, no. 4, pp. 511–518, 2001.

[70] G. Paganelli, S. Delprat, T.-M. Guerra, J. Rimaux, and J.-J. Santin, "Equivalent consumption minimization strategy for parallel hybrid powertrains," in *Vehicular Technology Conference (VTC)*, vol. 4, pp. 2076–2081, IEEE, 2002.

[71] S. Delprat, T. M. Guerra, G. Paganelli, J. Lauber, and M. Delhom, "Control strategy optimization for an hybrid parallel powertrain," in *American Control Conference (ACC)*, vol. 2, pp. 1315–1320, IEEE, 2001.

[72] S. Delprat, J. Lauber, T. M. Guerra, and J. Rimaux, "Control of a parallel hybrid powertrain: optimal control," *Vehicular Technology, IEEE Transactions on*, vol. 53, no. 3, pp. 872–881, 2004.

[73] P. Pisu and G. Rizzoni, "A supervisory control strategy for series hybrid electric vehicles with two energy storage systems," in *Vehicle Power and Propulsion, 2005 IEEE Conference*, pp. 8–pp, IEEE, 2005.

[74] P. Pisu, K. Koprubasi, and G. Rizzoni, "Energy management and drivability control problems for hybrid electric vehicles," in *Conference on Decision and Control and European Control Conference (CDC-ECC)*, pp. 1824–1830, IEEE, 2005.

[75] C. Musardo, G. Rizzoni, Y. Guezennec, and B. Staccia, "A-ecms: An adaptive algorithm for hybrid electric vehicle energy management," *European Journal of Control*, vol. 11, no. 4, pp. 509–524, 2005.

[76] S. Kermani, S. Delprat, R. Trigui, and T.-M. Guerra, "Predictive energy management of hybrid vehicle," in *Vehicle Power and Propulsion Conference, 2008. VPPC'08. IEEE*, pp. 1–6, IEEE, 2008.

[77] L. Serrao and G. Rizzoni, "Optimal control of power split for a hybrid electric refuse vehicle," in *Proceedings of the 2008 American Control Conference*, pp. 4498–4503, 2008.

[78] L. Serrao, S. Onori, and G. Rizzoni, "ECMS as a realization of pontryagin's minimum principle for HEV control," in *American Control Conference (ACC)*, pp. 3964–3969, IEEE, 2009.

[79] N. Kim and A. Rousseau, "Assessment by simulation of benefits of new hev powertrain configurations," in *Internatiional Scientific Conference on Hybrid and Electric Vehicles (RHEVE)*, pp. 1–13, IFPEN, 2011.

[80] L. Serrao, S. Onori, A. Sciarretta, Y. Guezennec, and G. Rizzoni, "Optimal energy management of hybrid electric vehicles including battery aging," in *American Control Conference (ACC)*, pp. 2125–2130, IEEE, 2011.

[81] S. Ebbesen, P. Elbert, and L. Guzzella, "Battery state-of-health perceptive energy management for hybrid electric vehicles," *Vehicular Technology, IEEE Transactions on*, vol. 61, no. 7, pp. 2893–2900, 2012.

[82] D. Ambühl and L. Guzzella, "Predictive reference signal generator for hybrid electric vehicles," *Vehicular Technology, IEEE Transactions on*, vol. 58, no. 9, pp. 4730–4740, 2009.

[83] C. Zhang and A. Vahidi, "Real-time optimal control of plug-in hybrid vehicles with trip preview," in *American Control Conference (ACC)*, pp. 6917–6922, IEEE, 2010.

[84] E. Finkeldei and M. Back, "Implementing an mpc algorithm in a vehicle with a hybrid powertrain using telematics as a sensor for powertrain control," in *Proceedings of the 1st IFAC Symposium on Advances in Automotive Control, Salerno, Italy*, 2004.

[85] A. Vahidi, A. Stefanopoulou, and H. Peng, "Model predictive control for starvation prevention in a hybrid fuel cell system," in *American Control Conference (ACC)*, vol. 1, pp. 834–839, IEEE, 2004.

[86] F. Borrelli, P. Falcone, T. Keviczky, J. Asgari, and D. Hrovat, "Mpc-based approach to active steering for autonomous vehicle systems," *International Journal of Vehicle Autonomous Systems*, vol. 3, no. 2-4, pp. 265–291, 2005.

[87] V. L. Bageshwar, W. L. Garrard, and R. Rajamani, "Model predictive control of transitional maneuvers for adaptive cruise control vehicles," *Vehicular Technology, IEEE Transactions on*, vol. 53, no. 5, pp. 1573–1585, 2004.

[88] L. Johannesson, M. Åsbogård, and B. Egardt, "Assessing the potential of predictive control for hybrid vehicle powertrains using stochastic dynamic programming," *Intelligent transportation systems, IEEE transactions on*, vol. 8, no. 1, pp. 71–83, 2007.

[89] L. Johannesson, M. Åsbogård, and B. Egardt, "Assessing the potential of predictive control for hybrid vehicle powertrains using stochastic dynamic programming," in *Intelligent Transportation Systems*, pp. 366–371, IEEE, 2005.

[90] S. Biswas, R. Tatchikou, and F. Dion, "Vehicle-to-vehicle wireless communication protocols for enhancing highway traffic safety," *Communications Magazine, IEEE*, vol. 44, no. 1, pp. 74–82, 2006.

[91] G. Ripaccioli, D. Bernardini, S. Di Cairano, A. Bemporad, and I. Kolmanovsky, "A stochastic model predictive control approach for series hybrid electric vehicle power management," in *American Control Conference (ACC), 2010*, pp. 5844–5849, IEEE, 2010.

[92] Y. Wang and S. Boyd, "Fast model predictive control using online optimization," *Control Systems Technology, IEEE Transactions on*, vol. 18, no. 2, pp. 267–278, 2010.

[93] C.-C. Lin, H. Peng, and J. Grizzle, "A stochastic control strategy for hybrid electric vehicles," in *American Control Conference (ACC)*, vol. 5, pp. 4710–4715, IEEE, 2004.

[94] J. Liu and H. Peng, "Modeling and control of a power-split hybrid vehicle," *IEEE Transactions on Control Systems Technology*, vol. 16, no. 6, pp. 1242–1251, 2008.

[95] I. Arsie, M. Graziosi, C. Pianese, G. Rizzo, and M. Sorrentino, "Optimization of supervisory control strategy for parallel hybrid vehicle with provisional load estimate," *Proc. of AVEC04*, pp. 23–27, 2004.

[96] R. Bellman, *Dynamic programming*. Princeton University Press, 1957.

[97] F. L. Lewis and V. L. Syrmos, *Optimal control*. John Wiley & Sons, 1995.

[98] A. Brahma, Y. Guezennec, and G. Rizzoni, "Optimal energy management in series hybrid electric vehicles," in *American Control Conference (ACC)*, vol. 1, pp. 60–64, IEEE, 2000.

[99] C.-C. Lin, J.-M. Kang, J. Grizzle, and H. Peng, "Energy management strategy for a parallel hybrid electric truck," in *American Control Conference (ACC)*, vol. 4, pp. 2878–2883, IEEE, 2001.

[100] C.-C. Lin, H. Peng, J. W. Grizzle, and J.-M. Kang, "Power management strategy for a parallel hybrid electric truck," *IEEE Transactions on Control Systems Technology*, vol. 11, no. 6, pp. 839–849, 2003.

[101] J. Pu and C. Yin, "Optimal control of fuel economy in parallel hybrid electric vehicles," *Proceedings of the Institution of Mechanical Engineers, Part D: Journal of Automobile Engineering*, vol. 221, no. 9, pp. 1097–1106, 2007.

[102] J. Liu and H. Peng, "Control optimization for a power-split hybrid vehicle," in *American Control Conference, 2006*, pp. 6–pp, IEEE, 2006.

[103] O. Sundström, L. Guzzella, and P. Soltic, "Optimal hybridization in two parallel hybrid electric vehicles using dynamic programming," in *Proceedings of the 17th IFAC world congress*, vol. 17, pp. 4642–4647, 2008.

[104] L. Serrao, S. Onori, and G. Rizzoni, "A comparative analysis of energy management strategies for hybrid electric vehicles," *Journal of Dynamic Systems, Measurement, and Control*, vol. 133, no. 3, p. 031012, 2011.

[105] A. Piccolo, L. Ippolito, V. Z. Galdi, and A. Vaccaro, "Optimisation of energy flow management in hybrid electric vehicles via genetic algorithms," in *International Conference on Advanced Intelligent Mechatronics*, vol. 1, pp. 434–439, IEEE/ASME, 2001.

[106] M. Montazeri-Gh, A. Poursamad, and B. Ghalichi, "Application of genetic algorithm for optimization of control strategy in parallel hybrid electric vehicles," *Journal of the Franklin Institute*, vol. 343, no. 4, pp. 420–435, 2006.

[107] M. J. Gielniak and Z. J. Shen, "Power management strategy based on game theory for fuel cell hybrid electric vehicles," in *Vehicular Technology Conference, 2004. VTC2004-Fall. 2004 IEEE 60th*, vol. 6, pp. 4422–4426, IEEE, 2004.

[108] C. Dextreit and I. V. Kolmanovsky, "Game theory controller for hybrid electric vehicles," *Control Systems Technology, IEEE Transactions on*, vol. 22, no. 2, pp. 652–663, 2014.

[109] E. D. Tate and S. P. Boyd, "Finding ultimate limits of performance for hybrid electric vehicles," tech. rep., SAE Technical Paper, 2000.

[110] X. Hu, L. Johannesson, N. Murgovski, and B. Egardt, "Longevity-conscious dimensioning and power management of the hybrid energy storage system in a fuel cell hybrid electric bus," *Applied Energy*, 2014.

[111] T. Nüesch, P. Elbert, M. Flankl, C. Onder, and L. Guzzella, "Convex optimization for the energy management of hybrid electric vehicles considering engine start and gearshift costs," *Energies*, vol. 7, no. 2, pp. 834–856, 2014.

[112] S. Boyd and L. Vandenberghe, *Convex optimization*. Cambridge university press, 2009.

[113] B. Geng, J. K. Mills, and D. Sun, "Energy management control of microturbine-powered plug-in hybrid electric vehicles using the telemetry equivalent consumption minimization strategy," *IEEE Transactions on Vehicular Technology*, vol. 60, no. 9, pp. 4238–4248, 2011.

[114] J. Torres, R. Gonzalez, A. Gimenez, and J. Lopez, "Energy management strategy for plug-in hybrid electric vehicles. a comparative study," *Applied Energy*, vol. 113, pp. 816–824, 2014.

[115] D. Feroldi, M. Serra, and J. Riera, "Energy management strategies based on efficiency map for fuel cell hybrid vehicles," *Journal of Power Sources*, vol. 190, no. 2, pp. 387–401, 2009.

[116] N. J. Schouten, M. A. Salman, and N. A. Kheir, "Energy management strategies for parallel hybrid vehicles using fuzzy logic," *Control Engineering Practice*, vol. 11, no. 2, pp. 171–177, 2003.

[117] L. Damiani, M. Repetto, and A. P. Prato, "Improvement of powertrain efficiency through energy breakdown analysis," *Applied Energy*, vol. 121, pp. 252–263, 2014.

[118] X. Hu, N. Murgovski, L. Johannesson, and B. Egardt, "Energy efficiency analysis of a series plug-in hybrid electric bus with different energy management strategies and battery sizes," *Applied Energy*, vol. 111, pp. 1001–1009, 2013.

[119] V. Sezer, M. Gokasan, and S. Bogosyan, "A novel ECMS and combined cost map approach for high-efficiency series hybrid electric vehicles," *IEEE Transactions on Vehicular Technology*, vol. 60, no. 8, pp. 3557–3570, 2011.

[120] G. M. Masters, *Renewable and efficient electric power systems*. John Wiley & Sons, 2004.